

MICRO & NANO TECHNOLOGIES

# Micromachining Using Electrochemical Discharge Phenomenon

Fundamentals and Applications of Spark Assisted Chemical Engraving



Rolf Wüthrich

# **MICRO & NANO TECHNOLOGIES**

**Series Editor: Jeremy Ramsden**

*Professor of Nanotechnology*

*Microsystems and Nanotechnology Centre, Department of Materials  
Cranfield University, United Kingdom*

The aim of this book series is to disseminate the latest developments in small scale technologies with a particular emphasis on accessible and practical content. These books will appeal to engineers from industry, academia and government sectors.

William Andrew is an imprint of Elsevier  
Linacre House, Jordan Hill, Oxford OX2 8DP, UK  
30 Corporate Drive, Suite 400, Burlington, MA 01803, USA

First edition 2009

Copyright © 2009 Elsevier Inc. All rights reserved

No part of this publication may be reproduced, stored in a retrieval system or transmitted in any form or by any means electronic, mechanical, photocopying, recording or otherwise without the prior written permission of the publisher

Permissions may be sought directly from Elsevier's Science & Technology Rights Department in Oxford, UK: phone (+44) (0) 1865 843830; fax (+44) (0) 1865 853333; email: [permissions@elsevier.com](mailto:permissions@elsevier.com). Alternatively visit the Science and Technology website at [www.elsevierdirect.com/rights](http://www.elsevierdirect.com/rights) for further information

#### Notice

No responsibility is assumed by the publisher for any injury and/or damage to persons or property as a matter of products liability, negligence or otherwise, or from any use or operation of any methods, products, instructions or ideas contained in the material herein. Because of rapid advances in the medical sciences, in particular, independent verification of diagnoses and drug dosages should be made

#### British Library Cataloguing in Publication Data

A catalogue record for this book is available from the British Library

#### Library of Congress Cataloging-in-Publication Data

Wüthrich, Rolf.

Micromachining using electrochemical discharge phenomenon: fundamentals and applications of spark assisted chemical engraving/Rolf Wüthrich.

p. cm. – (Micro & nano technologies)

Includes bibliographical references.

ISBN 978-08155-1587-6

1. Micromachining. 2. Electrochemical cutting. 3. Electric discharges—Industrial applications. 4. Plasma etching. I. Title

TJ1191.5.W83 2009

620'.5—dc22

2008046698

ISBN: 978-0-81-551587-6

|   |
|---|
| For information on all Elsevier publications<br>visit our website at <a href="http://elsevierdirect.com">elsevierdirect.com</a> |
|---|

Printed and bound in United States of America

09 10 11 12 11 10 9 8 7 6 5 4 3 2 1

Working together to grow  
libraries in developing countries

[www.elsevier.com](http://www.elsevier.com) | [www.bookaid.org](http://www.bookaid.org) | [www.sabre.org](http://www.sabre.org)

ELSEVIER

BOOK AID  
International

Sabre Foundation

*To my wife Evgenia and my children Sandra and Alexandre  
for their continuous support during my work.*



# Series Editor's Preface

The possibility of modifying materials using electrical discharges has fascinated mankind ever since he observed the results of lightning striking objects in nature. We do not, of course, know when the first observation took place, but we may be reasonably sure that it was a sufficiently long time ago that many millennia had to pass before electricity was “tamed,” and subsequently put to work modifying materials in a systematic, “scientific” way—as exemplified by Humphry Davy’s electrolysing common salt to produce metallic sodium at the Royal Institution in London.

But these are essentially faradaic processes (named after Davy’s erstwhile assistant Michael Faraday), and such processes are also used extensively today for (micro)machining, as exemplified by electrochemical machining (ECM). They are relatively well known, and are applicable to conducting workpieces. Far less well known is the technology of what is now called spark-assisted chemical engraving (SACE), in which the workpiece is merely placed in the close vicinity of the pointed working electrode, and is eroded by sparks jumping across the gas bubbles that develop around the electrode to reach the electrolyte in which everything is immersed, the circuit being completed by the presence of a large counter-electrode.

This technology can therefore be equally well used for workpieces made from non-conducting materials such as glass, traditionally difficult to machine, especially at the precision microlevel needed for such applications as microfluidic mixers and reactors. The development of attractive machining technologies such as SACE is in itself likely to play a decisive part in the growth of microfluidics-based methods in chemical processing and medical diagnostics, to name just two important areas of application.

Since, as the author very correctly points out, knowledge about non-faradaic ECM methods is presently remarkably scanty within the microsystems community, this book is conceived as a comprehensive treatise, covering the entire field, starting with a lucid explanation of the physicochemical fundamentals, and ending with a thorough discussion of the practical questions likely to be asked, and an authoritative exposition of the means to their resolution.

I therefore anticipate that this book will significantly contribute to enabling the rapid growth of micromachining of non-conducting materials, for which there is tremendous hitherto unexploited potential.

Jeremy Ramsden  
Cranfield University, United Kingdom  
December 2008

# Preface

Micromachining using electrochemical discharges is a fairly new and still largely unknown micromachining technology for glass and other non-conductive materials, like composites for example. While first reports go back to the end of the 1950s in Japan, it is only recently that the fundamental phenomenon behind the process has been elucidated. Paradoxically, one of the main effects, the electrochemical discharges, has been known for more than 150 years, and was used previously for various technical applications ranging from X-ray imaging to wireless telegraphy. However, today only a very specialised research community is aware of it.

Even though micromachining using electrochemical discharges has been known for a half a century, so far, no industrial application is available, and it is only quite recently that a systematic investigation about the process's parameters has begun in earnest. The interest in micromachining with electrochemical discharges witnessed a renaissance a few years ago. Significant work on the fundamental and application side were made, some of which showed the highly promising potentials of this technique. In the growing field of microfluidics this micromachining technology could become a very useful tool for simple and rapid prototyping. Its capacity for machining high aspect ratio structures also makes the technique very interesting for microdevice connections.

This book is a first attempt to collect the state-of-the-art knowledge on micromachining using electrochemical discharges and to establish the fundamentals of this exciting technology. For glass material, the degree of knowledge reached a level high enough to allow several interesting applications. For other materials, work is still needed before applications may emerge. This monograph will hopefully contribute and stimulate new research activities and applications. The author is convinced that the great potential of electrochemical discharges is far from being exploited completely. For example, it is only recently that a completely new field was opened by showing that these phenomena could be used to synthesise metallic nanoparticles.

In preparing this book I benefited from discussions with my colleagues and coworkers. It is not possible to mention all of them here. I would like to express in particular my appreciation to Prof. Dr. Hannes Bleuler who gave me the great opportunity of working in his group over the course of many years; to Dr. Hans Langen who introduced me to the field of micromachining with electrochemical discharges; to Prof. Dr. Christos Comninellis who revealed to me many secrets of electrochemistry; to Dr. hab. Philippe Mandin who initiated me to multi-phase flow simulations; and to Prof. Dr. Max Hongler who guided me in my researches in non-linear dynamics. I would like to also thank the whole Department of Mechanical and Industrial Engineering from Concordia University, who offered me an excellent and stimulating working environment. A great thank you as well to my current research group who in the recent two years worked out several important results adding definitively an important contribution to the present book.

I would like to thank William Andrew Inc. for giving me the opportunity to write this book, and for their help during all the phases of the manuscript, making publication possible.

Last but not least I would like to thank my spouse, Evgenia, and my children, Alexandre and Sandra, for their patience and understanding. Without their support this book would never have been possible.

The research of the author in the field of electrochemical discharges is sponsored by the Swiss Foundation of Science, the Natural Sciences and Engineering Research Council of Canada, and the Fonds Québécois pour la Recherche sur la Nature et les Technologies.

Rolf Wüthrich  
Montreal, Canada  
December 2008

# 1 Machining with Electrochemical Discharges—An Overview

---

Since the very beginning of history, and even prehistory, humanity has invested a lot of effort in developing the skill of processing materials. There is no need to present the fundamental importance of the capability of machining in any technology. Any new technology requires new machining skills. In the last century, the need for using more and more specialised materials (e.g., silicon, composites, or ceramics) greatly increased the already large arsenal of machining technologies.

The last century also saw the birth of micromachining, in particular micromachining of silicon. At present, a huge variety of micromachining techniques are available for silicon. A similar situation exists for electrically conductive materials, where, in particular, electrochemical machining (ECM) and electrical discharge machining (EDM) are two very powerful tools available. However, several electrically non-conductive materials are also of great interest for many applications. Glass and composite materials are two examples. The technical requirements for using glass in microsystems are growing. Medical devices requiring biocompatible materials are only one of many examples.

The importance of glass is also growing in the field of *microelectromechanical systems* (MEMS). The term MEMS refers to a collection of microsensors and actuators. MEMS emerged in the 1990s with the development of processes for the fabrication of integrated circuits. In particular, Pyrex<sup>®</sup> glass is widely used because it can be bonded by *anodic bonding* (also called *field-assisted thermal bonding* or *electrostatic bonding*) to silicon. Glass has some very interesting properties such as its chemical resistance or biocompatibility. It is amorphous and can therefore be chemically attacked in all directions. As glass is transparent, it is widely used in optical applications or in applications where optical visualisation of a process is needed. Some promising applications for glass in the MEMS field are microaccelerometers, microreactors, micropumps, and medical devices (e.g., flow sensors or drug delivery devices).

A representative example in which glass-to-silicon bonding is used are bulk micromachined accelerometers [121]. In this case, glass serves several functions:

- provides a seal and the desired damping;
- can be used as a capacitor when a metal plate is placed on it;
- can be an overload protection.

The use of glass is also very common in other sensors than accelerometers using capacitive sensing technology.

## 1.1 Spark-Assisted Chemical Engraving

Various techniques are available to micromachine glass. However, one of the main limiting factors in incorporating glass into microdevices is its limited machinability. A similar situation exists for other hard-to-machine materials such as ceramics and composite materials. A possible answer to these issues could be spark-assisted chemical engraving (SACE), or electrochemical discharge machining (ECDM).

### 1.1.1 What is SACE?

SACE makes use of electrochemical and physical phenomena to machine glass. The principle is explained in Fig. 1.1 [128]. The workpiece is dipped in an appropriate electrolytic solution (typically sodium hydroxide or potassium hydroxide). A constant DC voltage is applied between the *machining tool* or *tool-electrode* and the *counter-electrode*. The tool-electrode is dipped a few millimetres in the electrolytic solution and the counter-electrode is, in general, a large flat plate. The tool-electrode surface is always significantly smaller than the counter-electrode surface (by about a factor of 100). The tool-electrode is generally polarised as a cathode, but the opposite polarisation is also possible.

When the cell terminal voltage is low (lower than a critical value called *critical voltage*, typically between 20 and 30 V), traditional electrolysis occurs

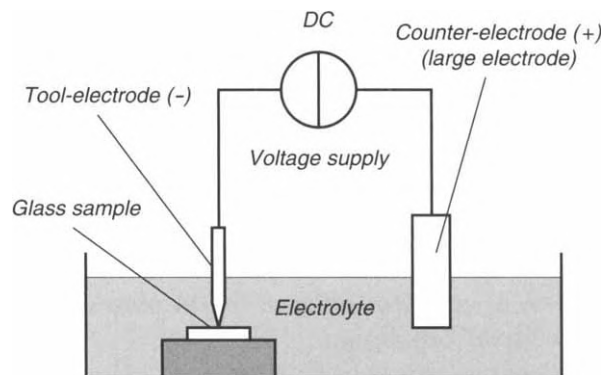


**Figure 1.1** Principle of SACE technology: the glass sample to be machined is dipped in an electrolytic solution. A constant DC voltage is applied between the tool-electrode and the counter-electrode. Reprinted from [128] with permission from Elsevier.

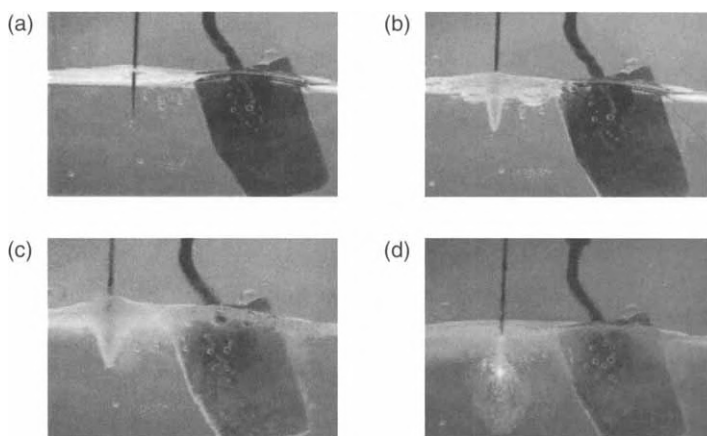


**Figure 1.2** Successive steps towards the electrochemical discharge phenomena: (a) 0 V; (b) 7.5 V; (c) 15 V; (d) 40 V. Two electrodes are dipped into an electrolyte. The terminal voltage is progressively increased from 0 to 40 V. At around 25 V a gas film is formed around the cathode, and at around 30 V the electrochemical discharges are clearly visible. Reprinted from [128] with permission from Elsevier.

(Fig. 1.2). Hydrogen gas bubbles are formed at the tool-electrode and oxygen bubbles at the counter-electrode depending on their polarisation and the electrolyte used. When the terminal voltage is increased, the current density also increases and more and more bubbles are formed. A *bubble layer* develops around the electrodes. As presented in Chapter 3, the density of the bubbles and their mean radius increase with increasing current density. When the terminal voltage is increased above the critical voltage, the bubbles coalesce into a *gas film* around the tool-electrode. Light emission can be observed in the film when electrical discharges, the so-called electrochemical discharges, occur between the tool and the surrounding electrolyte. The mean temperature of the electrolytic solution increases in the vicinity of the tool-electrode to about 80–90°C. Machining is possible if the tool-electrode is in the near vicinity of the glass sample (Fig. 1.3). Typically, the tool-electrode has to be closer than 25  $\mu\text{m}$  from the workpiece for glass machining to take place.

However, things are not as simple as they seem. The gas film around the tool-electrode is not always stable. Microexplosions may occur destroying the machined structure locally. During drilling of holes, the local temperature can increase to such an extent, resulting in heat affected zones or even cracking.

### 1.1.2 Machining Examples

SACE technology can be used for flexible glass microstructuring. Channel-like microstructures and microholes can be obtained. Two examples are illustrated in Fig. 1.4. The channel microstructure was machined with a cylindrical 90  $\mu\text{m}$

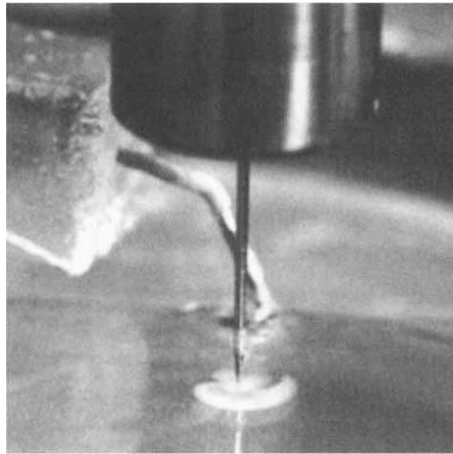


**Figure 1.3** Close-up view of micromachining with electrochemical discharges.

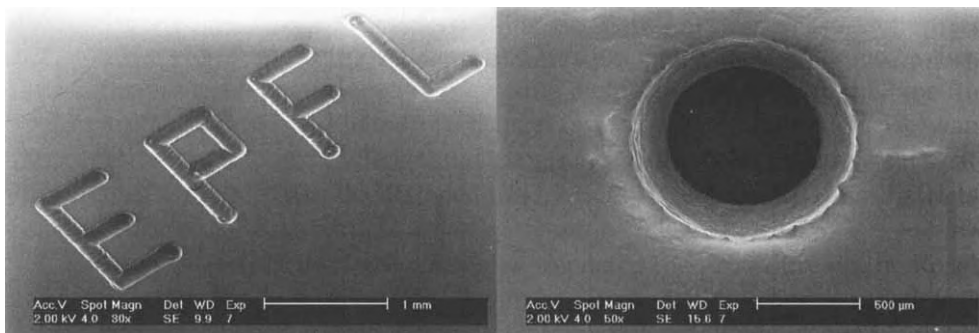


**Figure 1.4** Micrographs of a SACE-machined channel-like structure (left) and a microhole (right) in Pyrex® glass. Reprinted from [128] with permission from Elsevier.

diameter tool-electrode at an applied voltage of 30 V. Machining was done in one step with a tool speed of 0.05 mm/s. The channels are about 100 µm wide and 200 µm deep. The microhole illustrates the possibility of machining relatively deep structures. In this case the microhole is 1 mm deep.

The most interesting characteristic of SACE is its flexibility. No mask is needed, and just as in traditional machining, the desired structure can be machined directly. A typical four axes SACE machining facility is shown in Fig. 1.5. This facility includes two processing units. The first unit, called the *WEDG unit*, allows the manufacturing of tools with different shapes using the wire electrical discharge grinding (WEDG) technology [85]. The second processing unit is the *SACE-unit*, in which glass machining is done. The unit is designed for a maximum of 10 inch glass wafers. An interesting aspect of this machining prototype is the possibility to machine glass and the tool-electrodes

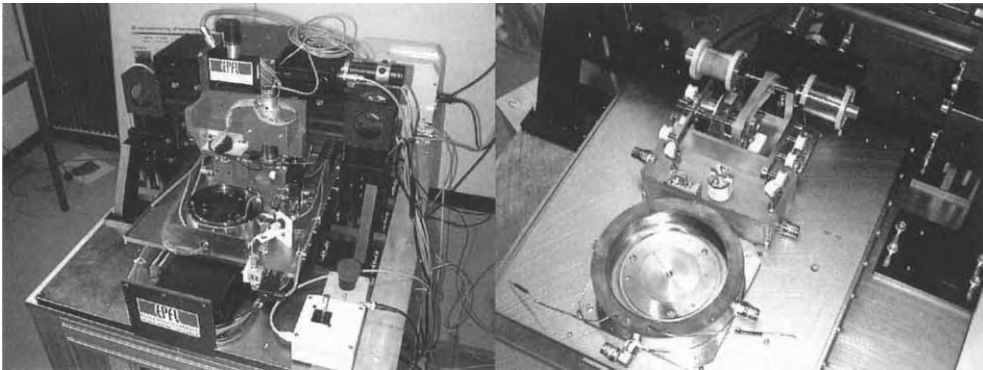


**Figure 1.5** Overview of a SACE prototype (left) and close-up view of the processing units (right) [32,123].

needed in the same facility, which avoids alignment problems and offers more flexibility.

### 1.1.3 A Short Historical Overview

SACE was first developed in Japan in the late 1950s with some applications in diamond die workshops (Table 1.1). The paper by Kurafuji and Suda, in 1968, was one of the pioneering reports about this new technology, which they termed *electrical discharge drilling* [76]. The authors demonstrated that it was possible to drill microholes in glass, and they studied the effect of electrolyte chemical composition and tool-electrode material. The machining mechanism was open to debate and questions were raised about the similarities with EDM and ECM. This debate went on five years, until the paper by Cook et al. [21]. The authors stressed that the process described by Kurafuji and Suda is different from EDM and ECM and suggested a new name for it, *discharge machining of non-conductors*. They showed that the process can be applied to a broad range of non-conductive materials and investigated further the effect of the electrolyte. The authors also quantified drilling rates as a function of the

**Table 1.1** Some Important Dates in the History of SACE

|      |  |
|------|--|
| 1968 | First report by Kurafuji and Suda                    |
| 1973 | First characterisations by Cook et al.               |
| 1985 | Extension to travelling wire-ECDM by Tsuchiya et al. |
| 1990 | First functional devices                             |
| 1997 | First models by Ghosh et al. and Jain et al.         |
| 2000 | Study of SACE in the light of electrochemistry       |
| 2004 | SACE and nanotechnology                              |



microhole depth and compared the machining between negatively and positively polarised tool-electrodes. However, the material removal mechanism remained an open question.

In 1985, Tsuchiya et al. [105] presented a new variant of the process developed by Kurafuji and Suda by using a wire as a tool-electrode. They termed this process *wire electrochemical discharge machining* and showed that glass and various ceramics can be cut using this technique. This variant was further developed by Jain et al. [58] under the name *electrochemical spark machining*. The authors highlighted the similarity with electrochemical arc machining (ECAM), a variant of ECM.

In the 1990s, the first applications in the field of MEMS were published [30]. Simultaneously, several studies on the fundamentals of the process were undertaken [2,7,60]. In particular, Ghosh et al. established, for the first time, a clear link between the machining process and the electrochemical discharge phenomenon. At that time, the main material removal mechanism was believed to be the melting of the workpiece. The chemical aspect of the material removal mechanism was investigated more systematically at the beginning of this century. A pioneering work in this area is the one by Yang et al. [132] who defined the material removal mechanism as a high-temperature etching process. Further investigations on the electrochemical contributions were done by Fascio et al. [32–34]. Based on their results and to avoid further confusion with ECM and EDM, the group proposed to use the terminology *spark-assisted chemical engraving* (SACE). This acronym, which is used throughout this book, emphasises the contribution of chemical etching to the machining process. The same group also conducted further studies on the mechanisms behind the formation of the gas film with practical application to the improvement of the machining process [123,125,129]. The application of the SACE technology to microfactories was also suggested [127]. In 2005, a first review paper on the process was published [128].

In years to come, the interest in SACE is expected to show a huge increase. Several new groups have appeared across the world and already a large number of publications followed. (The number of publications on SACE from 1968 to 2005 and between 2005 and 2008 are about the same.) Systematic investigations of the various machining strategies were published and new ways to increase the precision and repeatability of the process were proposed. Besides other developments, the utilisation of pulsed voltage machining is a very promising technique [71,136,137]. One of the latest developments so far is the application of electrochemical discharges to nanotechnology [78,126,141].

## 1.2 SACE as a Micromachining Technology

Several machining technologies can be used to microstructure workpieces. These different technologies are often complementary and are sometimes used together. Machining technologies can be classified into mechanical, chemical,

and thermal technologies. The following sections present a succinct overview of some of the most commonly used micromachining techniques.

### 1.2.1 Mechanical Machining

- *Mechanical drilling* (with diamond tool) or diamond cutting can be used for glass machining. This is not a typical micromachining technology. The main limitation is the tool size. So far, only drilling or cutting is used and no 3D microstructuring can be achieved. Typical diameters that can be obtained are around 400  $\mu\text{m}$ .
- *Water jet machining* uses water mixed with abrasive materials projected with high pressure (typically 0.7 MPa) and focussed on the workpiece.
- *Powder blasting*, or *abrasive jet machining*, is a technique in which a particle jet (typically  $\text{Al}_2\text{O}_3$  particles of 3–30  $\mu\text{m}$ ) is directed towards a target for mechanical material removal. It is a fast (typically, 500  $\mu\text{m}$  depth in 20 minutes), inexpensive, and accurate directional etch technique for brittle materials like glass, silicon, and ceramics. For complex and small structures a mask can be used.
- In the *ultrasonic machining* process, the tool, made of softer material than that of the workpiece, oscillates at high frequency (typically 20 kHz) with an amplitude about 25  $\mu\text{m}$ . Ultrasonic machining, used on very hard ceramics, works by grinding or eroding material away. A liquid slurry around the drill bit contains loose hard particles that are smashed into the surface by the vibrations, eroding material away and creating more loose hard particles.

### 1.2.2 Chemical Machining

- *Photofabrication* or photoforming is an optical method that is similar to the stereolithography or the photomask layering process, which involves the solidification of a photochemical resin by light exposure.
- *Chemical etching*: For glass, chemical etching can be classified into two types: dry and wet etching. Typical wet etching is done by using hydrofluoric acid (HF) or potassium hydroxide (KOH). Selective etching is obtained by using masks. The typical etching rate in 50 wt% HF at 40°C is 6  $\mu\text{m}/\text{min}$  and 80 nm/hour for a 35 wt% KOH solution.
- *ECM* achieves controlled material removal by electrochemical dissolution of the workpiece, which consequently should be electrically conductive. The technique is characterised by the excellent surface qualities that can be achieved.

### 1.2.3 Thermal Machining

- *Laser machining* is based on the local supply of energy to materials. At the surface of the material, the laser light is transformed into heat, which is available for processing. Glass can be micromachined with relatively high accuracy using this technology (better than 5  $\mu\text{m}$  for structures of typical sizes of 50  $\mu\text{m}$ ). However, the surface quality obtained is not always very good and not all types of structuring are possible.
- *EDM* is one of the most commonly used unconventional micromachining technologies. The process is limited to electrically conductive materials. Electrical arcs are produced in a controlled way between the tool and the workpiece in order to achieve material removal by melting and evaporation.

In general, chemical machining technologies achieve high surface qualities; however, they have the restriction of slow machining rates. Therefore, these technologies are most interesting for batch processes. The possibility of machining high aspect ratio structures is challenging. Mechanical and thermal machining usually result in lower surface qualities but offer more flexibility in machining high aspect ratio structures.

SACE is a hybrid process. As discussed in the following chapters, material removal is achieved by thermal and chemical processes. Sometimes SACE is erroneously defined as a combination of EDM and ECM. This is actually not correct, as no electrochemical dissolution of the workpiece takes place.

## 1.3 Scope of the Book

Micromachining using electrochemical discharges is a fairly new process and still largely unknown in the micromachining community. Mastering this process involves the knowledge from various fields and in particular a deep understanding of the electrochemical discharge phenomenon. Consequently, this book is organised into two parts.

First, the fundamentals of the electrochemical discharge phenomenon are discussed. After a historical overview (Chapter 2) and a detailed discussion on gas evolving electrodes (Chapter 3), a more specific discussion on the mechanisms leading to their onset follows (Chapter 4).

Part 2 presents the process of micromachining using electrochemical discharges. Chapter 5 starts by presenting the fundamentals of the material removal process. The thermal and chemical contributions are discussed. In Chapter 6 the most commonly used machining strategies are presented. The state-of-the-art knowledge is discussed in depth and the main limitations are highlighted. Chapter 7 presents the main strategies used to overcome these

limitations. Some inputs to stimulate new research in the field of control of micromachining using electrochemical discharges are also presented.

Chapter 8 outlines how an electrochemical discharge micromachining facility can be built. Finally, Chapter 9 provides an outlook on new possible applications.

## 2 Historical Overview of Electrochemical Discharges

---

The history of electrochemical discharges can be written as a succession of rediscoveries of the same phenomenon. Electrochemical discharges were first used by physicists in the middle of the nineteenth century as a light source with a rich spectra and then as non-linear electrical components by electrical engineers in the beginning of the twentieth century. They were rediscovered in the middle of the last century by chemists and used as a source of non-faradaic electrochemical reactions before being applied to micromachining and surface engineering in the second half of the twentieth century. The latest development in this field is the application of electrochemical discharges to the synthesis of nanoparticles. Each of these applications is actually hosted in different fields of science and engineering. This explains why the electrochemical discharge phenomenon was rediscovered several times and only later related to earlier observations reported in other fields. This chapter reviews the history of electrochemical discharges from a multidisciplinary perspective.

### 2.1 Discovery and Early Applications

The discovery of electrochemical discharges was, as is often in science, not a planned observation. During the nineteenth century there was a broad interest in the measurement of the spectrum of light sources. Any phenomenon emitting light was observed and recorded, like, for instance, electrical arcs between two carbon electrodes as first described by Sir Humphry Davy (1778–1829). In 1844 the French physicists Hippolyte Fizeau (1819–1896) and Léon Foucault (1819–1868) published a paper in *Annales de Chimie et Physique* entitled “Recherches sur l’intensité de la lumière émise par le charbon dans l’expérience de Davy” (Study of the intensity of the light emitted by the carbon in the experiment of Davy) [35]. In this paper the authors reported the experimental spectral observations of light sources. They compared the spectra obtained by electrical discharges between two carbon electrodes and those from the sun. At the end of their publication the authors mentioned a light source obtained during the electrolytic decomposition of water with two thin platinum wires. This short note was the first description in the literature of a phenomenon that is today called *electrochemical discharges*, *plasma electrolysis* or, at times, *electrode effects*. In fact, Foucault and Fizeau were most probably not the first to have observed electrochemical discharges. This phenomenon was described in experiments of water decomposition using static electricity as early as in 1789 [108]. However,

Foucault and Fizeau can be considered as the discoverers of electrochemical discharges as they were the first to associate these with electrical discharges.

The publication of Fizeau and Foucault's paper is an inspiration for several studies (mainly in France) on the subject, some of which will be translated into German by *Annalen der Physik* and into English by the *Journal of the Franklin Institute*. It was probably Sir William Robert Grove (1811–1896), well known for his invention of the fuel cell in 1839, who promoted the phenomenon in the English scientific community [43]. With the development of more stable and powerful power sources, several quantitative studies were conducted. In 1889, Jules Violle (1841–1923) and Michel Chassagny (1865–1918) published a quantitative study on the effect discovered by Fizeau and Foucault [110] in *Comptes rendus hebdomadaires des séances de l'Académie des Sciences*. Let us examine the work of Violle and Chassagny to get a better understanding of electrochemical discharges.

The French scientists used two thin platinum wires (1.6 and 4.5 mm in diameter) dipped in sulphuric acid. By applying a constant voltage to them, Violle and Chassagny decomposed water into hydrogen and oxygen. However, when experimenting with a voltage higher than 32 V they observed a new phenomenon: the thinner platinum wire became surrounded by a gas film in which discharges took place. By studying the effect of geometry and electrode polarisation they identified that the electrochemical discharges take place only above a *critical voltage*, which they determined experimentally as a function of various parameters. The researchers noted that the gas film always appeared on the thinner of the two wires and that, in general, discharges are harder to obtain in case the thinner wire is an anode (a voltage of more than 50 V is needed in this case). Just as many others, they were also fascinated by the light emitted during the process.

A large number of communications on this new phenomenon followed in the second half of the nineteenth century. Most of the studies related to electrochemical discharges dealt with observation of the spectrum of the light emitted and the heat produced. This is understandable if we recall that the middle of the nineteenth century was a time when significant research was done on the fundamental understanding of light generation and heat. But the physics behind the electrochemical discharges was also questioned. It became clear from the very beginning, that the observed light, and the abrupt decrease in current, has its origin in a gas film built around an electrode that was called the *active electrode* [56]. Spectral studies of the light emitted led researchers to conclude that the chemical composition of the gas must be a mixture of hydrogen with components from the electrolyte (e.g., sodium) and the electrode itself (e.g., platinum or silver). The formation of this gas film was, however, much more debated. This intense discussion led to new discoveries.

In 1894, the French physicists E. Lagrange and P. Hoho carried out a series of studies on the gas film formation. They were probably the first to consider not only the gas film formed, but they also tried to understand the various steps leading to its formation. They studied and described the decomposition

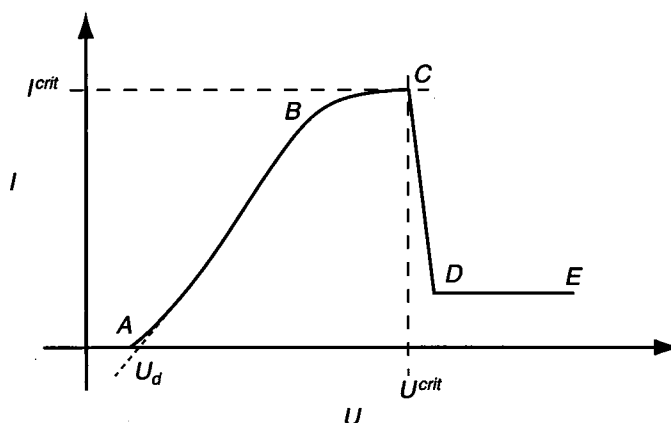


**Figure 2.1** Typical  $I$ - $U$  characteristics of electrolytic water decomposition as described by Hoho [56]. See text for explanations related to the various phases.

of water as a function of the applied voltage (Fig. 2.1). For low voltages, higher than the decomposition potential of water  $U_d$ , water is decomposed into hydrogen and oxygen. The current increases proportionally to the voltage. Starting from a critical voltage  $U^{crit}$ , the electrolysis becomes unstable. Very large bubbles are produced and the electrolyte seems to boil locally. The current fluctuates and some lightning can be observed. Lagrange and Hoho called this phase the *instability region* (*période instable* in French). For higher voltages, the phenomenon becomes more stable; bright lightning can be observed.

During their studies Lagrange and Hoho also described a practical application of electrochemical discharges for welding and hardening of metals [56]. The physicist Arthur Wehnelt (1871–1944), who came across the work of Lagrange and Hoho, repeated their experiments. The very regular noise produced by the electrochemical discharges when the active electrode was brought in the vicinity of a metal plate intrigued the German scientist. After several experiments he was able to master the effect and use it for a practical application in the form of a high-frequency current-interrupter. In 1899 he published a paper in *Annalen der Physik*<sup>1</sup> entitled “Ein elektrolytischer Stromunterbrecher” (an electrolytic interrupter), presenting a new device that was later called the *Wehnelt interrupter* [119]. In 1905, Wehnelt was awarded for his invention with the John Scott Medal, a prestigious award of North America, by the Franklin Institute [37].

## 2.2 The Wehnelt Interrupter

The publication of Wehnelt’s paper on his current-interrupter in 1899 provided a new turn to the research on electrochemical discharges. For the first time a technological application was developed based on the electrochemical discharge phenomenon. In the same year, Wehnelt’s invention was commercialised

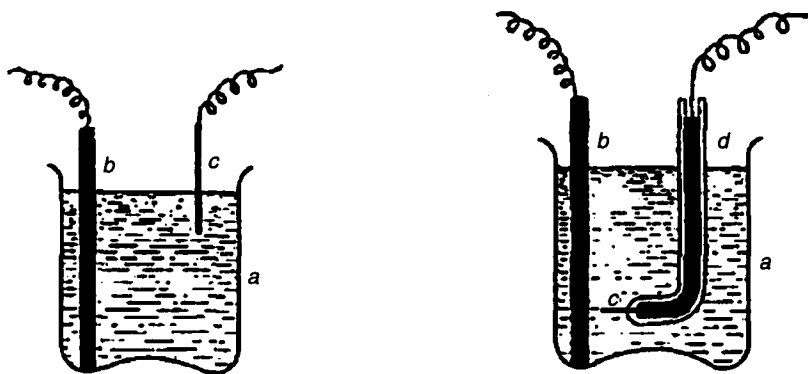


**Figure 2.2** Experimental apparatus used by Wehnelt for his studies on electrochemical discharges [119]. After a first series of experiments (left), he improved the set-up by enclosing the active electrode *c* in a glass tube *d* (right).

by several companies; for example, by Ferdinand Ernecke and Siemens & Halske in Germany [119] and by Armagnat-Carpentier in France [10]. The device, with a wide range of applications, became popular rapidly and was widely used.

Wehnelt first repeated the experiments on electrochemical discharges using two dissimilar sized electrodes dipped in sulphuric acid (Fig. 2.2). The smaller electrode, the active electrode, was a platinum wire while the larger one was made of lead. Wehnelt quickly identified the need to enclose the active electrode in a glass tube in order to have a well-defined geometry and avoid projection of the electrolyte during the experiment. In order to be able to study the discharge activity in more detail and to verify his idea that the phenomenon taking place at the active electrode acts as an interrupter, Wehnelt used an external circuit (Fig. 2.3) consisting of a capacitor and an induction coil. The induction coil (or spark coil) is a device made up of two concentric coils wound around a common iron core. The current was supplied to the primary coil with a lower number of windings. The secondary coil with large number of windings was connected to two electrodes between which it was possible to have an electrical discharge. In present-day language an induction coil would be called a high-voltage transformer.

During his experiments Wehnelt found that the apparatus consisting of the two electrodes and the electrochemical cell (which he named *electrolytic interrupter*; *Elektrolytischer Unterbrecher* in German) can be used as a current-interrupter. The frequency of interruption can be controlled by the external circuit, in particular by the inductance of the induction coil, resulting in high frequencies for low values of inductance. He showed that 1000–2000 interruptions per second can be achieved. The best results were obtained when the active electrode is polarised as the anode. Using these high interruption numbers, together with the induction coil, it became possible to produce very high voltages from a low-voltage source (such as the one produced by an electrochemical cell).

Wehnelt's current-interrupter became very popular and a competitor to the Ruhmkorff coil, a device that most of us still know from physics lessons



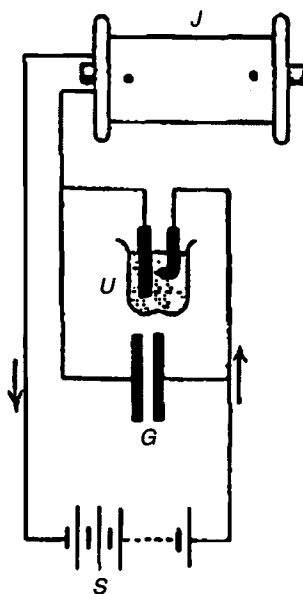


**Figure 2.3** Experimental apparatus used by Wehnelt for his studies on electrochemical discharges [119]. The electrolytic cell  $U$  with the active electrode and counter-electrode is connected to a capacitor  $G$  and an induction coil  $J$ .

at secondary school. However, compared with Ruhmkorff's coil, Wehnelt's electrolytic interrupter could provide higher interruption numbers and generally worked more reliably. The applications were numerous, and several patents were submitted during the beginning of the last century. The device was used for the production of electrical arcs, when connected to an induction coil, with application in many fields, among others in the study of electrical conduction of gases. Another use was as a current rectifier, an application of electrochemical discharges that was actually first described about thirty years earlier in France by Bouchotte [13] and Alexandre Edmond Becquerel (1820–1891) [9], but their work seems to have been overlooked at that time. The current-interrupter also played a significant role in the development of wireless telegraphy because of its capability to generate high-frequency interruptions, an application first suggested by Jacques-Arsène d'Arsonval (1851–1940) [27] when he presented Wehnelt's device to the Académie des Sciences in Paris. In 1903, the Canadian inventor Reginald Aubrey Fessenden (1866–1932) patented a wireless telegraphy receiver based on Wehnelt's device [36]. Wehnelt's interrupter also became a key component in early X-ray imaging devices. This last application was connected to a large medical market [138]. Since 1899, many companies across the world started to build the electrolytic interrupter (Fig. 2.4). Many laboratories owned such devices. Wehnelt's device played a significant role in various important discoveries in physics. Rutherford's experiment on radiation energy [52] and Von Laue's discovery of X-ray diffraction by crystals [25] are only two of several examples. In the beginning of nineteenth century, the

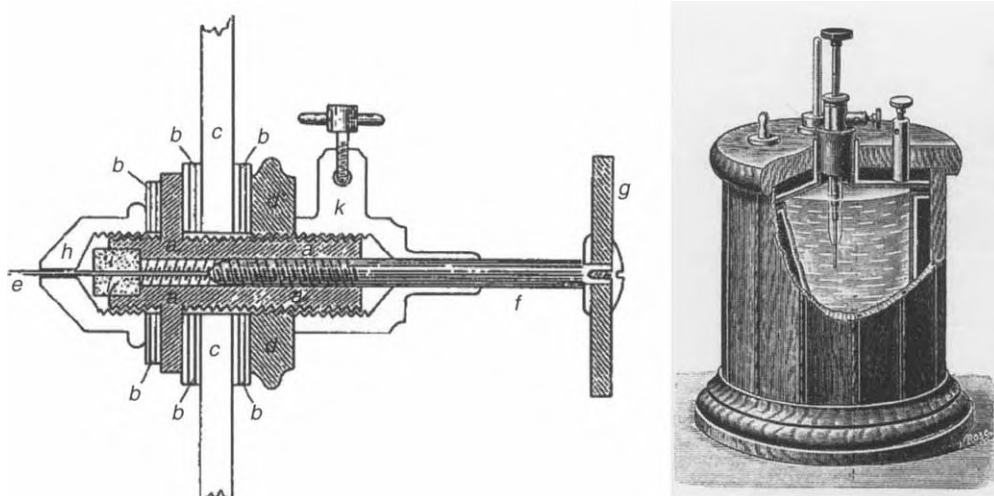


**Figure 2.4** The Wehnelt interrupter commercialised in 1899 by the German company Ferdinand Ernecke (left). The length of the platinum electrode *e* could be adjusted. The electrical contact was made with the help of the cooper rod *f* [119]. On the right is shown a model commercialised in France by Armagnat-Carpentier [10].

current-interrupter became a low-cost device. The *Radio Amateur's Hand Book* of 1922, for example, mentioned that “an electrolytic interrupter can be bought for as little as \$3.00” [20].

In the same year as Wehnelt's first publication on his current-interrupter, E.W. Caldwell [17] and H.Th. Simon invented independently a different version of the electrolytic interrupter. Their interrupter used a small hole drilled in a wall separating the cathodic and anodic compartments of an electrolysis cell. As in the Wehnelt interrupter, the periodic formation of a gas film regularly interrupts the current.

As a direct consequence, a rich source of literature about Wehnelt's interrupter and the modified Caldwell–Simon current-interrupter emerged. For example, in the same year as Wehnelt's first publication, one article in *Physical Review*, four papers in *Annalen der Physik*, and seven communications in *Comptes rendus hebdomadaires des séances de l'Académie des Sciences* were published. But this was only the beginning. An impressive number of works reporting theories about the operation principle and studies of the spectrum of the emitted light followed. Major contributions to the theory of operation of the device were written by H.Th. Simon [99], A. Voller and B. Walter [118], P. Ludewig [83], and Karl Taylor Compton (1887–1954) [26]. Electrochemical discharges were now no longer known only in France but also in the whole of Europe and North America. As expected, with the development of new current-interrupters, in particular interrupters based on electronics, the Wehnelt interrupter progressively disappeared from the market. Today, the device is almost unknown, except in some specialised communities (e.g., in the community

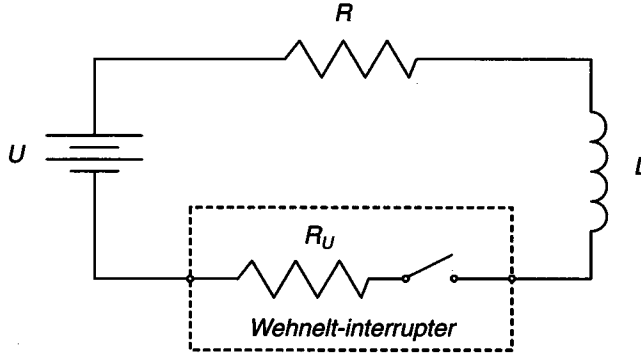


**Figure 2.5** Model of the Wehnelt interrupter. The switch is closed as long as no electrochemical discharges take place. As soon as the gas film is built, the switch is opened.

of old radio amateurs). Nevertheless, one can still find this device on the market today, but only for educational purposes.

Considering the importance of this first technological application of electrochemical discharges, we will present here a simplified theory of Wehnelt's current-interrupter. A resistance  $R$  and inductance  $L$  is connected to the Wehnelt interrupter. Based on early mathematical models of the device [83,99], the Wehnelt interrupter is considered to be a resistance  $R_U$  in series with an electrical switch (Fig. 2.5).

Once the device is connected to a constant voltage  $U$ , the current in the Wehnelt interrupter grows (the switch in the equivalent circuit is closed). An increasing volume of gas is produced until a gas film is built, isolating the active electrode from the electrolyte. The switch in the equivalent circuit is now open. The unstable gas film is quickly removed from the active electrode and the process starts again. From the equivalent circuit, the evolution of the current is given by:

$$I(t) = \frac{U}{R_k} \left( 1 - e^{-\frac{t}{\tau}} \right), \quad (2.1)$$

where the total resistance  $R_k = R + R_U$  and the circuit time constant  $\tau = L/R_k$ . Note that the resistance  $R_U$  of the Wehnelt interrupter is not constant as gas bubbles are progressively shadowing the electrode surface. The description of this process is presented in Chapters 3 and 4. For the sake of simplicity, we will neglect this effect in the rest of this section.

The time  $t_f$  needed to build the gas film is given by the time interval in which the current reaches a critical value  $I^{crit}$  (depending on the geometry of the active electrode, as we will see in Section 3.7.2):

$$I^{crit} = \frac{U}{R_k} \left( 1 - e^{-\frac{t_f}{\tau}} \right). \quad (2.2)$$

From this last relation, and introducing the critical voltage  $U^{crit} = R_k I^{crit}$ , one can directly deduce the number of current interruptions  $n$  per second:

$$n = \frac{1}{t_f} = \frac{R_k/L}{\ln\left(\frac{U}{U-U^{crit}}\right)}. \quad (2.3)$$

Note, as we will see in Section 3.7.2, that the critical voltage  $U^{crit}$  is a value that is a function only of the geometry of the active electrode and the electrolyte conductivity. It is therefore a parameter of the device and is not influenced by the external circuit. This was recognised experimentally for the first time in 1925 by Crowther and Stephenson.

Equation (2.3) is able to explain the operation of the Wehnelt interrupter. The number of interruptions is inversely proportional to the inductance  $L$ . As  $R_k = R + R_U$  and  $R_U \propto 1/l$ , the inverse of the active electrode length (cylindrical geometry), it follows that  $n$  will increase inversely proportional to  $l$ , as first experimentally observed by Ludewig [83].

By introducing the normalised voltage  $\mathcal{U} = U/U^{crit}$ , a quantity that is important for further theoretical description of electrochemical discharges, one obtains a particularly elegant relation for the Wehnelt interrupter (Fig. 2.6):

$$\frac{t_f}{\tau} = \ln\left(\frac{\mathcal{U}}{\mathcal{U}-1}\right). \quad (2.4)$$

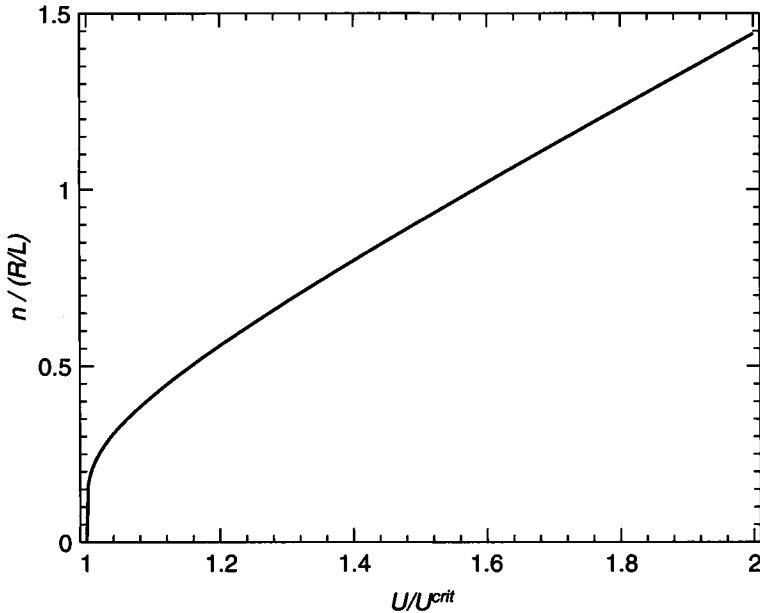


**Figure 2.6** Number of interruptions  $n$  in the Wehnelt interrupter as a function of the voltage  $U$ , as predicted by Equation (2.3).

According to this model, interruption numbers  $n$  virtually as large as desired can be obtained with the Wehnelt interrupter. This is obviously not correct. In reality, for very short electrical time constants  $\tau$ , the time needed to build up the gas film is limited by the time needed for gas bubbles to grow on the active electrode surface. Relation (2.3) will overestimate  $n$  for small  $\tau$ . As explained later, the typical growth times for gas bubbles are a few milliseconds. This timescale gives the limit of validity of Equation (2.3). The proportionality between the electrical time constant  $\tau$  and the interruption period  $T$ , as well as the importance of the gas film formation time, was first recognised by Compton [26] in his master's thesis in 1910.

## 2.3 Spectrum of the Electrochemical Discharges

Since the discovery of electrochemical discharges, the spectrum of the light emitted during the phenomenon was studied intensively. Early observations [56,119] of the light spectra emitted by electrochemical discharges showed that if the active electrode is polarised as a cathode, the hydrogen rays can be observed, as well as the rays from the electrode material and the electrolyte components. In case the active electrode is an anode, Wehnelt [119] observed only the hydrogen rays (besides the rays from the electrolyte and the electrode material) and he was surprised not to observe the oxygen ray. In fact, it seemed that even if the active electrode is an anode, a large quantity of hydrogen is produced besides oxygen. Wehnelt could confirm this finding by analytical analysis of the gas collected from the active anode. This surprising result was confirmed in the same year by other researchers who could also identify other gazes (in particular ozone) [3,57,118]. The production of hydrogen at an anode where electrical discharges take place was already described in 1853 by Quet [94].

A first in-depth study of the spectra emitted by the light from electrochemical discharges (in case the active electrode is an anode) was reported by Harry W. Morse in 1904 and 1905 [89,90]. He used photographic techniques to quantify the spectra obtained.<sup>2</sup> Morse found the presence of the hydrogen ray, but, like Wehnelt, was surprised not to find any oxygen ray. However, he could identify bands related to metallic oxides. Morse could prove that the spectra observed were the same regardless of the metal being present in the active electrode or in the electrolyte. He also compared the spectra obtained from electrochemical discharges with those obtained from arc discharges and sparks. His conclusion was that electrochemical discharges showed similarities with both. This finding suggests that during an electrochemical discharge, the temperature of the system most probably passes through a series of temperatures, consequently producing spectra similar to arc and spark discharges. Morse's achievement was to recognise that, although this description seems straightforward, it cannot be correct. Electrochemical discharges are a more complex phenomenon.

His argument was that, for a given metal, only some of the arc and some of the spark discharge rays are present but never all rays, as should be expected if electrochemical discharges behave like arcs and sparks, depending on the temperature of the system during the discharge. Morse could not give a convincing explanation to this apparent paradox. We will come back to this point in Section 2.5. The oxygen ray was identified only in 1910 by Compton [26].

More recent studies confirm these early findings [5,45,46]. Electrochemical discharges at a cathode are, in general, more light intense than at an anode under identical conditions. In the case of an active cathode, the colour of the light is related to the electrolyte composition for alkaline solutions and to the composition of the electrode for an acid. In the case of an anode, the colour is, in general, rose except for alkaline solutions where the same colour as for the cathode is observed. Observations with high-speed cameras [46] showed that the duration of the electrochemical discharges are typically in the range of 0.1 ms and are, in general, separated by 1 ms. The main results for an active anode can be summarised as follows:

1. Spectral rays from the hydrogen and O(II) and the 3064 Å band spectra from OH can always be observed.
2. Several other emission rays are present depending on the electrolyte used. For example, in the case of a NaOH solution, the emission ray at 4668 Å of the sodium is observed.
3. The emission rays from the metal of the electrode can be observed but are very faint.

For an active cathode, the observed spectra are more complex and rich. The excitation temperature was estimated from the measured spectra. For an active anode, using the O(II) ray, a temperature of 35,000 K was estimated [46], which corresponds to quite high excitation energies of about 25–30 eV. Using the Mg(I) and Ca(I) rays an excitation temperature of about 4000 K was estimated [46]. For an active cathode similar temperatures were estimated (21,500 K for the O(II) ray and 4500 for the Ca(I) ray).

## 2.4 Nature of the Electrochemical Discharges

The observations on the spectra of electrochemical discharges raise the question about their nature. Today, the term *electrical discharge* is used to indicate the passage of current through space (as distinct from passage through solid bodies). There are three types of gas discharges:

1. Townsend discharge
2. Glow discharge
3. Arc discharge

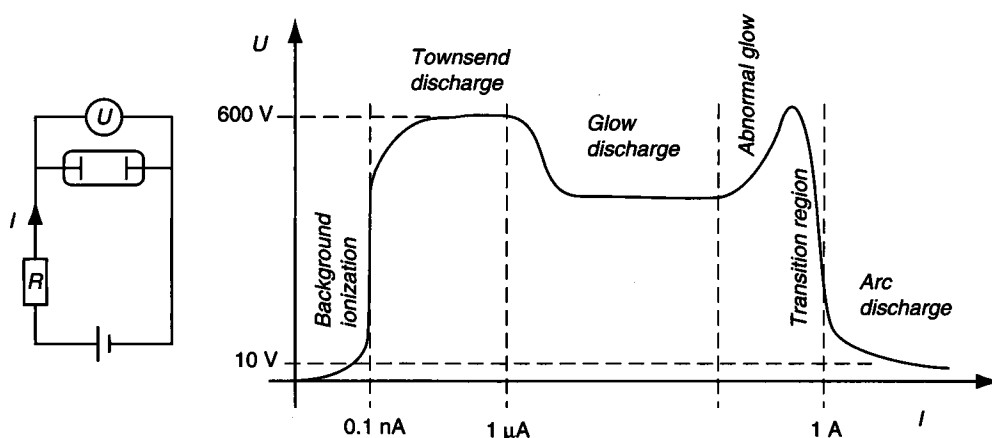


**Figure 2.7** Gas discharge circuit and corresponding  $U$ - $I$  characteristics.

Note that this classification is done for discharges where the current is carried by electrons. For electrochemical discharges this is the case when the active electrode is a cathode: the electrons travel through the gas film from the electrode to the electrolyte, where they will somehow undergo electrochemical reactions with the ions of the electrolyte. It is harder to imagine that this would also be the case if the active electrode is an anode. Indeed, this would raise serious questions about how electrons would be emitted from the electrolyte and travel to the anode. As discussed in Section 2.5, the situation is very different for this case. For the time being, we restrict the discussion to the situation where the active electrode is a cathode.

Electrical discharges are characterised according the current  $I$  and voltage drop  $U$  of the discharge as shown in Fig. 2.7. Some typical values are reported on the axes. Townsend and glow discharges are high-voltage discharges (a few hundred volts). Arc discharges happen typically at 10 V. Glow and arc discharges are accompanied by light emission. Arc discharges carry high currents (from one to several hundred amperes) whereas glow and Townsend discharges are characterised by very small currents.

### 2.4.1 Townsend Discharges

In Townsend discharges, free electrons ionise the gas molecules. Several processes for *gas ionisation* are known. Table 2.1 lists the most important ones. The ionisation of a neutral gas molecule  $A$  takes place if the kinetic energy of the electron  $e^-$  is greater than the ionisation potential  $V_i$  of the gas molecule (see Table 2.2):



**Table 2.1 Some Ionisation Processes in a Gas**

| Reactions   | Description        |
|---|--------------------|
| $A + e^- \rightarrow A^+ + e^- + e^-$             | Ionization         |
| $A + B^{(\pm)} \rightarrow A^+ + B^{(\pm)} + e^-$ | Thermal ionization |
| $A + h\nu \rightarrow A^+ + e^-$                  | Photoionization    |
| $A + e^- \rightarrow A^* + e^-$                   | Excitation         |

**Table 2.2 Excitation and Ionisation Potentials of Some Gases [14]**

| Gas                | Excitation Potential<br>$V^*$ (eV) | Ionization Potential<br>$V_I$ (eV) | Ionization Process            |
|--------------------|------------------------------------|------------------------------------|-------------------------------|
| Argon (Ar)         | 11.7                               | 15.7                               | $Ar \rightarrow Ar^+ + e$     |
| Hydrogen ( $H_2$ ) | 7.0                                | 15.4                               | $H_2 \rightarrow H_2^+ + e$   |
| Nitrogen ( $N_2$ ) | 6.3                                | 15.6                               | $N_2 \rightarrow N_2^+ + e$   |
| Water ( $H_2O$ )   | 7.6                                | 12.6                               | $H_2O \rightarrow H_2O^+ + e$ |

In general, a positive ion and two slow moving electrons result. The probability of the process increases nearly linearly with the kinetic energy of the impacting electron up to a maximum (at around 100–200 eV). After this maximum the probability decreases slowly.

The two electrons produced by the process are accelerated by the electrical field and may ionise other gas molecules. An *avalanche* is formed. The frequency of the ionisation process is characterised by the *first Townsend coefficient*  $\alpha$ . This coefficient depends on the *reduced electrical field*  $E/p$ , where  $p$  is the pressure of the gas. The increase  $dn$  of the  $n$  electrons after a distance  $dx$  is given by:

$$dn = n\alpha dx. \quad (2.6)$$

The *amplification factor*  $M$  after a distance  $d$  is defined by:

$$M = \frac{n(d)}{n_o} = \exp\left[\int_o^d \alpha(x)dx\right], \quad (2.7)$$

where  $n_o$  is the initial number of electrons.

One of the earliest models for the first Townsend coefficient was given by Rose and Korff [96] in 1941 and later standardised by Zastawny [134] in 1997:

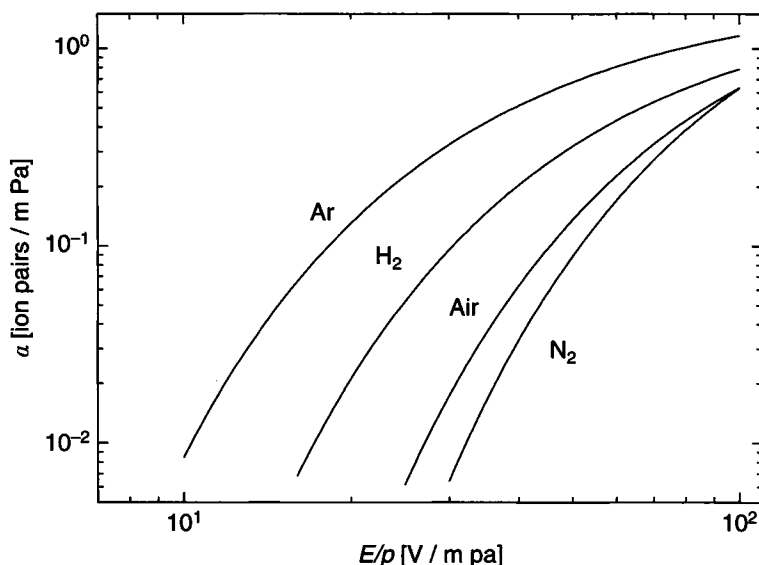
$$\frac{\alpha}{p} = A \exp\left(-\frac{Bp}{E}\right). \quad (2.8)$$

$A$  and  $B$  are experimental constants that vary depending on the type of gas and, in general, also on the range of the reduced electrical field  $E/p$  (Table 2.3 and Fig. 2.8).



**Table 2.3** Constants in the Rose and Korff Formula (2.8) for the Ionisation Coefficient [96]

| Gas            | $A \text{ (m}^{-1} \text{ Pa}^{-1}\text{)}$ | $B \text{ (V m}^{-1} \text{ Pa}^{-1}\text{)}$ |
|----------------|---|---|
| Ar             | 12  | 180   |
| H <sub>2</sub> | 5   | 130   |
| Air            | 15  | 365   |
| N <sub>2</sub> | 12  | 342   |

**Figure 2.8** First Townsend coefficient  $\alpha$  for argon, hydrogen, air, and nitrogen. Plotted using data from [134].

After ionising the gas molecules, the positive ions generated migrate to the cathode and can liberate secondary electrons. The efficiency of this secondary electron production is given by the *second Townsend coefficient*  $\gamma$  which is the fraction of secondary electrons liberated. This coefficient depends on the material of the cathode and is typically in the range around 0.1 [14].

The secondary electrons produced can also ionise the gas. The phenomenon becomes self-sustained if following condition is met:

$$M = 1 + \frac{1}{\gamma}. \quad (2.9)$$

In other words, if  $M \approx 11$ . This relation allows the determination of the *breakdown voltage* of the system, as given by the Paschen curve.

Let us now discuss whether electrochemical discharges could be Townsend discharges. Electrochemical discharges take place through a gas film formed

around the active electrode of radius  $b$ . Recall that the phenomenon can be observed for voltages as low as 20–30 V. If  $d$  is the thickness of this gas film, and if it is assumed that almost all the voltage drop happens across it, the electrical field  $E$  through the film can be modelled by a cylindrical field:

$$E(x) = \left( \frac{1}{b+x} \right) \frac{U}{\ln\left(\frac{b+d}{b}\right)}, \quad (2.10)$$

where  $U$  is the inter-electrode voltage and  $x$  is the distance inside the film measured from the electrode surface. Applying definition (2.7), the amplification factor  $M$  is evaluated as [123]:

$$\ln(M) = \frac{A \cdot U}{B \ln\left(\frac{b+d}{b}\right)} \left[ \left( \frac{b+d}{b} \right)^{-\frac{bBp}{U}} - \left( \frac{b+d}{b} \right)^{-\frac{(b+d)Bp}{U}} \right]. \quad (2.11)$$

Figure 2.9 shows for a thin electrode (200  $\mu\text{m}$  diameter) the amplification factor  $M$  as a function of the gas film thickness  $d$  for  $U = 30$  V. The calculations are done for various gas compositions. The numerical values for the coefficients  $A$  and  $B$  are taken from [95] and [134]. The resulting amplification factor is relatively small. A maximum is reached for a film thickness of a few micrometres.

As shown in Fig. 2.9, the calculated amplification factor  $M$  for the gas film around the active electrode is far less than the critical value of 11 needed for self-sustained discharges. This is an indication that electrochemical discharges

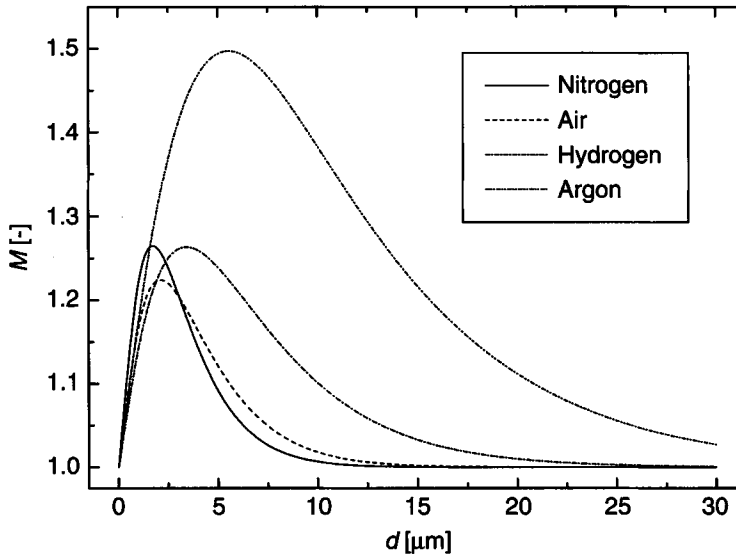


**Figure 2.9** Amplification factor  $M$  for an active electrode of 200  $\mu\text{m}$  diameter and a voltage of 30 V as a function of the gas film thickness  $d$  for various gas compositions.

are not likely to be self-sustained Townsend discharges. Some researchers [107], proposed this mechanism to explain electrochemical discharges. They presented several arguments to justify why the observed breakdown voltage could be much smaller than the one from the Paschen curve of a pure gas (between 100 and 500 V):

- The gas film in electrochemical discharges is not a pure hydrogen gas film, but more of a mixture of hydrogen and vaporised electrolyte.
- The surface roughness of the active electrode is relatively high.
- The thickness of the gas film is very small (they proposed a thickness of 5  $\mu\text{m}$ ).

The last argument about the thickness of the gas film is not likely to be correct, as shown from the previous calculation. Even for a small gas film thickness, the amplification factor of the gas is too low to allow the formation of a self-sustained avalanche. The second argument also seems not very convincing. It is well known that locally the electrical field can be very high because of high surface roughness. But the field will be high only over a small distance. This will not significantly increase the amplification factor, which is a function of the ionisation distance also. Moreover, if this argument were true, self-sustained Townsend discharges should be observed at small voltages in similar geometries (e.g., between two very sharp needles). However, this is not the case to the best of our knowledge. Finally, only the first argument remains. One hypothesis could be that the vaporised electrolyte is already ionised somehow and therefore the first Townsend coefficient is significantly higher than normal.

If electrochemical discharges are not Townsend discharges for low voltages, the situation becomes different for higher potentials. It is very likely that for voltages higher than the Paschen breakdown voltage, electrochemical discharges become self-sustained Townsend discharges.

### 2.4.2 Arc Discharges

Arc discharges are high-pressure discharges (pressures ranging from 0.5 up to 100 atm) characterised by low voltages (in the range 10–50 V) and high currents (in the range 1–100 A). A well-known example is the arc discharge at atmospheric pressure between two carbon electrodes (as in the carbon arc lamps). The arc voltage drop is more or less independent of the arc current and typically of the order of magnitude of the ionisation potential of the gas [95]. The arc voltage drop varies inversely with the molecular weight of the gas at a given pressure and inversely with the pressure for a given gas [73]. An arc discharge is always a local phenomenon. The *cathode spot* (the point from which the arc is initiated) moves quickly over the electrode surface.

The physical difference between glow and arc discharges is the electron production mechanism at the cathode. In glow discharges the electron emission

from the cathode is mainly due to secondary electron production by heavy ion impacts. In arc discharges the electron production is due to thermionic or field emission. These mechanisms are able to supply a greater electron current from the cathode, nearly equal to the discharge current. This eliminates the need for considerable amplification of the electron current as in Townsend discharges or glow discharges.

The thermionic electron emission current  $j_T$  is described by the Dushman–Richardson relation [93,95]:

$$j_T = A_R T^2 \exp\left(-\frac{e\phi}{k_B T}\right), \quad (2.12)$$

where  $e\phi$  is the *work function* expressed in electron volts,  $T$  is the temperature,  $k_B$  is the Boltzmann constant, and  $A_R$  is an empirical constant (see Table 2.4).

The field emission current density  $j_F$  is described by the Fowler–Nordheim equation [93,95]:

$$j_F = 6.2 \cdot 10^{-6} \frac{\sqrt{E_F/e\phi}}{E_F + e\phi} E^2 \exp\left(-\frac{6.85 \cdot 10^9 e\phi^{3/2}}{E}\right), \quad (2.13)$$

where  $E_F$  is the *Fermi level* and  $e\phi$  is the *work function* of the electrode (see Table 2.4). Both are expressed in electron volts. In general, the electrical field  $E$  at the electrode surface has to be increased by a factor (up to 10) in order to reproduce the experimental values. This is because a real surface is never totally smooth and therefore the electrical field can be very high locally.

Arc discharges are characterised by high current densities that allow heating up of the cathode and therefore results in thermionic emission. This happens typically for current densities higher than  $10^{-4}$  A/m<sup>2</sup>.

For the ignition of an arc discharge a higher voltage than the voltage drop at steady-state operation is needed (higher than the breakdown voltage predicted by Paschen's law). Another method to initiate an arc discharge is by first establishing a contact between the two electrodes. A high current heats up the electrodes, initiating the thermionic emission required for producing an arc discharge. In this case, the applied voltage does not need to be higher than the voltage drop at steady-state operation of the arc.

**Table 2.4 Constants in the Dushman–Richardson and Fowler–Nordheim Formulas [95]**

| Element | $e\phi$ (eV) | $A_R$ (cm <sup>2</sup> · K) | $E_F$ (eV) |
|---------|--------------|-----------------------------|------------|
| C       | 4.7          | 30–170                      |            |
| Cu      | 4.4          | 60–100                      | 7.0        |
| Fe      | 4.31         | 60–700                      | 11.1       |
| W       | 5.32         | 40–100                      | 8.95       |

A *spark* is a non-self-sustaining arc discharge. The distance, at atmospheric pressure, over which a spark can occur for a given voltage is called the *spark distance*. For air, typical values are around 20 cm for a voltage of  $10^5$  V. A well-known example of spark is lightning, which is believed to be the longest (tens of kilometres) known spark.

Electrochemical discharges have all the characteristics of arc discharges. They occur in a very similar voltage range with similar currents and at atmospheric pressure. The question remains as to how these arcs can be initiated. We have proposed the hypothesis that the ignition is thermal [123]. The cathode temperature required is probably reached before the gas film is totally formed,<sup>3</sup> when the active electrode bubble coverage fraction reaches its maximum value.

The increase of the cathode temperature is confirmed by several studies. Guilpin [45] and Fascio [32] studied the onset of the gas film by assuming that joule heating is the mechanism of its formation. They evaluated the time required to attain, by joule heating, an electrolyte temperature of  $100^\circ\text{C}$  in the vicinity of the active electrode. They also measured the time needed for the formation of the gas film. Their experimental results showed that this time is similar to the time needed to heat up the electrolyte. Guilpin [45] measured the cathode temperature using thermocouples. He found typical values to be around  $100^\circ\text{C}$ , as did Kellogg [70] previously under similar conditions (see also Section 4.1).

### 2.4.3 Electrochemical Discharges

In the light of the above discussion of electrical discharges, it may be concluded that electrochemical discharges produced at a cathode are most likely non-self-sustained arc discharges (i.e., sparks) for voltages lower than the Paschen breakdown voltage. For higher voltages, the discharges are believed to switch to self-sustained Townsend discharges. The ignition mechanism is probably thermal-assisted field emission.

For electrochemical discharges produced at an anode, the situation is more complex and is discussed later in the chapter. As will be discussed, chemical and electrochemical reactions taking place in the gas film play an important role and are responsible for the formation of hydrogen and the behaviours similar to arc and Townsend discharges observed by Morse.

## 2.5 Contact Glow Discharge Electrolysis

As Wehnelt's current-interrupter was progressively replaced by electronic devices, the interest in electrochemical discharges decreased and the phenomenon was soon forgotten. In the middle of last century, electrochemical discharges were rediscovered with the studies by Kellogg [70] and Hickling [53,54]. In the beginning electrochemical discharges were mainly studied by physicists and electrical engineers, but the works of Kellogg and Hickling were motivated by

chemical applications. Kellogg's studies were motivated by the understanding of the anode effect in molten salts, whereas Hickling was mainly interested in *glow discharge electrolysis*. Both phenomena are actually manifestations of electrochemical discharges.

Glow discharge electrolysis was first described by Faraday. In 1887, Gubkin [44] published a first systematic description of the phenomenon. Since this work, several studies followed during the first half of last century. At the end of the first half of the twentieth century, Hickling and his coworkers conducted a series of studies on glow discharge electrolysis and in 1961 they published a paper in which they reported an "unusual phenomenon" that they observed when a thin platinum wire was used for electrolysis at relatively high voltages. They termed this phenomenon *contact glow discharge electrolysis*. Later, the authors realised that they had actually rediscovered the phenomenon of electrochemical discharges. Nevertheless, the work of Hickling and coworkers revived the interest in electrochemical discharges and, more importantly, brought a completely new dimension by awakening the interest of chemists in the phenomenon.

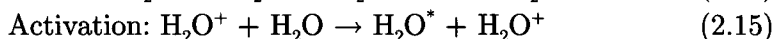
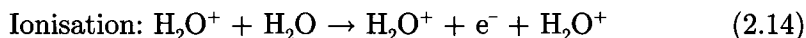
### 2.5.1 Glow Discharge Electrolysis

Glow discharge electrolysis occurs when an electric discharge is passed from an electrolyte to an electrode (anode) situated above the solution. This can be realised for thin electrodes placed in the vicinity of an electrolyte (with a gap of a few millimetres). The voltages needed are typically a few hundred volts. In his pioneering work, Gubkin [44] showed that glow discharge electrolysis can be used to reduce metallic salts in an electrolytic solution. In the beginning of the nineteenth century, chemists noted that the main product of glow discharge electrolysis is hydrogen peroxide ( $\text{H}_2\text{O}_2$ ), but surprisingly the yield was greater than that predicted by Faraday's law. It was established that two processes must be involved, namely a *polar* and an *apolar* process [54]. The polar process corresponds to the charge transfer reaction that is expected to occur during electrolysis. The apolar process is responsible for oxidation accompanied by the evolution of hydrogen from the solution.

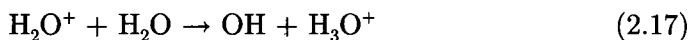
Hickling and coworkers, after having studied several model systems with anode glow discharge electrolysis, clarified the second process and proposed a mechanism to explain the phenomenon of glow discharge electrolysis [54]. They recognised that the chemical reactions involved in glow discharge electrolysis must primarily arise in the liquid phase. Their argument is that, on one hand, the qualitative and quantitative results do not depend on the nature of the gas between the electrode and the electrolyte, and, on the other hand, if electrical discharges take place between two metallic electrodes, none of the effects observed in glow discharge electrolysis can be reproduced. They also noted that there is a large similarity between the effects observed in glow discharge electrolysis and the reactions observed in radiation chemistry. In particular, if

alpha particles are used to bombard electrolytes, the similarities are especially striking. Based on these observations and the conviction that the emission of electrons from the electrolyte towards the anode seems to be quite an unlikely process, Hickling and Ingram proposed following mechanism [54].

They assumed that  $\text{H}_2\text{O}^+$  ions are accelerated by the high electrical field in the gap between the anode and the electrolyte through the gas phase. These ions may have energies up to several hundred electron volts depending on the voltage used. The presence of  $\text{H}_2\text{O}^+$  ions inside the gas phase in the vicinity of the anode is possible considering the high temperature below the glow spot that is able to vaporise the water from the electrolyte. The accelerated ions will penetrate the liquid with energies that are sufficiently high to ionise or activate water molecules from the electrolyte by collision (compare with Table 2.1):



These reactions take place in a small region of the solution, which was termed the primary reaction zone by Hickling and Ingram. They estimated its thickness to be about 10 Å based on the analogy with radiation chemistry. The  $\text{H}_2\text{O}^+$  may also undergo the charge transfer reaction:



Note that the ultimate results of all these processes are OH free radicals. These radicals can interact, as it is expected that they are produced in a very small space, and produce hydrogen peroxide. In summary, the reactions taking place during glow discharge electrolysis, as proposed by Hickling and Ingram, are:



This mechanism explains the formation of hydrogen peroxide and hydrogen during glow discharge electrolysis with an anode as the active electrode. It also explains why a higher yield than that predicted by Faraday's law is obtained. Hickling and Ingram proposed the following equation to compute the rate of hydrogen peroxide formation [54]:

$$\frac{d(\text{H}_2\text{O}_2)}{dt} = G_o \frac{I}{F} - G_o \frac{I}{F} k \cdot [\text{H}_2\text{O}_2], \quad (2.20)$$

where  $G_o$  is the initial production rate and  $k$  is a coefficient characterising the decomposition rate of hydrogen peroxide. Integration of this equation results in:

$$[\text{H}_2\text{O}_2] = \frac{V}{k} (1 - e^{-G_o k q / V}), \quad (2.21)$$

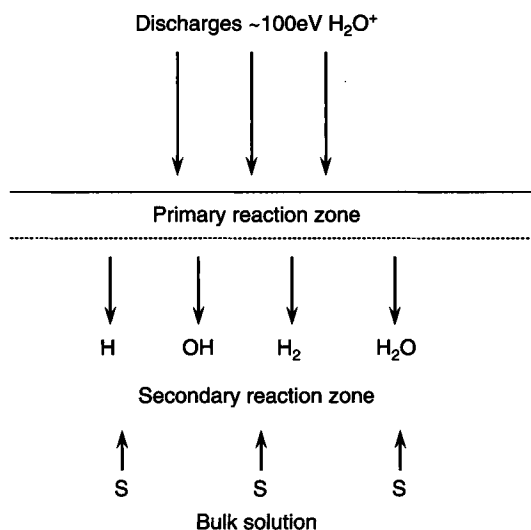


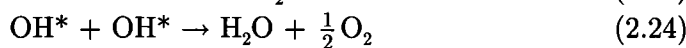
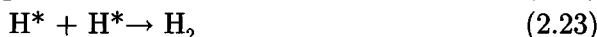
**Figure 2.10** Mechanism of glow discharge electrolysis according to Hickling and Ingram [54]. Reprinted from [54] with permission from Elsevier.

where  $q$  is the quantity of electricity and  $V$  is the volume of the solution. This equation shows good agreement with the experimental results.

Not all OH radicals will react. Consequently, the primary reaction zone is a mixture of H, OH,  $\text{H}_2\text{O}_2$ , and  $\text{H}_2$ . These products will diffuse towards the bulk electrolyte forming a secondary reaction zone (Fig. 2.10). In this zone the diffusion products can undergo oxidation and reduction reactions with the components of the electrolyte.

### 2.5.2 Anodic Contact Glow Discharge Electrolysis

As for glow discharge electrolysis, Hickling and Ingram [53] showed that in contact glow discharge electrolysis hydrogen peroxide is synthesised at a rate higher than that predicted by Faraday's law. Later, in 1998, Sengupta et al. [98] extended the Hickling mechanism by distinguishing two reaction zones: the first inside the gas film and the second in the liquid phase near the gas film–electrolyte interface. The authors proposed that the electrochemical discharges inside the gas film will dissociate the water vapour into hydrogen and oxygen (the later being in excess to Faraday's law) by the following mechanism:





This mechanism is consistent with the observation of H lines and OH bands in the emission spectra of electrochemical discharges at an active anode.

In the liquid phase, the authors proposed a mechanism that is very similar to the Hickling mechanism, forming  $\text{H}_2\text{O}_2$  and excess oxygen by the bombardment of  $\text{H}_2\text{O}^+$ .

In summary, today it is believed that the following mechanisms take place during electrochemical discharges at an active anode [98]:

1. Traditional electrolytic charge transfer at the gas film–electrolyte interface forming oxygen according Faraday’s law (0.25 mol/mol electron).
2. Decomposition of water vapour inside the gas film by the electrochemical discharges by energy transfer resulting in the formation of hydrogen and excess oxygen. This mechanism is probably responsible for the observation of H lines and OH bands in the emission spectra.
3. The formation of  $\text{H}_2\text{O}_2$  in the liquid phase by bombardment of  $\text{H}_2\text{O}^+$ . This mechanism produces non-faradaic yields of  $\text{H}_2$ ,  $\text{H}_2\text{O}_2$ , and  $\text{O}_2$ . Depending on the nature of the electrolyte, further chemical reactions may take place in the secondary reaction zone as in glow discharge electrolysis.

### 2.5.3 Cathodic Contact Glow Discharge Electrolysis

Although cathodic contact glow discharge electrolysis is quite similar to the anodic version, there are some major differences. Physically, the gas film formed during the process is less stable when the active electrode is a cathode than in the case of an anode [70]. According to Hickling and Ingram this effect may be attributed to the different thermal transfer processes [53]. In the case of an active anode, most of the heat produced seems to be transferred to the electrolyte, helping in the formation of a stable gas film, whereas in the case of an active cathode, most of the heat is removed through the electrode. The authors explained this behaviour by the different glow discharge location.

Another significant difference is the nature of the discharges. As discussed previously in Section 2.4, in the case of an active cathode, the electrochemical discharges are most likely electrons emitted from the active electrode by thermionic emission, whereas in the case of an active anode, the discharges result from the accelerated ions across the gas film.

Chemically, the effects in anodic and cathodic contact glow discharge electrolysis are similar [54]. The major difference is the reduced rate of the various reactions taking place. In particular, no  $\text{H}_2\text{O}_2$  production is observed. Nevertheless,  $\text{O}_2$  and OH radicals can be produced by the bombardment of the electrolyte–gas film interface by the electron streams.

## Notes

<sup>1</sup>At that time, the journal *Annalen der Physik* was cited as *Wiedemann's Annalen* in honour of its publisher.

<sup>2</sup>Note that, at that time, taking a photograph of a weak light source, such as the spectrum of electrochemical discharges, was not a straightforward task. Morse had to expose its photographs for several hours!

<sup>3</sup>Note the similarity of this ignition mechanism with the one often used to initiate arc discharges by first establishing a contact between the two electrodes in order to heat them up.

## 3 Gas Evolving Electrodes

---

In order to understand the occurrence of electrochemical discharges, it is necessary to have in-depth knowledge of the phenomena taking place at gas evolving electrodes. The gas is produced electrochemically according to Faraday's law. However, the growth of gas bubbles on the electrode surface affects the area available for electrochemical reactions. The description of the electrochemically active surface as a function of the bubble activity on a gas evolving electrode is the main topic of this chapter. This understanding will allow us to derive an evolution equation for the bubble coverage fraction of the electrode during electrolysis. This equation will have important applications in the description of electrochemical discharges.

### 3.1 Introduction to Electrochemistry

To give a complete overview of electrochemistry, even at an introductory level, is beyond the scope of this book. The aim of this section is to provide only the minimal background knowledge needed for the understanding the phenomenon of electrochemical discharges. The interested reader can find more detailed and advanced presentations in specialised textbooks about electrochemistry.

#### 3.1.1 The Nernst Equation

Consider a metallic electrode dipped in an electrolyte. From thermodynamics it is known that the *chemical potential*  $\mu_i$  of the chemical species  $i$  is given by:

$$\mu_i = \mu_i^\circ + \mathcal{R}T \ln a_i, \quad (3.1)$$

where  $\mathcal{R}$  is the universal gas constant,  $T$  is the temperature of the system, and  $a_i$  is the activity of the chemical species  $i$ . At thermodynamic equilibrium we have for all  $i$ :

$$\mu_i(\text{metal}) = \mu_i(\text{solution}). \quad (3.2)$$

For example, if we consider a copper electrode we have:

$$\mu_{\text{Cu}^{2+}}(\text{metal}) = \mu_{\text{Cu}^{2+}}(\text{solution}). \quad (3.3)$$

This relation is generally not satisfied at the moment the electrode is dipped inside the electrolyte. The system will evolve to the equilibrium state imposed

by (3.2) by progressively dissolving metal from the electrode into the electrolyte or depositing metal from the electrolyte on the electrode:



As consequence an *electrochemical double layer* is formed around the electrode. A potential difference appears between the electrode and the electrolyte and Equation (3.2) has to be completed by the energy of the electrical field

$$\mu_i(\text{metal}) + z_i F \phi(\text{metal}) = \mu_i(\text{solution}) + z_i F \phi(\text{solution}), \quad (3.5)$$

where  $F$  is the Faraday constant ( $F = eN_A = 96,485$  C/mol, the product of the elementary charge  $e$  and the Avogadro number  $N_A$ ) and  $z_i$  is the charge number of the species  $i$  ( $z_i = 2$  for  $\text{Cu}^{2+}$ ). According to Edward Armand Guggenheim (1901–1970), the *electrochemical potential*  $\mu_i^*$  of species  $i$  is commonly defined as [48]:

$$\mu_i^* = \mu_i + z_i F \phi = \mu_i^\circ + \mathcal{R}T \ln a_i + z_i F \phi. \quad (3.6)$$

The equilibrium will be reached when  $\mu_i^*(\text{metal}) = \mu_i^*(\text{solution})$ . It follows that:

$$\Delta\phi_o = \phi_{\text{metal}} - \phi_{\text{solution}} = \frac{\mu_{\text{M}^{z+}}^\circ - \mu_{\text{M}}^\circ}{zF} + \frac{\mathcal{R}T}{zF} \ln \frac{a_{\text{M}^{z+}}}{a_{\text{M}}}. \quad (3.7)$$

The physical meaning of this equation is that if a metal is dipped in an electrolyte, at thermodynamic equilibrium, there will be a potential difference  $\Delta\phi_o$  between the metal and the electrolyte. This potential difference is called the *Galvani potential*.

Usually, one defines  $a_{\text{M}^{z+}} = 1$  to fix the standard Galvani potential. Based on this convention, and defining  $\Delta\phi_{oo} = (\mu_{\text{M}^{z+}}^\circ - \mu_{\text{M}}^\circ)/zF$ , the previous equation is written as:

$$\Delta\phi_o = \Delta\phi_{oo} + \frac{\mathcal{R}T}{zF} \ln a_{\text{M}^{z+}}. \quad (3.8)$$

Equation (3.8) is known as the Nernst equation for a metal electrode. Similar considerations can be used to derive the Nernst equations for other electrochemical reactions. For the general redox reaction



one finds:

$$\phi_o = \phi_{oo} + \frac{\mathcal{R}T}{zF} \ln \frac{a_{\text{Red}}}{a_{\text{Ox}}}, \quad (3.10)$$

according to a fixed standard reference.

For a gas evolving electrode where, for example, the hydrogen evolution reaction



takes place, the Nernst equation can be written as:

$$\phi_o = \phi_{oo} + \frac{\mathcal{R}T}{F} \ln \frac{a_{\text{H}_3\text{O}^+}}{\sqrt{p_{\text{H}_2}}}, \quad (3.12)$$

where  $p_{\text{H}_2}$  is the partial pressure of  $\text{H}_2$ . The reference is fixed by choosing the activity of water  $a_{\text{H}_2\text{O}} = 1$ .

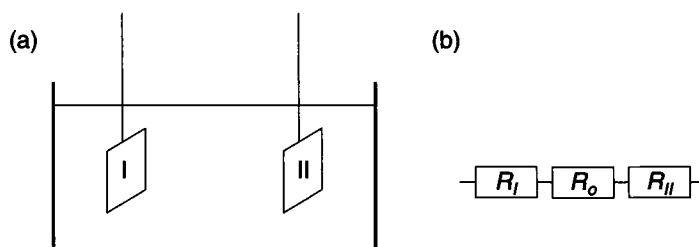
### 3.1.2 Electrochemical Cell Out of Thermodynamic Equilibrium

Figure 3.1(a) shows a typical electrochemical cell consisting of two electrodes dipped in an electrolyte. Electron transfers take place at the electrodes. In electrochemistry, it is common to introduce an equivalent electrical circuit<sup>1</sup> as shown in Fig. 3.1(b). The three resistances in series are the *inter-electrode resistance* (or electrolyte resistance)  $R_o$  and the *charge transfer resistances*  $R_I$  and  $R_{II}$ . The first resistance is an ohmic resistance function of the electrolyte conductivity and the cell geometry. Its physical origin is the electrical conductivity of the charged ions in an electrolyte. The two charge transfer resistances are non-linear resistance functions of the current. Their origins are the electrochemical processes taking place at the electrode and they result from the energy needed for the electron transfer between the electrodes and the ions in the electrolyte.

The electrochemical reactions can be written as:



Each reaction is called a *half reaction*. The first reaction is a *reduction reaction*, whereas the second is an *oxidation reaction*. As discussed later, electrochemical reactions may actually be much more complex, involving intermediates, but the principle remains the same.



**Figure 3.1** (a) An electrochemical cell with two electrodes; (b) simplified equivalent circuit.

The potential difference between the two electrodes is called the *terminal voltage* or the *cell voltage*  $U$ . By convention it is often measured as:

$$U = \phi^I - \phi^{II}. \quad (3.15)$$

When no current is flowing in the cell (at thermodynamic equilibrium) the terminal voltage can be computed using the Nernst equations for the two electrodes:

$$U_o = \phi_{oo}^I - \phi_{oo}^{II} - \frac{\mathcal{R}T}{zF} \ln \left( \frac{a_{X_{\text{red}}} a_{Y_{\text{ox}}}}{a_X a_Y} \right). \quad (3.16)$$

The quantity  $U_o$  is known as the *electromotive force* of the electrochemical cell.

When a current is flowing, the system is driven away from the thermodynamic equilibrium and the electrode potentials change. The way the potentials change depends how the electrochemical cell is connected to the external environment.

If the cell is connected to an external charge, the cell is called a *galvanic cell*. The system will try, by letting a current flow through the external charge, to move to the new equilibrium in which both electrodes have the same potential. Therefore, in a galvanic element, the terminal voltage decreases with increasing current (Fig. 3.2(a)).

If the cell is connected to an external power source, *electrolysis* takes place. The system, called an *electrochemical cell*, is now driven away from the thermodynamical equilibrium by an imposed flux, the electrical current. Internal entropy is produced. With increasing current, the terminal voltage will increase (Fig. 3.2(b)).

In electrochemistry it is common to introduce the difference between the potential  $\phi$  of an electrode and the potential  $\phi_o$  of the electrode at thermodynamic equilibrium (when no current is flowing). This potential difference is called the *over potential*  $\eta$ :

$$\eta = \phi - \phi_o. \quad (3.17)$$

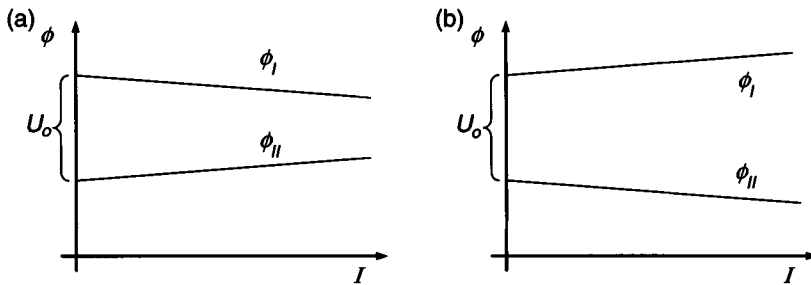


**Figure 3.2** Schematic evolution of the cell voltage with the current  $I$ : (a) galvanic element; (b) electrochemical cell.

From the point of view of thermodynamics, the over potential is the thermodynamic force driving the system out of equilibrium and it is responsible for the production of internal entropy  $d_i S$  by the electrochemical reactions [77]:

$$\frac{d_i S}{dt} = \frac{\eta^I + \eta^{II}}{T} I. \quad (3.18)$$

The over potential plays a central role in electrochemistry as it controls the electrochemical reactions. By convention it is generally measured as a positive value for reactions where electrons are transferred *to* the electrode. The associated current is also counted positively. In this case the electrode is called an *anode*. If electrons are transferred *from* the electrode to the ions of the electrolyte, the over potential and the associated current are measured as negative values. The electrode is termed *cathode*. Using the definition of the over potential, the terminal voltage for an electrochemical cell is given by (see Fig. 3.2(b)):

$$U = U_o + \sum |\eta| + R_o I. \quad (3.19)$$

The term  $R_o I$  is called the *ohmic drop*.<sup>2</sup> Figure 3.3 shows the schematic potential distribution in an electrochemical cell. At the anode a potential drop  $U_a$  occurs, which is given by the sum of the equilibrium potential  $U_{eq,a}$  and the anodic over potential  $\eta_a$ . An analogous situation takes place at the cathode. Note that the electromotive force of the cell is  $U_o = U_{eq,a} + U_{eq,c}$ . In practical applications of Equation (3.19), one has to pay attention to the sign convention attributed to the various quantities.

If the kinetics of the charge transfer at each electrode is known, or, in other words, if the relation  $I(\eta)$  is known for each electrode, it is possible, using Equation (3.19), to predict the current–voltage characteristics of an electrochemical cell. One of the goals of electrochemistry is to describe the charge transfer current

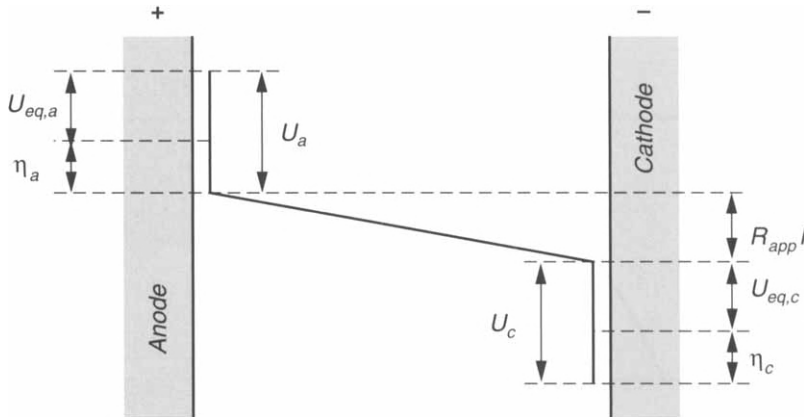


**Figure 3.3** Potential distribution in an electrochemical cell (see text for definitions of the different physical quantities).

characteristics, the function  $I(\eta)$ , for a given electrochemical reaction and electrode configuration.

### 3.1.3 The Charge Transfer Current Characteristics

Consider following oxido-reduction reaction involving the charge transfer of  $z$  electrons:



As described above, if this electrochemical reaction is driven out of equilibrium with the thermodynamic force  $\eta$ , a current  $I$  will flow. One of the great successes of electrochemistry is its ability to provide a quantitative description of the charge transfer current characteristics. Max Volmer (1885–1965) and John Alfred Valentine Butler (1899–1977) proposed the following relation, which is known today as the Butler–Volmer equation, between the over potential  $\eta$  and the current density  $j$  (Fig. 3.4):

$$j(\eta) = j_o \left( \exp \left[ \frac{(1-\alpha)zF}{RT} \eta \right] - \exp \left[ -\frac{\alpha zF}{RT} \eta \right] \right). \quad (3.21)$$

The quantity  $j_o$  is the *exchange current density* and is related to the kinetics of the electrochemical reactions considered and the local concentration of the reactants. It also depends on the electrode material. The parameter  $\alpha$  is the symmetry factor and typically has a value of around 0.5. The Butler–Volmer

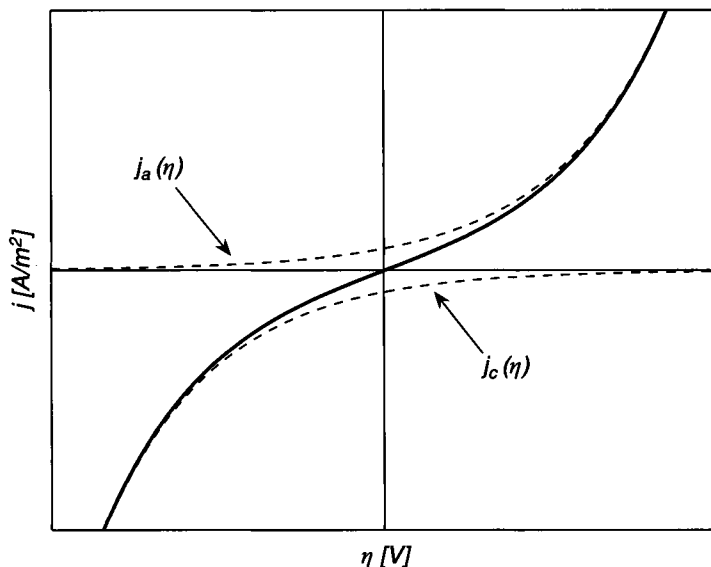


**Figure 3.4** Charge transfer current characteristics according to the model of Butler and Volmer.



equation is actually the sum of two contributions: one from the anodic reaction  $j_a(\eta)$  and the other from the cathodic reaction  $j_c(\eta)$ .

The Butler–Volmer equation, together with Equation (3.19), allows the prediction of the current–voltage characteristics of a galvanic or an electrochemical cell. In applications where the current density is high (or the overpotential is high), the exponential law of the Butler–Volmer equation implies that  $\eta$  can be approximated by a constant value independent of  $j$ . Relation (3.19) can then be written in its simplified form (Fig. 3.5):

$$U = U_d + R_o I, \quad (3.22)$$

where  $U_d = U_o + \sum |\eta|$  is a potential characteristic of the given electrochemical reactions. In the case of electrolysis of water, this potential is called the *water decomposition potential*. Depending on the electrode material, typical values are in the range 1.7–2.0 V. Note that the response of the electrochemical cell is linear, or in other words the cell exhibits ohmic behaviour.

### 3.1.4 Hydrogen and Oxygen Evolution

Electrochemical reactions are usually complicated by several intermediate processes. As an example let us first discuss the *hydrogen evolution reaction*. It should be noted that although the hydrogen evolution reaction is probably one of the most studied, its mechanism is still not yet clearly established. In alkaline solutions it is generally believed that the production of hydrogen proceeds by chemisorption of water molecules on free electrode sites M, through the so-called *Volmer reaction*:

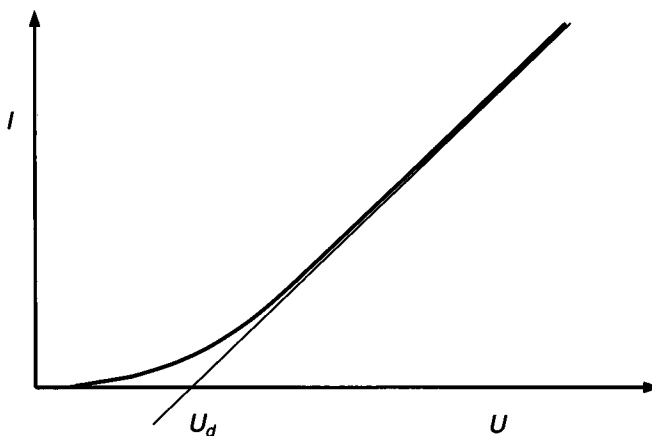
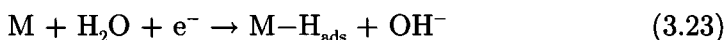
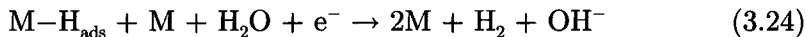
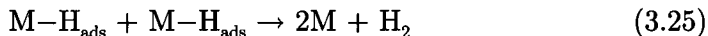


**Figure 3.5** Definition of the decomposition potential  $U_d$

followed by either the electrochemical desorption mechanism, known as the *Heyrovsky reaction*:



or the chemical desorption mechanism, known as the *Tafel reaction*:



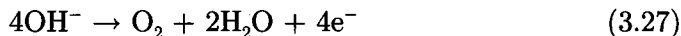
The quantity  $\text{M-H}_{\text{ads}}$  denotes the hydrogen adsorbed on the electrode surface.

Even by considering some hypotheses to compute the kinetics of these reactions, the relations obtained contain several parameters to be adjusted by the experiment. This makes the comparison between theoretical models and experimental measurements difficult. Until now no model is generally accepted.

The *oxygen evolution reaction* is, similar to the hydrogen evolution reaction, complicated by several intermediates. It is generally admitted that in an acid medium the overall reaction is:



and in an alkaline solution:



It should be noted that in an acid medium the situation is complicated by the corrosion of the electrode as, at the over potential needed for oxygen evolution, the electrode material corrodes and is often passivated. In alkaline electrolytes the situation is generally better as the electrodes can resist the corrosion. However, in this case the formation of the metal oxide has to be taken into account, which complicates the interpretation of the experimental results. The situation can be very different depending on whether the metal oxide formed is electrically insulating (e.g., platinum, gold, or nickel), conductive (e.g., ruthenium and iridium), or semi-conductive (e.g., boron-doped diamond electrodes). The situation is even more complex as the surface of an oxidised electrode can undergo surface restructuring, modifying the adsorption sites available for the  $\text{OH}^-$  radicals. Surface restructuring results from the competition between minimisation of energy  $E$  and maximisation of entropy  $S$  as expressed in the Helmholtz free energy equation  $F = E - TS$ .

Very often, some by-products such as hydrogen peroxide or organic molecules that are more or less stable can be formed.

The consequence of all these effects is that oxygen, or hydrogen, evolution reactions follow quite different kinetics than would be expected from thermodynamical considerations. For example, oxygen evolution on a platinum electrode starts at a potential significantly higher than that predicted by the Nernst equation. The reason for this is the formation of surface oxide and its associated dynamics as elucidated, besides others, by B. Conway [4].

### 3.1.5 Electrical Conductivity in Electrolytes

In an electrolytic solution the electrical current is transported by the ions. When an electrical field  $\vec{E}$  is applied, ions migrate with a constant *drift velocity*  $\vec{v}_d$ :

$$\vec{v}_d = u\vec{E}, \quad (3.28)$$

where  $u$  is the *ion mobility* characterising the electrical transport process in an electrolyte. Typical values for  $\text{H}^+$  and  $\text{OH}^-$  ions in water at 25°C are:  $u_{\text{H}^+} = 36.3 \cdot 10^{-4} \text{ cm}^2 \text{ V}^{-1} \text{ s}^{-1}$  and  $u_{\text{OH}^-} = 20.5 \cdot 10^{-4} \text{ cm}^2 \text{ V}^{-1} \text{ s}^{-1}$  (Table 3.1). The ion mobility depends only on the ion considered and increases with the electrolyte temperature. The *electrical conductivity*  $\kappa$  of the electrolytic solution is given by:

$$\kappa = e(n_+ z_+ u_+ + n_- z_- u_-), \quad (3.29)$$

where  $n_+$  and  $n_-$  are the number of cations and anions per volume with charges  $z_+$  and  $z_-$ , respectively, and  $e$  is the magnitude of electron charge.

It is common to introduce  $\Lambda$  the *molar ionic conductivity* for electrolytes, which is the conductivity of a specific volume of an electrolyte containing one mole of solution between electrodes placed one meter apart:

$$\Lambda = \frac{\kappa}{C}, \quad (3.30)$$

where  $C$  is the *electrolyte concentration* expressed in  $\text{mol m}^{-3}$ .

At very low electrolyte concentrations, each ion of the electrolyte contributes independently to the molar conductivity. For an electrolyte of the form  $(\text{A}^{z_+})_{\nu_+} (\text{X}^{z_-})_{\nu_-}$ , Kohlrausch's law of independent ion migration can be written as:

$$\Lambda^\circ = \nu_+ \Lambda_+^\circ + \nu_- \Lambda_-^\circ, \quad (3.31)$$

where  $\Lambda^\circ$  is the *molar conductivity at infinite dilution* ( $C \rightarrow 0$ ; Table 3.2)

**Table 3.1 Ion Mobility in Water at 18°C for Infinite Dilution**

| Cation           | $u_+ \cdot 10^{-4} \text{ (cm}^2 \text{ V}^{-1} \text{ s}^{-1}\text{)}$ | Anion         | $u_- \cdot 10^{-4} \text{ (cm}^2 \text{ V}^{-1} \text{ s}^{-1}\text{)}$ |
|------------------|---|---------------|---|
| $\text{H}^+$     | 31.5  | $\text{OH}^-$ | 17.4  |
| $\text{Li}^+$    | 3.3   | $\text{Cl}^-$ | 6.9   |
| $\text{Na}^+$    | 4.3   | $\text{Br}^-$ | 6.7   |
| $\text{K}^+$     | 6.5   | $\text{I}^-$  | 6.7   |
| $\text{Ag}^+$    | 5.4   |               |   |
| $\text{Zn}^{2+}$ | 4.8   |               |   |

**Table 3.2 Individual Molar Conductivities in Water at 25°C for Infinite Dilution**

| Cation           | $\Lambda^{\circ}$ ( $\Omega^{-1} \text{ cm}^2 \text{ mol}^{-1}$ ) | Anion           | $\Lambda^{\circ}$ ( $\Omega^{-1} \text{ cm}^2 \text{ mol}^{-1}$ ) |
|------------------|---|-----------------|---|
| Li <sup>+</sup>  | 349.9   | OH <sup>-</sup> | 197.6   |
| Na <sup>+</sup>  | 38.7  | F <sup>-</sup>  | 55.0  |
| K <sup>+</sup>   | 50.1  | Cl <sup>-</sup> | 76.3  |
| Ag <sup>+</sup>  | 73.5  | Br <sup>-</sup> | 78.4  |
| Zn <sup>2+</sup> | 61.9  | I <sup>-</sup>  | 76.8  |
| Li <sup>+</sup>  | 52.8  |                 |   |

There are two classes of electrolytes: *weak electrolytes* and *strong electrolytes*. For weak electrolytes,  $\Lambda$  varies with the concentration  $C$ , according to Arrhenius, as:

$$\Lambda(C) = \alpha(C)\Lambda^{\circ}, \quad (3.32)$$

where  $\alpha$  is the *degree of dissociation of the electrolyte*. In this case, the molar ionic conductivity is linked to the drift velocity by:

$$\Lambda = \alpha F(v_+ z_+ u_+ + v_- z_- u_-). \quad (3.33)$$

For strong electrolytes, Kohlrausch (1876) determined the following empirical relationship:

$$\Lambda(C) = \Lambda^{\circ} - K_{s-e} \sqrt{C}. \quad (3.34)$$

The constant  $K_{s-e}$  can be calculated by the Debye–Hückel–Onsager theory.

For weak electrolytes, at small concentrations, the electrical conductivity is almost proportional to the electrolyte concentration. For higher concentrations, the degree of dissociation decreases. Consequently, the electrical conductivity reaches a maximum as a function of the electrolyte concentration. For strong electrolytes this maximum also exists, because when the electrolyte concentration is increased, the ionic interaction becomes stronger. This is illustrated for a NaOH solution in Fig. 3.6. In this figure the influence of the electrolyte temperature on the conductivity can be seen. The temperature mainly influences the viscosity of the electrolyte, which influences the drift velocity of the ions. Other effects are the changes in the dielectric function of water and the degree of dissociation of the electrolyte.

### 3.2 Bubble Formation during Electrolysis

During electrolytic decomposition of water, gas bubbles are produced at the electrodes. The formation of a bubble involves two steps. As a concrete example

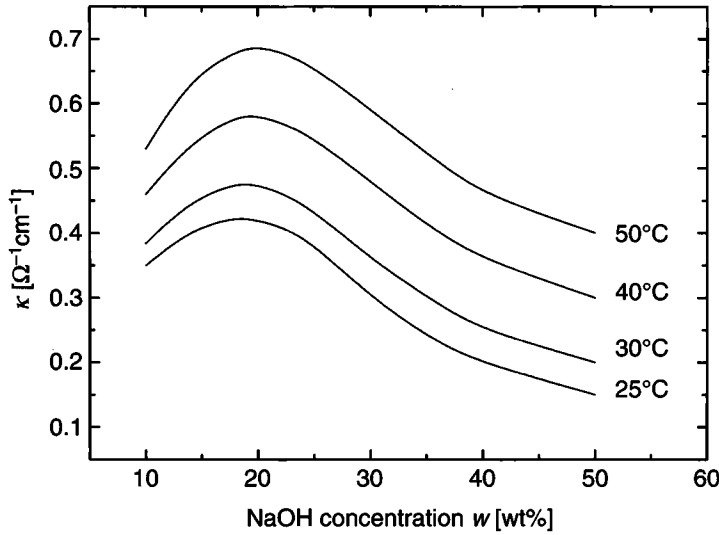
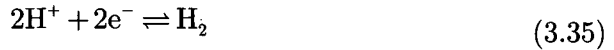


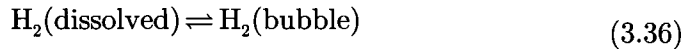
**Figure 3.6** Electrical conductivity  $\kappa$  of NaOH as a function of the electrolyte mass concentration  $w$  and temperature. Plotted using data from [135].

let us consider the formation of hydrogen gas bubbles. The first step is the microscopic formation of  $H_2$  by an electrochemical process:



Note that, as discussed in Section 3.1.4, this step is more or less complex depending on the electrolyte and the electrode used.

The second step is the macroscopic formation of bubbles by accumulation of the dissolved  $H_2$  in the vicinity of the electrode:



This physical step follows a cycle. The *bubble growth* starts at defects (such as cavities) on the electrode surface. The nucleation and growth of bubbles is possible only if the electrolyte in the vicinity of the electrode is supersaturated with dissolved gas. During their growth, the bubbles are fed from the highly supersaturated surrounding electrolyte [12,113,114]. Two forces act on the bubbles: the buoyancy force  $F_B$  and the capillary force  $F_c$  (Fig. 3.7):

$$F_B = \frac{4}{3}\pi R_b^3 \rho g, \quad (3.37)$$

$$F_c = 2\pi D \gamma \sin \vartheta, \quad (3.38)$$

where  $\rho$  is the density of the electrolyte,  $\gamma$  is the surface tension of the electrolyte,  $R_b$  is the bubble radius,  $D$  is the order of magnitude of the aperture of an active nucleation site, and  $\vartheta$  is the contact angle.

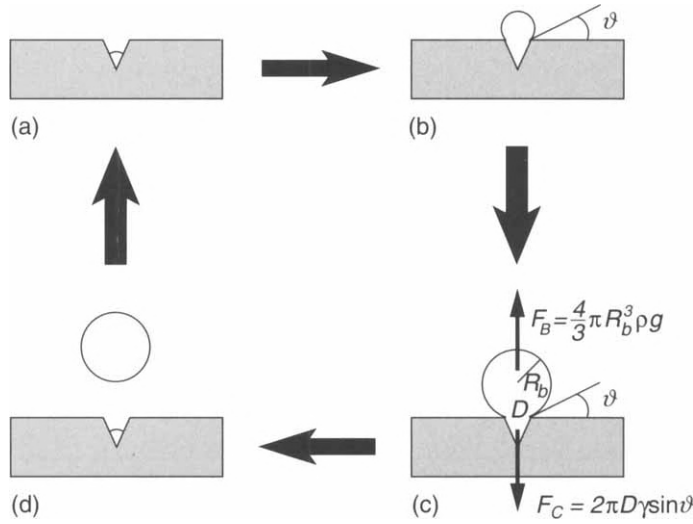


**Figure 3.7** Schematic representation of the bubble production cycle (according to [68,81]; reprinted with permission from [81]; copyright (2002) American Electrochemical Society): (a) a bubble starts growing at a nucleation site; (b) formation and growth of the bubble; (c) equilibrium between the buoyancy force and capillary force is reached; (d) bubble detachment.

The detachment of the bubble occurs if the condition  $F_B = F_C$  is satisfied. It follows that the *mean bubble departure radius*  $\langle R_d \rangle$  is well defined for a given electrode–electrolyte configuration (typical values are around 50  $\mu\text{m}$  [115]). It may be expected that the mean bubble departure radius is mainly a property of the electrode (the electrode surface roughness which influences  $D$ ), the electrode wettability (through the contact angle  $\vartheta$ ), and the electrolyte (density and surface tension of the electrolyte), but not of the current density  $j$ . However, the question is whether a cavity (nucleation site) is active or non-active. The current density may influence the activation of the nucleation sites.

Actually, many external parameters influence the bubble diameter distribution such as concentration, pH of the electrolyte, polarity and potential of the electrode, wetting conditions, and the current density [115].

Several authors have studied the dependence of the mean bubble departure radius  $\langle R_d \rangle$  on the current density. Venczel [109] found that for small current densities (typically  $j < 2 \text{ kA/m}^2$ ) the radius decreases with decreasing current density. It seems to become independent of the current density for higher values, while the number of growing bubbles increases. Vogt [115] observed a similar behaviour for small current densities. Other authors [18,38,42] found that the mean departure radius increases with the current density  $j$  according to the following empirical power law:

$$\langle R_d \rangle = aj^n. \quad (3.39)$$

The exponent  $n$  was identified to be equal to 0.22 by Janssen et al. [18] and to be equal to  $\frac{1}{3}$  by Gabrielli et al. [38] and Glass et al. [42]. The coefficient  $a = 46$

if  $j$  is expressed in  $\text{kA/m}^2$  and  $\langle R_d \rangle$  in  $\mu\text{m}$  according to Janssen et al. [18]. Glass et al. found that this coefficient depends on the growing time and the mass diffusivity of the participating ions in solution.

It has to be stressed that all these empirical laws were obtained for relatively small current densities ( $j < 10 \text{ kA/m}^2$ ). Gabrielli et al. [38] observed that for sufficiently high current densities the departure radius becomes independent of  $j$ . Depending on the nature of the gas, there seems to be a maximum bubble diameter. They found that this maximum diameter would be reached for  $j \simeq 90 \text{ kA/m}^2$  in the case of hydrogen bubbles.

Another important point to realise is that  $\langle R_d \rangle$  depends not only on the equilibrium condition between the buoyancy force and the capillary force, but also on the bubble coalescence. Coalescence becomes more and more important for higher current densities. As measured by Janssen and van Stralen [66], the number of growing bubbles increases with the current density and thus coalescence becomes more and more probable. In the same paper, Janssen showed that the mean departure radius of bubbles can strongly depend on the quality of the electrode (he compared unused electrodes with used electrodes of the same type).

Despite the important implications in many applications, such as in industrial electrolysis, the theoretical description of the electrolytic bubble formation remains mainly phenomenological. As shown by this discussion, the problem is actually very complex and no general consensus can be found in the literature. In the rest of this chapter some models that are useful for understanding the phenomenon of electrochemical discharges are presented.

### 3.3 Bubble Layer

The bubbles around a gas evolving electrode form a *bubble layer* structured in three regions [12,67] (Fig. 3.8):

- adherence region,
- bubble diffusion region, and
- bulk region.

In the *adherence region* the bubbles adhere to the electrode surface and grow. The typical thickness of this layer is the mean bubble diameter. During the growing phase if the bubbles have mechanical contact, they coalesce [111].

Once the bubbles leave the electrode surface (when they have a radius equal to the departure radius) they diffuse into the *bubble diffusion region*. This region has a very high bubble concentration [12] with a typical thickness of a few millimetres. The bubbles can still grow.

The third region is the *bulk region*, which contains only a few dispersed bubbles. It is generally acknowledged that in this region the supersaturation of gas is close to the level of the bulk solution and therefore bubbles do no longer grow. Sometimes large bubbles that jump directly from the adherence region to the bulk region are observed.

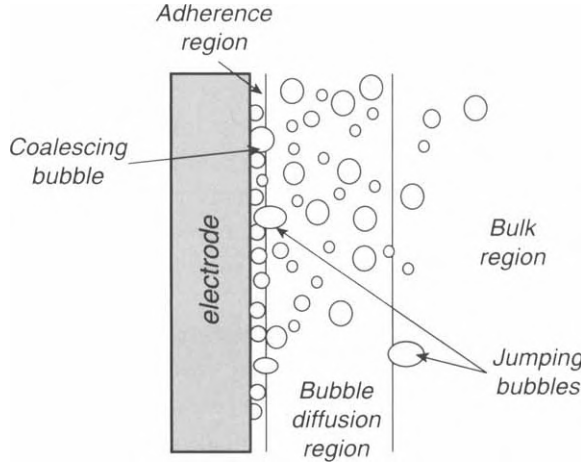


**Figure 3.8** Schematic representation of the bubble layer structure (according to Janssen [67] and Boissonneau and Byrne [12], with kind permission from Springer Science+Business Media). Three regions are identified: the adherence region, the bubble diffusion region, and the bulk region.

Each of these three regions contributes differently to the inter-electrode resistance. During their growth in the adherence region, the bubbles partially shadow the active surface of the electrode. The covered fraction is electrochemically inactive. The *bubble coverage fraction*  $\theta$ , defined as the fraction of the electrode area shadowed by the bubbles, quantifies this effect [29,109,112]. For a given bubble coverage fraction  $\theta$ , the *local current density*  $j_{local}$  is increased compared with the *nominal current density*  $j_n = I/A$ , where  $I$  is the current flowing through an electrode of surface  $A$ :

$$j_{local} = \frac{1}{1-\theta} \frac{I}{A}. \quad (3.40)$$

The bubbles in the inter-electrode gap (bubble diffusion region and bulk region) increase the inter-electrode resistance, as they affect the electrical conductivity of the electrolyte. The parameter describing this increase is the *gas void fraction*  $\varepsilon$ , defined as the fraction between the volume of gas and the total volume of liquid and gas. Several relations are used in the electrochemical literature to quantify this effect. The most widely used are the relations from Bruggeman [16]:

$$\kappa_{eff} = \kappa(1-\varepsilon)^{3/2} \quad (3.41)$$

and Maxwell [87]:

$$\kappa_{eff} = \kappa \left( 1 + 1.5 \frac{\varepsilon}{1-\varepsilon} \right)^{-1}, \quad (3.42)$$

where  $\kappa_{eff}$  is the conductivity of the electrolytic solution taking into account the bubbles and  $\kappa$  is the electrical conductivity without bubbles. Numerically



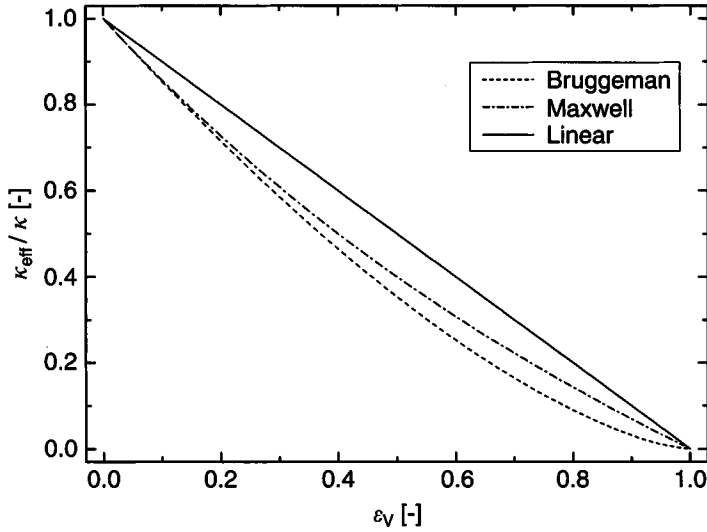


**Figure 3.9** Relative conductivity  $\kappa_{\text{eff}}/\kappa$  of an electrolytic solution as a function of the gas void fraction  $\varepsilon$  according to Bruggeman [16] and Maxwell [87].

both relations give almost the same results and can be approximated by a linear expression (Fig. 3.9).

### 3.4 The Bubble Diffusion Region

Let us first start with the description of the bubble diffusion region that is directly accessible to visual observations. The important parameters that characterise the bubble diffusion region are the gas void fraction  $\varepsilon$  and the geometrical shape of the bubble layer, both of which are dependent on the cell geometry. We will restrict the discussion to the case that is most representative of micromachining with electrochemical discharges: the case of a thin electrode dipped inside an electrolyte. The electrochemical cell is much larger than the electrode.

Figure 3.10 shows the bubble diffusion layers around a cylindrical electrode of a few millimetres length for various terminal voltages. One can see that in all cases the bubble layer has a similar conical shape, more or less independently of the terminal voltage. The bubble builds a random close packing structure. Note that the volume void fraction of a random close packing structure for identical spheres is about 0.64 [64].

To describe the contribution to the inter-electrode resistance a simplified model will be used. Let us assume that the bubble diffusion layer has a mean thickness  $d$  and that the gas void fraction is constant and equal to  $\varepsilon$  over the whole electrode height  $h$ . The efficient conductivity of the electrolyte is

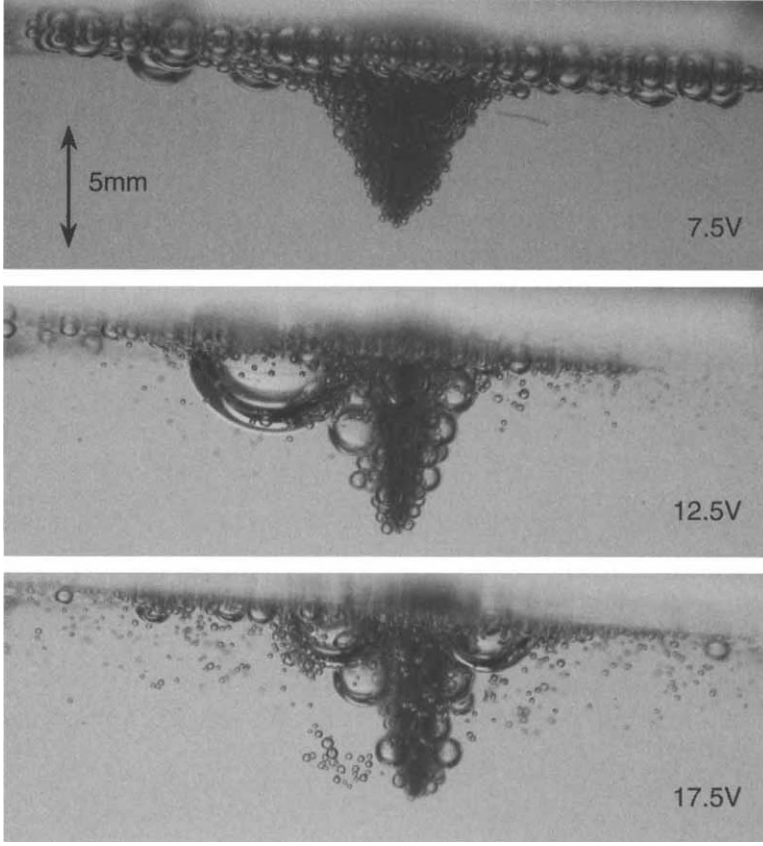


**Figure 3.10** Bubble diffusion layers around a cylindrical electrode of a few millimetres length at various terminal voltages [123].

computed using the Bruggeman relation (3.41). The resistance of the bubble diffusion region is then given by:

$$R^{diff}(\varepsilon) = \frac{1}{(1-\varepsilon)^{3/2}} \frac{1}{2\pi\kappa h} \ln\left(\frac{b+d}{b}\right), \quad (3.43)$$

where  $b$  is the radius of the electrode and  $\kappa$  is the conductivity of the electrolyte. In order to compute the total inter-electrode resistance one has to add the resistance of the electrolyte in the bulk region.

The consequence of the existence of the bubble diffusion region is that the potential distribution at a gas evolving electrode contains an additional potential drop compared with Equation (3.22):

$$U = U_o + |\eta_a| + |\eta_c| + R^{bulk} I + R^{diff} I, \quad (3.44)$$

where  $R^{bulk}$  is the resistance of the bubble bulk region. This equation is illustrated in Fig. 3.11, which shows a schematic representation of the potential distributions at a gas evolving electrode.

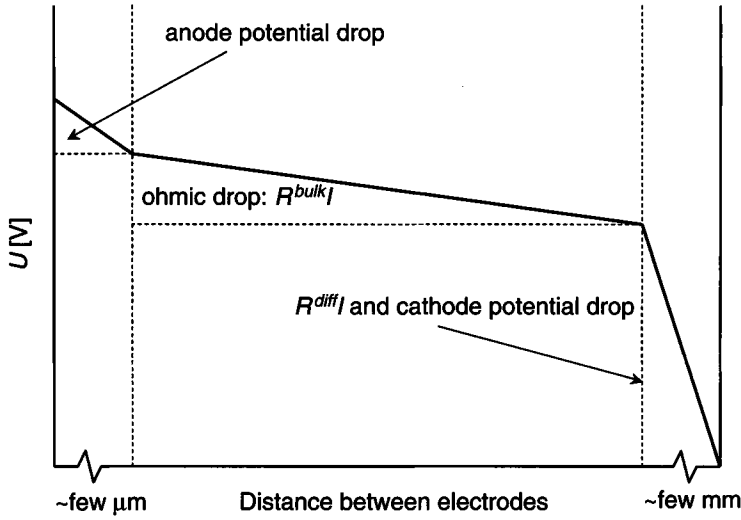


**Figure 3.11** Schematic representation of the potential distribution at a gas evolving electrode, adapted from [1,41].

Note that, in this description, the shadowing of the surface by the bubbles in the adherence region was not considered. With increasing bubble coverage fraction  $\theta$ , the resistance in the diffusion region  $R^{diff}$  will also increase. A possible ansatz is to write (3.44) as:

$$U = U_o + |\eta_a| + |\eta_c| + R^{bulk}I + \frac{R^{diff}}{1-\theta}I, \quad (3.45)$$

where  $R^{diff}$  is given by (3.43). This aspect is discussed further in Section 3.7.2. This relation shows the importance of the bubble coverage fraction  $\theta$ . The following sections will describe a way to estimate  $\theta$  as a function of the various problem parameters.

### 3.5 The Bubble Adherence Region

Of particular interest for the onset of electrochemical discharges is the distribution of the bubbles formed electrochemically on the electrode surface. Depending on their size, the bubbles may be able to leave the adherence region or remain in the adherence region, thereby significantly influencing the apparent inter-electrode resistance. In order to describe quantitatively the bubble size distribution, an idealised model of the nucleation sites on the electrode is introduced [123]. The geometry of the model is depicted in Fig. 3.12. The electrode of radius  $b$  and height  $h$  is dipped into the electrolytic solution. The lateral electrode surface  $\Omega$  is subdivided into a lattice of size  $L$ . Each lattice site represents a nucleation site on the lateral electrode surface where a bubble

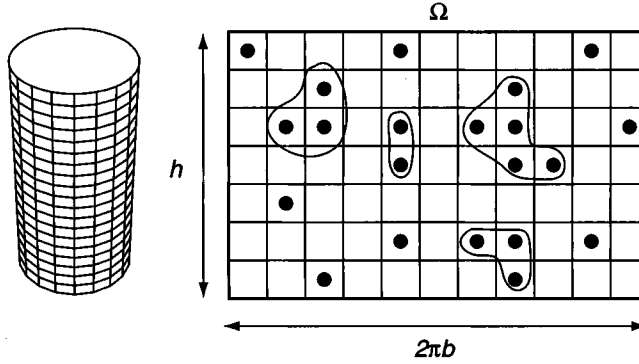


**Figure 3.12** Percolation model of the bubble adherence region: the lateral active electrode surface  $\Omega$  is subdivided into a lattice of size  $L$ . Sites are occupied with a mean occupation probability  $p$ . Neighbouring bubbles are assumed to coalesce and build a new larger bubble [123].

may grow and is identified by the index  $i \in \{1, L\}$ . The probability that a bubble grows at a given site is  $p$ .

### 3.5.1 Clusters and Bubbles

A *cluster* is defined as a group of neighbouring occupied sites. Bubble coalescence is allowed. Recall that bubbles coalesce if they have mechanical contact. Therefore, all sites of a cluster are considered to have coalesced and formed a new larger bubble.

Each cluster is characterised by its size  $s$ , which is defined as the number of sites belonging to the cluster. A cluster of size  $s$  is called an  $s$ -cluster. The *normalised cluster number*  $n_s$  is defined as the number of  $s$ -clusters per lattice site. An equivalent way to define  $n_s(p)$  is by noting that the probability that an arbitrary lattice site belongs to an  $s$ -cluster equals  $n_s \cdot s$ .

In order to quantify the effect of bubble screening on the apparent inter-electrode resistance, we have to quantify the bubble distribution and, in particular,  $n_s(p)$ . The mathematical theory dealing with this problem is *percolation theory*.

The remainder of this section is dedicated to the description of percolation theory and how it can be applied to model the bubble adherence region. Providing a complete description of the percolation theory is beyond the scope of this book. Only the important concepts required for our purpose will be presented. The interested reader can find more information in specialised textbooks. For example, the book by Stauffer and Aharony [101] provides an excellent introduction to the subject.

### 3.5.2 Percolation Theory

As a mathematical subject, percolation is a product of the 1950s and goes back to the studies by Broadbent and Hammersley [15,49]. Broadbent studied

the problem of active carbon-filled filters for gas masks in mines. The size of the carbon particles is a critical parameter in these devices. If the filter is filled with very small particles, it does not allow air filtration. If, on the other hand, the filter is filled with very coarse particles, it is not efficient. An optimal intermediate value has to be found. Together with Hammersley, he formulated the problem in a more general way. In their pioneering paper [15], they raised the question: "At what density of pores (holes) in a large porous rock does it become possible for a fluid to flow through the rock?"

Generally speaking, percolation deals with the effect of varying the richness of interconnections present in a random system. The basic idea is the existence of a sharp transition at which the long-range connectivity of the system disappears (or appears). This transition occurs abruptly when some generalised density in this system reaches a critical value (the so-called *percolation threshold*). Today, percolation theory is a well-developed branch in the theory of disordered systems and critical phenomena and has become very popular in modern physics. This is due to the universality of the phenomena studied as shown by the various applications in several different disciplines like physics, chemistry, biology, or sociology (see Table 3.3). Percolation theory is mainly used to explain phase transitions and has emerged as a cornerstone of the theories of disordered physical systems. The correspondence between percolation theory and phase transition was formulated in a mathematical theorem by Kasteleyn and Fortuin [69] in 1969.

The main difficulty in percolation theory is expressing the number of  $s$ -clusters per lattice site  $n_s(p)$ . For one-dimensional problems, this is straightforward [101]:

$$n_s = p^s(1 - p)^2. \quad (3.46)$$

**Table 3.3 Some Applications of Percolation Theory (according to [139])**

| Phenomenon or System                         | Transition                  |
|--|-----------------------------|
| Flow of liquid in porous media               | Local/extended wetting      |
| Spread of disease in a population            | Containment/epidemic        |
| Communication or resistor networks           | Disconnected/connected      |
| Conductor–insulator composite material       | Insulator/metal             |
| Composite superconductor–metal material      | Normal/superconducting      |
| Discontinuous metal film                     | Insulator/metal             |
| Stochastic star formation in spiral galaxies | Non-propagation/propagation |
| Quarks in nuclear matter                     | Confinement/non-confinement |
| Thin helium films on surface                 | Normal/superfluid           |
| Dilute magnets                               | Para/ferromagnetic          |
| Polymer gelation                             | Liquid/gel                  |
| Glass transition                             | Liquid/glass                |
| Forest fire                                  | Confined/not confined       |

But already in two dimensions, no general expression in closed form is known. The difficulty becomes clear by considering the following expression for  $n_s$  in two dimensions [101]:

$$n_s = \sum_k n'_{sk} p^s (1-p)^k, \quad (3.47)$$

where  $k$  is the perimeter (number of nearest neighbours of a site in the lattice) and  $n'_{sk}$  is the number of different geometrical configurations of an  $s$ -cluster with perimeter  $k$  (this quantity is often called the number of animals in percolation literature). For small values of  $k$ ,  $n'_{sk}$  are tabulated. But, so far, no general expression for  $n'_{sk}$  is known.

However, if exact results are very difficult to obtain, it is possible to use numerical simulations. The main difficulty is that every simulation is feasible only for finite lattice sizes. The percolation phenomenon is a statistical phenomenon and only mean values are relevant. Thus the simulations should ideally be done over all possible lattice configurations. This is not possible for large lattices. Monte Carlo simulation techniques are generally used to overcome this difficulty. Some sample algorithms can be found in the textbook by Stauffer and Aharony [101].

An example of such a simulation is shown in Fig. 3.13 where the evolution of the clusters with the mean occupation probability  $p$  on a square lattice is shown. The evolution of the single clusters  $n_1$ , all multi-clusters  $\sum_{s=2}^{\infty} n_s = \sum_{s=1}^{\infty} n_s - n_1$ , and all clusters  $\sum_{s=1}^{\infty} n_s$  are depicted. The simulation was done on a  $100 \times 100$  square lattice.

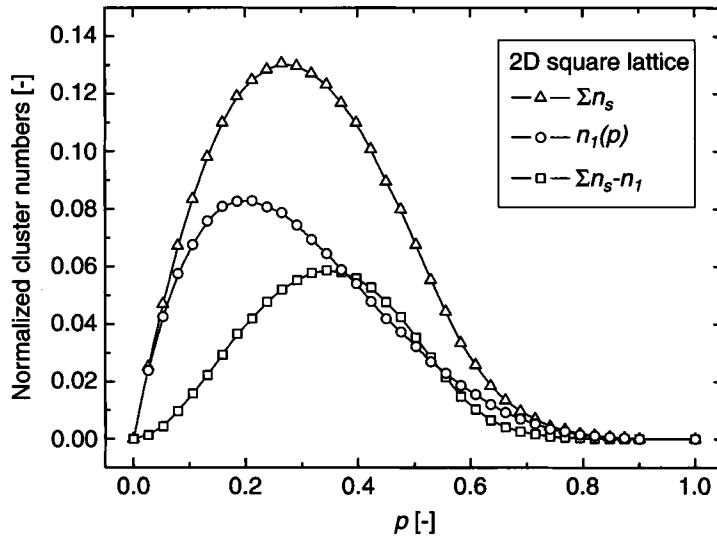


**Figure 3.13** Simulated normalised cluster numbers for a  $100 \times 100$  square lattice. The evolution, with the mean occupation probability  $p$ , of the normalized cluster numbers of single and multi-clusters as well as the evolution of the total cluster density are plotted. The simulation of  $n_1$  follows the analytical expression  $n_1 = p(1-p)^4$ .

By inspecting Fig. 3.13, one can see how single clusters become less and less numbered with increasing  $p$  after having passed a maximum. In term of bubbles, this means that with increasing nucleation probability more and more bubbles are growing on the electrode surface until a maximum is reached. After this maximum the number of small bubbles decreases. Comparatively, the larger bubbles (the mutli-clusters) increase and become equal in number to the small ones. This is well confirmed by visual observations (compare with Fig. 3.10).

The mean bubble size is given by the *mean cluster size*  $S$  defined as the average number of sites of the cluster to which the origin of the lattice (or every other occupied site chosen arbitrarily) belongs to:

$$S = \frac{\sum_s s^2 n_s}{\sum_s s n_s}. \quad (3.48)$$

An exact calculation of this quantity is generally not possible. There are some specials cases where an exact solution is known. In the case of the Bethe lattice with three branches (see Section 3.5.3 for the definition of this lattice), one can find [101]:

$$S = \frac{1+p}{1-2p}. \quad (3.49)$$

If  $p = 0.5$ , the mean cluster size becomes infinite. This critical probability is called the *percolation threshold*  $p_c$ . As discussed in Section 3.5.3, this *infinite cluster* always appears for  $p \geq p_c$  and is unique.

### 3.5.3 The Infinite Cluster and Percolation Threshold

The central result of percolation theory is the existence of the critical probability  $p_c$ , the *percolation threshold* at which a cluster of infinite size appears. In a one-dimensional lattice, the percolation threshold is obviously equal to one. For higher dimensions,  $p_c$  will be smaller than one. To illustrate this central result, we consider the *Bethe lattice* (also called the *Cayley tree*).

The Cayley tree is formed of nodes from each of the  $z$  links that join the next nearest neighbours (Fig. 3.14). If one starts at an arbitrary node and progressively builds the tree, one gets a lattice of size  $1 + z + z^2 + \dots + z^R = z^{R+1} - 1$  if the generation of  $R$  nodes is considered.

Suppose that the sites (the nodes of the tree) are occupied with a probability  $p$ . We need to determine under which conditions it is possible to find an infinite cluster. An equivalent way to address this problem is to search for a path, passing through only occupied sites, that never ends. Let us start from an occupied site. From each of its neighbours  $z - 1$  branches are connecting to the next node generated. The probability of finding at least one connected path (a path using only occupied sites) from the initial site to the second node

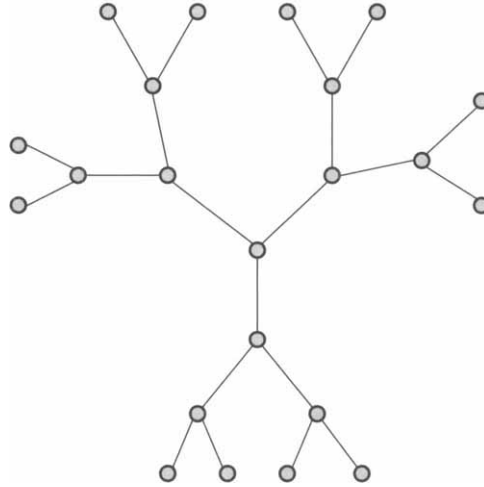


**Figure 3.14** Cayley tree, or Bethe lattice, with  $z = 3$  branches. The generation of three branches are shown.

generated will be  $p(z - 1)$ . To reach the next node generated the probability will be  $p^2(z - 1)^2$  and so on. Thus the condition to have a never-ending path is:

$$p \geq p_c = \frac{1}{z-1} \quad (3.50)$$

Let us now determine the probability  $P(p)$  that an arbitrary site belongs to the infinite cluster. For  $p < p_c$ , obviously  $P(p) = 0$ . To compute  $P(p)$  for  $p > p_c$  let us define  $Q$ , the probability that a given occupied site does not belong to the infinite cluster. The probability that an arbitrary site is occupied but does not belong to the infinite cluster is given by  $p - P(p)$ . This probability can also be expressed by  $pQ^z$ . It follows that

$$\frac{P(p)}{p} = 1 - [Q(p)]^z. \quad (3.51)$$

The probability  $Q$  can be evaluated using the following considerations. The probability  $Q_1$  that the nearest neighbour of a given site is occupied but none of its  $z - 1$  remaining branches is connected to the infinite cluster is given by  $Q_1 = pQ^{z-1}$ . The probability  $Q$  is the sum of  $Q_1$  and the probability that the neighbouring node is not occupied:

$$Q(p) = 1 - p + Q_1 = 1 - p + pQ^{z-1}. \quad (3.52)$$

This is an equation for  $Q$ . In the particular case of  $z = 3$ , one can easily solve this equation to find:

$$Q(p) = \frac{p-1}{p} \quad (3.53)$$



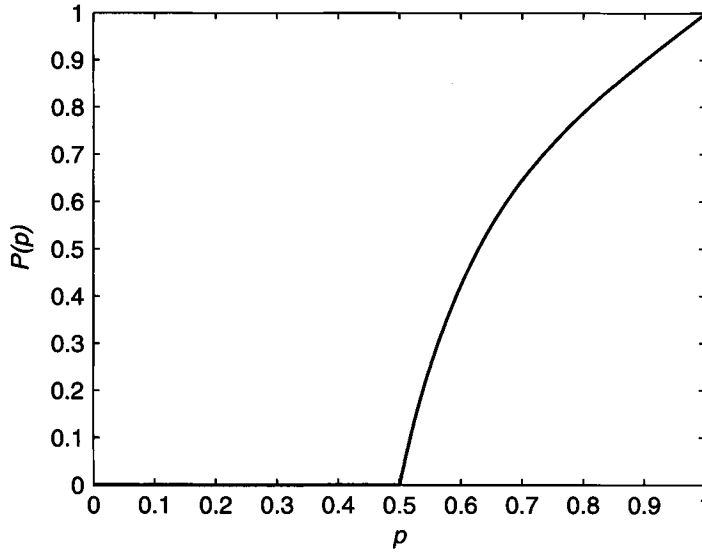


**Figure 3.15** Evolution of the probability  $P(p)$  that a site belongs to the infinite cluster as a function of the occupation probability  $p$  for the Bethe lattice with three branches. The percolation threshold is  $p_c = 0.5$ .

from which it follows, together with Equation (3.51), that for  $p \geq p_c$ ,  $P(p)$  is given by (Fig. 3.15):

$$P(p) = p - \frac{(1-p)^3}{p^2}. \quad (3.54)$$

The probability  $P(p)$  plays the role of the order parameter in the percolation phase transition.

From the existence of an infinite cluster, the following important equation (valid for any kind of lattice) is obtained:

$$p = \sum_s s n_s(p) + P(p), \quad (3.55)$$

which states that the probability that an arbitrary site is occupied is the sum of the probabilities that the site belongs to either an  $s$ -cluster or the infinite cluster. Note that as  $p \rightarrow 1$ , we have  $P(p) \rightarrow p$  (also valid for any kind of lattice). In other words, for high occupation probability, almost all occupied sites belong to the infinite cluster.

Lattices other than the Bethe lattice were also studied [101]. Table 3.4 summarises the value of the percolation threshold for some other lattices.

### 3.5.4 Model of the Bubble Adherence Region

Table 3.5 summarises the main definitions from percolation theory and their interpretation in terms of bubbles in the adherence region. The main idea is,

**Table 3.4 Percolation Thresholds for Some 2D Lattices [101]**

| Lattice    | $p_c$    |
|------------|----------|
| Honeycomb  | 0.6962   |
| Square     | 0.592746 |
| Triangular | 0.5      |

**Table 3.5 Main Definitions of the Percolation Model and Their Interpretation as Bubbles in the Adherence Region [123]**

| Percolation Theory  | Interpretation                     |
|---|------------------------------------|
| $p$ = Occupation probability of lattice sites   | Density of active nucleation sites |
| $s$ = Cluster size  | Bubble size                        |
| $n_s$ = Number of $s$ -clusters per lattice site  | Density of bubbles of size $s$     |
| $= \lim_{L \rightarrow \infty} \frac{\text{Total number of } s\text{-clusters}}{L}$           |                                    |
| $P(p) = \lim_{L \rightarrow \infty} \frac{\text{Number of sites in the infinite cluster}}{L}$ | Coverage fraction of the gas film  |
| $\sum_s s n_s = p$ for $p \leq p_c$   | Bubbles able to leave              |
| $\sum_s s n_s = p - P(p)$ for $p > p_c$   | The adherence region               |
| $S(p)$ = Mean size of the clusters  | Mean size of adhering bubbles      |
| $= \left( \sum_s s^2 n_s \right) / \left( \sum_s s n_s \right)$                               |                                    |

as discussed previously, to interpret the lattice sites as bubble nucleation sites. Clusters are interpreted as coalesced bubbles. Using percolation theory, the distribution of the clusters and therefore of the bubbles can be quantified. In particular, their mean size can be evaluated. Recall that large bubbles cannot leave the adherence region as the buoyancy force can no longer overcome the adhesion force, which is the situation in the case of an infinite cluster. Therefore,  $P(p)$  is interpreted as the fraction of the electrode covered by a bubble that is no longer able to leave the adherence region. This is nothing other than the gas film built around an electrode at the onset of the electrochemical discharges.

In order to be able to apply this model, the nucleation probability  $p$  has to be linked to the electrochemical, electrode, and cell properties such as the current density and the terminal voltage. Due to the lack of knowledge in this field, in particular the knowledge about the activation of nucleation sites, this is not a straightforward task. In the next section, a simplified approach that is able to explain the important effects is presented.

### 3.6 Bubble Evolution on a Gas Evolving Electrode

The evolution of bubbles on a gas evolving electrode is a dynamic process. As described in previous sections, percolation theory can help to quantify the bubble size distribution in the adherence region if the mean bubble coverage fraction  $\theta$  is known. In order to derive an equation describing the evolution of  $\theta$  for gas evolving electrodes, we will write a mass balance equation between the amount of gas produced and the quantity of gas leaving the adherence region [125,129]. Faraday's law computes  $\dot{V}_G$ , the amount of gas produced per unit time at an electrode:

$$\dot{V}_G = \beta I, \quad (3.56)$$

where  $\beta$  is the coefficient of faradic gas generation:

$$\beta = \frac{\mathcal{R}T}{(z/\nu)FP}, \quad (3.57)$$

where  $\mathcal{R}$  is the universal gas constant,  $T$  is the temperature at the electrode surface,  $F$  is Faraday's constant,  $P$  is the pressure,  $z$  is the charge number, and  $\nu$  is the stoichiometric number. Using Equation (3.40), one obtains:

$$\dot{V}_G = \beta j_{local}(1-\theta)A. \quad (3.58)$$

The amount of gas leaving the electrode surface is given by the mean number of bubbles leaving the electrode per unit time. To evaluate the number of bubbles leaving the electrode surface, we have to count all bubbles that are able to leave the adherence region. We assume that only bubbles of size smaller than  $s^{max}$  can leave the electrode surface. The value of  $s^{max}$  is a function of the electrode geometry and wettability. The fraction of nucleation sites covered on the surface by the growing gas bubbles that are able to leave the electrode is given by  $\sum_{s=0}^{s^{max}} s n_s(\theta)$ . If  $V_b$  is the mean volume of a bubble growing on a nucleation site at the moment of coalescence with its neighbours,  $N$  is the mean number of nucleation sites per electrode surface, and  $\Delta t_b^{-1}$  is the mean bubble detachment frequency, then the mean total volume of gas leaving the electrode per unit of time and surface is:

$$\dot{V}_G = \frac{V_b}{\Delta t_b} N A \sum_{s=0}^{s^{max}} s n_s(\theta). \quad (3.59)$$

Considering (3.58) and (3.59), we can write the following mass balance equation:

$$\frac{d}{dt}(V_b N A \theta) = \beta j_{local}(1-\theta)A - \frac{V_b}{\Delta t_b} N A \sum_{s=0}^{s^{max}} s n_s(\theta). \quad (3.60)$$

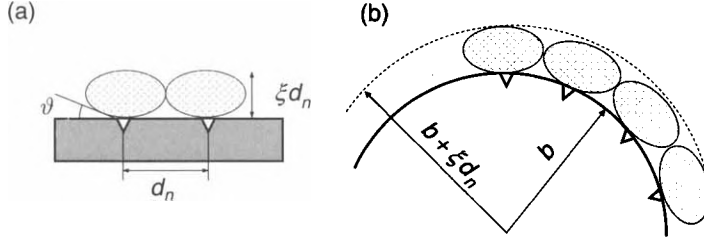


**Figure 3.16** Geometry of two coalescing bubbles in the adherence region in the case of a (a) flat and (b) cylindrical electrode.

Note that the product  $V_b NA$  is the volume occupied by the gas bubbles if all nucleation sites are active at the same time. In order to take into account the wettability of the electrode surface, we write the volume of a single isolated bubble as  $V_b = \sigma_b \cdot \xi d_n$ , where  $\sigma_b = 1/N$  is the surface occupied by this bubble and  $\xi d_n$  is its height written as the product of  $d_n$  (the mean distance between two nucleation sites) and  $\xi$  (the parameter describing the degree of flatness of the bubble). Note that, as shown in Fig. 3.16,  $\xi$  is function of the wettability  $\vartheta$  and the electrode geometry. In particular, for small cylindrical electrodes, where the electrode radius is similar to the bubble radius,  $\xi$  can typically reach values around 2.

The evolution equation of the bubble coverage fraction  $\theta$  is as follows:

$$\frac{d\theta}{dt} = \frac{\beta j_{local}}{\xi d_n} (1 - \theta) - \frac{1}{\Delta t_b} \sum_{s=0}^{s^{max}} s n_s(\theta). \quad (3.61)$$

Let us give some orders of magnitudes. The mean bubble height  $\xi d_n$  is typically in the range of a few hundred micrometres according to visual observations. The mean bubble detachment time  $\Delta t_b$  is controlled by the time needed by a bubble to reach the detachment radius. As the bubble growth is diffusion controlled, this time is more or less constant for high current densities. Typical values are in the range of a few milliseconds.

To discuss (3.61) the normalised time  $\bar{t} = t/\Delta t_b$  is introduced. Equation (3.61) can be written as [124,125]:

$$\frac{d\theta}{d\bar{t}} = \frac{\beta \Delta t_b}{\xi d_n} j_{local} (1 - \theta) - \sum_{s=0}^{s^{max}} s n_s(\theta). \quad (3.62)$$

Figure 3.17 shows the stationary solution of Equation (3.62) considering the approximation  $s^{max} \rightarrow \infty$ :

$$\sum_{s=0}^{s^{max}} s n_s(\theta) \equiv \theta - P(\theta) \quad (3.63)$$

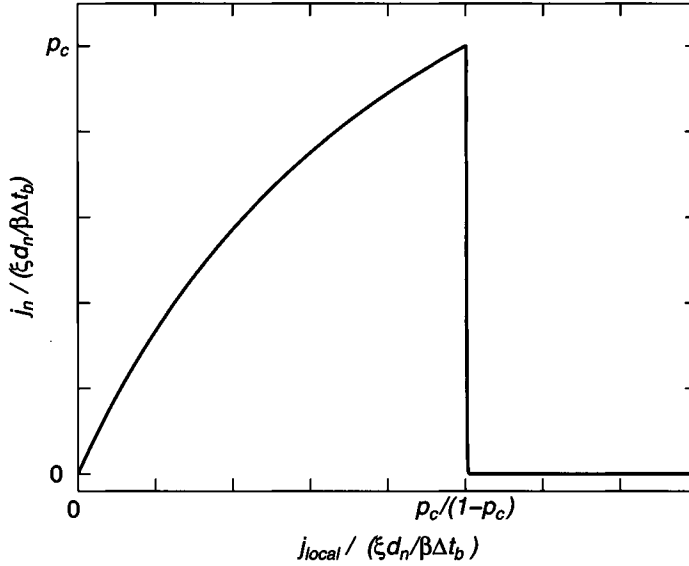


**Figure 3.17** Stationary nominal current density  $j_n = I/A$  as a function of the local current density  $j_{local}$  at a gas evolving electrode.

and that the nominal current density  $j_n = I/A = j_{local}(1 - \theta)$  according to Equation (3.40).

From Fig. 3.17 it can be observed that with increasing local current density  $j_{local}$ , the nominal current density  $j_n$  differs more and more from  $j_{local}$ . This is particularly striking for  $j_{local}$  larger than  $\frac{p_c}{1-p_c} \frac{\xi d_n}{\beta \Delta t_b}$ , where  $\theta > p_c$ . The predication  $j_n = 0$  is due to the fact that the dynamics of the infinite cluster was neglected (the mean life time of the gas film is considered to be infinite).

If the mean lifetime  $\Delta t_g$  of the gas film is included in the model, then Equation (3.61) has to be replaced by

$$\frac{d\theta}{dt} = \frac{\beta j_{local}}{\xi d_n} (1 - \theta) - \frac{1}{\Delta t_b} \sum_{s=0}^{s_{max}} s n_s(\theta) - \frac{1}{\Delta t_g} P(\theta). \quad (3.64)$$

The stationary solution now presents a bistability [124]. This bistability is the reason for the existence of the instability region that was first described by Hoho [56] (see Section 2.1). Another consequence is a hysteresis in the stationary  $I-U$  characteristics (see Section 4.4.1).

### 3.7 Mean Stationary Current–Voltage Characteristics

The bubble growth on an electrode can be followed by considering the mean stationary current–voltage characteristics obtained by measuring the mean

stationary current  $I$  at a fixed terminal voltage  $U$ . If no bubble grows, current and voltage would be related, according to (3.22), by:

$$U - U_d = R_o I, \quad (3.65)$$

where  $R_o$  is the inter-electrode resistance. The presence of the bubbles affects the inter-electrode resistance and therefore the  $I-U$  characteristics as described by (3.44). The deviation from the ideal law (3.65) will give an indication of the bubble growth on the electrode. In order to see the effect on one electrode only (e.g., the cathode), it is important to choose a configuration in which the counter-electrode has a much larger surface. In this case, the current density at the counter-electrode will be significantly lower than at the working electrode and therefore the bubble growth activity will also be lower.

### 3.7.1 Experimental Description

Let us take a closer look at the  $I-U$  characteristics of a gas evolving electrode showing the mean stationary current  $I$  passing through the electrodes at a fixed terminal voltage  $U$ . The typical characteristics are shown in Fig. 3.18. Five different regions are distinguished (numerical values are given for a working electrode of about  $1 \text{ mm}^2$  and a counter-electrode of a few centimetres):

1. *Thermodynamic and over potential region:* For a terminal voltage smaller than the water decomposition potential  $U_d$  ( $U_d \simeq 2 \text{ V}$ ), no significant electrolysis happens and no current flows between the electrodes.
2. *Ohmic region AB* (typically from 2 to 10–12 V): The mean current  $I$  increases nearly linearly with the terminal voltage  $U$ .

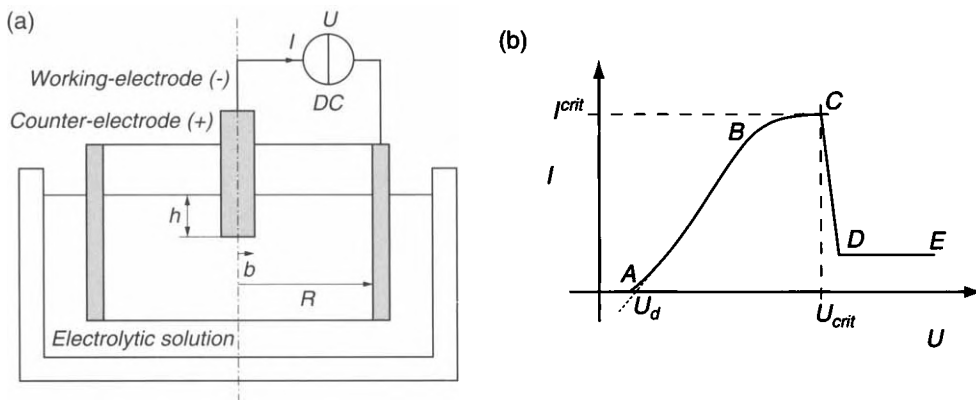


**Figure 3.18** Cell geometry: (a) the cathode of radius  $b$  is surrounded by the anode of radius  $R$ . A voltage  $U$  is applied between the two electrodes. (b) Corresponding  $I-U$  characteristics.

Bubbles evolve around the working electrode and a compact bubble layer is formed. The typical thickness of the bubble layer is a few millimetres. All bubbles have almost the same diameter around 100  $\mu\text{m}$ .

3. *Limiting current region BC*: The mean current  $I$  reaches a limiting value and is almost constant. In this voltage range, bubbles coalesce. Not only small bubbles, as in the ohmic region, but larger bubbles are also observed (typically from 300 to 700  $\mu\text{m}$ ). The mean temperature of the electrolyte increases. The extent, and in general the presence, of this region depends on the wettability of the electrode [32,126]. The end of the limiting current region is reached at the critical point  $C$  characterised by the critical voltage  $U^{crit}$  (typically around 20–30 V) and a critical current  $I^{crit}$  (typically around 1 A). Beyond this point, the current decreases very rapidly with the terminal voltage  $U$ .
4. *Instability region CD*: The mean stationary current decreases quickly with the terminal voltage  $U$ . The electrolyte resistance diverges and a gas film is formed around the working electrode. This region is called instability region because the system can be in a state similar to either the limiting current region  $BC$  or the electrochemical discharge region  $DE$ .
5. *Electrochemical discharge region DE*: The last region is characterised by the existence of a gas film around the electrode. The working electrode is completely isolated from the electrolyte. The mean current is very small (in the milliampere range). The instant current can be described as a succession of short pulses (a few hundred microseconds with an amplitude up to 1 A). Electrochemical discharges take place through the gas film.

### 3.7.2 Theoretical Description

Using the results from this chapter, the first phases up to the critical voltage of the current–voltage characteristics during electrolysis with gas evolution can be described.

The stationary mean bubble coverage fraction  $\theta^s$  is given by the stationary solution of Equation (3.61):

$$\frac{\beta \Delta t_b}{\xi d_n} j_{local} (1 - \theta^s) = \sum_{s=0}^{s^{max}} s n_s(\theta^s) \quad (3.66)$$

as described in Section 3.6. Note that in practise the terminal voltage  $U$  is imposed but not the local current density  $j_{local}$ .

If the terminal voltage  $U$  is higher than the water decomposition potential  $U_d$ , electrolysis takes place and the current is related to  $U$  according to (3.40) and (3.22) by:

$$I = (1 - \theta) j_{local} A = \frac{U - U_d}{R(\theta)}, \quad (3.67)$$

where  $R(\theta)$  is the apparent inter-electrode resistance. Combining (3.66) with (3.67), the stationary bubble coverage fraction  $\theta^s$  is given by the solution of:

$$\sum_{s=0}^{s^{max}} s n_s(\theta^s) = \frac{\beta \Delta t_b}{\xi d_n} \frac{I}{A} = \frac{\beta \Delta t_b}{\xi d_n} \frac{U - U_d}{R(\theta^s) A}. \quad (3.68)$$

Equation (3.68) does not constitute a close description of the mean stationary  $I$ – $U$  characteristics unless the expression for the apparent inter-electrode resistance  $R(\theta)$  is known.

The expression for  $R(\theta)$  contains three contributions. The first is the resistance of the bulk electrolyte. The second is due to the bubble diffusion region. As discussed in Section 3.4, this contribution is almost constant. The third comes from the shielding effect of the bubbles growing on the electrode surface. This contribution is a function of  $\theta$ . A possible ansatz for  $R(\theta)$  is (see also Fig. 3.11 and the corresponding discussion):

$$R(\theta) = R^{bulk} + \frac{R^{diff}}{1 - \theta}, \quad (3.69)$$

where  $R^{bulk}$  is the inter-electrode resistance of the bulk region and  $R^{diff}$  is the resistance of the bubble diffusion region. However, this expression is only a rough approximation, in particular for low bubble coverage fractions. Indeed, for low bubble coverage fractions only small bubbles are present in the adherence region (see Fig. 3.13), which will not significantly affect the inter-electrode resistance. Therefore, for low bubble coverage fraction, as long as only small bubbles are growing in the adherence region, we have  $R(\theta) = R^{bulk} + R^{diff}$ . The value of  $\theta$  until which this relation is satisfied will depend on the aspect ratio of the growing bubbles, and therefore the wettability of the system.

To evaluate the sum from Equation (3.68), we will use the approximation  $s^{max} = \infty$  in the following paragraphs. As long as  $\theta$  is smaller than the percolation threshold  $p_c$ , the stationary bubble coverage fraction is given by:

$$\theta^s = \frac{\beta \Delta t_b}{\xi d_n} \frac{I}{A}. \quad (3.70)$$

This relation is valid as long as  $\theta^s < p_c$ , or equivalently as long as the current is smaller than the critical current  $I^{crit}$  given by (compare with Fig. 3.17):

$$\frac{I^{crit}}{A} = \frac{\xi d_n}{\Delta \beta t_b} p_c. \quad (3.71)$$



In a similar manner, one can write a relation between the terminal voltage and the stationary bubble coverage fraction ( $\theta^s < p_c$ ):

$$U - U_d = R(\theta^s)I = R(\theta^s)A \frac{\xi d_n}{\beta \Delta t_b} \theta^s. \quad (3.72)$$

The terminal voltage at which the critical current is reached is the critical voltage given by:

$$U^{crit} = U_d + R(p_c)A \frac{\xi d_n}{\beta \Delta t_b} p_c. \quad (3.73)$$

By introducing the *normalised current*:

$$\mathcal{J} = \frac{I}{I^{crit}} \quad (3.74)$$

and the *normalised voltage*:

$$\mathcal{U} = \frac{U - U_d}{U^{crit} - U_d}, \quad (3.75)$$

these relations can be written in a particularly elegant form:

$$\mathcal{J} = \frac{\theta^s}{p_c} \quad (3.76)$$

and

$$\mathcal{U} = \frac{R(\theta^s)}{R(p_c)} \frac{\theta^s}{p_c}. \quad (3.77)$$

By combining these relations, one gets the normalised mean stationary current characteristics for terminal voltages lower than the critical voltage (i.e.  $\mathcal{U} < 1$ ):

$$\mathcal{J} = \frac{R(p_c)}{R(\theta^s)} \mathcal{U} = \frac{R(p_c)}{R(\mathcal{J})} \mathcal{U}. \quad (3.78)$$

An interesting consequence of these calculations is that the normalised mean stationary current–voltage characteristics are similar for different electrodes and electrolytes. An example is shown in Fig. 3.19 where the normalised mean current–voltage characteristics for a sodium hydroxide solution with different concentrations is depicted.

We will now discuss qualitatively the mean current–voltage characteristics. For not too high voltages (or currents), it follows from (3.68) that the bubble

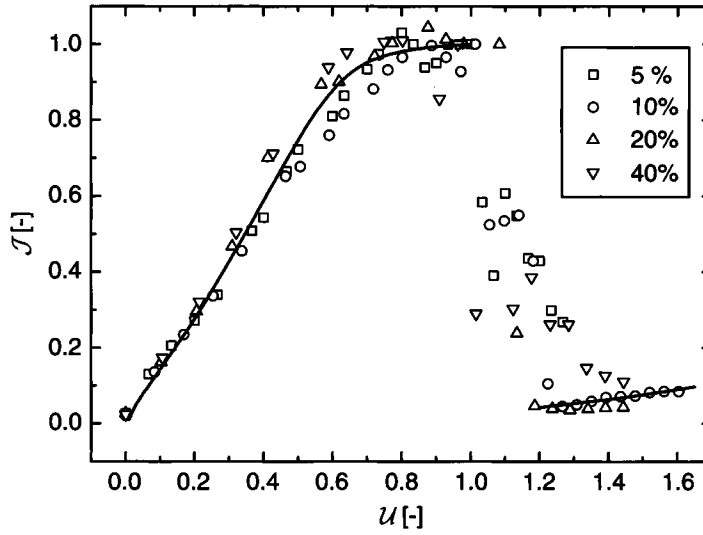


**Figure 3.19** Normalised mean  $I-U$  characteristics for a NaOH solution with different concentrations. Reprinted from [128] with permission from Elsevier.

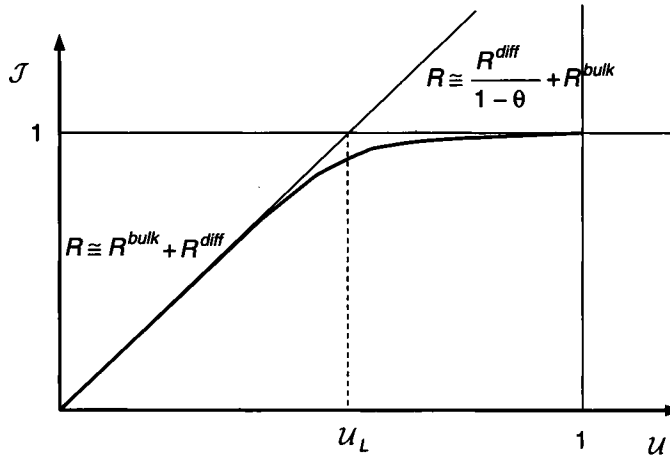


**Figure 3.20** Normalised mean  $I-U$  characteristics as predicted by the percolation model.

coverage fraction will also be small. In a first approximation,  $R(\theta) \equiv R^{bulk} + R^{diff}$ , that is, the inter-electrode resistance is given only by the electrolyte resistance and the effect of the bubble diffusion region. In other words, the current increases linearly with the terminal voltage (Fig. 3.20):

$$J = \frac{R(p_c)}{R^{bulk} + R^{diff}} U. \quad (3.79)$$

This is the ohmic region. For higher currents,  $\theta^s$  will grow and significantly affect the inter-electrode resistance. The current will saturate at its maximal

value  $\mathcal{J} = 1$  (i.e.,  $I = I^{crit}$ ). This qualitative behaviour is shown in Fig. 3.20. From this figure, one can directly read that the transition from the ohmic region to the limiting current region takes place at the voltage:

$$\mathcal{U}_L = \frac{R^{bulk} + R^{diff}}{R(p_c)}, \quad (3.80)$$

or written explicitly:

$$U_L = U_d + (R^{bulk} + R^{diff})A \frac{\xi d_n}{\beta \Delta t_b} p_c. \quad (3.81)$$

Although the expressions derived in this section are approximations, they are very useful in several applications related to micromachining with electrochemical discharges. For example, Equation (3.73) allows to observe qualitatively how the various parameters affect the critical voltage. This will allow us to design methods for machining at lower terminal voltages, a feature that is desired to improve the precision of the machining.

## Notes

<sup>1</sup>To be more precise, the capacity of the double layer around the electrodes should be added.

<sup>2</sup>Note that the term ohmic drop often also refers to the potential difference between the working electrode and the reference electrode.

## 4 The Gas Film—A Key Element

---

Spark-assisted chemical engraving takes advantage of the electrochemical discharges generated in a gas film around an electrode, as described in Chapter 2. This gas film is a key element of the process. On one hand, the gas film is necessary for machining but, on the other hand, it conditions the quality of the machining. A fundamental understanding of the processes related to the gas film is essential. Of particular interest are:

- The formation of the gas film
- The shape of the gas film
- The discharge activity inside the gas film
- The dynamical properties of the gas film

An understanding of the process that builds the gas film is important for machining applications, as this mechanism conditions the terminal voltage at which the gas is formed. As will be seen in Chapter 7, machining at low voltages results in improved quality. The shape of the gas film influences the discharge activity and therefore important parameters such as the machining over-cut. Equally important are the dynamical properties. For example, the stability of the gas film directly affects the repeatability of the machining. Its formation time limits the material removal rate. Finally, the discharge activity controls the heat produced locally and therefore the material removal rate. It has to be noted that all these aspects of the gas film are interacting more or less strongly. For example, the discharge activity is related to the stability of the gas film and to its thickness.

### 4.1 Formation of the Gas Film

Experimentally the formation of the gas film can be well understood by observing the current flowing in the system. Figure 4.1 shows a typical example. A 0.17 mm stainless steel cylinder active cathode is dipped in a 30 wt% NaOH solution. A voltage step of 30 V is applied. One can clearly see how after 2 ms the gas film is formed and the first discharges appear.

Two main mechanisms are responsible for the formation of the gas film: local evaporation of the electrolyte due to joule heating and coalescence of the electrochemically formed bubbles on the electrode surface. A combination of both processes is also possible.

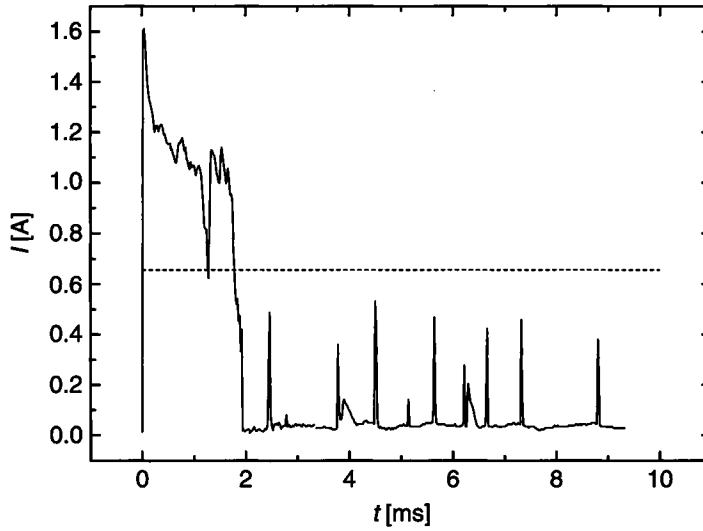


**Figure 4.1** A typical example of a voltage step input of 30 V. The active cathode has a diameter of 0.17 mm and the electrolyte used is 30 wt% NaOH. Reprinted from [128] with permission from Elsevier.

#### 4.1.1 Gas Film Formation by Local Electrolyte Evaporation

The formation of the gas film around a thin electrode is possible if locally the electrolyte temperature reaches the electrolyte evaporation temperature. This mechanism is at the origin of the Caldwell–Simon current-interrupter (Section 2.2).

Let us discuss this mechanism for a thin electrode of radius  $b$  with the length  $h$  dipped inside the electrolytic solution. The counter-electrode is supposed to be significantly larger and far away. If the heat dissipation by thermal conduction through the electrode and the electrolyte is neglected, the heat  $Q$  brought to the electrolyte of mass  $m$  will increase its temperature by  $\Delta T$  according to:

$$Q = mc\Delta T = \rho Vc\Delta T, \quad (4.1)$$

where  $\rho$  is the density of the electrolyte and  $c$  is its heat capacity. The heat provided to the electrolyte in the time interval  $\Delta t$  comes from joule heating by the current  $I$ :

$$Q = RI^2\Delta t, \quad (4.2)$$

where  $R$  is the resistance of the electrolyte. In the vicinity of the thin electrode the current is essentially radial. Considering the heat produced in a shell of thickness  $a - b$  around the thin electrode, it follows that:

$$\frac{1}{2\pi kh} \ln\left(\frac{a}{b}\right) I^2 \Delta t = \rho\pi(a^2 - b^2)hc\Delta T, \quad (4.3)$$

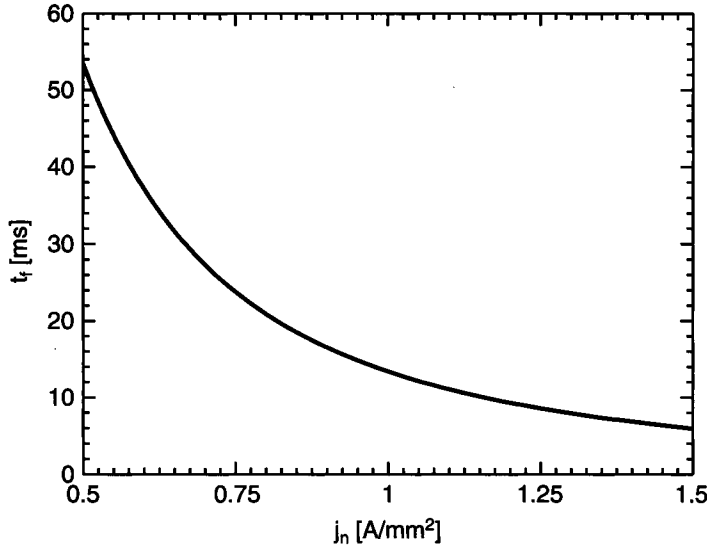


**Figure 4.2** Estimation of the gas film formation time  $t_f$  if only local joule heating is considered (heat dissipation is neglected). Computed using Equation (4.4).

where  $\kappa$  is the electrical conductivity of the electrolyte. A gas film can be built if a thin shell around the electrode reaches the evaporation temperature  $T_e$  of the electrolyte. Considering the limit  $a \rightarrow b$ , the time  $t_f$  needed to build the gas film is given by:

$$t_f = \frac{2\pi^2 h^2 \kappa \rho c}{I^2} 2b^2 (T_e - T_o) = \frac{\kappa \rho c}{j_n^2} \Delta T, \quad (4.4)$$

where  $j_n = I/(2\pi bh)$  is the nominal current density at the electrode surface and  $T_o$  is the temperature of the electrolyte at the beginning (or of the bulk). Figure 4.2 shows for typical values of an electrolyte ( $\kappa = 0.4 \Omega^{-1}$ ,  $c = 4.18 \times 10^3 \text{ J} \cdot \text{kg}^{-1} \text{ K}^{-1}$ ,  $\rho = 10^3 \text{ kg} \cdot \text{m}^{-3}$ ) the estimation of the gas film formation time as a function of the nominal current density.

In 1902, Klupathy [72] derived this equation for the Wehnelt interrupter. He compared his calculation with experimental data. For a nominal current density of about  $0.6 \text{ A/mm}^2$ , he measured gas film formation times of 4 ms (the frequency of operation of the Wehnelt interrupter). His conclusion was that, based on the experimentally measured formation times, the joule heating inside the electrolyte cannot account for the gas film formation for the geometries he considered. More recently, Guilpin [45] and Fascio [32] showed, for different geometries than those considered by Klupathy, that the measured gas film formation times are of a similar order of magnitude as the one predicted by Equation (4.4).

Equation (4.4) underestimates the gas film formation time, or overestimates the increase in the temperature of the electrolyte, at the electrode surface as

the heat transport through the electrolyte is neglected. A more precise estimation can be obtained by taking into account the heat dissipation inside the electrolyte. Therefore, Fourier's equation has to be solved:

$$\nabla^2 T + \frac{j^2}{\kappa\lambda} = \frac{\rho c}{\lambda} \frac{\partial T}{\partial t}, \quad (4.5)$$

where  $\lambda$  is the thermal conductivity of the electrolyte. For any point at a distance  $r$  from the electrode's axis of symmetry, a current density  $j(r)$  flows through the electrolyte. In the vicinity of the electrode, the current density is radial and is given by:

$$j(r) = \frac{I}{2\pi r h}. \quad (4.6)$$

By assuming that at any time the temperature of the electrode is equal to the temperature of the electrolyte in contact with it, a first boundary condition follows:

$$\frac{\partial T}{\partial r} = 0. \quad (4.7)$$

A second boundary condition is given by imposing that at a distance  $R$  far enough from the electrode the temperature of the electrolyte is equal to the ambient temperature  $T_o$ :

$$T(R) = T_o \quad (4.8)$$

To solve Equation (4.5) let us introduce the normalised temperature ( $\bar{T} = T/T_o$ ), the normalised distance  $\bar{r} = r/b$ , and the normalised time  $\bar{t} = t/\tau$  with the typical time constant

$$\tau = \frac{\rho c}{\lambda} b^2. \quad (4.9)$$

For an aqueous electrolyte, the parameters of water can be considered ( $\lambda = 0.587 \text{ W m}^{-1} \text{ K}^{-1}$ ,  $c = 4.18 \times 10^3 \text{ J kg}^{-1} \text{ K}^{-1}$ ,  $\rho = 10^3 \text{ kg m}^{-3}$ ). It follows that  $\tau$  is typically about one second for electrodes with diameters around a millimetre ( $\tau = 1.8 \text{ s}$  for  $b = 0.5 \text{ mm}$ ).

By introducing the constant

$$K = \frac{1}{\kappa\lambda} \left( \frac{I}{2\pi h} \right)^2 \frac{1}{T_o} = \frac{(bj)^2}{\kappa\lambda} \frac{1}{T_o}, \quad (4.10)$$

Equation (4.5) can be written as:

$$\frac{1}{\bar{r}} \frac{\partial}{\partial \bar{r}} \left( \bar{r} \frac{\partial \bar{T}}{\partial \bar{r}} \right) + \frac{K}{\bar{r}^2} = \frac{\partial \bar{T}}{\partial \bar{t}}. \quad (4.11)$$

From this relation and considering the initial condition  $T(r, t=0) = T_o$ , it follows directly, for the case discussed previously where the heat dissipation is neglected, that

$$\frac{T(b)-T_o}{T_o} = K \frac{t}{\tau}, \quad (4.12)$$

which is equivalent to Equation (4.4) derived by Klupathy. The stationary solution of Equation (4.11) is given by:

$$\frac{T(b)-T_o}{T_o} = \frac{1}{2} K \ln^2 \left( \frac{R}{b} \right). \quad (4.13)$$

The numerical solution of Equation (4.11) is shown in Fig. 4.3. As can be seen from this figure, the effect of the arbitrary choice of  $R$  is not significant for short times. The temperature of 100°C ( $\bar{T} \cong 1.3$ ) is reached quite fast. Also note that at these short times, Klupathy's equation (4.4) is an excellent approximation of the solution, as can be seen in Fig. 4.3(b).

Note that the gas film formation time is still underestimated as at least two important effects are neglected: the heat dissipation through the active electrode (this point is discussed in more detail in the chapters on machining applications) and the heat needed for the evaporation of the electrolyte (latent heat). The conclusion to be drawn here is that this simplified model shows that in principle it is possible to build the gas film by local joule heating. Experimentally it is known that a gas film can be built around an active electrode without any gas evolution (using, for example, copper sulphate as the electrolyte and a copper electrode). It was also shown experimentally that, prior to the formation of the gas film, the electrode temperature reaches about 100°C [5,70].

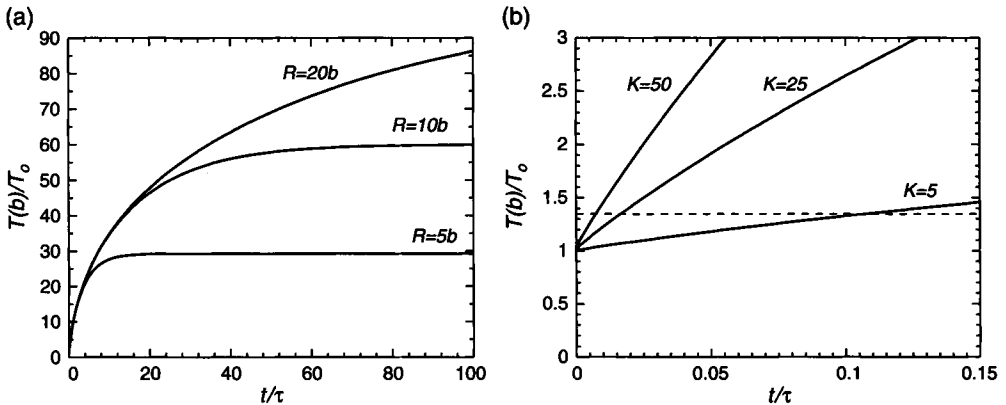


**Figure 4.3.** Temperature increase at the active electrode as predicted by the joule heating model (4.11). (a) Computation for  $K = 23$  (typical value corresponding to a current density of 1 A/mm<sup>2</sup>). (b) Computation for various  $K$  and for  $R = 10b$ . The dashed line represents  $T(b) = 100^\circ\text{C}$ .



### 4.1.2 Gas Film Formation by Electrochemical Gas Evolution

As described in Chapter 3, at high current densities bubbles coalesce to form larger bubbles. It becomes possible to create a large enough structure on the electrode surface such that the buoyancy force can no longer overcome the adherence force of the coalesced bubble. Thus, a gas film forms at the electrode surface.

Recall that the evolution of the bubbles growing on the electrode surface is given by (3.61), which can be written for the stationary situation:

$$\frac{\beta j_{local}}{\xi d_n}(1-\theta) = \frac{1}{\Delta t_b} \sum_{s=0}^{s^{max}} s n_s(\theta). \quad (4.14)$$

This equation states the equality between the amount of electrochemically produced gas and the gas removed from the electrode surface. As soon as a bubble of size larger than  $s^{max}$  appears, the formation of the gas film starts. If we consider the approximation  $s^{max} = \infty$  (a bubble of similar size as the electrode is formed), the formation of the gas film starts at the critical voltage  $U^{crit}$ , as computed in Section 3.7:

$$U^{crit} = U_d + R(p_c)A \frac{\xi d_n}{\beta \Delta t_b} p_c, \quad (4.15)$$

or equivalently at the critical current  $I^{crit}$

$$\frac{I^{crit}}{A} = \frac{\xi d_n}{\beta \Delta t_b} p_c. \quad (4.16)$$

Some typical order of magnitudes can be computed. If one considers an active cathode with hydrogen evolution, then  $\beta = 0.26 \text{ cm}^3 \text{ A}^{-1} \text{ s}^{-1}$ . For a cylindrical cathode of a few hundred micrometres, it is known experimentally that  $\Delta t_b \simeq 1 \text{ ms}$  and  $\xi d_n = 0.4 \text{ mm}$  [129]. It follows that  $j^{crit} \simeq 1 \text{ A/mm}^2$  (with  $p_c \simeq 0.5$ ) and that  $U^{crit} = 20\text{--}30 \text{ V}$ , depending on  $R(p_c)$ .

Equation (4.14), or (4.15) and (4.16), captures several important parameters that are responsible for the formation of the gas film. The following scenarios for its formation result [117]:

- *Increase in the nominal current density:* With increasing nominal current density  $I/A$ , the bubble coverage fraction increases. When it reaches a critical value, as computed by (4.16), a gas film is formed. Such a scenario happens, for example, in current-controlled cells or, as will be seen in Section 4.1.3, in a voltage-controlled cell if for some reason the inter-electrode resistance decreases.
- *Deteriorated wetting:* The wetting of the electrode directly influences the bubble shapes (through the parameter  $\xi$ ). For a given bubble volume, the shadowed surface on the electrode will increase with deteriorated wetting [116]. Several parameters affect the wetting such as the electrode surface roughness and porosity

and also the local over potential. As will be discussed in Section 4.4.1, changing the wetting of the electrode–electrolyte–gas interface can be used to change significantly the critical voltage.

- *Decreasing rate of bubble release:* The mean bubble detachment frequency  $\Delta t_b^{-1}$  directly controls the onset of the gas film. For large enough bubbles, such as the infinite cluster, the bubble detachment time  $\Delta t_b$  becomes so large that the gas film can be formed.  $\Delta t_b$  is affected by other parameters such as the wetting of the electrode, viscosity and density of the electrolyte, or the local hydrodynamical fluxes.
- *Increased rate of gas production:* The rate of bubble formation is directly controlled by the local current density. Note that the local current density can be only indirectly controlled in experiments using the nominal current density or the terminal voltage. The formation of vapour by local joule heating can also contribute to this increase.

#### 4.1.2.1 Critical Voltage as a Random Variable

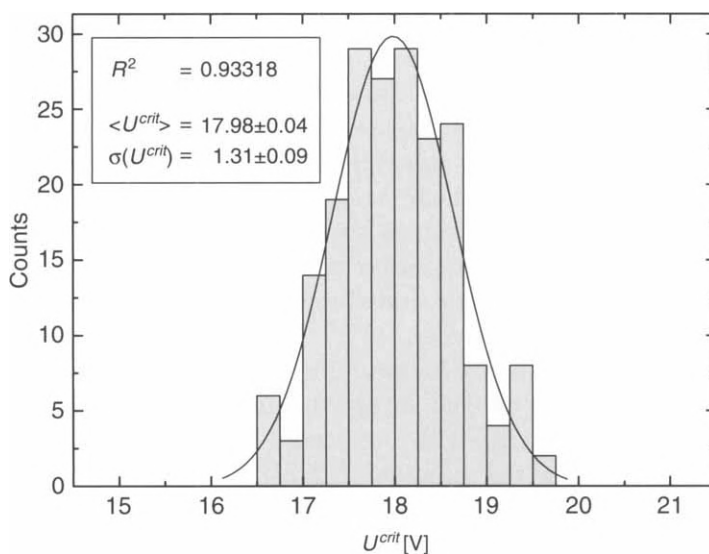
As the bubble growth and coalescence is a stochastic process, it is not surprising that the critical voltage is actually a random variable. Even if the critical voltage is a well-defined quantity, its measurement is not a straightforward task. Only a mean value can be measured. The following measurement protocol is commonly used [32,45,123]. A slowly increasing voltage is applied to the system (typically a constant voltage increase with a 10 V/s scan rate). The voltage at which the current vanishes is the critical voltage.

Figure 4.4 shows a typical frequency count distribution of  $U^{crit}$  obtained by this procedure with a 75  $\mu\text{m}$  cylindrical active electrode in 20 wt% NaOH electrolyte. The measurements were repeated 200 times. It can be seen that the critical voltage is widely distributed and follows a Gaussian distribution. The first moment of this distribution defines the *mean critical voltage*  $\langle U^{crit} \rangle$ .

As expected, the voltage scan rate may influence these measurements. The mean critical voltage measured in this manner is expected to be slightly too high. Ideally, at every measurement point  $(I, U)$  the system should be in a stationary state. For this, the scan rate has to be chosen slow enough. However, a very slow scan rate will introduce several complications in the measurement. The temperature of the electrolyte will increase due to joule heating and therefore change the experimental conditions. The scan rate of 10 V/s is a good compromise as shown by Guilpin [45] and Fascio [32]. The system can reasonably be considered to be in a stationary situation and the temperature increase of the electrolyte is low.

#### 4.1.2.2 Influence of the Electrode Geometry

For an ideal cylindrical geometry, according to (3.73) and (3.71), the critical voltage is independent of the length of the active electrode, whereas the critical



**Figure 4.4** Frequency count of the critical voltage  $U^{crit}$  for a cylindrical active electrode of 75  $\mu\text{m}$  diameter. Two hundred measurements were taken in 20 wt% NaOH at 30°C. The superimposed curve is the fitted Gaussian distribution.

current is proportional to it. Both quantities are proportional to the active electrode radius (for the critical voltage in a first approximation only, when the dependence in the logarithmic function is neglected). An example for KOH is shown in Fig. 4.5.

#### 4.1.2.3 Influence of the Electrolyte Concentration

The electrolyte concentration affects the critical voltage and the critical current by the change in the electrical conductivity, which results in a change

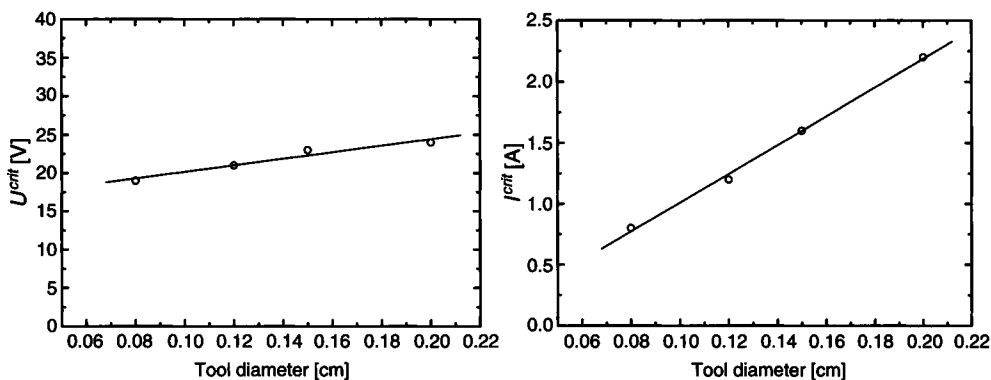


**Figure 4.5** Critical voltage  $U^{crit}$  and critical current  $I^{crit}$  as a function of the electrode diameter (length 0.05 cm) for a 40 wt% KOH solution. Reprinted from [7] with permission from Elsevier.

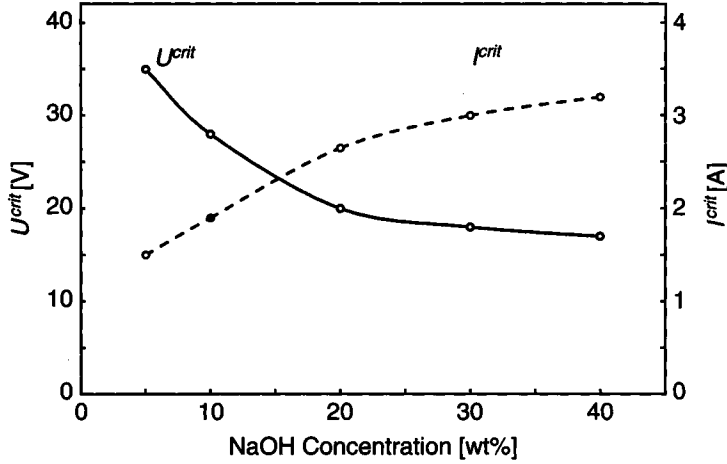


**Figure 4.6** Critical voltage  $U^{crit}$  and critical current  $i^{crit}$  as a function of the electrolyte concentration for a 1.1 mm cylindrical electrode immersed by 2 mm in a NaOH electrolyte. Plotted according data from [6].

in the inter-electrode resistance  $R$ , and also by the change in the wettability, which will affect the mean bubble height  $\xi d_n$ . Another parameter affected is  $\Delta t_b$ , the bubble detachment time, as the concentration affects the viscosity and density of the electrolyte. An example of the effect of concentration on the critical voltage and the critical current for sodium hydroxide is shown in Fig. 4.6. The decrease in  $U^{crit}$  with the electrolyte concentration is typical and not specific to NaOH.

#### 4.1.2.4 Gas Film Formation Time

In order to estimate the gas film formation time, the bubble evolution equation (3.61) is used. For simplicity, it is considered that the inter-electrode resistance  $R(\theta)$  may be estimated using:

$$R(\theta) = \frac{R^{bulk}}{1-\theta}. \quad (4.17)$$

Using this equation, one can compute from expression (3.73) for the critical voltage  $U^{crit}$ :

$$\frac{\beta \Delta t_b}{\xi d_n} = \frac{p_c}{1-p_c} \frac{R^{bulk} A}{U^{crit} - U_d} = \frac{p_c}{1-p_c} \frac{R(\theta) A}{U^{crit} - U_d} (1-\theta). \quad (4.18)$$

Substituting into the bubble evolution equation (3.61) yields:

$$\frac{d\theta}{dt} = \frac{p_c}{1-p_c} \frac{R(\theta) A (1-\theta)}{U^{crit} - U_d} j_{local} (1-\theta) - \sum_{s=0}^{s^{max}} s n_s(\theta). \quad (4.19)$$

Recalling that  $R(\theta)A(1-\theta)j_{local}=R(\theta)I=U-U_d$  and introducing the normalised time  $\bar{t}=t/\Delta t_b$ , one gets the normalised bubble evolution equation:

$$\frac{d\theta}{d\bar{t}} = \frac{p_c}{1-p_c} \mathcal{U} \cdot (1-\theta) - \sum_{s=0}^{s^{max}} s n_s(\theta). \quad (4.20)$$

where  $\mathcal{U}$  is the normalised voltage defined as in (3.75).

Let us solve this equation for a voltage step input in order to estimate the gas film formation time. For terminal voltages lower than the critical voltage ( $\mathcal{U} < 1$ ), the normalised bubble evolution equation can be written as (using the approximation  $s^{max} \rightarrow \infty$ ):

$$\frac{d\theta}{d\bar{t}} = \frac{p_c}{1-p_c} \mathcal{U} \cdot (1-\theta) - \theta. \quad (4.21)$$

The solution for a step input is (Fig. 4.7(a)):

$$\theta(\bar{t}) = \frac{\mathcal{U}}{\mathcal{U} + \frac{1-p_c}{p_c}} (1 - e^{-a\bar{t}}), \quad (4.22)$$

where

$$a = 1 + \frac{p_c}{1-p_c} \mathcal{U}. \quad (4.23)$$

To compute the corresponding current we use:

$$\frac{I}{A} = \frac{U-U_d}{R^{bulk}A} (1-\theta), \quad (4.24)$$

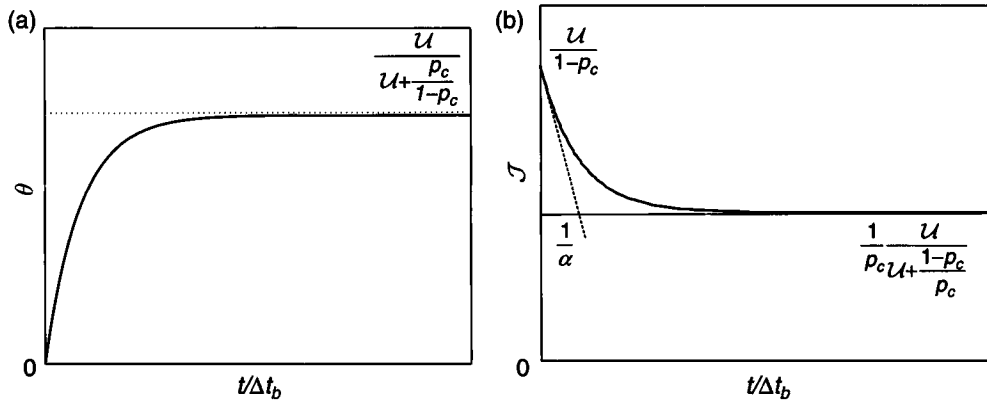


**Figure 4.7** Step input for a terminal voltage lower than the critical voltage: (a) bubble coverage fraction  $\theta$  step input; (b) normalised current  $\mathcal{I}$  step input.

which follows from Equation (3.67). Using the definition of the normalised current  $\mathcal{J}$  and normalised voltage  $\mathcal{U}$  it follows:

$$\mathcal{J} = \frac{1-\theta}{1-p_c} \mathcal{U}. \quad (4.25)$$

Together with (4.22), we obtain the step input for the normalised current  $\mathcal{J}$  (Fig. 4.7(b))

$$\mathcal{J}(\bar{t}) = \frac{\mathcal{U}}{1-p_c} \left[ 1 - \frac{\mathcal{U}}{\mathcal{U} + \frac{1-p_c}{p_c}} (1 - e^{a\bar{t}}) \right]. \quad (4.26)$$

For higher terminal voltages, the bubble coverage fraction will grow according to Equation (4.22) until it reaches the percolation threshold where the gas film forms. The time  $t_f$  until  $p_c$  is attained is given by the solution of  $\theta(\bar{t}_f) = p_c$ . One obtains for the gas film formation time (Fig. 4.8):

$$\frac{t_f}{\Delta t_b} = \frac{1}{1 + \frac{p_c}{1-p_c} \mathcal{U}} \ln \left[ \frac{\mathcal{U}}{(1-p_c)(\mathcal{U}-1)} \right]. \quad (4.27)$$

For terminal voltages around  $\mathcal{U} \approx 1.5$  (which are, as will be seen in Part 2 of this book, typical for micromachining applications), the gas film formation time is similar to the mean detachment time of the gas bubbles.

Note that the formation of the gas film takes place at the current  $\mathcal{J} = \mathcal{U}$ , as can be seen immediately from Equation (4.25).

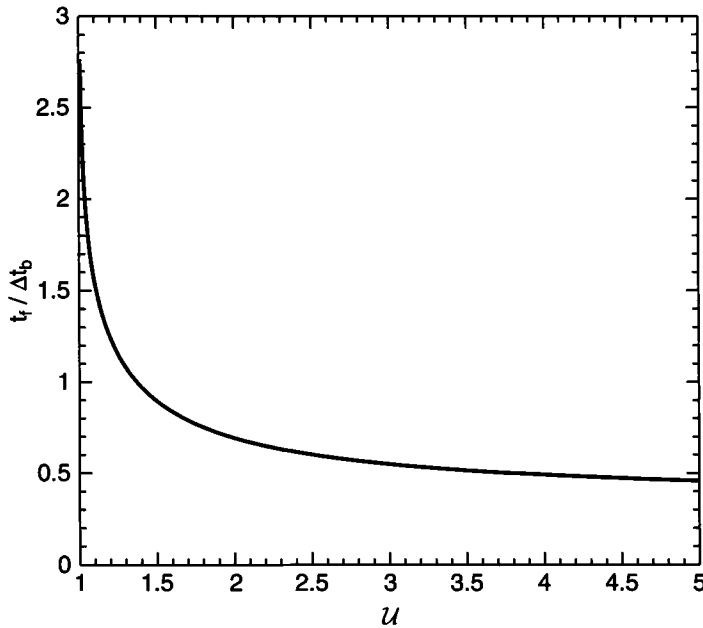


**Figure 4.8** Gas film formation time according the bubble coalescence model as predicted by (4.27). The value used for the percolation threshold is  $p_c = 0.5$ .

### 4.1.3 Hybrid Mechanisms

The gas film responsible for the appearance of electrochemical discharges can be formed by local electrolyte evaporation due to joule heating or by bubble coalescence. As seen in the previous sections, both mechanisms take place at high current densities (typically around  $1 \text{ A/mm}^2$ ) and lead to very similar gas film formation times in the range of a few milliseconds. Also note that if the bubble growth becomes more and more dense with increasing voltage, or current, the local current density also shows a similar increase. When reaching a coverage fraction at the percolation threshold (or very close to it) the local joule heating of the electrolyte also becomes very high and may lead to local evaporation. It is very likely that both mechanisms are more or less involved together in the formation of the gas film.

This is well confirmed by the experiments of Kellogg [70]. During his investigations, he could observe how prior to the formation of the gas film the bubble growth is very intense, which confirms that the gas film is formed by coalescence of gas bubbles. At the same time he could also measure the increase in the temperature of the active electrode surface, which reaches  $100^\circ\text{C}$  at the moment the gas film is formed and, finally, increases dramatically to  $400^\circ\text{C}$  and more at the onset of the discharges (Fig. 4.9). An interesting feature is that the temperature of  $100^\circ\text{C}$  is almost reached in the limiting current region a few volts before the critical voltage is reached (in the case of an electrolyte preheated at  $89^\circ\text{C}$ , even more than 15 V before the critical voltage). This observation indicates that local evaporation by joule heating cannot be the only effect involved in the formation of the gas film, but on the contrary is only one of the effects contributing to its formation.

There are also other mechanisms that lead to the formation of the gas film [130]. An example of the voltage step input for different terminal voltages  $U$  in

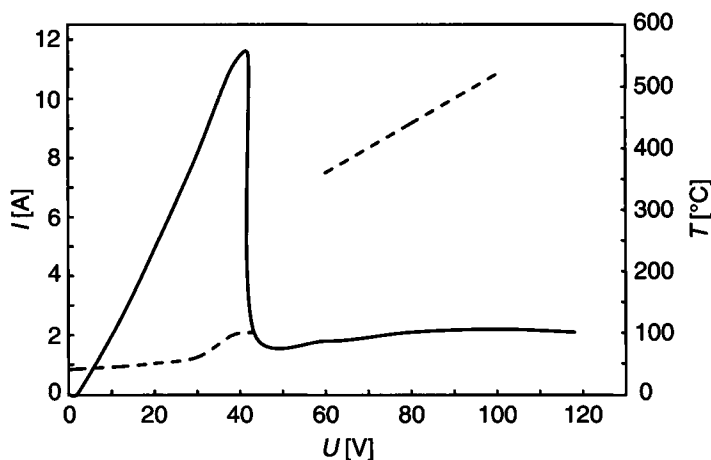


**Figure 4.9** Temperature increase on a cylindrical 3.5 mm active steel anode in normal NaOH according to [70]. Reproduced by permission of The Electrochemical Society.

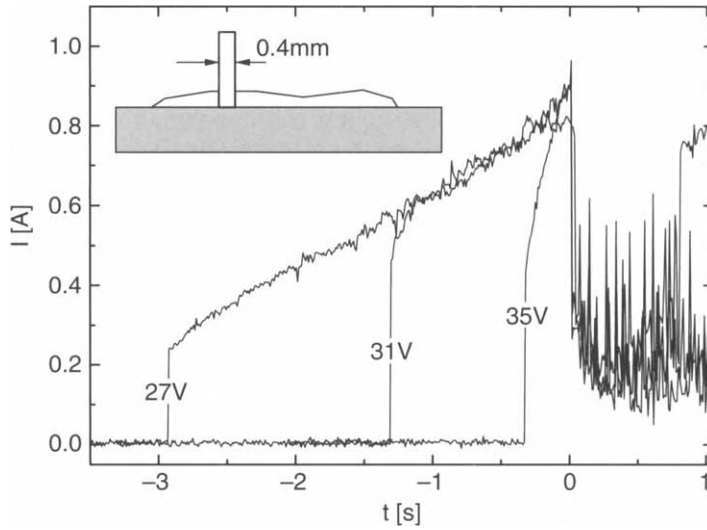


**Figure 4.10** Voltage step input for various voltages in the case of a high inter-electrode resistance. Reprinted from [130] with the permission of the *Journal of Micromechanics and Microengineering*.

the case of a high inter-electrode resistance  $R$  is shown in Fig. 4.10. The experiment was done with a cylindrical stainless steel electrode of 0.4 mm diameter. The electrolyte (sodium hydroxide at 30 wt%) was deposited in the form of a small droplet on a glass substrate, just enough to wet it. The initial current, given by  $U/R$ , is too low to lead to the formation of a gas film. However, due to the high inter-electrode resistance and the low quantity of the electrolyte, the electrolytic solution progressively heats up. This results in lowering of the inter-electrode resistance over time. The current increases until it reaches the critical value necessary for the formation of the gas film. Note that this process is much slower than the other two processes described in the previous sections.

Other mechanisms may be considered. For example, decrease in the active electrode surface due to a change in the wettability by electro-wetting or the formation of an electrically insulating layer on the electrode. These mechanisms are not discussed further in the text due to the lack of knowledge and experimental evidences to analyse them.

## 4.2 Shape of the Gas Film

In 1908, almost ten years after Wehnelt's publication on his electrolytic interrupter, for the first time Ludewig made precise visual observations of the formation of the gas film responsible for electrochemical discharges using photographic techniques [83]. He illuminated an electrolytic interrupter with a light source formed by arc discharges between two carbon electrodes. The scene was recorded on a photographic plate mounted on a drum. With the help of a perforated wheel, synchronised with the drum holding the photographic



plate, Ludewig was able to record the formation of the gas film. The author described how the active electrode of an electrolytic interrupter is progressively covered by gas bubbles and finally surrounded by a compact gas film. He also estimated, by recording the current during the experiment, the amount of gas produced electrochemically (estimated from Faraday's law) and by local joule heating (using formula (4.4) from Klupathy). His results indicate that, for the configuration used (an active platinum electrode of 1 mm diameter), the electrolytic contribution is about ten times more important (in volume). He also estimated the mean diameter of the gas film as a function of the interruption number of his electrolytic interrupter. He found values in the range of a few hundred micrometres.

The experiment done by Kellogg [70] in 1949 confirms these values. He describes how the gas film surface behaves like a vibrating structure (see Fig. 4.11). Kellogg also stressed that once the gas film is formed, no further bubble generation can be observed. He concluded that the electrochemical reactions must now take place at the gas-electrolyte interface.

Another important finding by Kellogg was that the thickness and uniformity of the gas film is a function of the electrolyte's bulk temperature. At higher temperatures the gas film becomes more uniform, vibrates only slightly, and is thinner. Kellogg attributed these observations to the mechanism that maintains

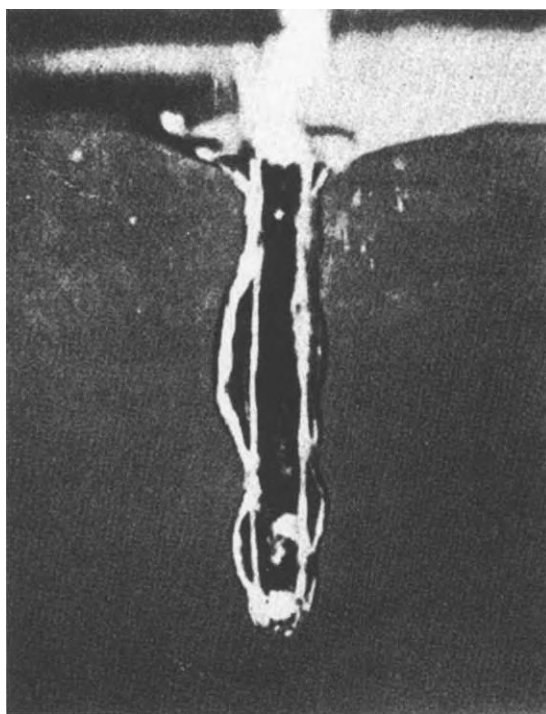


**Figure 4.11** An active cathode in sulphuric acid. The terminal voltage is 70 V [70]. Reproduced by permission of The Electrochemical Society.

the gas film in place: evaporation of the electrolyte by the electrochemical discharges.

Kellogg's results were confirmed later by Guilpin and Garbaz-Olivier [47] using high-speed cameras. As new finding the authors mentioned that they could always observe at the most one discharge at a given time. The latest results from Azumi et al. [5] show that electrochemical discharges originate from a small spot on the active electrode and then expand to a large surface at the gas film–electrolyte interface. This is due to the lower electrical conductivity of the electrolyte than the ionised gas, which is probably in a state similar to a plasma.

### 4.3 Discharge Activity Inside the Gas Film

The formation of a gas film around an electrode significantly modifies the potential distribution, as illustrated in Fig. 4.12. When a gas film is present, the mean current is very small and there is nearly no ohmic drop in the electrolyte. As a consequence, almost all the potential drop takes place across the gas film resulting in quite high local electrical fields. Together with the increased electrode temperature, this results in electrochemical discharges by thermal-assisted field emission in the case of an active cathode. In the case of an active anode, the Hickling and Ingram mechanism is responsible for the discharges (see Section 2.5).

In this section a model describing the discharge activity inside the gas film is presented. The aim is to describe the evolution of the current with time and

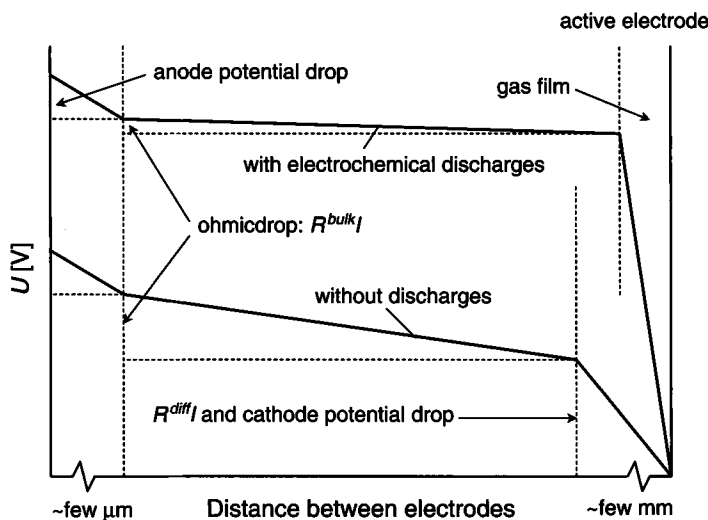


**Figure 4.12** Potential distribution at a cathode before and after the formation of the gas film (adapted from [1,41]).

to evaluate the *probability of discharge*. Because of the importance for machining applications, a detailed analysis of the current as a function of time is needed. Not only the mean current, but also its statistical distribution is of interest. The central hypothesis of the developed model is that the underlying stochastic process is a Poisson process [123]. The model is useful to derive important characteristics of the electrochemical discharges such as the mean energy carried by them. First, the mathematics related to this model are presented; then some experimental results are discussed.

#### 4.3.1 Definition of the Model

Each electrical discharge is characterised by a current pulse described by the function  $f(t)$ . The total current is written as the sum of the contribution of each discharge pulse (Fig. 4.13):

$$I(t) = \sum_{t_k} f(t - t_k), \quad (4.28)$$

where  $f(t - t_k)$  is the contribution to the total current by one discharge at time  $t_k$ . It is assumed that each discharge is characterised by a similar pulse and occurs independently.

#### 4.3.2 Probability Distribution of Electrochemical Discharges

To describe the stochastic process of the discharge activity, one introduces  $P(n, t)$ , the probability that  $n$  discharges had been initiated until time  $t$ :

$$P(n, t) = \text{Prob}\{N(t) = n\}, \quad (4.29)$$

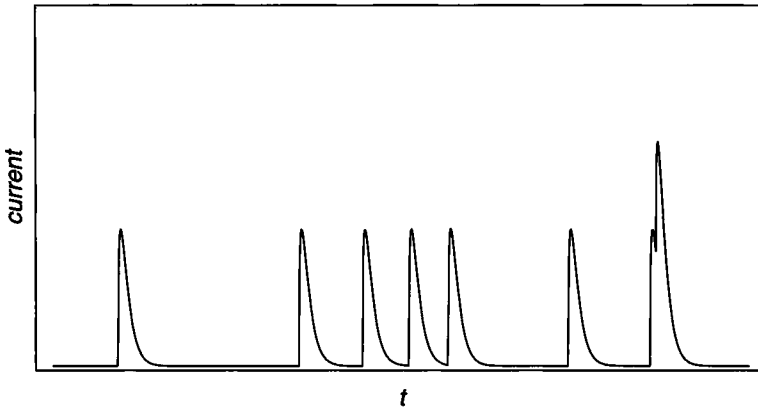


**Figure 4.13.** Identical pulses occurring at randomly distributed moments.

where the random variable  $N(t)$  is the number of discharges that occur until time  $t$ .

As a next step  $\lambda_d$ , the *electron yield* or the *probability of discharge* per unit time and surface  $A$  of the active electrode is introduced. Assuming that the probability that a discharge occurs in the time interval  $dt$  is independent of the time  $t$ , it follows:

$$P(n \rightarrow n+1, \text{ during } dt) = \lambda_d A dt. \quad (4.30)$$

Therefore, the master equation for the stochastic process can be written as:

$$P(n, t + \Delta t) = P(n, t)[1 - \lambda_d A \Delta t] + P(n-1, t)\lambda_d A \Delta t, \quad (4.31)$$

or in differential form:

$$\frac{\partial}{\partial t} P(n, t) = \lambda_d A [P(n-1, t) - P(n, t)]. \quad (4.32)$$

This master equation is characteristic of a Poisson process. For self-consistency of the text, the remainder of this section shows explicitly that the solution of (4.32) is a Poisson distribution.

To solve the master equation (4.32) of the stochastic process, the *generating function*  $G(s, t)$  defined by:

$$G(s, t) = \sum_n s^n P(n, t) \quad (4.33)$$

is introduced. Using the master equation (4.32) it follows that:

$$\frac{\partial}{\partial t} G(s, t) = \lambda_d A (s-1) G(s, t), \quad (4.34)$$

which has the following solution:

$$G(s, t) = \exp[\lambda_d A (s-1)t] G(s, 0). \quad (4.35)$$

As no discharge is generated before  $t = 0$ , one has  $P(0, 0) = 1$  and  $P(n, 0) = 0$  for all  $n > 0$ . It follows that:

$$G(s, 0) = 1. \quad (4.36)$$

By developing  $G(s, t)$  in a power series of  $s$  it follows that:

$$P(n, t) = \exp(-\lambda_d A t) \frac{(\lambda_d A t)^n}{n!}. \quad (4.37)$$

This means that the random variable  $N(t)$  follows a Poisson process. The mean number of discharges is given by:

$$\langle N(t) \rangle = \sum_{n=1}^{\infty} nP(n,t) = \lambda_d At, \quad (4.38)$$

in accordance with the intuitive understanding of  $\lambda_d$ .

### 4.3.3 Probability of Discharge as a Function of the Terminal Voltage

By counting the current pulses experimentally it is possible to verify that electrochemical discharges follow a Poisson process. Therefore, one can count the number of current pulses  $N(t)$  during a fixed time interval  $t$ . The experiment shows that the distribution of  $N(t)$  follows the Poisson distribution (4.37) as plotted in Fig. 4.14. This figure presents the counts of current pulses obtained at 28 V with a cylindrical active cathode of 172  $\mu\text{m}$  diameter [123]. The pulses were counted for a time interval of 40 ms. The experiment was repeated 500 times and the frequency distribution was evaluated. The superimposed curve is the fitted Poisson distribution. From this distribution, the parameter

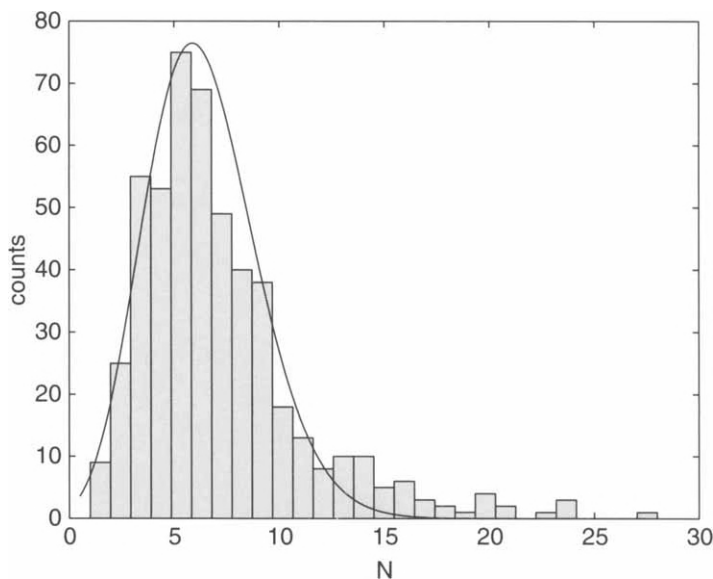


**Figure 4.14** The number of current pulses obtained at 28 V with a cylindrical active cathode of 172  $\mu\text{m}$  diameter for a time interval of 40 ms, by counting 500 times. The superimposed curve is the fitted Poisson distribution (4.37). The electrolyte used is 30 wt% NaOH [123].

$\lambda_d$  is evaluated (the electrode surface is estimated from the measurement of the immersion depth  $h$  of the electrode in the electrolyte).

By repeating this experiment for different conditions, it is possible to determine  $\lambda_d$  as a function of the terminal voltage  $U$ . At each value of  $U$ , the number of pulses in a fixed time interval (40 ms) are counted several times (500 times), and the probability of discharge  $\lambda_d$  is evaluated by fitting the corresponding Poisson distribution (4.37). Figure 4.15 shows the experimental results for a 0.4 mm active cathode.

Two qualitatively different behaviours are observed. For terminal voltages from the critical voltage  $U^{crit}$  to about 32 V, the probability of discharge decreases with the voltage as a power law such as:

$$\lambda_d \propto -(U - U^{crit})^2. \quad (4.39)$$

Above 32 V, the probability of discharge follows a law similar to field emission:

$$\lambda_d = AE^2 \cdot \exp(-B/E). \quad (4.40)$$

When  $A$  and  $B$  are two constants. Note that arc discharges follow a similar law as field emission [93]. Therefore, it is likely that for voltages higher than 32 V, arc discharges occur in the gas film around the active electrode.

These two different behaviours can also be seen in the current signal (see Fig. 4.16, which shows the current signals with time for  $U = 25$  and 32 V). For

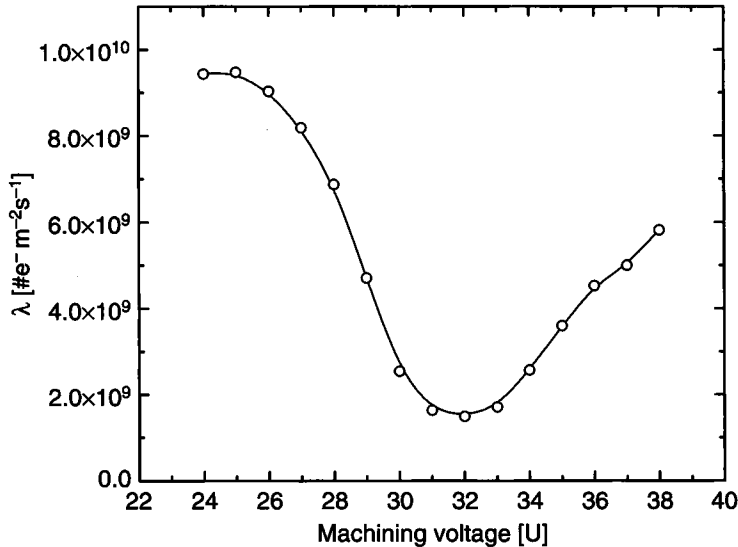


**Figure 4.15** The probability of gas discharges in a 30 wt% NaOH solution as a function of the terminal voltage  $U$  for a 0.4 mm active cathode. Reprinted from [84] with the permission of the *Journal of Micromechanics and Microengineering*.

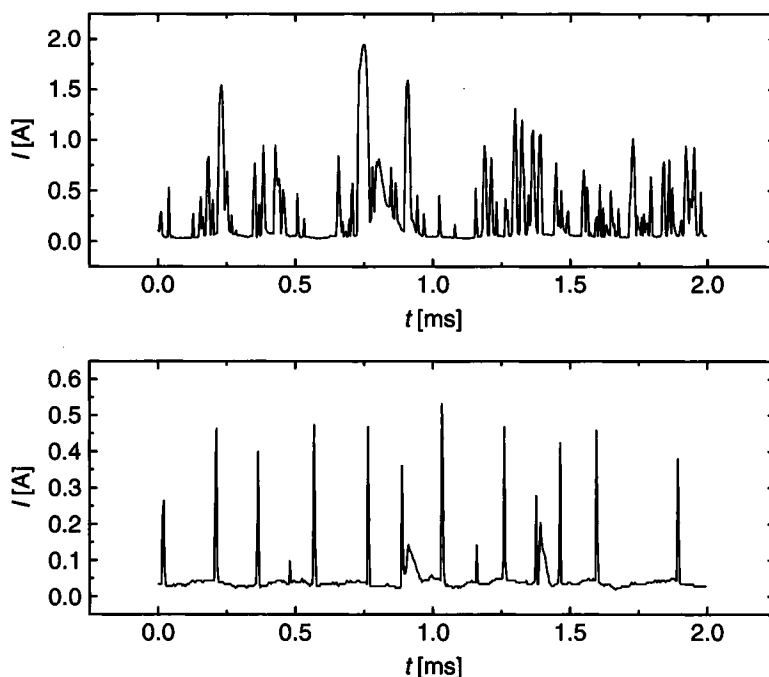


**Figure 4.16** Typical current pulses for terminal voltages of 25 V (top) and 32 V (bottom) for an active cathode. Reprinted from [123] with permission from Elsevier.

voltages in the range from the critical voltage to 32 V, pulses of a few 100  $\mu\text{s}$  together with short pulses of around 10  $\mu\text{s}$  are observed. Above 32 V only short pluses of around 10  $\mu\text{s}$  are observed.

How can situation for small terminal voltages be understood? The probability of initiating a discharge should increase with the voltage (electrical field). However, the experiment shows that  $\lambda_d$  is decreasing. As a hypothesis it is proposed that in this phase the gas film is not yet completely formed. In terms of the percolation model (see Table 3.5), the infinite cluster  $P(p)$  increases. In this phase, it is likely that only a part of the active electrode (the infinite cluster) is covered by a compact gas film. Therefore, it is proposed that  $P(p)$  be interpreted as the *gas film coverage fraction*. Some discharges may occur only in the gas film. In the remaining part of the active electrode surface, traditional current transport by electrolysis occurs, as well as local evaporation of the electrolyte by joule heating. The pulses observed (Fig. 4.16) in this phase are probably not all gas discharge pulses. There may be some current pulses from traditional electrolysis current occurring in the parts not covered by the gas film. These parts decrease with increasing terminal voltage while the gas film grows in size ( $P(p)$  increases with the mean occupation probability  $p$ ). Once the gas film reaches its maximal value ( $P(p) = 1$ ) and totally covers the electrode surface, only traditional arc discharges occur.

The region from the critical voltage  $U^{\text{crit}}$  to the onset of field emission behaviour can be seen as an extent of the *instability region* beginning for

voltages near the critical voltage. The voltage at which the transition to the field emission behaviour takes place is sometime called the *transition voltage* [80]. As will be seen in Part 2 of this book, this region is particularly interesting for machining applications. The region for higher voltages is termed the *arc discharge region*.

#### 4.3.4 Current Evolution Equation

Not only is the probability of discharge  $\lambda_d$  of interest, but also the current evolution with time. From the description of the current evolution with time one can deduce the mean current, which is easily accessible experimentally and is important to evaluate the quantity of heat generated by the process. From the description of the stochastic process of the discharge activity given previously, the current can be computed. In order to obtain the current evolution equation, an auxiliary random variable  $\mu(t)$  defined by the time derivation of the random variable  $N(t)$  is introduced:

$$\mu(t) = \frac{d}{dt}N(t) = \sum_k \delta(t - t_k), \quad (4.41)$$

where  $\delta(t - t_k)$  is the Dirac function and  $t_k$  is the emission time of the discharge. Using this auxiliary variable, the current  $I(t)$  is written as:

$$I(t) = \int_{-\infty}^{\infty} f(t-s)\mu(s)ds = \int_{-\infty}^{\infty} f(t-s)\frac{d}{ds}N(s)ds. \quad (4.42)$$

The function  $f(t-s)$  has to vanish for  $t < s$  (because no pulse can be produced before a discharge occurs) and for  $t \rightarrow \infty$ . From now on it is assumed that  $f(t)$  is of the form (see Fig. 4.17):

$$f(t) = \begin{cases} qe^{-t/\tau} & t > 0, \\ 0 & t < 0. \end{cases} \quad (4.43)$$

For this particular function  $f(t)$ , the current can be written as:

$$I(t) = \int_{-\infty}^t qe^{-(t-s)/\tau} \frac{d}{ds}N(s)ds. \quad (4.44)$$

By derivation according to the time of this last relation and using (4.41), a differential equation for the current is obtained:

$$\frac{d}{dt}I(t) = q\mu(t) - \frac{1}{\tau}I(t). \quad (4.45)$$

For further discussion, the *current fluctuations*  $\eta(t)$  are introduced:

$$\eta(t) = I(t) - \langle I(t) \rangle. \quad (4.46)$$



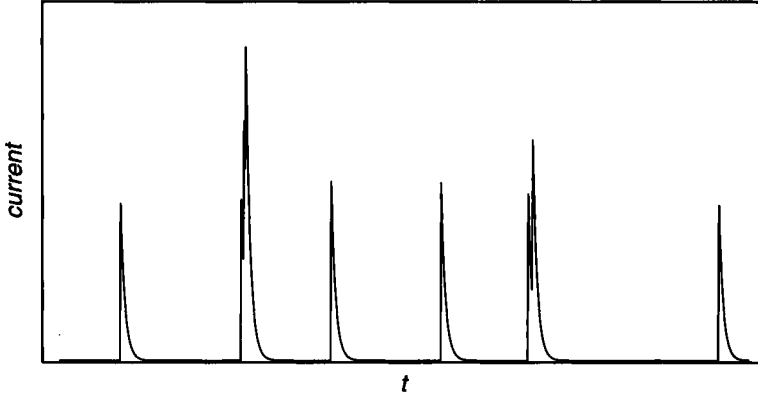


**Figure 4.17** Identical pulses ( $qe^{-t/\tau}$ ) arriving at time instants randomly distributed according to a Poisson distribution.

Now, as

$$\langle dN(t) \rangle = \lambda_d A dt, \quad (4.47)$$

it follows that

$$d\eta(t) = dN(t) - \langle dN(t) \rangle = \mu(t)dt - \lambda_d A dt. \quad (4.48)$$

Together with Equation (4.45), one obtains the current evolution equation:

$$dI(t) = \left[ \lambda_d A q - \frac{1}{\tau} I(t) \right] dt + q d\eta(t). \quad (4.49)$$

This evolution equation allows the description of the current during discharge activity with time. In particular, the mean current and the fluctuations in the current can be calculated, as shown in next section. Both quantities are important for the application of electrochemical discharges to machining.

### 4.3.5 Mean Current and Fluctuations in the Current

By considering the mean of the current evolution equation (4.49) it follows (because  $\langle d\eta(t) \rangle = 0$ ) that:

$$\frac{d}{dt} \langle I(t) \rangle = \lambda_d A q - \frac{1}{\tau} \langle I(t) \rangle, \quad (4.50)$$

with the solution ( $\langle I(t=0) \rangle = 0$ ):

$$\langle I(t) \rangle = \lambda_d A q \tau [1 - \exp(-t/\tau)]. \quad (4.51)$$

As seen in Section 4.3.3, typical values for  $\tau$  are in the microsecond range. Therefore, the following approximation is valid for practical applications:

$$\langle I \rangle \cong \lambda_d A q \tau. \quad (4.52)$$

The important consequence is that the mean current  $\langle I \rangle$  in the arc region is proportional to the number of discharges per unit time  $\lambda_d$ . This means that as  $\lambda_d$  increases with the terminal voltage  $U$ , the average energy of the discharges also increases with  $U$ . A consequence is the increase of the active electrode temperature as observed by Kellogg [70] (Fig. 4.9). More recently it was observed by Azumi et al. [5] that even for higher terminal voltages (about 200 V) the electrode temperature can reach up to 1300 K. The authors attribute this high increase to the bombardment of the active electrode by charged particles accelerated by the high electrical field.

In order to further study the discharge activity, one has to compute the standard deviation of the current. Therefore, let us start with

$$\langle d(I^2) \rangle = \langle (I + dI)^2 - I^2 \rangle = 2\langle IdI + (dI)^2 \rangle. \quad (4.53)$$

By developing it follows that:

$$\langle d(I^2) \rangle = 2 \left\langle I \left[ \lambda_d A q - \frac{1}{\tau} I \right] dt + q d\eta(t) \right\rangle + \left\langle \left[ \left[ \lambda_d A q - \frac{1}{\tau} I \right] dt + q d\eta \right]^2 \right\rangle \quad (4.54)$$

As  $\langle d\eta(t) \rangle = 0$  and  $\langle [d\eta(t)]^2 \rangle = \lambda_d A dt$ , it follows that:

$$\frac{1}{2} \langle d(I^2) \rangle = \left[ \lambda_d A q \langle I \rangle - \frac{1}{\tau} \langle I^2 \rangle + \frac{q^2 \lambda_d A}{2} \right] dt \quad (4.55)$$

From which the evolution equation for the current fluctuations is obtained as:

$$\frac{1}{2} \frac{d}{dt} \langle I(t)^2 \rangle = \lambda_d A q \langle I \rangle - \frac{1}{\tau} \langle I^2 \rangle + \frac{q^2 \lambda_d A}{2}, \quad (4.56)$$

with the solution

$$\langle I(t)^2 \rangle = \frac{\lambda_d A \tau q^2}{2} [1 - \exp(-2t/\tau)] + \langle I(t) \rangle^2. \quad (4.57)$$

As  $\tau$  is typically in the millisecond range, the following approximation is valid:

$$\langle I^2 \rangle \cong \frac{\lambda_d A \tau q^2}{2} + (\lambda_d A \tau q)^2 \quad (4.58)$$

$$\langle I^2 \rangle - \langle I \rangle^2 \cong \frac{\lambda_d A q^2}{2} \tau. \quad (4.59)$$

From these two relations, one can see how the fluctuations in the current increase with the number of discharges per unit time  $\lambda_d$  and therefore with the terminal voltage. The discharge activity, in terms of the mean current, becomes less stable with increasing terminal voltage.

## 4.4 Controlling the Gas Film

The gas film is a complex and dynamic structure. Taking control of the gas film appears to be a very challenging task. However, an unstable gas film will result in fluctuating discharge activity and consequently in nonrepeatable machining. Strategies to overcome this issue have to be developed. So far two strategies have been applied. The first strategy tries to reduce the critical voltage as much as possible with the aim of generating discharges at lower terminal voltages. The second strategy overcomes the instability of the gas film by building and destroying the gas film periodically in a controlled manner. The practical applications of these strategies are discussed in detail in Chapter 7.

### 4.4.1 Reducing the Critical Voltage

As discussed in Section 4.1, the gas film can be formed around the tool-electrode by coalescence of electrolytically generated gas bubbles, by local evaporation of the electrolyte by joule heating, or by hybrid processes. Processes involving local joule heating of the electrolyte offer few possibilities to influence the critical voltage. This is different for the process of gas film formation by bubble coalescence. A possibility is to influence the wettability of the electrode–electrolyte–gas interface [129]. This results in a change in the contact angle and therefore the shape of the growing gas bubbles (Fig. 4.18).

From Equation (3.73), one can read that for contact angles resulting in flat bubbles ( $\xi$  will be low) the critical voltage  $U^{crit}$  will be reduced. Adding surfactants to the electrolyte is a simple way to change the wettability of the

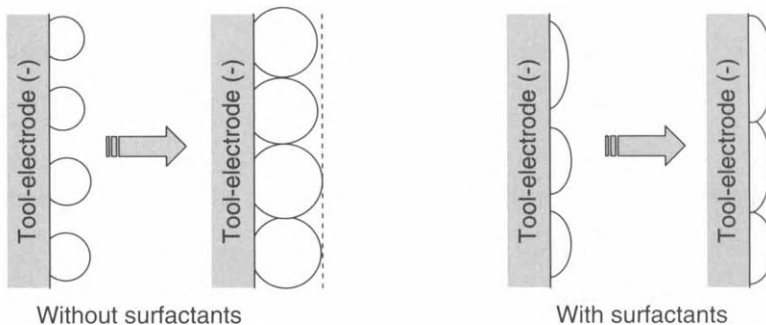


**Figure 4.18** Principle of gas film formation with surfactants. Reprinted from [129] with permission from Elsevier.

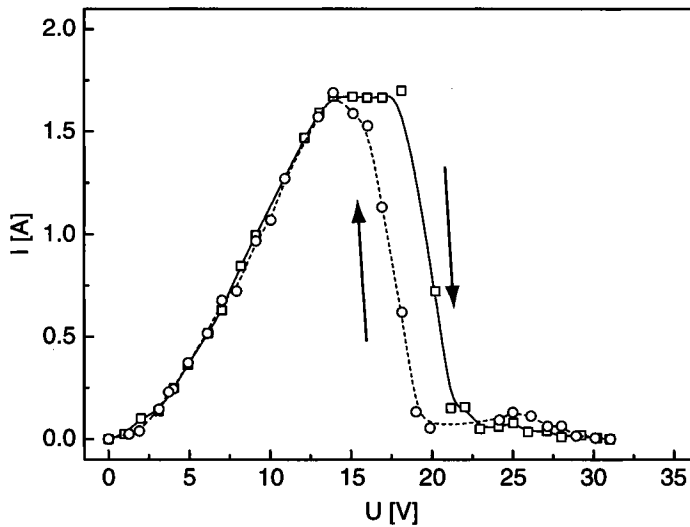


**Figure 4.19** Hysteresis in the current–voltage characteristics of a gas evolving electrode. Forward and reverse scans are done at 10 V/s. Reprinted from [124] with permission from Elsevier.

electrode–electrolyte interface. The critical voltage can be reduced in this way by several volts (from about 20 V to about 14 V) [55,126,129].

Another way to obtain a gas film at lower voltages is to take advantage of the hysteresis effect in the current–voltage characteristics (Fig. 4.19). As first described by Kellogg [70], once the gas film is formed at a terminal voltage  $U > U^{crit}$ , it is possible to slightly (1–2 V) reduce it below the critical voltage without losing the gas film around the active electrode (Fig. 4.19). This hysteresis is due to the dynamics of bubble formation on the active electrode [124]. As the possible reduction of the voltage is quite small compared with the previous method, it has never been used in practical applications to date.

A third way to influence the critical voltage is to play with the inter-electrode resistance. As seen in Equation (3.73), the higher the inter-electrode resistance, the higher will be the critical voltage. If low terminal voltages are desired for electrochemical discharges, attention has to be paid to the electrode geometry and the electrical conductivity of the electrolyte in order to minimise the inter-electrode resistance.

#### 4.4.2 Controlling the Gas Film Stability

As mentioned previously, the gas film is unstable. For micromachining applications, a stable gas film is desired. As the stability is difficult to achieve or control, an alternative way is to build and destroy the gas film periodically in a controlled manner by using pulsed voltage supplies. An interesting and low-cost alternative is to use the circuit proposed initially by Wehnelt [119]

(see also Section 2.2). The voltage pulses have to last longer than the time needed for the formation of the gas film (a few milliseconds).

#### 4.4.3 Controlling the Gas Film Shape

It was first noted by Kellogg [70] that it is possible to give a spherical shape to the gas film if the upper part of the active electrode is covered by some insulating material. In this case, due to the modified geometry, the gas film is no longer cylindrical but instead a single large gas bubble forms around the free electrode surface. This larger bubble breaks off periodically (a few times per second, depending on the particular geometry). For electrodes that are long enough (a few millimetres), a gas film builds in the lower part and a bubble in the upper part.

Under these conditions, the spark activity is modified and becomes in particular more regular [32,33,51]. This may be attributed to the better controlled active surface of the electrode, and also to the fact that the large gas bubble is more stable than a gas film.

The amplitude of the discharges is also directly correlated to the size of the bubble. As shown by Han et al. [51], the amplitude of the discharge peaks follows the same inverse volcano dependence as the bubble diameter. The minimum is reached for an active electrode length equal to its radius.

## 5 Material Removal Mechanism

---

In this first chapter about micromachining with electrochemical discharges, the fundamentals of the material removal mechanism are discussed. Electrochemical discharges provide the energy needed for machining. For a long time it was believed that material removal takes place through melting of the workpiece, similar to electrical discharge machining, and it is only quite recently that the important contribution from chemical etching was recognised. Both these aspects are discussed in this chapter.

### 5.1 General Considerations

Since the pioneering work of Kurafuji and Suda [76] on glass microdrilling, it is known that machining with electrochemical discharges is possible. Not only can glass be drilled, but several other non-conducting materials can also be machined using this technology (e.g., granite, refractory fire-brick, aluminium oxide, plexiglas, quartz) [21]. In particular ceramic material can be drilled (e.g.,  $\text{Al}_2\text{O}_3$ ,  $\text{Si}_3\text{N}_4$ ,  $\text{MgO}$ ,  $\text{Y}_2\text{O}_3$ ) [11,61,82,104]. Typically, holes of 1 mm diameter can be produced using various electrolytes and salts (e.g.,  $\text{NaF}$ ,  $\text{NaNO}_3$ ,  $\text{NaCl}$ , and  $\text{NaOH}$ ) with relatively high machining voltages (around 80 V compared with 30 V for glass and quartz). The material removal rate is, however, about one order of magnitude smaller than for glass and quartz (about 0.1–0.4 mg/min) and the surface quality is lower [11].

An active cathode (direct polarity machining) or active anode (reverse polarity machining) [63] can be used as a tool, of which the use of the former is most popular. As the discharge activity, and especially the discharge mechanism, differs for an active cathode and anode, the machining performances will also be different.

Investigations on the mechanism of material removal are still underway. Several processes may contribute to the material removal [2,58], including:

- melting and vaporisation due to electrochemical discharges,
- high-temperature chemical etching,
- differential expansion of constituents and weathering,
- random thermal stresses and microcracking and spalling, and
- mechanical shock due to expanding gases and electrolyte movement.

So far only thermal effects and chemical etching have been investigated systematically, mostly for glass machined with an active cathode. The following discussion will therefore concentrate on glass micromachining.

The dominant mechanism in machining is local heating of the workpiece by the electrochemical discharges. Material removal is achieved by intensive heating of the workpiece surface, leading to melting and maybe even vaporisation. Another contributing effect is chemical etching of the workpiece, a mechanism that is accelerated by the local high temperature. Analytical [8] and numerical [32,34,60] calculations support the thermal mechanism. However, two major difficulties are encountered when using such models.

First, the temperature needed for machining to take place has to be estimated. For glass this is not straightforward as it does not present a sharp phase transition. The viscosity of glass decreases progressively with increasing temperature until it reaches a state in which it can flow easily. In the case of SACE micromachining, it is important to know the viscosity at which glass can be removed from the machining zone by the electrolyte. The value of this critical viscosity has not been clearly established so far. The effects of chemical etching are also important, which are discussed in Section 5.4. In summary, the value of the temperature needed for machining to take place is still an open question.

The second difficulty is to estimate the amount of energy released by the electrochemical discharges and the fraction that is actually used for the machining process. Basak and Ghosh [8] proposed, using analogies with electrical discharge machining and telecommunication switches, that each discharge carries a mean energy of 2000 J/cm<sup>2</sup> and has a duration of 0.1 ms. An alternative way to estimate the mean heat power  $P_E$  released by the discharges is to use following relation [34,60,88]:

$$P_E = (U - U_d)\bar{I} - R\bar{I}^2, \quad (5.1)$$

where  $U$  is the terminal voltage applied during machining (termed machining voltage in the following),  $U_d$  is the water decomposition potential,  $\bar{I}$  is the mean current, and  $R$  is the inter-electrode resistance of the electrolyte. In other words, the mean energy of the sparks is the mean energy given to the system minus the energy lost by joule heating. Fascio [32,34] improved this idea by estimating the mean energy and mean duration of a spark from a statistical analysis of the current signal in the arc region. The proposed models reproduce the experimental observations of the material removal rate fairly well, except at low voltages (below 30 V), where the predicted machining rate is significantly smaller. This suggests that the chemical contributions can no longer be neglected for these voltages. These aspects are discussed in more detail in Sections 5.3 and 5.4.

Nevertheless several experimental evidences confirm the importance of the thermal mechanism in machining. It is known that the tool-electrode may reach temperatures up to 500°C during microdrilling [6,7,70]. Allesu et al. [2] showed, by a simple experiment, that the heat produced during electrochemical discharges is able to attack glass. They used an electrolysis cell separated into two compartments by a glass wall perforated with a small hole of 1.5 mm diameter. For a cell terminal voltage of 60 V, the hole inside the glass wall rapidly fills with

a gas bubble formed by local evaporation of the electrolyte due to joule heating. Electrochemical discharges are observed inside the gas and the diameter of the hole increases from 1.5 mm to 2.5 mm within a few minutes.

Kulkarni et al. [75] showed by various measurements that after each discharge, the temperature of the workpiece increases above the melting temperature and sometimes even above the vaporisation temperature of the machined material. They estimated that about 77–96% of the energy supplied to the process is used to heat the electrolyte and tool-electrode and only 2–6% is used for heating up the workpiece. However, it should be emphasised that the experiments by Kulkarni et al. were performed on metallic workpieces that have very different heat conductivities compared with materials that are machined traditionally using electrochemical discharges (e.g., glass or ceramics).

Another experimental evidence for the thermal mechanism in machining is the observation of thermal cracks inside the machined materials, which appear at high voltage machining [11,40,58,84,106,122].

On the other hand, there are strong evidences for the chemical contribution in machining. Particularly striking are the very smooth surfaces that can be achieved at low machining voltages. Chemical analysis of the electrolyte after machining also confirms the chemical mechanism [63]. The latest experimental results for glass machining seem to indicate that the temperature  $T_M$  in the machining zone is quite low (500–600°C, a temperature at which glass still has quite a high viscosity) [65,88]. Section 5.4 discusses this aspect in more detail.

The material removal mechanism for glass machining is shown in Fig. 5.1. The electrochemical discharges heat up the workpiece locally, which results in lowering of the viscosity of glass and enhancing of chemical etching by OH radicals from the electrolyte. A zone of glass with lowered viscosity and electrolyte salt forms in front of the tool-electrode (water evaporates at that temperature). If sodium hydroxide is used as the electrolyte, etching takes place probably by complexation of silicate, as discussed in Section 5.4.

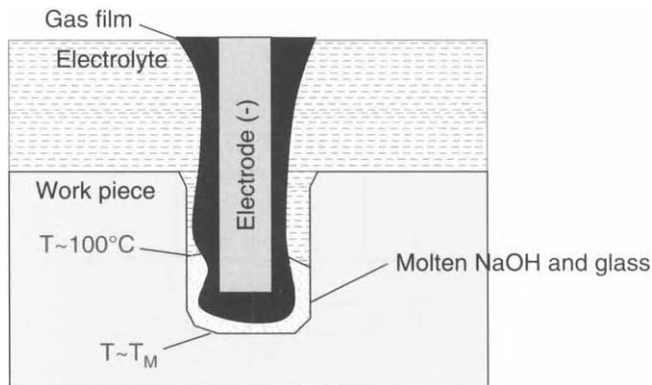


**Figure 5.1** Schematic of glass machining with electrochemical discharges.  $T_M$  is the temperature needed for machining to take place (see text for the discussion about its value).



As the electrochemical discharges are the heat source, machining at low and high depths will be very different. With increasing depth, it will be more difficult for the electrolyte to flow to the tip of the tool-electrode (especially in the case of microhole drilling), which results in a reduced discharge activity. Chemical etching will also be reduced. Both effects result in a significant lowering of the material removal rate. Therefore, the material removal rate is a function of the machining depth. Two limiting cases are described in Sections 5.2 and 5.3.

The first case is machining at low depths, which is defined as the case where machining is limited by the heat propagation inside the workpiece. The second case is machining at high depths, where machining is limited by leaking of the electrolyte at the machining zone and the difficulty in removing the machined material from it.

## 5.2 Machining at Low Depths

When machining a workpiece using electrochemical discharges at low depths, the electrolyte can reach the machining zone without difficulty. The electrochemical discharges take place almost similar to a case where no workpiece is present. As soon as the machining temperature is reached, material is removed by melting and/or chemical etching. For simplification, we consider that the limiting mechanism for machining is the heat propagation in the workpiece (i.e., material removal itself is very fast). Chemical contributions are discussed later in Section 5.4.

### 5.2.1 Thermal Model

A simplified model, where the heat brought to the substrate by the electrochemical discharges is approximated by a cylindrical uniform heat source of radius  $b$  and heat power  $P_0$  inside a homogenous material of density  $\rho$ , heat capacity  $c$  and thermal conductivity  $\lambda$ , is considered (Fig. 5.2). Similar models have been applied successfully in electrical discharge machining [39].

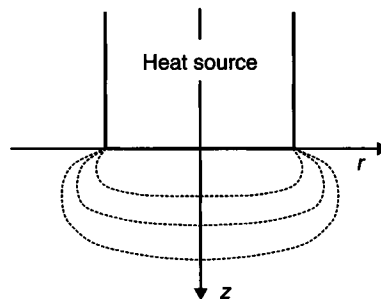


**Figure 5.2** Model of the temperature distribution for low-depth machining. A cylindrical homogenous heat source provides the heat power needed to locally heat up the workpiece.

The following boundary conditions are applied. At infinity, the temperature is assumed to be constant and equal to  $T_o$ . A second boundary condition is given by:

$$\lambda \frac{\partial T}{\partial z}(r, z=0, t) = \begin{cases} 0 & r > b, \\ -\frac{P_o}{\pi b^2} & r \leq b. \end{cases} \quad (5.2)$$

In the space outside the heat source, the temperature distribution  $T$  satisfies:

$$\frac{\rho c}{\lambda} \frac{\partial T}{\partial t} = \nabla^2 T. \quad (5.3)$$

The solution for this problem in cylindrical symmetry is well known. The temperature reached after a time  $t$  and at a distance  $z$  from the heat source (located on the symmetry axis of the cylinder) is given by [8]:

$$T(z, t) - T_o = \frac{2P_o \sqrt{at}}{\lambda \pi b^2} \left[ ierfc\left(\frac{z}{\sqrt{4at}}\right) - ierfc\left(\frac{\sqrt{z^2 + b^2}}{\sqrt{4at}}\right) \right], \quad (5.4)$$

where  $a = \lambda/\rho c$  is the thermal diffusivity of the workpiece and  $ierfc(x) = \frac{1}{\sqrt{\pi}} e^{-x^2} - x \cdot erfc(x)$ , where  $erfc(x)$  is the complementary error function.

The steady-state solution, reached at  $t \rightarrow \infty$ , is:

$$T_\infty(z) - T_o = \frac{P_o}{\lambda \pi b^2} (\sqrt{b^2 + z^2} - z). \quad (5.5)$$

The maximum temperature will be reached on the symmetry axis. Thus machining can take place only if the following condition is satisfied:

$$\lambda(T_M - T_o) \leq \frac{P_o}{\pi b}, \quad (5.6)$$

where  $T_M$  is the temperature needed for material removal to take place. This temperature is known as the *machining temperature*. The radius  $b$  of the heat source is similar to the tool radius if a uniform spark distribution is assumed.

Criterion (5.6) is only a rough estimation. On one hand, the hypothesis of cylindrical geometry is not necessarily satisfied (in particular the uniformity of the heat source) and, on the other hand, the various thermal properties of a material are not independent of the temperature. Besides these approximations, there is the major difficulty in defining the temperature  $T_M$  required for machining to take place. In particular, for amorphous materials, such as glass, this is not straightforward. An amorphous material shows no phase transition but rather its viscosity decreases progressively with increasing temperature (Fig. 5.3). Further, as discussed in Section 5.4, chemical etching also helps in machining.

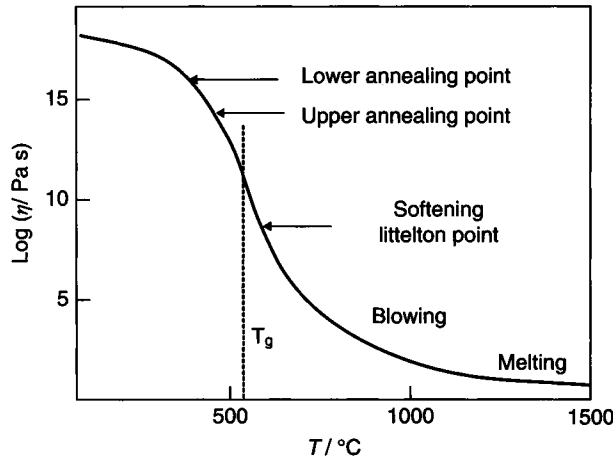


**Figure 5.3** Schematic representation of the viscosity of glass as a function of the temperature.

In order to estimate  $P_o$ , one has to first estimate the heat power  $P_E$  of the electrochemical discharges. Therefore, Equation (5.1) can be used. The inter-electrode resistance  $R$  can be evaluated by inspecting the slope of the mean  $I - U$  characteristics in the ohmic region (the linear part from 5–15 V of the mean  $I - U$  characteristics). Typical values for  $P_E$  are around a few watts (for machining voltages in the range of 30–40 V).

The heat power  $P_E$  will only partially be transferred to the machined substrate (i.e.,  $P_o = \varepsilon P_E$ ). The fraction  $\varepsilon$  of the heat flux transmitted to the substrate will depend on, besides the geometry of the problem, the ratio of the coefficients of thermal conductivity of the electrolyte (typically around  $0.6 \text{ W} \cdot \text{m}^{-1} \text{K}^{-1}$  for NaOH) and the substrate. Another important parameter is the heat conductivity of the tool-electrode. As the tool-electrode has the highest heat conductivity, most part of the heat is evacuated through it.

Consider the example of glass machining. In this case the thermal conductivity of the workpiece is slightly higher than that of the electrolyte. It is expected that a significant amount of the heat power will be transferred to the glass. Applying criterion (5.6) shows that, in the case of glass, machining can be achieved if  $P_o$  is around 0.5 W if  $T_M \cong 600^\circ\text{C}$  is assumed. A similar conclusion can be drawn for quartz, which, like glass, is reported in literature to be machinable quite easily by SACE. The material removal rate is higher for glass than for quartz under identical conditions [40]. For ceramic material, such as alumina, SACE machining is reported to be possible at high voltages (around 50 V and higher [104] compared with 20–30 V for glass and quartz). According to criterion (5.6), a mean power of about 35 W is needed to machine alumina. These values can be achieved in NaOH electrolytes using machining voltages higher than 50 V.

### 5.2.2 Material Removal Rate

The material removal rate is the amount of material removed in a certain amount of time. To discuss this quantity, the evolution of the isotherm  $T(z, t) = T_M$ , the solution of the heat equation (5.3) is analysed. For simplification, it is assumed that material removal is very fast and takes place as soon as the machining temperature is reached. This hypothesis is justified and discussed further in Section 5.4 and [65].

Equation (5.3) is written in dimensionless form, using the normalised temperature defined by:

$$\bar{T} = \frac{T - T_o}{P_o / (\lambda \pi b)}, \quad (5.7)$$

the normalised length  $\bar{z} = z/b$ , and the normalised time  $\bar{t} = t/\tau$  with the characteristic time:

$$\tau = \frac{b^2}{4a}. \quad (5.8)$$

Using these variables, the solution for (5.3) can be written as:

$$\bar{T}(\bar{z}, \bar{t}) = \sqrt{\bar{t}} \left[ \operatorname{ierfc} \left( \frac{\bar{z}}{\sqrt{\bar{t}}} \right) - \operatorname{ierfc} \left( \frac{\sqrt{\bar{z}^2 + 1}}{\sqrt{\bar{t}}} \right) \right]. \quad (5.9)$$

The evolution of  $z(t)$ , the distance reached by the isotherm  $T_M$ , is evaluated by solving (5.9) according to:

$$\bar{T}(\bar{z}, \bar{t}) = \frac{T_M - T_o}{P_o / (\lambda \pi b)} = \frac{1}{\kappa}. \quad (5.10)$$

The number  $\kappa$ , the normalized heat power, is the ratio of the applied heat power  $P_o$  and the minimal heat power  $P^{\min} = (T_M - T_o)\pi b$  required for machining according to Equation (5.6) (i.e.,  $P_o = \kappa P^{\min}$ ).

The time  $\bar{t}_o$  at which machining starts is given by the instant at which the temperature of the workpiece reaches the machining temperature  $T_M$ :

$$\bar{T}(0, \bar{t}_o) = \frac{1}{\kappa}, \quad (5.11)$$

or written explicitly:

$$\bar{T}(\bar{z} = 0, \bar{t}_o) = \sqrt{\bar{t}_o} \left[ \frac{1}{\sqrt{\pi}} - \frac{1}{\sqrt{\pi}} e^{-1/\bar{t}_o} + \frac{1}{\sqrt{\bar{t}_o}} \operatorname{erfc} \left( \frac{1}{\sqrt{\bar{t}_o}} \right) \right] = \frac{1}{\kappa}. \quad (5.12)$$

Under the assumption that material removal takes place as soon as the machining temperature  $T_M$  is reached, the material removal rate is given by the velocity at which the isotherm  $T(z, t) = T_M$  propagates through the workpiece. This velocity is the slope of the curve defined by  $\bar{T}(0, \bar{t}_o) = 1/\kappa$ . Applying the theorem of implicit functions to (5.12), one obtains:

$$\frac{d\bar{z}(\bar{t}_o)}{d\bar{t}} = \frac{1}{2\sqrt{\pi}} \frac{1 - e^{-1/\bar{t}_o}}{\sqrt{\bar{t}_o}}. \quad (5.13)$$

Together, Equations (5.12) and (5.13) give the material removal rate as shown in Fig. 5.4. The two limiting cases are interesting.

For large heat power ( $\kappa \gg 1$ ,  $\bar{t}_o \rightarrow 0$ ), the material removal rate (5.13) can be approximated by:

$$\frac{d\bar{z}(\kappa)}{d\bar{t}} \cong \frac{\kappa}{2\pi} \left(1 - e^{-\kappa^2/\pi}\right). \quad (5.14)$$

The time  $\bar{t}_o$  before machining starts is given by

$$\bar{t}_o \cong \frac{\pi}{\kappa^2}. \quad (5.15)$$

On the contrary, for small heat power ( $\kappa \approx 1$ ,  $\bar{t}_o \gg 1$ ), the material removal rate (5.13) can be approximated by:

$$\frac{d\bar{z}(\kappa)}{d\bar{t}} \cong \frac{\kappa - 1}{2\kappa} \left[1 - \exp\left(-\frac{\pi(\kappa - 1)^2}{\kappa^2}\right)\right], \quad (5.16)$$

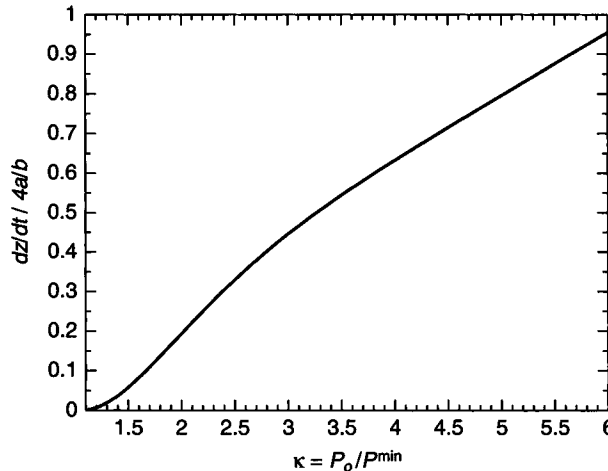


**Figure 5.4** Machining speed  $dz/dt$  as a function of the normalised heat power  $\kappa$ .

and the time  $\bar{t}_o$  before machining starts is given by

$$\bar{t}_o \cong \frac{1}{\pi} \left( \frac{\kappa}{\kappa - 1} \right)^2. \quad (5.17)$$

For practical applications, one should be able to estimate the normalised heat power  $\kappa$  as a function of the machining voltage. A qualitative estimation can be obtained if it is assumed that each discharge transfers a similar heat quantity  $q_E$  to the workpiece. The heat power  $P_o$  can be related to the mean number of discharges using Equation (4.38):

$$P_o = \frac{d}{dt} [\langle N(t) \rangle \cdot q_E] = \lambda_d A q_E, \quad (5.18)$$

where  $A$  is the surface at which the discharges take place. In general the discharges take place on the lateral tool-electrode surface (i.e.,  $A \sim b \cdot h_d$ , where  $h_d$  is the height over which the discharges are observed). It follows that:

$$\kappa = \frac{\lambda_d \pi b h_d q_E}{\lambda \pi b (T_M - T_o)} = \lambda_d \cdot \frac{h_d q_E}{\lambda (T_M - T_o)}. \quad (5.19)$$

Even this calculation is only a rough estimation; it shows that  $\kappa$  is proportional to the mean number of discharges per time  $\lambda_d$ , which is itself a function of the terminal voltage  $U$  as described in Section 4.3.

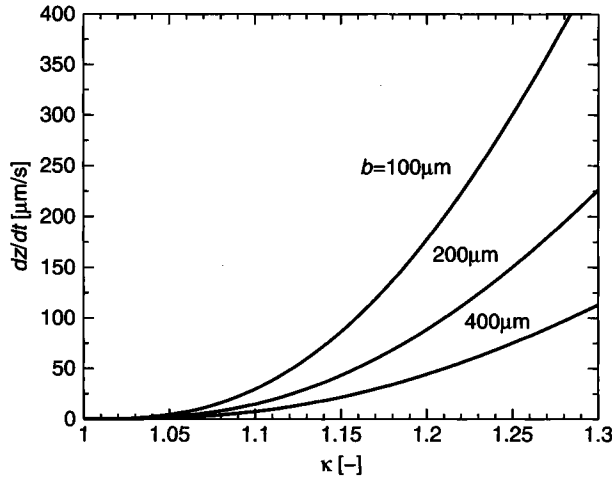
### 5.2.3 Application to Glass Micromachining

According to criterion (5.6), glass micromachining requires only low heat power (below 1 W), and approximation (5.16) can be used to describe the machining speed. Written in the form of non-normalised variables:

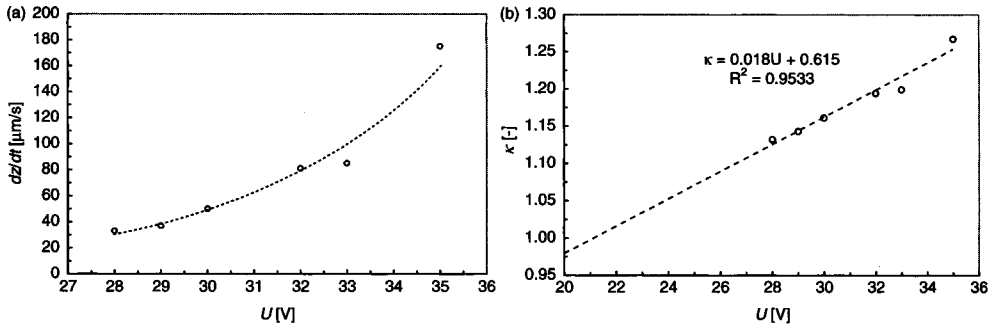
$$\frac{dz(\kappa)}{dt} = \frac{4a}{b} \frac{\kappa - 1}{2\kappa} \left[ 1 - \exp \left( - \frac{\pi(\kappa - 1)^2}{\kappa^2} \right) \right]. \quad (5.20)$$

Figure 5.5 shows the expected material removal rate as a function of the normalised heat power  $\kappa$  for various tool-electrode radii  $b$ . In order to determine the relation between  $\kappa$  and the machining voltage  $U$ , one has to compare these results with experimental data.

Figure 5.6a shows experimentally measured drilling speeds in glass with a 0.4 mm stainless steel tool-cathode. The electrolyte used was 30 wt% NaOH. By comparing the measured drilling speeds with that computed using Equation (5.20), it is possible to determine the dependence of the normalised heat power



**Figure 5.5** Machining speed  $dz/dt$  as a function of the normalised heat power  $\kappa$  for glass at various tool-electrode radii  $b$  as predicted by (5.20).



**Figure 5.6** (a) Experimental glass machining speed  $dz/dt$  for a 0.4 mm stainless steel tool-electrode as a function of the machining voltage  $U$ . (b) Normalised heat power  $\kappa$  as a function of the machining voltage  $U$  [65].

$\kappa$  on the machining voltage  $U$  (Fig. 5.6b). The data can be approximated by a linear dependence in the voltage range considered. As predicted by Equation (5.19), this dependence follows that from the mean number of discharges per time (compare with Fig. 4.15). In particular, note that when approaching the critical voltage (about 20 V),  $\kappa \cong 1$  as in this case almost no discharges happen and therefore the heat power generated is very low.

When using an active anode, the discharge activity is lower, but very different shapes and surface roughness and sometime higher material removal rates are observed in the case of glass and quartz machining [21,63,120]. This is due to the different discharge mechanisms. In the case of an active anode, the Hickling and Ingram mechanism generates electrochemical discharges (Section 2.5). A large number of OH radicals are generated which, in the case of glass and quartz, etches the workpiece. In Section 5.4 this aspect is discussed in more detail.

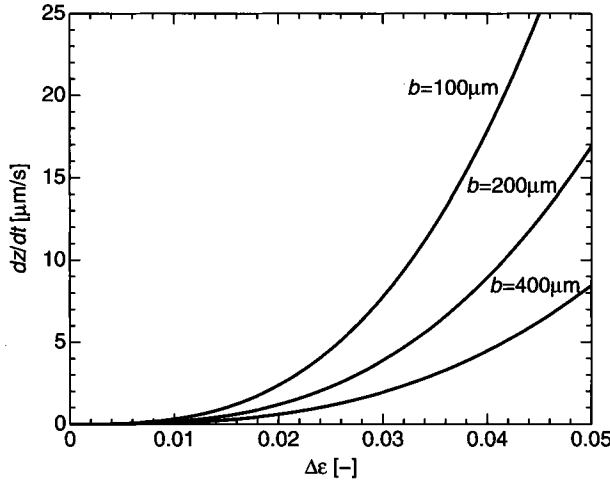


**Figure 5.7** Machining speed  $dz/dt$  as a function of the excess heat power  $\Delta\epsilon$  for alumina at various tool-electrode radii  $b$  as predicted by Equation (5.21).

### 5.2.4 Application to Ceramic Micromachining

If ceramic micromachining is considered, much higher energies are needed. According to criterion (5.6), typically about 35 W is needed in the case of alumina. Although these energies may be achieved with high voltage (typically about 50 V), it will not be possible to obtain high values of  $\kappa$ . Actually,  $\kappa$  will be nearly equal to one. In this case, Equation (5.20) can be further approximated to:

$$\frac{dz(\kappa)}{dt} = \frac{2a}{b}\pi(\kappa-1)^3 = \frac{2a}{b}\pi(\Delta\epsilon)^3, \quad (5.21)$$

where  $\Delta\epsilon$  is the fraction of excess energy that is applied compared with the minimal heat power  $P^{\min}$  needed for machining to take place.

In the case of alumina ( $a \cong 5 \cdot 10^6 \text{ m}^2/\text{s}$ ), if an excess energy  $\Delta\epsilon$  of a few percent is assumed, a drilling speed of a few micrometers per second can be expected (Fig. 5.7), which is what is actually observed experimentally [19,97,106].

## 5.3 Machining at High Depths

When machining at high depths the electrolyte cannot reach the machining zone as easily as in the case of low depths. As a consequence, material removal by chemical etching or melting of the workpiece is lowered. The process is mostly limited by the ability to bring the electrolyte to the machining zone and to remove the machined material out of this zone, both of which are highly geometry dependent aspects.



As presented in next chapter, machining at high depths results in significantly lower material removal rates than at low depths. It is therefore justified to consider steady-state temperature distributions in order to get a first understanding of the process.

As an example, the drilling of glass at high depths is discussed. The geometry is depicted in Fig. 5.1. In order to obtain a first estimation of the temperature distribution, one solves the steady heat equation:

$$\nabla^2 T = 0. \quad (5.22)$$

Figure 5.8 shows the numerical solution for this equation (see [88] for details of the various boundary conditions). The electrochemical discharges are modelled as a uniformly distributed heat source at the bottom surface of the cylindrical tool-electrode and the gas film, with a heat flux  $\phi$  given by:

$$\phi = \frac{P_E}{A_e + A_g}, \quad (5.23)$$

where  $P_E$  is the electric power,  $A_e$  is the cross-sectional area of the cylindrical tool-electrode, and  $A_g$  is the cross-sectional area of the gas film around the

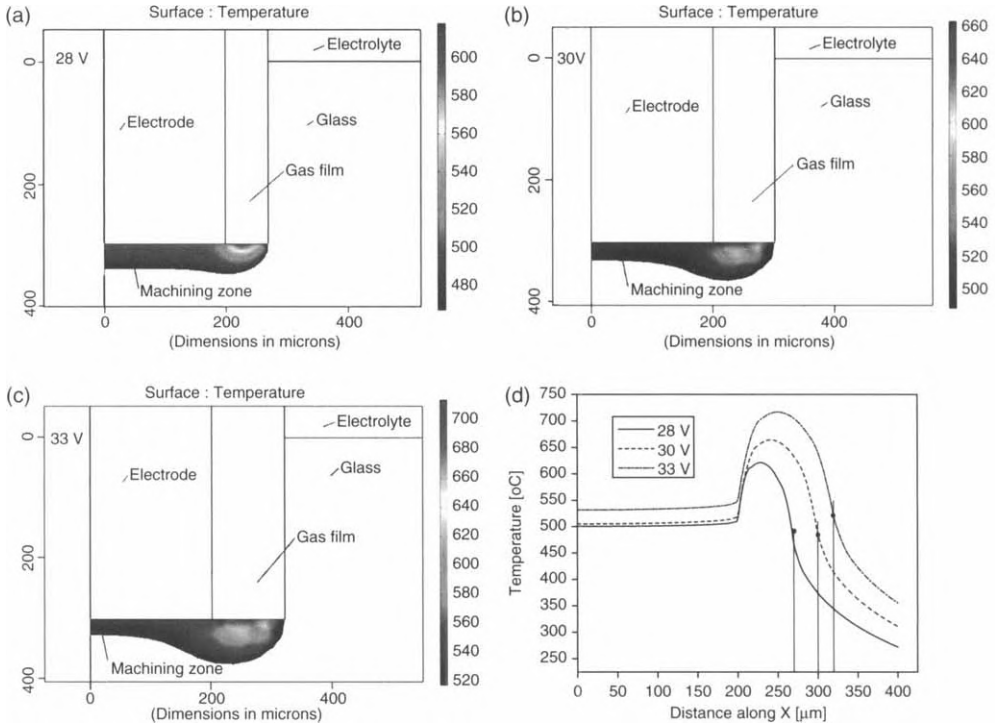


**Figure 5.8** Temperature distribution at high-depth machining for three different machining voltages according to the model of Mishra et al. [88].

cylindrical tool-electrode. The electric heat power was estimated using Equation (5.1). The cylindrical tool-electrode of 400  $\mu\text{m}$  diameter and 50 mm length is located at a depth of 300  $\mu\text{m}$  inside the glass workpiece. The model takes into account the heat conductivities of the workpiece, the tool-electrode, and the gas film. As the calculations confirm, a significant amount of heat supplied by the electrochemical discharges is removed through the tool-electrode. The gas film (modelled as a mixture of hydrogen and steam) appears to have a central role in helping to focus the heat in the region of the tool tip.

The diameters of the microholes were chosen according to experimentally known over-cut (see Section 6.2.6). For simplification, it was further assumed that the lateral space between the tool-electrode and the glass is filled with the gas film.

Figure 5.8d shows the radial temperature distribution at the drilling depth of 300  $\mu\text{m}$ . The tool reaches a temperature of around 500°C, as measured experimentally by Kellog [70] and Basak and Ghosh [6,7]. The marked points are the microhole diameters. The temperature at the border of the microhole is the machining temperature. It is remarkable that for all simulated voltages, the machining temperature  $T_M$  is found to be similar (around 500–600°C).

This indicates that the thermal mechanism is not the only material removal mechanism in glass machining by SACE, even at higher depths, as the temperature at the bottom surface of the electrode might not be sufficient to cause melting. The machining is probably aided by the chemical etching of glass caused by the small amount of electrolyte that manages to reach the machining zone.

From Fig. 5.8d one can observe that the temperature of the workpiece at the bottom of the tool-electrode is lower than that at the edges, near the gas film (the difference is more than 100°C). Figure 5.8a–c gives a clear picture of the machining zone. The depth of the machining zone is higher near the edge of the tool-electrode than under the electrode.

The heat at the edge of the tool-electrode, near the gas film, melts the glass workpiece and forms a crater. The molten electrolyte that is present at such high drilling depths reaches that zone and chemical reactions occur. The electrolyte etches away the viscous glass material. Material removal proceeds towards the area below the tool-electrode with the electrolyte permeating to the region removed previously. As the material under it gets removed, the tool-electrode can progress deeper into the workpiece. Note that the contact force between the tool-electrode and the workpiece will be the drag force due to the penetration of the tool inside the viscous zone in front of the tool tip.

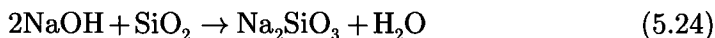
The shapes depicted in Fig. 5.8a–c are typical for microholes obtained by drilling at high depth or, more generally, when melting is the dominant mechanism for material removal. These effects are not restricted to glass but are also observed in other materials such as ceramics [104].

## 5.4 Chemical Contributions

Since the first investigations on micromachining with electrochemical discharges, the effects of the electrolyte on machining performances were investigated. A pioneering study about the influence of several parameters, such as electrolyte properties, machining voltage, and others, on the material removal rate was reported by Cook et al. [21]. In particular, the authors described how the material removal rate increases with the machining voltage, the electrolyte temperature, and the electrolyte concentration.

The effect of an electrolyte on machining is complex and cannot be described only as a function of concentration and temperature. The nature of the electrolyte strongly influences the machining behaviour. NaOH seems to have the most interesting properties compared with other electrolytes (KOH, NaCl, NaNO<sub>3</sub>, NaF, HCl, and H<sub>2</sub>SO<sub>4</sub>), in particular for glass and quartz [21,76,132] and also for ceramics such as alumina [106]. In general, acid electrolytes result in very poor material removal rates compared with alkaline ones [132]. The surface roughness of the machined workpiece is influenced by the electrolyte. In particular, molten salt electrolytes (e.g., a eutectic of NaOH and KOH melting at 170°C) can drastically improve the smoothness of the machined surface [21].

In the case of glass machining using sodium hydroxide, the workpiece is probably etched by complexation of silicate [2,31,32,34,104,132]:



The sodium silicate formed is removed by the electrolyte. This chemical reaction is strongly enhanced by increasing the temperature [32,132]. Similar results are reported for ceramic materials [104]. In the case of quartz machining, a similar process was suggested by Jain and Adhikary [63] who also showed the presence of sodium silicate in the electrolyte after machining. Yang et al. [132] defined the process as a high-temperature etching and conducted several experiments in order to elucidate the chemical etching effects. By visually comparing the surface quality obtained at high-temperature etching of glass with NaOH, electrical discharge machining of indium-tin oxide (ITO, an electrically conducting glass), and glass machining by electrochemical discharges, they concluded that SACE is mostly like to be a combination of thermal melting and chemical etching.

Energy dispersive X-ray (EDX) analysis of the machined structures for sodalime glass confirms that Na<sup>+</sup> concentration decreases whereas H<sup>+</sup> concentration increases in the machining area [32], and suggests that besides etching, leaching occurs during the SACE process. Local surface modification may also occur depending on the electrolyte used. Basak [6] suggested that in the case of KOH, the larger K<sup>+</sup> ions from the electrolyte replace Na<sup>+</sup> ions of the glass surface and decreases its strength. This effect may explain why higher material removal rates are observed for KOH compared with NaOH for the same concentrations and machining voltages [132].

The polarity of the tool-electrode also influences greatly the machining process [21,63,120]. As shown first by West and Jadhav [120], using an active anode as the tool-electrode during drilling, the shape of the drilled hole is more spherical than that obtained by cathodic machining. Although the exact mechanism has not yet been elucidated, a possible explanation could be as follows. When using an active anode, the Hickling-Ingram mechanism is responsible for the discharge activity (Section 2.5). In this mechanism, water inside the gas film is dissociated and as a result a large number of OH radicals are formed inside the gas film. Therefore, the concentration of OH radicals, as a function of the hole depth  $z$ , is more or less uniform. The workpiece is etched isotropically resulting in a spherical shape (Fig. 5.9). This is not the case when using an active cathode as the tool-electrode. In this case, only OH radicals from the electrolyte (NaOH) are present. During drilling, electrolyte is mostly present at the top of the hole. The concentration of OH radicals decreases with  $z$ , resulting in a larger entrance diameter. This mechanism will result in a conical hole shape.

As more OH radicals are present in the case of an active anode than for an active cathode, chemical etching is also more important. Consequently, the surfaces are smoother than those obtained by cathodic machining [63,120]. However, when using anodic polarisation, the tool-electrode will be anodically dissolved resulting in high tool wear.

Recently, Didar et al. [24] showed that micromachining with electrochemical discharges changes the glass surface locally. Using nanoindentation tests, the authors showed that the hardness and density of glass increases. This effect is attributed to the rapid cooling that takes place right after machining (during machining the workpiece temperature is at least 500°C). While the tool-electrode moves further, the workpiece is in contact with the electrolyte which

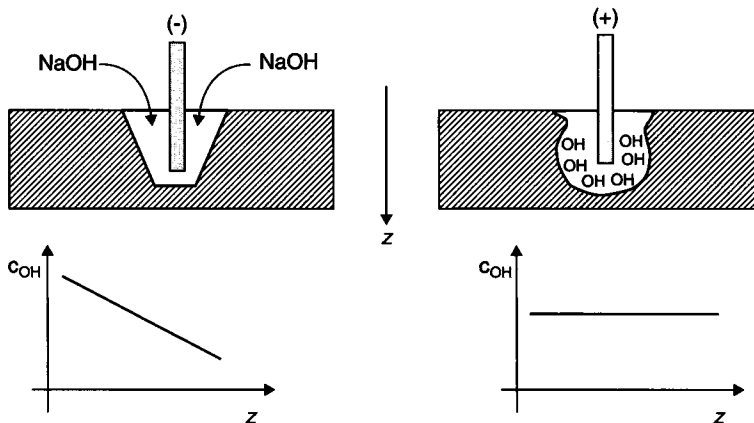


**Figure 5.9** Comparison of machining with an active cathode and an active anode. In the case of an active cathode, the concentration of OH radicals decreases with the hole depth resulting in a conical shape, whereas in the case of an active anode, the Hickling-Ingram mechanism will produce an uniform OH concentration along the hole resulting in a spherical shape.

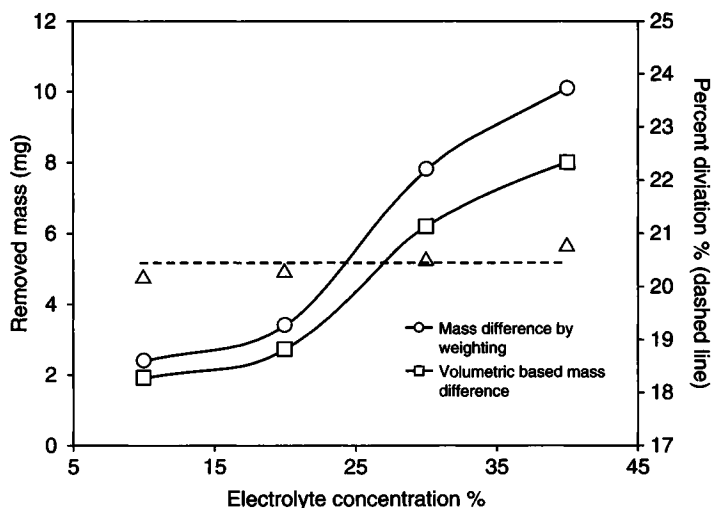


**Figure 5.10** Comparison of material removed by machining evaluated by weighting the sample and based on the removed volume as a function of various electrolyte concentrations. Reprinted from [24] with permission from Elsevier.

is, at maximum, at a temperature of about 80–90°C. The increase in glass density after machining is also confirmed by comparing the amount of material removed, computed based on workpiece weighting, and the volume of material removed. Microchannels machined using different electrolyte concentrations were analysed. The removed mass was calculated based on the geometry of the microchannels and from the change in mass of the machined samples assuming constant glass density before and after machining. As shown in Fig. 5.10, the measured removed mass, by weighting, is higher than the computed removed mass, based on the geometry of the microchannels. This difference can be explained by the change in glass density during the machining process. Note that for all electrolyte concentrations a difference of about 20% is obtained.

## 5.5 Summary

Machining using electrochemical discharges is a complex process. Material removal is achieved by following steps. First, the workpiece is heated up locally by the electrochemical discharges. The water in the electrolytic solution is evaporated locally leaving only molten salt in the vicinity of the tool-electrode. High-temperature etching of the softened workpiece takes place. The chemical etching process needs the presence of OH radicals. The hydrodynamics around the tool-electrode, which is highly influenced by the discharge activity, the gas film, and the geometry of the machined shape, will affect the etching kinetics.

Figure 5.11 summarises the effects of the main parameters, as discussed in this chapter, on the material removal rate when machining with electrochemical discharges.

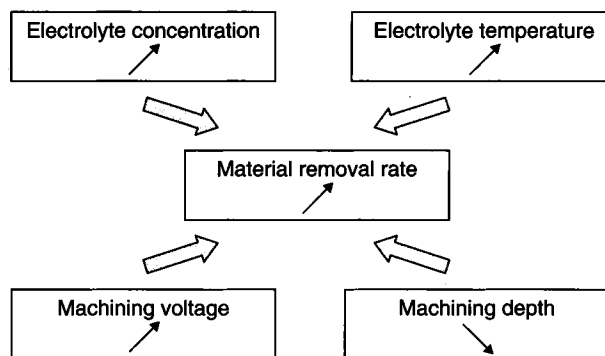


**Figure 5.11** Overview of the influence of the main parameters on the material removal rate when machining with electrochemical discharges.

## 6 Common Machining Strategies

---

Spark-assisted chemical engraving (SACE) was first developed for glass microdrilling. Today, it is the most advanced application and this chapter is essentially dedicated to discussing glass microdrilling using the SACE technique. SACE is also applied to materials other than glass, but compared with glass micromachining, very little is known.

### 6.1 General Overview

During SACE, the heat source produced by the electrochemical discharges has to be in close vicinity to the workpiece. Typically, a distance of a maximum of 25  $\mu\text{m}$  from the workpiece is required in the case of glass [31]. To achieve this goal, several basic feeding mechanisms of the tool-electrode can be applied.

The simplest feeding mechanism is the *gravity-feed* mechanism. In this case, a constant force is applied to the tool-electrode in order to guarantee mechanical contact with the workpiece. The second option is to move the tool-electrode at a speed lower than the mean material removal rate. The third option is to control the tool feed as a function of the status of the actual machining process. Although this last strategy is highly desirable, it has never been achieved to date. Preliminary, very promising results were published by Morrison et al. [140] recently.

As discussed in this chapter, the first two feeding mechanisms, gravity-feed and *constant velocity feed*, can give excellent results although they are actually open-loop strategies. Gravity-feed is a very popular strategy for drilling because of its simplicity and a few other advantages that are discussed in Section 6.2. For 2D machining, constant velocity feed is the most popular strategy.

The tool feeding mechanism during machining is actually only one of the elements affecting machining. The material removal rate and surface quality are also influenced by the locally generated heat power and the local electrolyte concentration. Both are more or less directly controlled by the gas film, and more particularly the discharge activity inside the gas film. The terminal voltage controls the discharge activity. Its value has to be adjusted depending on the desired machining performances and the workpiece. Typical values for glass are around 30 V, and for ceramics and composite materials higher values of about 50–80 V are generally needed.

An important issue is the stability of the heat source during the machining process. As this cannot generally be achieved, two alternative strategies are used. The first option is to machine at as low power as possible. In this case, an

unstable discharge activity will not affect the machining too dramatically. As expected, the main drawback is the reduced material removal rate. In the second case, one tries to take control of the gas film. As the stability of the gas film cannot be controlled directly over a long period of time, one chooses to build and destroy the gas film periodically in a controlled manner. This can be achieved by using a pulsed voltage supply or by adding an external inductive circuit to the power supply, as done for the Wehnelt current interrupter in the last century. Similar to the first strategy, the main drawback is the reduced material removal rate. However, both strategies result in higher machining quality and higher reproducibility of the machining.

Finally, tool-electrodes in the form of both rods and wires can be used. The utilisation of a wire as a tool-electrode is discussed at the end of the chapter. In this situation, as the special geometry of the process provides additional possibilities for observations, it is possible to control the feeding mechanism of the electrode as a function of the gap between the wire and the workpiece.

## 6.2 Gravity-Feed Drilling

In gravity-feed drilling a constant force is applied on the tool-electrode in order to ensure close contact between the heat source (the electrochemical discharges in the gas film) and the workpiece. Although this method is particularly simple and gives excellent results, the major drawback is the mechanical contact between the tool and the workpiece.

The principle is explained in Fig. 6.1. The tool-electrode is guided vertically and a force is acting on it in the drilling direction. The practical implementation of such a set-up is discussed later in Section 8.2. One important aspect is to reduce, as much as possible, the frictional forces that arise during the vertical guidance of the tool-electrode.

During gravity-feed drilling as the tool-electrode is constantly in contact with the workpiece, drilling can be followed by a measurement of the progress

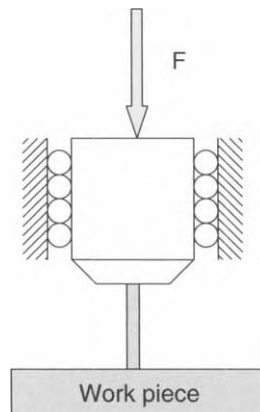


**Figure 6.1** Principle of SACE gravity-feed drilling.



of the tool-electrode. The wear of the tool-electrode will affect this measure. However, the wear of SACE tool-electrodes is generally quite low. According to Kurafuji and Suda [76], who measured the wear for various materials, for a drilling time of 3 minutes, the tool-electrode wear remains in the range of a maximum of 20  $\mu\text{m}$ , but is mostly in the range of a few micrometres only (Table 6.1).

Typical examples for glass drilling as a function of various machining voltages are shown in Fig. 6.2. Drilling was done with a 0.4 mm cylindrical stainless steel cathode in 30 wt% NaOH [131]. After a first phase, where the drilling speed is fast, a progressive slow down of the material removal rate is observed

**Table 6.1 Tool-Electrode Wear for Gravity-Feed Drilling [76]**  
(Drilling Time is 3 min)

| Electrode Material | Voltage (V) | Current (A) | Wear ( $\mu\text{m}$ ) |
|--------------------|-------------|-------------|------------------------|
| Cu                 | 34          | 0.15        | 18                     |
| Brass              | 33          | 0.15        | 22                     |
| Steel              | 36          | 0.17        | 7                      |
| Fe-Cr              | 36          | 0.16        | 3                      |
| Ni-Ag              | 37          | 0.12        | 14                     |
| Ni-Cr              | 37          | 0.16        | 3                      |
| Ni                 | 36          | 0.15        | 6                      |
| W                  | 35          | 0.17        | 7                      |
| Pt-Ir              | 35          | 0.16        | 2                      |

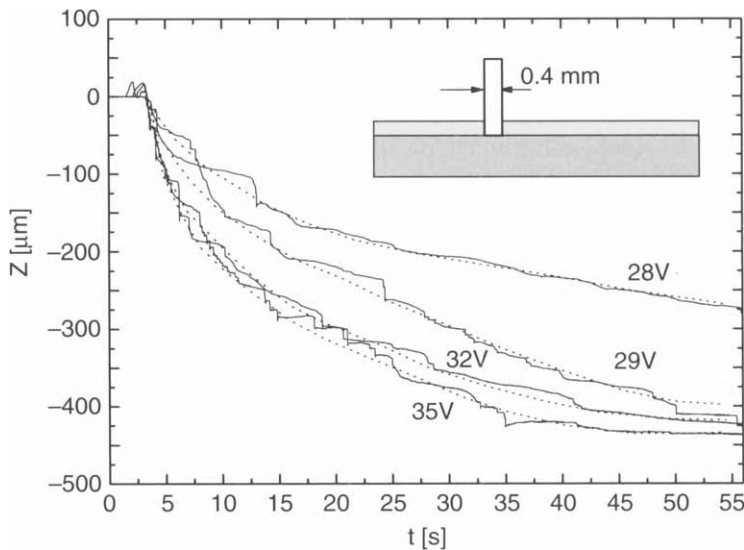


**Figure 6.2** Typical evolution at various voltages of SACE glass gravity-feed drilling using a cylindrical tool (cathode) of 0.4 mm diameter with a force of 0.8 N acting on it. The electrolyte (30 wt% NaOH) level above the workpiece is about 1 mm. Reprinted from [131] with the permission of the *Journal of Micromechanics and Microengineering*.

until a *limiting drilling speed*  $v_{lim}$  almost independent of the machining voltage is reached. The first fast regime is termed the *discharge regime* (as the discharge activity controls the drilling speed) and the second regime, where the limiting speed is reached, is called the *hydrodynamic regime* (as the ability of the electrolyte to reach the machining zone limits the drilling) [131]. Also note the staircase-like evolution.

As glass drilling by gravity-feed is the most studied mechanism to date, this technique is discussed in detail in the remainder of this section.

A simple model for the evolution of the drilling depth  $z(t)$  in glass gravity-feed drilling can be given. Due to the progressive transition from the discharge regime to the hydrodynamic regime, the drilling speed  $v(z)$  decreases with depth  $z$ . If a constant rate with characteristic length  $\delta$  is assumed, one can write [65]:

$$\frac{dv(z)}{dz} = -\frac{1}{\delta}(v(z) - v_{lim}). \quad (6.1)$$

As  $\dot{z} = v(t)$  and using the initial conditions  $z(0) = 0$  and  $v(0) = v_o$ , one obtains the solution of Equation (6.1) as:

$$z(t) = \delta \cdot \ln \left[ \frac{v_o}{v_{lim}} e^{\frac{v_{lim}}{\delta} t} - \frac{v_o - v_{lim}}{v_{lim}} \right]. \quad (6.2)$$

Note that for  $t \rightarrow \infty$  one gets

$$z(t) \rightarrow v_{lim} t + \delta \ln \left( \frac{v_o}{v_{lim}} \right). \quad (6.3)$$

The initial speed  $v_o$  can be computed as described in Section 5.2. By fitting Equation (6.2) to experimental evolutions, the remaining parameters  $v_{lim}$  and  $\delta$  can be determined. Typical values for glass machining with a cylindrical 0.4 mm stainless steel cathode are about 1.5  $\mu\text{m/s}$  for  $v_{lim}$  and about 70–80  $\mu\text{m}$  for  $\delta$  [65].

For very high depths (more than a few millimetres), the limiting speed  $v_{lim}$  vanishes and the model (6.2) is no longer valid. Drilling reaches a limiting depth which becomes a function of the machining voltage [21].

For ceramic drilling the situation is different. The material removal rate is very low. No clear difference between the discharge and the hydrodynamic regimes can be observed. This is probably due to the fact that the isotherm of the machining temperature  $T_M$  progresses very slowly (compare with Fig. 5.7). Therefore, the progress of heat inside the workpiece is the main limiting factor for ceramic drilling.

### 6.2.1 Discharge Regime

The discharge regime in glass gravity-feed drilling is characterised by a high drilling speed of typically 100  $\mu\text{m/s}$  [131]. It takes place in the first 100–200  $\mu\text{m}$ .

The drilling speed is controlled by the discharge activity and is directly related to the machining voltage (Fig. 5.6). Machining takes place by softening of the glass followed by material removal through chemical etching of the workpiece by the hot electrolyte in the form of a molten salt. The drilling speed is limited by the propagation of heat inside the workpiece and can be estimated using Equation (5.22) as explained in Section 5.2.3.

### 6.2.2 Hydrodynamic Regime

As drilling progresses deeper, the limiting factor in the material removal rate is no longer the heat propagation in the workpiece, but the ability of the electrolyte to reach the machining zone and the ability to remove the machined material [131]. A zone of softened glass forms at the tip of the tool-electrode. The tool is pushed by the force applied during gravity-feed drilling inside this viscous region. The drilling speed  $v_{lim}$  is limited by the drag force exerted on the tool:

$$v_{lim} = \frac{F}{d(\eta)}, \quad (6.4)$$

where  $F$  is the force exerted on the tool by gravity-feed drilling and  $d(\eta)$  is the drag coefficient, which is a function of the tool-electrode geometry and the viscosity of the material in the machining zone. Note that  $\eta$  is a function of the temperature in the machining zone. Typical values for the limiting speed are a few micrometres per second. The drilling speed is almost independent of the machining voltage, as even a quite large change in the temperature of the machining zone will result only in a small change of the glass viscosity (Fig. 5.3).

From the experimentally determined limiting speed, in the case of soda lime glass, and Equation (6.4), the mean viscosity  $\eta$  of the material in the machining zone can be estimated [65]. Typical values are  $1.4 \cdot 10^8$  Pa s. This viscosity corresponds to a temperature of around 600°C for glass, similar to the *glass transition temperature*. However, it is less than the *softening Littleton point* (720°C). Recall that the softening Littleton point corresponds to the temperature at which a rod of glass increases its length by 1 mm/min under its own weight. Note that glass is typically blown at the *working point* when  $\eta = 10^3$  Pa s. It is difficult to explain how the material could be removed under such conditions without the use of chemical etching. As the chemical etching of the substrate is the main mechanism for material removal in glass micromachining by electrochemical discharges, the leak of the electrolyte at the machining zone limits not only the discharge activity, but also essentially the material removal. As a consequence, the material inside the machining zone is removed only slowly from the top of this zone where a small electrolyte–workpiece interface exists.

As discussed below, the hydrodynamic regime is responsible for the increase in the machining over-cut and for the formation of heat affected zones around the microhole. This is an undesired effect and one should try to avoid machining in this situation. Strategies to reduce this regime are presented in Chapter 7.

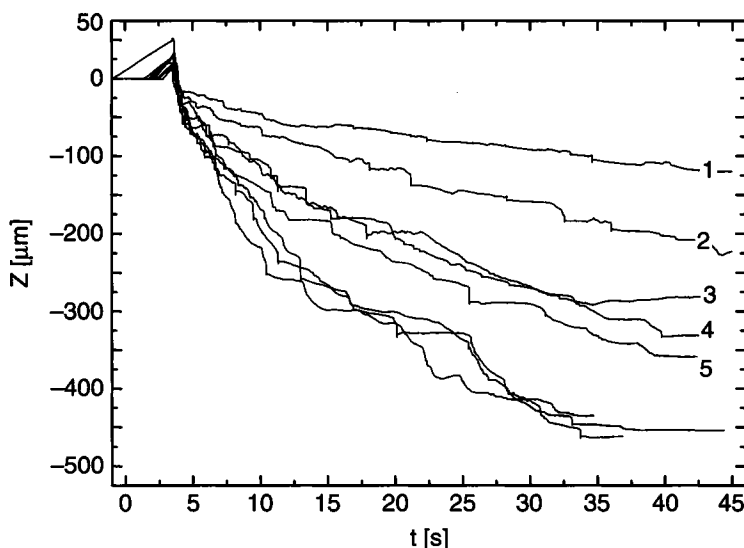


**Figure 6.3** Several consecutive glass gravity-feed drillings at 29 V with a cylindrical stainless steel tool-cathode of 0.4 mm diameter. The applied force was 0.8 N. After five successively drilled holes, the evolutions become similar. Reprinted from [131] with the permission of the *Journal of Micromechanics and Microengineering*.

### 6.2.3 Repeatability of Drilling

Gravity-feed drilling is quite a reproducible process, although it is an open-loop machining process. Precise quantitative values are not available to date. However, it is known that it generally takes a few first drillings before the process becomes reproducible. This is illustrated in Fig. 6.3. Consecutive drilling at 29 V in glass with a cylindrical stainless steel tool-cathode of 0.4 mm diameter is shown [131]. Note how, after about five drilled holes, the evolutions become more and more similar finally reaching a steady-state situation. In the following sections only the results obtained in this steady-state situation are discussed. This effect is due to the time needed for the various local parameters (local temperature and electrolyte concentration distribution) to reach their stationary value. A preheated electrolyte can be used to diminish this effect.

### 6.2.4 Drilling Time

The drilling time in gravity-feed machining is mainly determined by the drilling depth of the hole and the machining voltage, as shown in Fig. 6.4 for the case of a 0.4 mm cylindrical stainless steel tool-cathode in 30 wt% NaOH [84]. Other parameters such as inter-electrode resistance, tool-electrode shape, and tool-electrode material also influence the drilling time, as discussed below. Another important factor is the electrolyte bulk composition and temperature, as this affects the chemical contribution to the material removal rate. In general, higher electrolyte concentration and higher bulk temperature result in lower

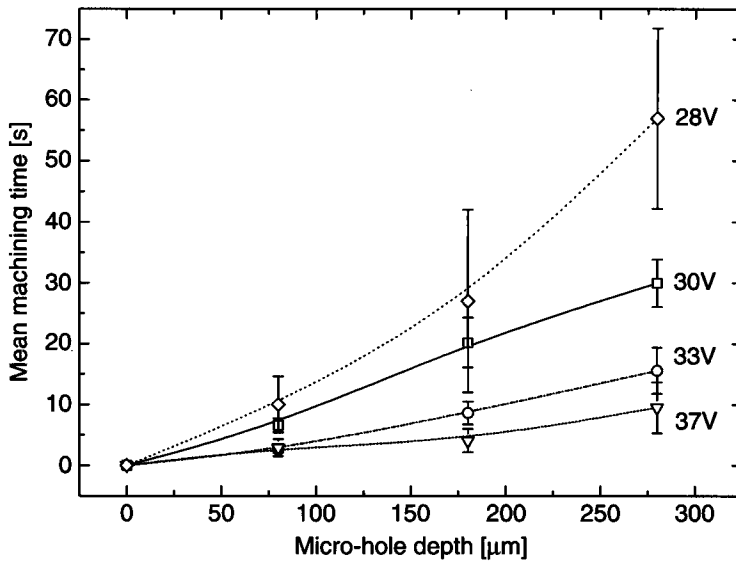


**Figure 6.4** The drilling time in SACE glass gravity-feed drilling for a 0.4 mm cylindrical stainless steel tool-cathode in 30 wt% NaOH. Reprinted from [84] with the permission of the *Journal of Micromechanics and Microengineering*.

drilling times. The utilisation of alkaline electrolytes results in faster drilling times than in the case of acids [132]. It was also observed that KOH results in faster drilling than NaOH for the same concentration and machining voltage [132]. This may be attributed to the fact that the  $K^+$  ion has a higher mobility than the  $Na^+$  ion. Consequently, the inter-electrode resistance is lower for KOH compared with NaOH, resulting in higher discharge activity. Another effect may arise from the chemical attack mechanism of glass, which differs for NaOH and KOH (see Section 5.4).

The typical drilling times for glass are a few seconds for microholes of about 200–300  $\mu m$ . For deeper holes, the machining switches to the hydrodynamic regime and the drilling times increase significantly. For ceramics (e.g., alumina) the drilling times are significantly higher (typically a few minutes for 100  $\mu m$  [19,97,106]).

The fluctuation in the drilling time increases with the machining voltage. Due to these large fluctuations, the drilling time cannot be used as a control parameter for the drilling depth.

### 6.2.5 Influence of the Inter-electrode Resistance

Depending on the inter-electrode resistance, the gas film formation may be fast (a few milliseconds) if formed electrochemically (Section 4.1.2) and/or by joule heating (Section 4.1.1), or the gas film formation may be slow (a few seconds) in the case of a hybrid process (Section 4.1.3). As the gas film is unstable (i.e., the gas film often collapses and has to be built up again), the gas film formation time is an important parameter for the mean machining speed of SACE.

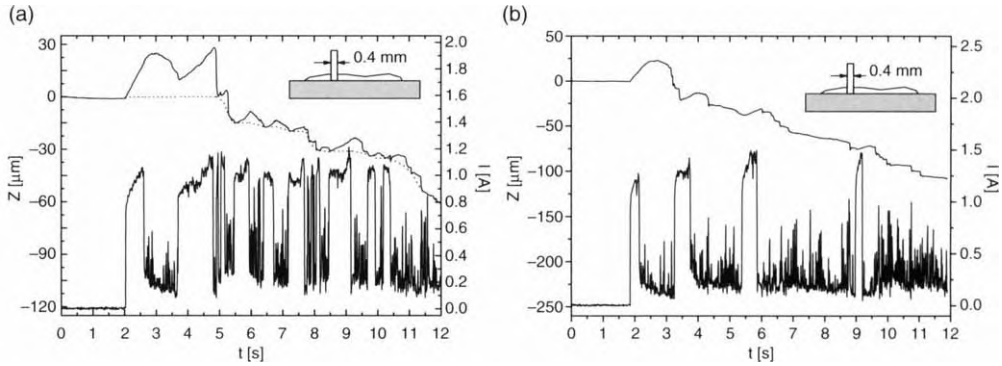


**Figure 6.5** Example of SACE glass gravity-feed drilling with a 0.4 mm stainless steel tool-cathode at 31 V in the case of high inter-electrode resistance. In situation (a) the gas film needs to be built up more often than in situation (b). This results in an overall slower machining for situation (a) than situation (b). Reprinted from [130] with the permission of the *Journal of Micromechanics and Microengineering*.

Figure 6.5 shows an example of SACE glass gravity-feed drilling with a 0.4 mm stainless steel tool-cathode at 31 V in the case of high inter-electrode resistance [130]. The high inter-electrode resistance is obtained by depositing a drop of electrolyte (30 wt% NaOH) on the workpiece surface just large enough to wet the surface. In this case the gas film is formed by a hybrid mechanism and needs about one second for its formation. This formation time becomes a significant limitation of the drilling speed as can be seen by comparing situation (a) where the gas film needs to be built up more often than in situation (b). This results in an overall slower machining for situation (a) than situation (b).

The inter-electrode resistance  $R$  also affects the quantity of heat available for machining at a given voltage, according to Equation (5.1), as  $P_E = UI - RI^2$ . The higher the inter-electrode resistance, greater will be the energy used for joule heating of the electrolyte.

The decrease in the material removal rate with decreasing inter-electrode resistance is not specific to glass drilling. The same effect was also observed in  $\text{Si}_3\text{N}_4$  drilling [97].

### 6.2.6 Microhole Dimensions

The dimensions of the drilled holes are a function of the machining voltage and the drilling depth. Figure 6.6 shows, as a function of the machining voltage and the drilling depth, the mean entrance diameter of microholes machined in glass with a 0.4 mm cylindrical stainless cathode tool-electrode [84]. Three zones can be distinguished. For depths up to 100  $\mu\text{m}$  the mean hole diameter is independent of the machining voltage (zone A). In this configuration drilling takes place only in the discharge regime. An increase in the voltage results in faster drilling but does not affect the mean diameter. The entrance holes are well defined cylindrical contours with a smooth surface. For deeper microholes, the

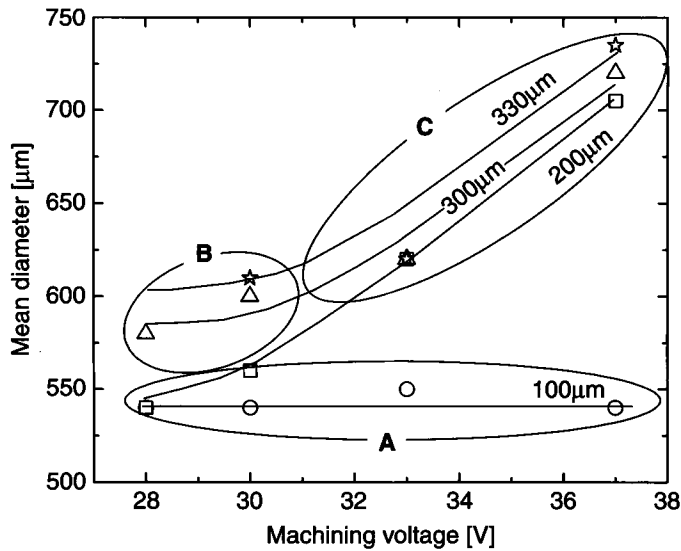


**Figure 6.6** Mean entrance diameter of microholes obtained by SACE glass gravity-feed drilling as a function of the machining voltage and the drilling depth for a 0.4 mm stainless steel tool-cathode. Reprinted from [84] with the permission of the *Journal of Micromechanics and Microengineering*.

difficulty of the electrolyte to reach the tool tip increases. The machining speed is no longer controlled by the number of discharges and becomes almost independent of the voltage, depending only on the drilling depth. This results in an increase in the hole diameter proportional to the drilling depth before it saturates at a maximal diameter (zone C) [136]. The holes are surrounded by a heat affected zone. In zone B, for low voltages (lower than 31 V) and deep holes (deeper than 200  $\mu\text{m}$ ), drilling takes place in the transition zone between the discharge and the hydrodynamic regimes. The entrance holes have a jagged contour.

For ceramic machining, the situation is similar. However, due to the very low material removal rate and the absence of two distinct machining regimes, the mean diameter is almost constant as a function of the drilling depth, increasing with the machining voltage (i.e., only zones B and C from Fig. 6.6 can be observed). As the machining voltage needed for ceramic processing is much higher than that for glass, the over-cut is generally quite large. Typical values for alumina are 300–700  $\mu\text{m}$  for a 1 mm cylindrical tool-cathode [11] and 200–400  $\mu\text{m}$  for  $\text{Si}_3\text{N}_4$  for a 0.4 mm cylindrical cathode tool [97].

The electrolyte composition and bulk temperature also affect the dimensions of the microholes. The mean microhole diameter increases with lower electrolyte concentration [132]. This effect is due to the lower machining speed at low electrolyte concentration, resulting in significantly higher drilling times. The chemical composition of the electrolyte has even more dramatic effects. For example, the use of KOH results in almost half as large diameters compared with the holes drilled using NaOH [132]. This is due to the different drilling times resulting from the use of KOH and NaOH electrolytes.

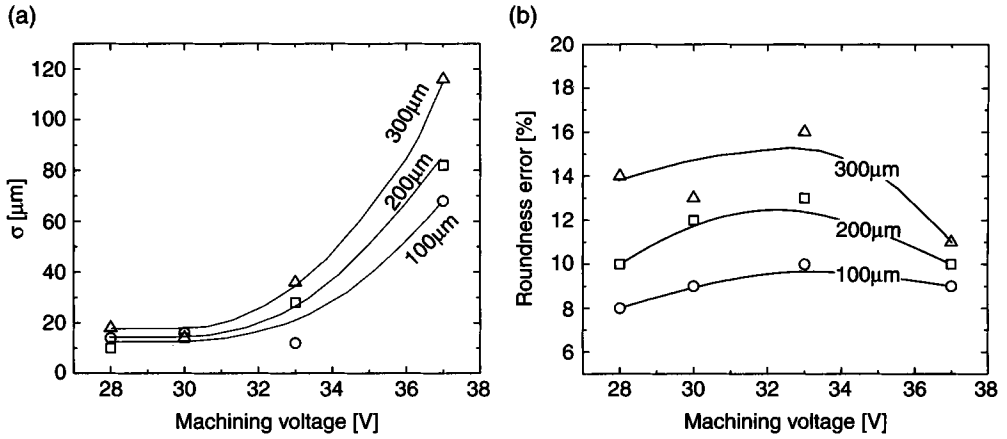


**Figure 6.7** (a) Standard deviation  $\sigma$  and (b) roundness error of microholes machined using SACE gravity-feed drilling in glass. Reprinted from [84] with the permission of the *Journal of Micromechanics and Microengineering*.

Figure 6.7 shows the standard deviation and the *roundness error* of the microholes drilled using a 0.4 mm stainless steel cathode [84]. The roundness error is defined as:

$$\text{Relative roundness error} = \frac{1}{d}(d_{\max} - d_{\min}), \quad (6.5)$$

where  $d$  is the mean hole diameter and  $d_{\max}$  and  $d_{\min}$  are the maximal and minimal diameters over a series of drillings.

The standard deviation increases with the voltage and the hole depth (Fig. 6.7(a)) becoming particularly high for voltages above 32 V, whereas it remains almost constant up to 30 V. This strong increase is due to two factors. First, the discharge activity becomes more and more unstable for high voltages (compared with Equation (4.59) in Section 4.3.5), and, second, variations in the spark activity have a larger impact at high voltages than at low voltages. The relative roundness error increases significantly with drilling depth (Fig. 6.7).

In general, an important contribution to the roundness error is the tool-electrode bending, which may result in highly deformed holes (see Fig. 6.8). The increase in the number of non-cylindrical holes with depth is significant [84]. Bending can be minimised by using as short tools as possible, very stiff materials, and a minimal force for the gravity-feed drilling.

Another important parameter is the electrode polarity. Using an anode compared with a cathode results in very different microhole shapes, as discussed in Section 5.4. The microhole profile is also a function of the tool shape. For cylindrical tools (cathodes), the typical profile is conical but the hole bottom presents in general two bumps. These bumps, due to localisation of the discharges at the tool edges, are more pronounced for ceramic and composite materials than for glass [19].



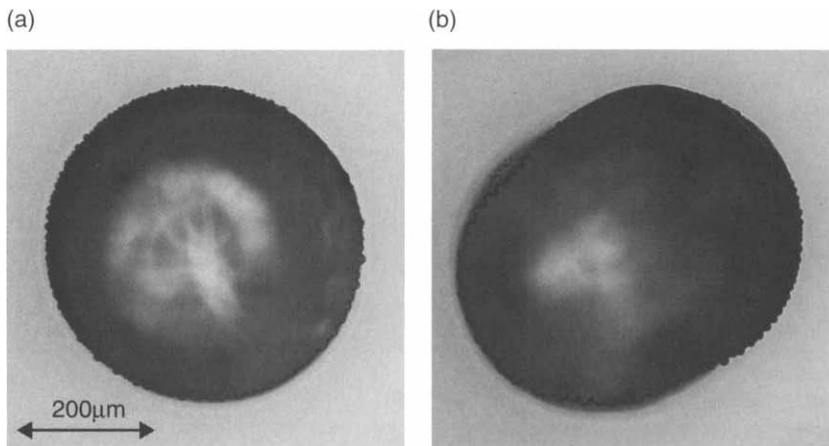


**Figure 6.8** (a) Cylindrical and (b) deformed microholes due to tool-electrode bending. Reprinted from [84] with the permission of the *Journal of Micromechanics and Microengineering*.

### 6.2.7 Machining Quality

The existence of the two machining regimes results in different drilling qualities as a function of the machining voltage and depth. In the case of a cathode tool, the holes drilled in glass can be classified into four different types (Fig. 6.9) [84]:

1. *Well defined cylindrical contours with smooth surface* (Fig. 6.9(a)): This type of contour is characteristic for low depths (100  $\mu\text{m}$ , 28–37 V) and low machining voltages (28 V, up to 300  $\mu\text{m}$ ). The entrance of the hole is well defined and characterised by a smooth surface.
2. *Jagged outline contours* (Fig. 6.9(b)): This type of hole appears at depths between 200 and 300  $\mu\text{m}$  using a machining voltage of about 30 V. The contour is no longer smooth but jagged.
3. *Hole with heat affected zone* (Fig. 6.9(c)): For machining voltages above 30 V and depths higher than 100  $\mu\text{m}$ , the hole is surrounded by a heat affected zone. The contour remains cylindrical.
4. *Hole with thermal cracks* (Fig. 6.9(d)): When machining at 37 V and higher, the hole is characterised by cracks and a large heat affected zone. The entrance holes are generally no longer cylindrical.

Figure 6.10 summarises the different types of microholes that are obtained by gravity-feed drilling as a function of the machining voltage and the drilling depth. This plot can be understood by taking into account the existence of the two machining regimes. Let us follow the drilling at a given voltage. Initially, machining is done only in the discharge regime (up to about 100  $\mu\text{m}$ ). The quality of the hole is not affected by the voltage. A higher voltage results in faster drilling without loss of quality. As the tool drills deeper into the workpiece,

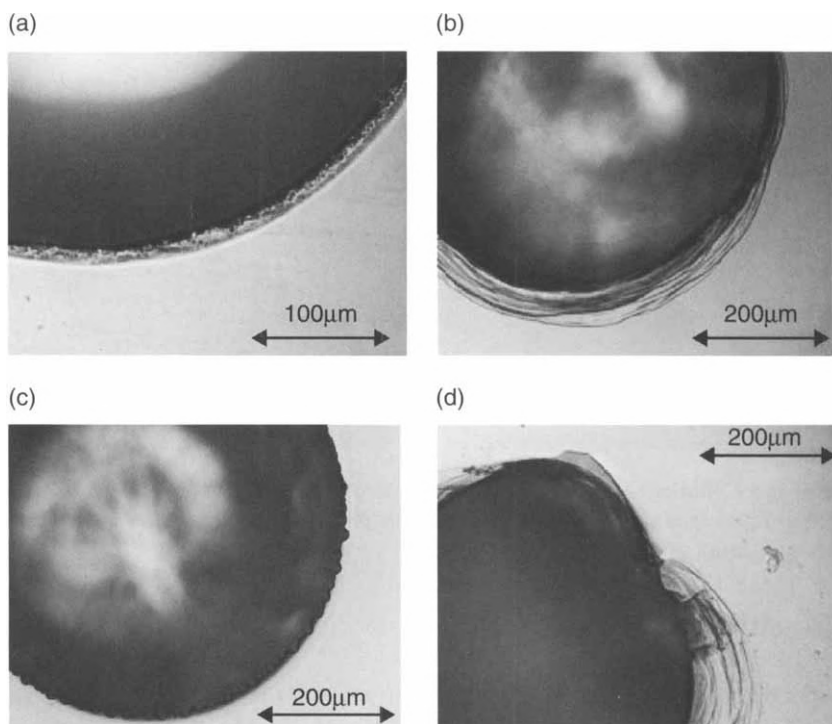


**Figure 6.9** Different microhole qualities obtained by gravity-feed drilling with a stainless steel tool-electrode of 0.4 mm diameter in glass. See text for detailed explanations. Reprinted from [84] with the permission of the *Journal of Micromechanics and Microengineering*.

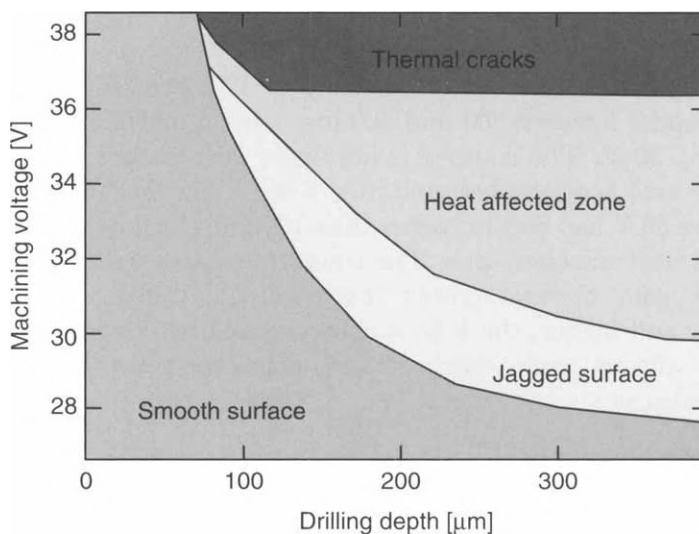


**Figure 6.10** Evolution of SACE glass gravity-feed drilling in the machining voltage–drilling depth plane. Reprinted from [84] with the permission of the *Journal of Micromechanics and Microengineering*.

the difficulty in removing the machined material and insufficient wetting of the tool tip increases. The machining moves into the hydrodynamic regime. More and more discharges take place in the upper part of the tool resulting in a jagged contour and an increase in the hole diameter. As the drilling continues, the hole diameter increases further until it reaches its maximal value (depending on the machining time and voltage). In this situation, the border of the hole is not heated enough to be melted or etched. The microhole does not increase any longer but a heat affected zone starts growing instead. If the heat power supplied is very high (for voltages above 36 V), thermal cracks appear.

According to this description, deep holes should always have a poorer quality than holes with a depth typically lower than 100  $\mu\text{m}$ . Machining at 28 V and lower seems to be an exception to this rule. The fact that machining at 28 V results in excellent surface qualities, even for deep holes, can be attributed to the discharge activity. As discussed in Section 4.3.3, the discharge activity is different for voltages from the critical voltage to the transition voltage than for higher voltages. These two types of discharge activities (instability and arc discharge region) result in two different machining qualities. For the low voltage region (instability region), the combination of discharges, together with chemical etching promoted by the hydrodynamical flows due to the incomplete gas film, results in the smooth surface observed. The variance in the machined diameter is small, whereas in the arc discharge region it starts growing significantly (Fig. 6.7(a)).

Another important aspect is the surface roughness of the drilled holes. Typical values for glass can be as low as a few hundred nanometres [132]. The use of NaOH results in smoother surfaces than KOH [132]. This is probably due to the lower heat available for machining in NaOH compared with KOH (due to the different electrical conductivities of NaOH and KOH).

### 6.3 Constant Velocity Feed Drilling

Another popular machining strategy for SACE is constant velocity feed drilling. Compared with gravity-feed drilling, constant velocity feed drilling avoids the mechanical contact between the tool-electrode and the workpiece. This can, in particular, overcome the problem of the tool-electrode bending. However, as the tool-feed rate is selected beforehand, the gap between the workpiece and the tool-electrode is not controlled and is generally not constant during machining. Consequently, the progress of drilling cannot be monitored online.

The tool-electrode feeding rate has to be selected properly. Feed rates faster than the mean material removal rate of the process will result in breaking either the workpiece or the tool-electrode. On the other hand, very slow feed rates will increase drilling times and may result in large heat affected zones around the microhole. So far only a few studies have been carried out on the optimal feeding rate. Typical values reported in the literature are, depending on the tool-electrode

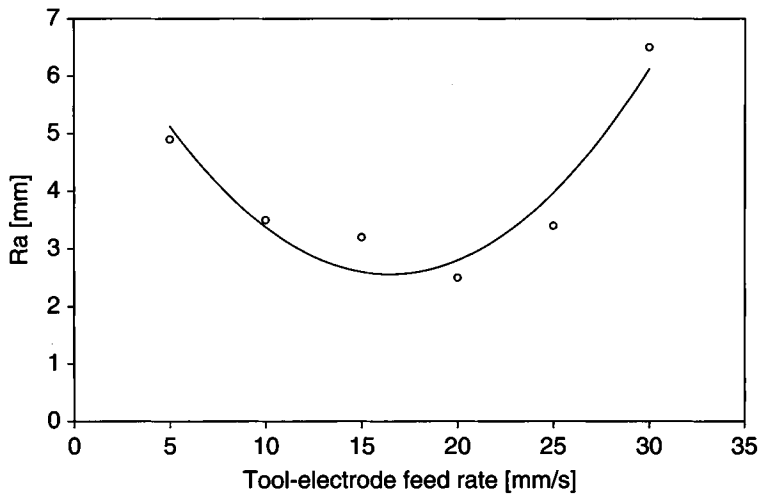


**Figure 6.11** Microhole surface roughness as a function of the tool-electrode feed rate, according to Han et al. [50]. Drilling was done with a 0.2 mm cylindrical tungsten carbide tool-cathode in 30 wt% NaOH electrolyte at 35 V. Reprinted from [50] with permission from Elsevier.

diameter, about 5–15  $\mu\text{m/s}$  [50,80,82], a value slightly higher than the limiting speed reached in the hydrodynamic regime during gravity-feed drilling.

As in gravity-feed drilling, the mean hole diameter increases with drilling depth [82]. For high enough depths, a maximal diameter will eventually be reached. This may be attributed to reduced electrolyte in the machining zone, as with increasing depth the electrolyte can no longer reach the bottom of the hole easily. Consequently, the discharge activity moves to the upper part of the tool-electrode causing enlargement of the hole entrance.

The feeding rate directly affects the microhole surface roughness. As shown by Han et al. [50], the surface roughness follows an inverse volcano dependence of the feeding rate (Fig. 6.11). This dependence is due to the competition between local heating of the workpiece and chemical high-temperature etching of the glass.

The main advantage of constant velocity feed drilling compared with gravity-feed drilling is that the motion of the tool-electrode is user controlled. This allows the machining of more complex shapes than cylindrical holes. An impressive example is the machining of threads in glass as shown by Lee et al. [79]. The authors were able to build microfluidic devices with removable tubing interconnects that could withstand pressures up to 200 kPa. They also demonstrated the fabrication of other interconnection shapes (conical and hourglass interconnections).

## 6.4 2D and 3D Machining

One of the very interesting features of SACE machining is that not only drilling is possible, but the machining of 2D structures also. To date this feature has

been investigated systematically only for glass and the remainder of this section is limited to this material. Two methods have been investigated until now. The first method involves moving the tool-electrode above the glass surface by following a specified path. The tool-electrode has to be closer than 20–25  $\mu\text{m}$  for machining to take place. The second method involves drilling down to a certain depth and then moving the tool-electrode laterally. In both cases the tool is moved at a constant velocity. Typical values are around 50–150  $\mu\text{m/s}$ . Such high speeds are possible as, in contrast to drilling, the machining is almost never limited by the ability of the electrolyte to reach the machining point. Machining is in other words always in the discharge regime. In the following sections the case where the tool is moved above the glass surface is discussed as only this machining strategy has been investigated systematically until now.

#### 6.4.1 Quality of Machined Microchannels

In 2D-SACE machining, two parameters can be adjusted: the *tool travel speed* and the machining voltage. In contrast to drilling, much more freedom is available for the tool travel speed. The selection of the appropriate combination of these two parameters is one of the most important issues in 2D-SACE machining. Microchannels are not formed for all velocities at which the tool is moved above the glass surface. Whether a microchannel is created or not depends not only on the tool travel speed but also on the applied voltage and the distance of the tool from the workpiece. As will be discussed in detail in Section 6.4.2, at some travel speeds it is not possible to have any microchannel formation. For example, when machining at 28 V it is not possible to have any acceptable channel shape for travel speeds higher than 40  $\mu\text{m/s}$ . Increasing the machining voltage to 30 V will allow moving the tool up to a velocity of 50  $\mu\text{m/s}$ .

On the other hand, using high machining voltages (more than 32 V) at low tool travel speeds results in a non-smooth channel surface with significant depth variation along the channel. As a general rule, the quality of the microchannels deteriorates as the tool travel speed is decreased. This can be attributed to the poor material removal rate and the accumulation of melted material inside the microchannel immediately behind the tool.

There are optimal conditions under which microchannels with edges and surfaces of acceptable quality are achieved. The channels so obtained can be subdivided into the following five categories [23]:

1. *Well-defined linear channel edges and smooth channel surface:* This type of contour is characteristic of low voltages with appropriate tool travel speeds. Typical values are 28 V with the tool travel speed ranging from 5 to 10  $\mu\text{m/s}$  and 30 V with the tool travel speed varying between 15 and 30  $\mu\text{m/s}$  (Fig.6.12(a)).
2. *Jagged outline contours with smooth channel surface:* This contour is observed for low machining voltages (less than 32 V) with tool travel speeds lower than in the previous contour type.

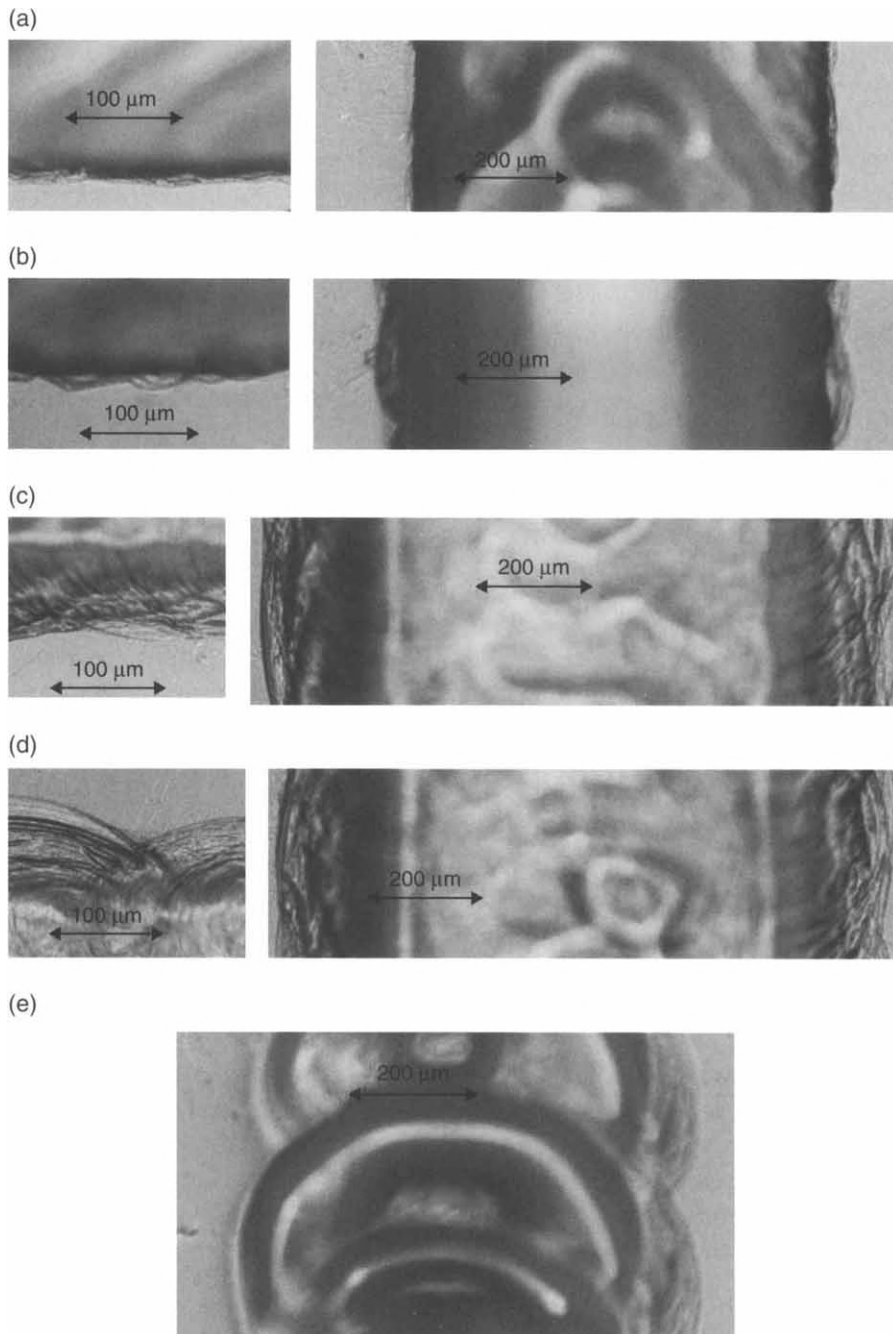


**Figure 6.12** Different types of channels in 2D-SACE machining. Machined using a 0.2 mm cylindrical stainless steel tool-cathode in 30 wt% NaOH: (a) well-defined linear channel edges and smooth channel surface; (b) jagged outline contours with smooth channel surface; (c) heat affected edges with smooth channel surface; (d) heat affected edges with rough channel surface; (e) deteriorated microchannels. Reprinted from [23] with the permission of the *Journal of Micromechanics and Microengineering*.

The microchannel edges are jagged but the channel surface is still flat and smooth (Fig. 6.12(b)).

3. *Heat affected edges with smooth channel surface:* This type of contour is obtained at high machining voltages (more than 32 V) with tool travel speeds high enough to remove the melted material. Under these conditions, the microchannels will exhibit smooth channel surface but the channel boundaries are not well defined due to the effect of heat generated (Fig. 6.12(c)).
4. *Heat affected edges with non-smooth channel surface and thermal cracks:* When the tool travel speed is low and the machining voltage is high (typically 32 V with speed less than 30  $\mu\text{m/s}$  and 35 V with speed less than 40  $\mu\text{m/s}$ ) the edges are unclear and heat affected and the surface is not flat and smooth. Thermal cracks are observed (Fig. 6.12(d)).
5. *Deteriorated microchannels:* As the tool travel speed is increased the channels are non longer continuous and the inner surface becomes very rough. For example, at 28 V increasing the tool travel speed above 40  $\mu\text{m/s}$  results in deteriorated microchannels (Fig. 6.12(e))

Figure 6.13 summarises the type of microchannel obtained for different combinations of the machining voltage and the tool travel speed. Machining voltages less than 32 V result in acceptable microchannel quality. In this voltage range, an appropriate selection of the tool speed will result in the best

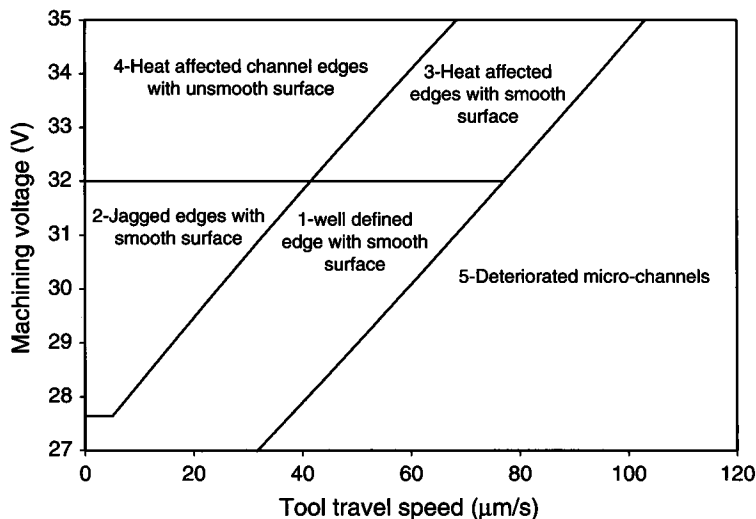


**Figure 6.13** Characterisation diagram for microchannels machined using SACE technology as a function of the machining voltage and the tool travel speed (for tool-electrode distances less than 15  $\mu\text{m}$ ). Machined using a 0.5 mm stainless steel cathode in 20 wt% NaOH. Reprinted from [23] with the permission of the *Journal of Micromechanics and Microengineering*.

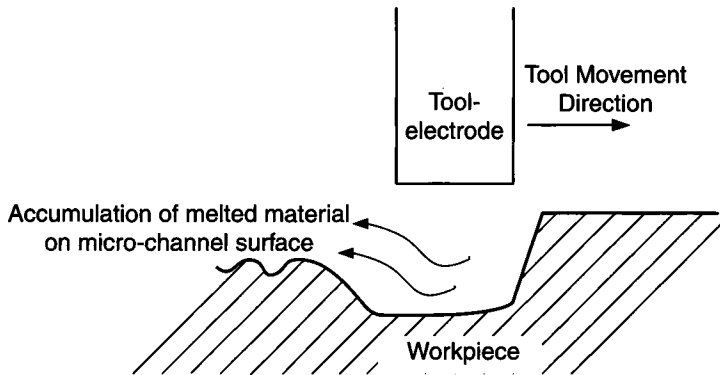


**Figure 6.14** Schematic representation of the accumulation of melted material on the microchannel surface for high machining voltages and low machining speeds (region 4 in Fig. 6.13). Reprinted from [23] with the permission of the *Journal of Micromechanics and Microengineering*.

microchannel quality (region 1) with a channel depth varying between 50 and 120  $\mu\text{m}$  depending on the parameters used. Lower travel speeds will result in deeper microchannels, but the quality of the edges will not be as good as for region 1, although the surface quality is still excellent. Note that decreasing the travel speed will increase the microchannel depth smoothly over time because of chemical etching (discussed in greater detail in Section 6.4.3). If the aim is to have a microchannel with the best quality and a constant depth of around 60  $\mu\text{m}$ , the best choice is to apply 28 V at 20  $\mu\text{m/s}$  tool travel speed.

When using machining voltages higher than 32 V, the microchannel borders are always heat affected. In this range, if the tool travel speed is chosen high enough, it is possible to have smooth microchannel surfaces (region 3 in Fig. 6.13). Decreasing the tool travel speed corrupts the microchannel surface and results in very poor surface quality (region 4 in Fig. 6.13). This is due to accumulation of the melted material inside the microchannel area and the inability to remove the melted material from the microchannel surface (Fig. 6.14).

Finally, region 5 in Fig. 6.13 is the result of excessive tool travel speed. In this region, there is not enough time for the glass to be machined and form an acceptable microchannel. As the tool is moved above the glass surface with high speeds, it is possible to see the effect of the tool on the glass during the machining process (Fig. 6.12(e)). In this region the machined microchannels look like discrete rings. For a 500  $\mu\text{m}$  cylindrical tool, rings of 700  $\mu\text{m}$  diameter are obtained. This value is actually the tool diameter plus the observed over-cut in the hydrodynamic regime for gravity-feed drilling.

#### 6.4.2 Maximal Allowed Tool Travel Speed

An important parameter in 2D-SACE machining is the maximal velocity at which the tool can be moved for machining to take place. Didar et al. [23] proposed a simple model to evaluate this quantity. Recall that the time  $t_0$



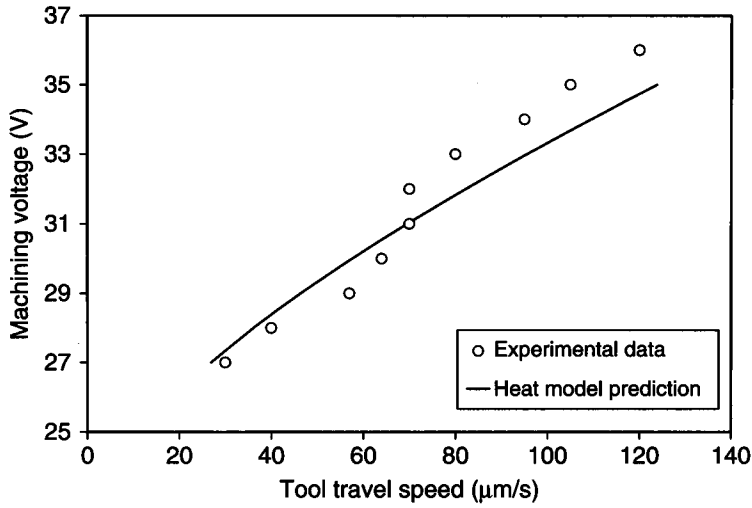


**Figure 6.15** Maximal machining speed in 2D-SACE machining as a function of the machining voltage [23]. The curve is computed using Equation (6.6). Reprinted from [23] with the permission of the *Journal of Micromechanics and Microengineering*.

needed for machining to start is given by Equation (5.13). For 2D-machining to take place at a travel speed  $v$ , the following condition has to be satisfied:

$$vt_o = d, \quad (6.6)$$

where  $d$  is the typical distance over which the discharges from the tool-electrode are distributed. For a cylindrical tool of radius  $b$  this distance would be  $d = 2b$  if the discharges are distributed uniformly. This is, however, not the case, as the discharges are mostly located at the edges of the tool-electrode. A typical order of magnitude for  $d$  is about 25 μm [23].

Figure 6.15 depicts the prediction of this simplified model and the experimental data. The general trend and the order of magnitude are well reproduced. Note the jump around 32 V of the experimental data. This jump is probably due to the different regime in the discharge activities below and above 32 V as described previously in Section 4.3.

### 6.4.3 Depth of Machined Microchannels

If the trajectory of a channel can be directly controlled by the motion of the tool-electrode, the depth of the channel cannot be monitored directly. Depending on the tool travel speed and the machining voltage, different depths are achieved. Another important issue is the chemical etching of the substrate. Due to this effect, the depth of the channels will not remain constant over machining time, but on the contrary increases slightly. A typical example is shown in Fig. 6.16, which illustrates the depth of a channel machined at 28 V

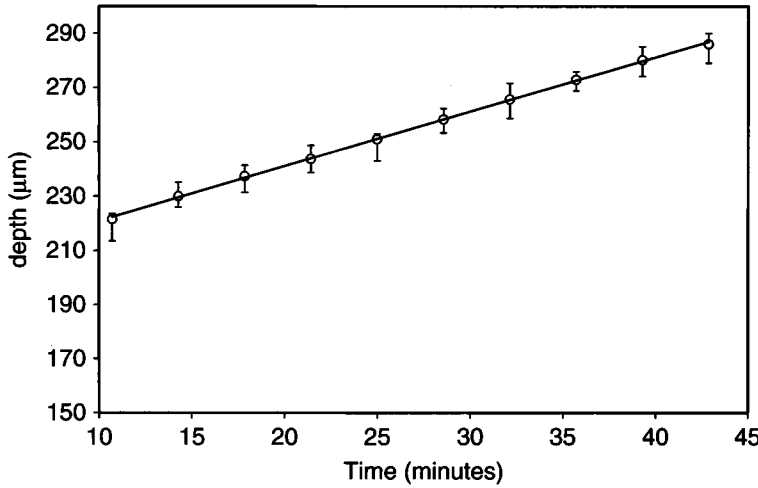


**Figure 6.16** Microchannel depth as a function of the machining time. Machining was done with a stainless steel cathode at 28 V and 5  $\mu\text{m/s}$  in 30 wt% NaOH. Reprinted from [23] with the permission of the *Journal of Micromechanics and Microengineering*.

and 5  $\mu\text{m/s}$  [23]. The tool was moved a few micrometres above the glass surface and the trajectory was corrected to take into account misalignment between the glass surface and the motion of the tool. At this low tool travel speed the effect is clearly visible.

Two parameters are useful in the design of a machined microchannel. The first parameter is  $z_o$ , the channel depth at time zero. This value is obtained by extrapolating the channel profile curves, such as the one in Fig. 6.16, to time  $t = 0$ . The second parameter is  $m_d$ , the average channel depth increase rate over time. The depth  $z(t)$  of the channel over time is then given by:

$$z(t) = m_d t + z_o. \quad (6.7)$$

Both parameters are functions of the machining voltage, as it controls the heat transferred by the electrochemical discharges to the workpiece and the electrolyte (recall that the rate of chemical etching is highly temperature dependent), and the tool velocity. Figure 6.17 shows the dependence of these two parameters on the tool travel speed for machining voltages of 28 and 30 V.

#### 6.4.4 Influence of Tool Distance from Workpiece

Figure 6.18 shows the profile of a microchannel machined at 30 V and with a tool travel speed of 30  $\mu\text{m/s}$  at different tool distances from the glass surface. The average depth of the microchannels decreases with higher tool distance. The quality of the machined microchannels does not change significantly for tool distances up to 15  $\mu\text{m}$ . Above 25  $\mu\text{m}$  no acceptable results can be achieved.

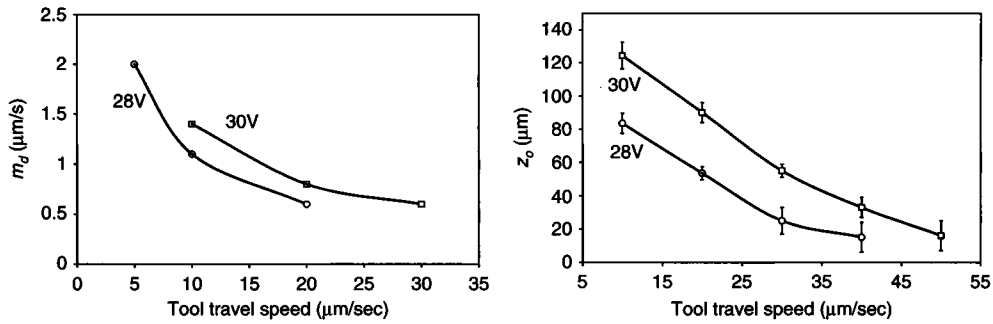


**Figure 6.17** Dependence of the microchannel depth increase rate  $m_d$  and the initial depth  $z_o$  on the tool travel speed. Reprinted from [23] with the permission of the *Journal of Micromechanics and Microengineering*.

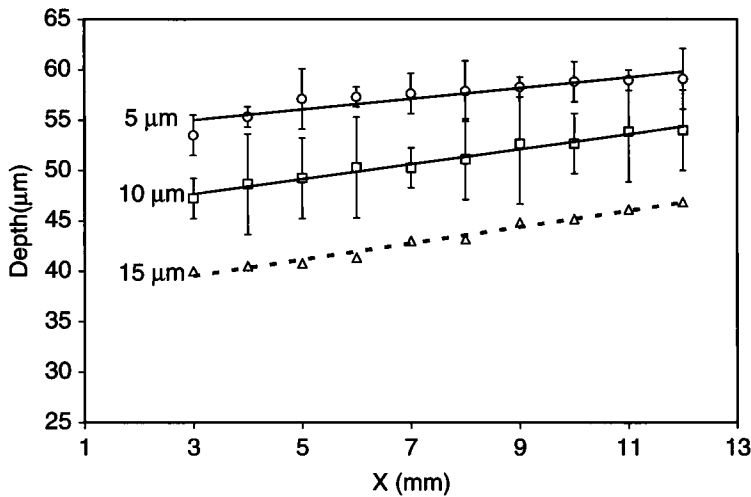


**Figure 6.18** Profile of microchannel depths at three different tool-electrode distances from the glass surface (machining voltage is 30 V and tool-electrode speed is 30  $\mu\text{m/s}$  in 30 wt% NaOH). Reprinted from [23] with the permission of the *Journal of Micromechanics and Microengineering*.

For tool distances greater than 15  $\mu\text{m}$ , the microchannel contours tend to deteriorate independently of the applied voltage and travel speed.

## 6.5 Wire Electrochemical Discharge Machining

An extension of machining with electrochemical discharges to wire machining, called *travelling wire electrochemical discharge machining* (TW-ECDM), was first proposed by Tsuchiya et al. [105] and studied further by Jain et al. [58,91] and Peng and Liao [92]. TW-ECDM is particularly interesting for slicing glass fibre composites [58,59,102,103], but may also be used for 2D contour cutting [105].

In TW-ECDM, a wire is used as the tool-electrode in a similar manner as in wire electrical discharge machining (WEDM). Copper wires [59,92], stainless steel wires [92], or brass wires [100,105,106] are typically used. The wire speed is a trade-off between high speed, in order to allow the cooling of the wire (avoiding overheating and breaking), and low speed for economical reasons [58]. Typical wire speeds vary from a few millimetres per minute [58] to a few centimetres per minute [105] depending on the set-up used. The wire may be guided horizontally or vertically.

Similar to hole drilling and 2D structuring, several materials can be machined using TW-ECDM: glass, quartz, alumina [91,92,105], piezoelectric (PZT) ceramics [100,106], and various composites (glass- and Kevlar-epoxy) [58]. NaOH is generally the preferred electrolyte. The applied voltage may be a direct current (DC) or pulsed voltage. Compared with hole drilling or 2D structuring the voltage is generally higher, which is due to the different geometry of the wire (larger surface area) compared with a cylindrical tool-electrode.

Workpiece feeding is done by gravity-feed, by constant speed (typically a few millimetres per minute for glass and 0.1 mm/min for ceramics), or by gap control [92]. In the last configuration the gap is controlled optically by a sensor. The thickness of the workpiece can be in the range of 1 mm to 1 cm (for glass). The gravity-feed mechanism generally results in poor cut shapes [133].

The stabilisation of the temperature during machining by appropriate flushing of the electrolyte is possible. However, too high flushing rates can destabilise the discharge activity.

The material removal rate and the machining over-cut increase with the machining voltage [100,105] and electrolyte concentration [105,133], which also increases the probability of wire breaking [105]. Polarising the wire as a cathode generally results in higher material removal rates than for a wire polarised as an anode.

An efficient method to decrease the machining over-cut involves adding abrasive particles into the electrolyte [133] or the use of a pulsed voltage supply. At the same time surface roughness is decreased and can reach values below 1  $\mu\text{m}$ .

## 7 Controlling the Machining Process

---

Until now no active control of micromachining with electrochemical discharges has been reported. This can be attributed to two main difficulties. The first difficulty is the observability of the process. As discussed at the end of this chapter, to date it is not clear how the actual machining status can be observed. Only partial information is available. The second difficulty concerns the question of how the machining process can be best influenced. For example, tuning the machining voltage  $U$  will only partially act on the machining. Not all the local parameters, such as local temperature or chemical composition, will be directly controlled by  $U$ .

Despite these difficulties, several passive control strategies have been developed and tested. As presented in this chapter, these strategies are effective and yield very promising results.

### 7.1 Process Analysis

As described in Chapter 5, machining using electrochemical discharges is a combination of softening, melting, and etching of the workpiece. As shown in Fig. 7.1, the electrochemical discharges heat up the machining zone locally resulting in softening and melting of the workpiece. Material is removed by high-temperature chemical etching.

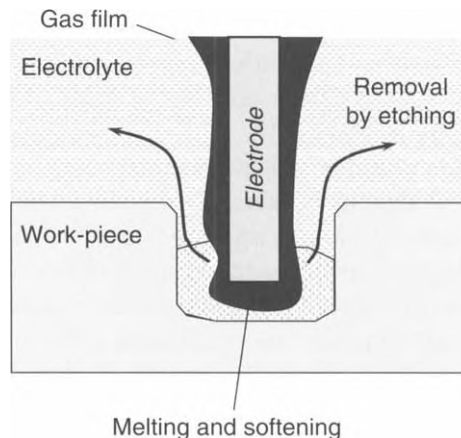


**Figure 7.1** An overview of the influence of the main parameters on the material removal rate in machining with electrochemical discharges.

Therefore, optimising machining by electrochemical discharges means taking control of the following three aspects:

- stable discharge activity,
- localised heating,
- high-temperature chemical etching.

Optimal surface quality is achieved by maximising the chemical etching and at the same time minimising the local heating in order to avoid the formation of heat affected zones. This implies in particular an optimal supply of electrolyte to the machining zone.

It is only quite recently that the importance of the chemical contribution, and therefore the importance of the local electrolyte flow, was identified. Compared with other machining technologies having similar problems, such as electrochemical machining (ECM) or electrical discharge machining (EDM), where several strategies were developed to overcome the problems, only a few have been tested until now and applied to spark-assisted chemical engraving (SACE). Moreover, compared with ECM and EDM, there is a major difficulty in SACE machining. The *machining gap* (the distance between the tool-electrode and the workpiece) cannot be controlled actively. This is a serious restriction, limiting the possibility of adopting control strategies inspired by the one developed in ECM and EDM to promote local flows. Another significant difference is the effect of the discharges. In EDM each discharge melts the workpiece locally. It is possible to control the machining based on the observation of electrical discharges by monitoring current pulses. In ECM, the machining can be controlled directly through the current, as in this case the material removal mechanism is anodic dissolution of the workpiece. In SACE machining the electrochemical discharges provide the heat needed for promoting the local chemical etching. To date no clear evidence about the effect of a single electrochemical discharge is known. This lack of knowledge is another serious limitation in developing control strategies for SACE machining.

The remainder of this chapter will present the newest developments in the field. The first family of strategies aims to promote the local electrolyte flow by appropriate tool-electrode shapes and motions. The second family regroups various strategies with the aim of taking control of the local heat generation. The most advanced and promising techniques use pulsed voltage machining that, as will be discussed, combine the promotion of local chemical etching and the optimisation of local heat generation by the electrochemical discharges.

## 7.2 Promoting Chemical Etching

The promotion of chemical etching during machining can be achieved by optimising the local electrolyte supply to the machining zone. This aspect is particularly important during drilling where with increasing hole depth the flow of the electrolyte to the machining zone becomes more and more difficult.

This effect is pronounced especially during gravity-feed drilling and is responsible for the hydrodynamic regime as discussed in Section 6.2.2. Note that during drilling in the hydrodynamic regime, the quality of the microholes deteriorates.

Increasing the electrolyte supply to the machining zone can be achieved by using appropriate tool-electrode shapes or by promoting the flow of the electrolyte by tool-electrode motions. These strategies are discussed below. Note that until now no attempt has been made to study the potential benefit of using hollow electrodes, which would allow injecting the electrolyte from inside the tool.

### 7.2.1 Effect of Tool-Electrode Shape

The effect of the tool shape in gravity-feed drilling is shown in Fig. 7.2 where the evolution of drilling using a needle shaped tool-electrode [131] is shown. On comparing Figs. 7.2 and 6.2 (drilling with a cylindrical tool), it becomes apparent that the needle shaped tool-electrode results in significantly higher drilling speeds for low voltages (smaller than 30 V), whereas similar evolutions are achieved for higher voltages. This can be explained by noting that in the needle shaped tool-electrode the discharges are concentrated at the tip of the electrode. The discharge density is higher for smaller cross-sections, resulting in higher material removal rate (compare with Equation (5.20)). This effect is more pronounced at low voltages and is significant only in the discharge regime (up to a depth of about 200–300  $\mu\text{m}$ ). Once the hydrodynamic regime is reached, the drilling speed becomes nearly independent of the voltage. For high voltages, the hydrodynamic regime is quickly reached and the difference between the

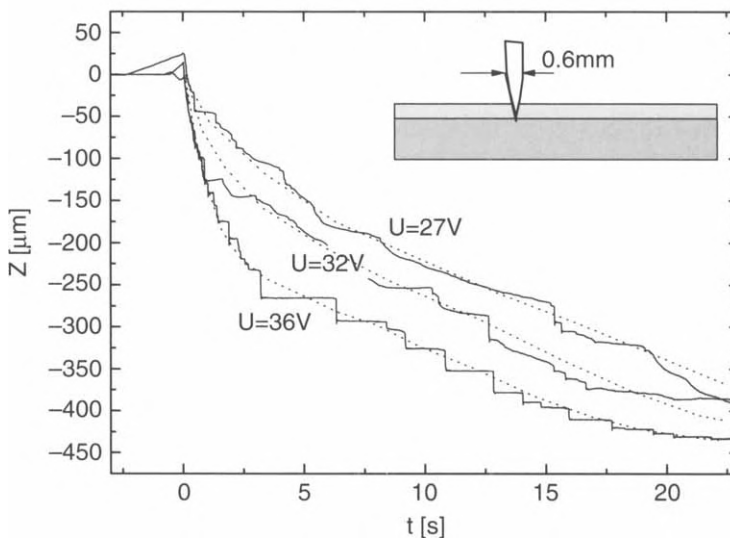


**Figure 7.2** Typical evolution at various voltages of SACE gravity-feed drilling using a needle shaped tool-electrode with a force of 0.8 N acting on it. The electrolyte level above the workpiece was about 1 mm. Reprinted from [131] with the permission of the *Journal of Micromechanics and Microengineering*.

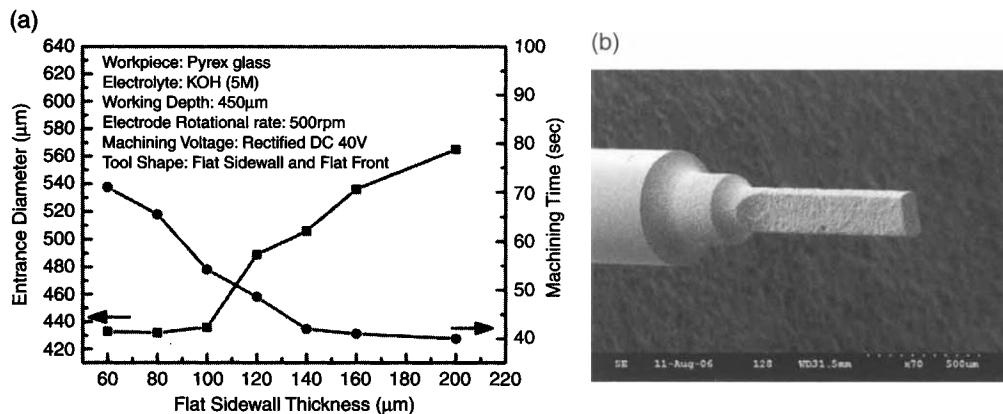


**Figure 7.3** SACE gravity-feed drilling with a flat sidewall shaped tool-electrode: (a) effect on the entrance diameter and the drilling time; (b) flat sidewall shaped tool-electrode. Reprinted from [136] with the permission of the *Journal of Micromechanics and Microengineering*.

cylindrical tool-electrode and the needle shaped tool-electrode is hardly observable. Also note that the mean drilling speed in the hydrodynamic regime is about ten times faster than the speed attained with a cylindrical tool-electrode.

A completely different effect can be achieved for another type of tool-electrode shape. For needle shaped tool-electrodes, the discharge regime was increased due to the concentration of the discharge activity at the electrode tip. It is possible to increase the extent of the discharge regime by selecting tool-electrode shapes that promote the electrolyte flow inside the microhole. This effect was studied by Zheng et al. [136]. They considered tungsten carbide flat sidewall-flat front tool-electrodes with various flat sidewall thicknesses (Fig. 7.3). In order to obtain cylindrical microholes tool-electrode rotation has to be added.

The flat sidewall tool-electrode shape promotes the flow of the electrolyte inside the microhole. This results in enhanced chemical etching and as a consequence in sharper microhole sidewalls compared with the microholes drilled under the same conditions using a cylindrical tool-electrode (Fig. 7.4). The decrease in the entrance diameter with the thickness of the flat sidewall thickness (Fig. 7.3(a)) illustrates this effect. However, the drilling time increases. This is attributed to the modified geometry of the heat source. Further improvements can be obtained by increasing the tool-electrode rotation (Section 7.2.3) or by using pulsed voltage machining (Section 7.3.3).

## 7.2.2 Effect of Tool-Electrode Vibration

The flow of the electrolyte inside holes during drilling can be promoted by appropriate tool vibrations [79,120,122]. This method is particularly well suited in combination with gravity-feed drilling. This machining strategy is sometimes also referred to as tapping mode machining [79,120].



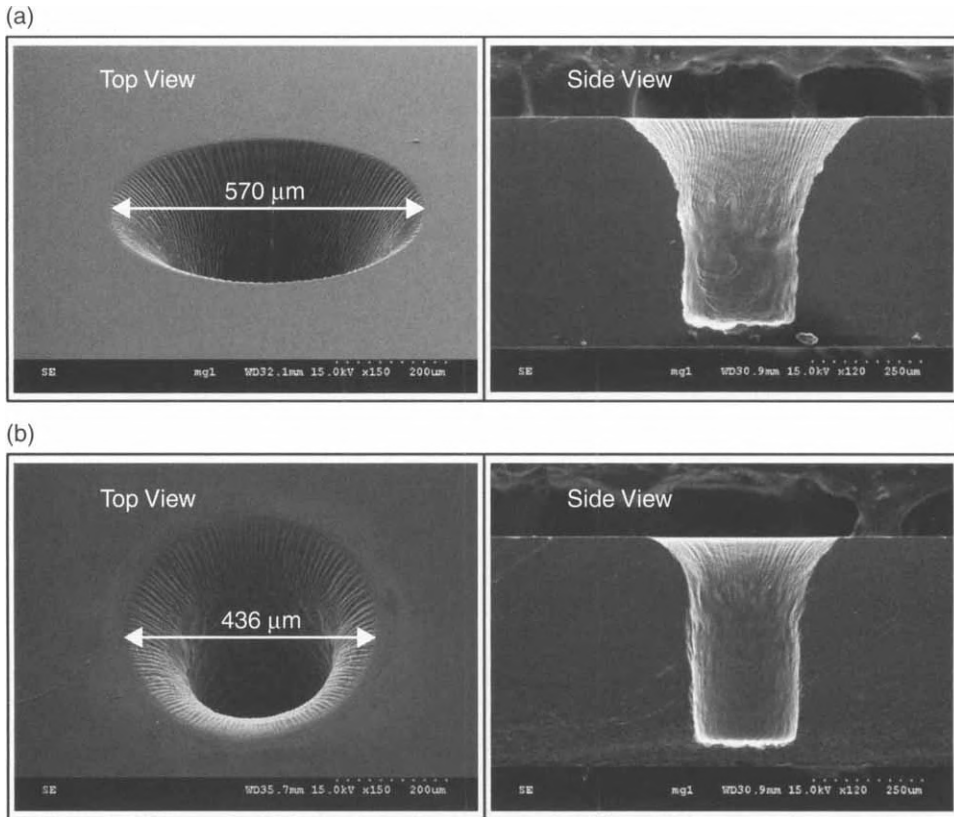


**Figure 7.4** Comparison of microholes drilled by gravity feed at 40 V using: (a) a 0.2 mm cylindrical tool-electrode; (b) a flat sidewall (0.1 mm thickness) shaped tool-electrode. In both cases a tool-electrode rotation of 500 rpm is used. Reprinted from [136] with the permission of the *Journal of Micromechanics and Microengineering*.

An example of the effect of tool-electrode vibration is shown in Fig. 7.5. The amplitude and frequency were varied from 0 to 30  $\mu\text{m}$  and from 0 to 30 Hz, respectively [28]. For each type of oscillation, fifteen microholes were drilled at 33 V. The mean machining time as a function of the applied sinusoidal oscillations for various drilling depths (100  $\mu\text{m}$ : drilling mainly in the discharge regime; 200  $\mu\text{m}$ : transition between the discharge and the hydrodynamic regimes; 300  $\mu\text{m}$ : drilling mainly in the hydrodynamic regime) is shown. Typical variations in the mean machining time (standard deviation from the fifteen successive drillings) are in the range of 10%.

In the range studied, the effect of frequency is not pronounced whereas a clear dependency on the vibration amplitude is observed. The effect is maximal at 300  $\mu\text{m}$  (in the hydrodynamic regime) where the machining time is reduced by half for an amplitude of 10  $\mu\text{m}$ .

The inverse volcano-like curve of the mean drilling time as a function of the oscillation amplitude is due to the competition between two effects. On one hand, increasing the vibration amplitude favours an increase in the drilling

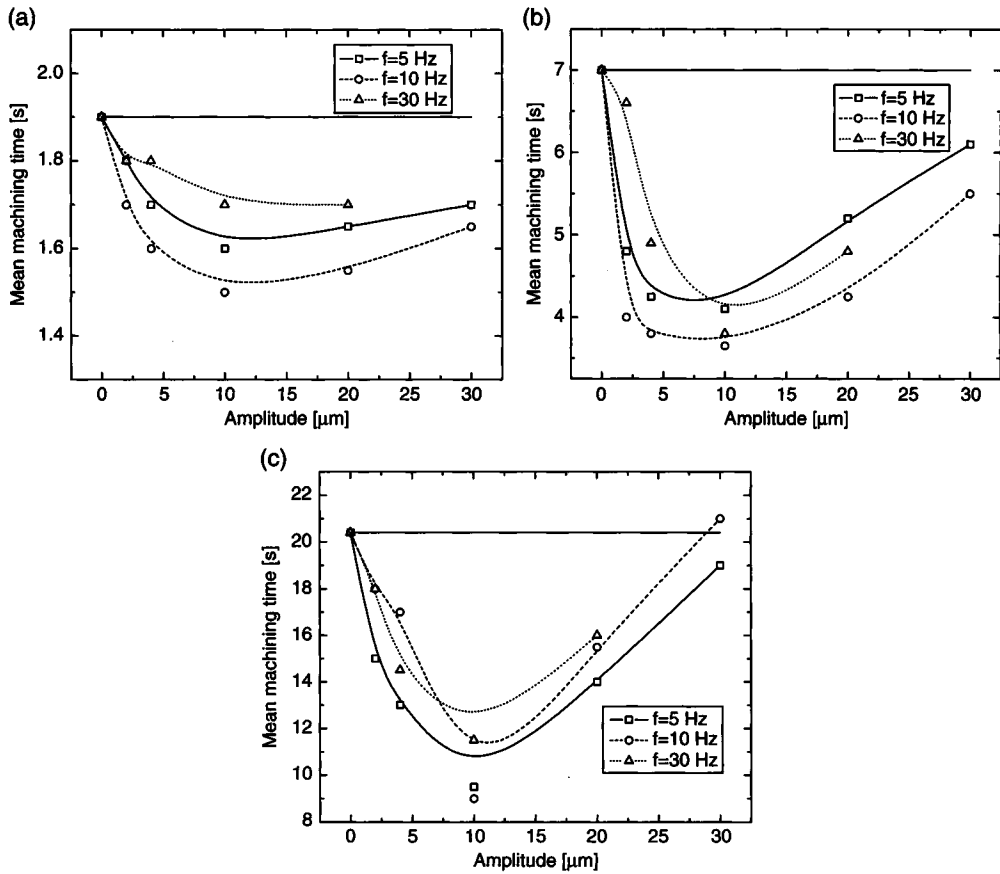


**Figure 7.5** Mean machining time as a function of the applied vibrations for (a) 100  $\mu\text{m}$ , (b) 200  $\mu\text{m}$ , and (c) 300  $\mu\text{m}$  deep microholes in glass. Reprinted from [28] with the permission of the *Journal of Micromechanics and Microengineering*.

speed as this motion promotes the flowing of the electrolyte inside the microhole and the removal of the machined material outside the microhole. On the other hand, the higher the vibration amplitude, the farther away the heat source is from the work sample. Recall that for a distance higher than 20–25  $\mu\text{m}$  between the tool and the workpiece, no glass micromachining takes place. This explains why the further increase in tool vibrations, above an amplitude of 10  $\mu\text{m}$ , no longer favours an enhancement in the drilling speed.

West and Jadhav [120] used periodic flushing of the microhole in order to improve machining at high depths. The cycle used was 5 s gravity-feed drilling followed by vertical removal and turning of the electrode for another 5 s period. They successfully drilled through holes in 500  $\mu\text{m}$  glass slides.

An alternative approach to constant tool vibration is to move the tool-electrode up and down at specific moments during drilling in order to allow fresh electrolyte to flush inside the hole [122]. A possible algorithm can be based on the measurement of the contact force between the tool-electrode and the workpiece. If this force is higher than a selected level, the tool-electrode is moved up in order to flush the microhole.

### 7.2.3 Effect of Tool-Electrode Rotation

As in the case of tool-electrode vibration, the electrolyte flow can be promoted by tool-electrode rotation. An example combining gravity-feed drilling with tool-electrode rotation is shown in Fig. 7.6. A tungsten carbide flat sidewall tool-electrode (Fig. 7.3b) with pulsed voltage supply was used [136]. The drilling time for the fixed depth of 450  $\mu\text{m}$  increases with the tool-electrode rotation rate due to the reduced heat power. The entrance diameter shows an inverse volcano dependence on the tool-electrode rotation rate. This effect was attributed by the authors to the competition between the promotion of the electrolyte flow and the increased drilling time [136].

The promotion of the electrolyte flow results not only in reduced entrance diameters, but also in sharper microhole sidewalls and reduced roundness errors [136].

As in gravity-feed drilling, the machining performances of constant feed drilling can be improved by using tool-electrode rotation. The most interesting result is that higher surface qualities are obtained. This was first demonstrated by Gautam and Jain [40], by drilling holes in the range of a few millimetres in diameter and depth in glass and quartz using various tool kinematics with NaOH electrolyte, and later confirmed by other research groups [79,132]. The cylindricity of the machined holes and the material removal rate can be improved by rotating the tool-electrode. The effect of the tool's rotational speed can be divided in two distinct types. For slow rotation (typically less than 25 rpm), the machining efficiency (the extent of the machined distance for a given machining time) increases. For higher rotational speeds (higher than 25 rpm), the efficiency decreases and may even become lower than for a non-rotated tool. Gautam and Jain [40] attributed this effect to a destabilisation

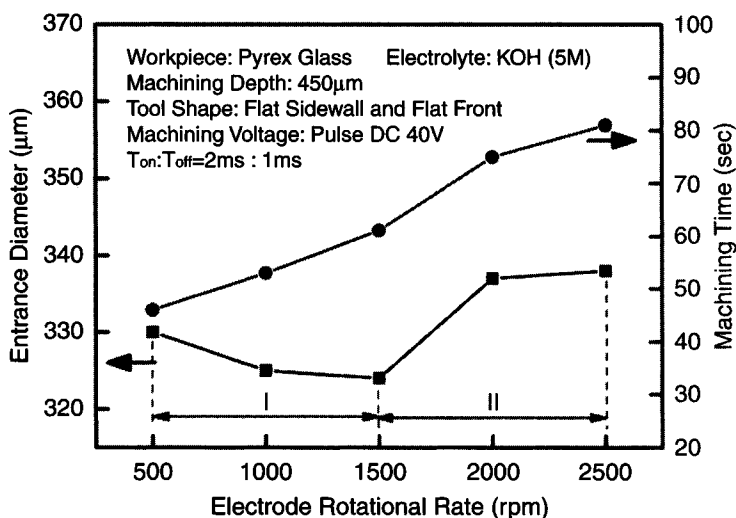


**Figure 7.6** Effect of tool-electrode rotation in gravity-feed drilling. Reprinted from [136] with the permission of the *Journal of Micromechanics and Microengineering*.

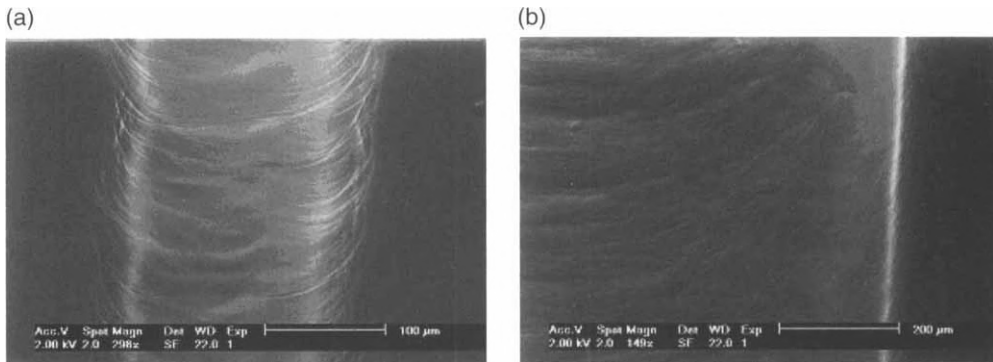


**Figure 7.7** Comparison between a channel machined (a) without and (b) with tool rotation. The sharpness of the edges is improved. Reprinted from [128] with permission from Elsevier.

of the discharge activity with increasing rotation speed. A similar conclusion was reached when using an exocentric rotational motion for the tool. Optimal performances can be achieved by using an eccentricity similar to the tool radius used [40].

In 2D-SACE machining, tool rotation also contributes to increased performances (Fig. 7.7). In particular, it sharpens the edges of the machined structures and smoothes the machined surface [123,128].

#### 7.2.4 Adding Abrasive to the Electrolyte

Adding abrasive material to the electrolyte does not itself promote the local chemical etching. This effect can, however, be achieved in combination with the appropriate tool-electrode motion (e.g., rotation or vibration). In this way, machining quality is improved by reducing the surface roughness [133].

As discussed in Section 7.3, the addition of abrasives can also help in influencing the heat transfer in the process.

### 7.3 Controlling the Heat Generated

Controlling the heat generated during SACE machining is one of the main issues, especially for micromachining applications. As discussed in Chapter 6, generating too much heat results in heat affected zones or thermal cracks. Machining is more reproducible and results in higher surface qualities when machined at low power. The over-cut is also reduced. All these aspects act as the driving forces in developing strategies to control the heat generated and maintain it in a well defined range.

Controlling the heat generated can be achieved passively or actively. Passive methods try to keep the heat generated in the machining zone within a reasonable range by removing excess energy through heat transfer. Heat transfer can be

influenced by acting on either the heat conduction of the electrolyte or the heat conduction of the tool-electrode.

Active methods try to keep the heat supplied to the workpiece in a well defined range by controlling the amount of energy supplied to the machining zone. This is achieved either by using small machining voltages or by reducing the time for which the voltage is applied. To date two strategies have been explored to control actively the heat generated during SACE machining. The first strategy tries to machine at as low power as possible. This means that one is interested in finding ways to reduce the critical voltage at which the gas film builds around the tool-electrode. The second strategy uses pulsed voltages machining. As will be seen, by selecting the appropriate parameters excellent surface qualities can be achieved.

It has to be stressed that the terminology active and passive does not refer to open- or closed-loop control strategies. All the methods presented in this section to control the heat generated are open-loop strategies.

### **7.3.1 Influencing the Heat Transfer**

The heat released by the electrochemical discharges is only partially transferred to the workpiece. Part of it is evacuated through the electrolyte and the tool-electrode. The greater the heat removed from the machining zone, the better is the machining in terms of quality. As expected, the major drawback is the decreased material removal rate. In general, a trade-off has to be reached between quality and fabrication time.

#### **7.3.1.1 Heat Transfer through the Electrolyte**

The heat transfer through the electrolyte can be influenced by local hydrodynamic flows (by convection) or by changing the heat conductivity of the electrolyte. The first strategy can be implemented by adding the appropriate tool-electrode motion such as vibration or rotation. Both do not only promote the heat transfer but also the local high-temperature chemical etching of the workpiece as discussed in Section 7.2.

One way to improve the heat conductivity of the electrolyte is to use powder-mixed electrolytes. Adding small conductive particles in the electrolyte will promote heat conduction and also reduce the dielectric strength in the gas film, with the effect of reducing the spark ignition voltage [50,133]. As shown by Han et al. [50], by choosing the appropriate amount of conductive particles, it is possible to improve significantly the surface roughness of microholes drilled at a constant feed rate. The same effect can also be observed in travelling wire electrochemical discharge machining (TW-ECDM) [133]. This effect was attributed by the authors to the reduction in the spark ignition voltage, but improved heat conduction of the electrolyte and promoted material removal due to the particles are certainly other effects contributing to this result.

7.3.1.2 Heat Transfer through the Tool-Electrode

The heat conductivity of the tool-electrode affects the machining in two ways. First, it controls the heat removed from the machining zone. The heat conductivity of the tool-electrodes is generally significantly higher than that of the electrolyte and the workpiece. It follows that a major part of the heat supplied by the electrochemical discharges is removed through it.

Second, the heat conductivity of the tool-electrode will affect the mean temperature of the tool during machining. The higher the heat conductivity, the greater the heat that passes through the tool-electrode, which becomes hotter for a given heat capacity of the electrode material. The electrode temperature affects the discharge activity. Recall that the electrochemical discharges are due to thermal-assisted field emission of electrons at the electrode (Section 2.4.3). Therefore, an increase in the temperature will result in more discharges.

These two effects are observed in the example of glass gravity-feed drilling with electrodes having different thermal properties [86]. Figure 7.8 shows a comparison of the evolution of drilling at various machining voltages using electrodes made of different materials (Table 7.1). First, let us consider stainless steel, high carbon steel, and copper. The higher the thermal conductivity of the tool-electrode, the slower the drilling in the hydrodynamic regime. Electrodes with high thermal conductivity remove more heat from the machining zone than

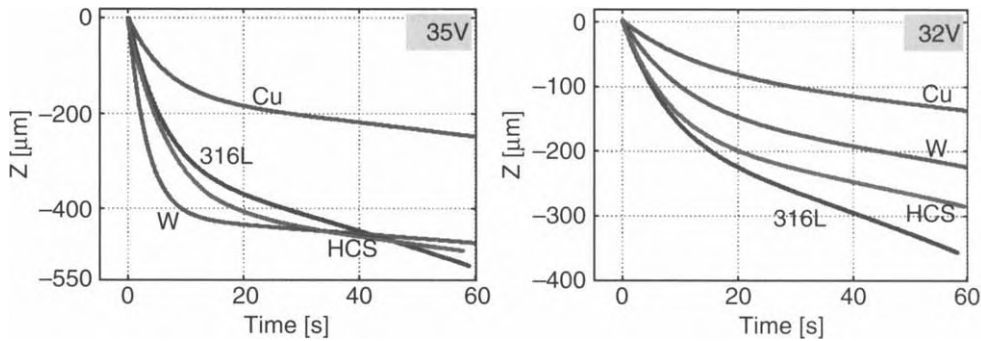


**Figure 7.8** Effect of the thermal properties of the tool-electrode (Table 7.1) in glass gravity-feed drilling. Reprinted from [86] with the permission of the *Journal of Micromechanics and Microengineering*.

**Table 7.1** Thermal Properties of Some Electrode Materials at 300 K

| Material                | Thermal Conductivity<br>(W m <sup>-1</sup> K <sup>-1</sup> ) | Specific Heat Capacity<br>(J kg <sup>-1</sup> K <sup>-1</sup> ) |
|-------------------------|--|---|
| Stainless steel (316L)  | 16   | 500   |
| High carbon steel (HCS) | 50   | 472   |
| Tungsten (W)            | 173  | 134   |
| Copper (Cu)             | 401  | 385   |

electrodes with lower heat conductivity, so the temperature of the workpiece will be lower. The viscosity of glass in the machining zone will also be lower, resulting in slower evolution of drilling.

The behaviour of tungsten is different. Tungsten has a significantly lower heat capacity than the other three materials. This results in an increase in the tool-electrode temperature, resulting in higher discharge activity. The discharge regime (observed particularly for high voltages) is significantly faster for tungsten than for the other materials. The situation is different in the hydrodynamic regime, which is not affected by the discharge activity. Here, the tungsten tool-electrode has a drilling speed that lies between the speed for high carbon steel and copper, similar to their respective thermal conductivities.

Note that the drilling evolution shown in Fig. 7.8 is also affected by the wear of the tool-electrode. However, the amount of tool-electrode wear during one minute of drilling is below a few micrometres (see [76] and Table 6.1).

### 7.3.2 Reducing the Critical Voltage

As discussed in Section 4.4.1, it is possible to reduce the critical voltage by changing the wettability of the electrode–electrolyte interface, which can be achieved by adding surfactants to the electrolyte. An example is shown in Fig. 7.9(a). Liquid soap was added to 30 wt% NaOH [129]. The critical voltage is reduced from around 30 to about 14 V. The critical current density and the gas film formation time are also reduced. Machining at lower voltages becomes possible. An example of successive drillings of microholes at 20 V is illustrated in Fig. 7.9(b). Very well-defined contours are achieved. The fluctuation of the mean diameter is less than 5  $\mu\text{m}$  (computed from a set of 50 microholes), which

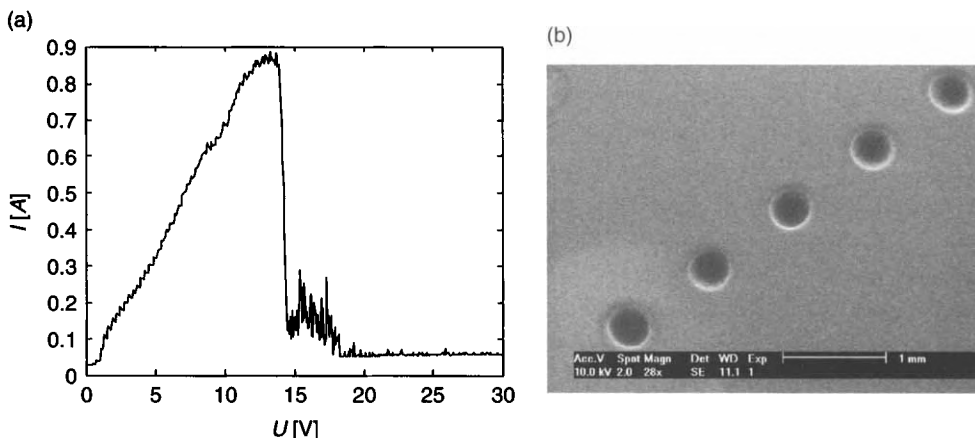


**Figure 7.9** Glass gravity-feed drilling with an electrolyte modified by adding a surfactant. (a) The critical voltage is reduced below 15 V. (b) Successive drillings at 20 V with a cylindrical stainless steel electrode of 0.5 mm diameter. The dispersion of the mean diameter is less than 5  $\mu\text{m}$ . Reprinted from [129] with permission from Elsevier.

is much lower than for higher machining voltages (compare with Fig. 6.7). The drawback is the increased drilling time (typically a factor 10).

### 7.3.3 Pulsed Voltage Machining

Two major benefits can be achieved by using pulsed voltages. First, one can get rid of the problems associated with the instability of the gas film by periodically destroying the gas film. Therefore, the time during which the voltage is switched on, the pulse-on time  $T_{on}$ , is selected such that it is shorter than the mean lifetime of the gas film. Second, by choosing the ratio between  $T_{on}$  and the pulse-off time  $T_{off}$  one can optimise the heat transferred to the workpiece. The pulse-on time has to be selected such to be longer than the mean formation time of the gas film, but short enough to avoid too much heat transfer to the workpiece. With  $T_{off}$  one can allow the system some time to cool down and therefore avoid problems like jagged contours and heat affected zones. The major drawback of pulsed voltage machining is the reduced material removal rate.

The use of pulsed voltages for micromachining of glass with electrochemical discharges was investigated recently by Kim et al. [71] and Zheng et al. [136,137]. They showed that excellent results can be achieved for microhole drilling and 3D microstructuring, especially if tool rotation is added.

#### 7.3.3.1 Microhole Drilling

By choosing high frequency voltage pulses and small duty ratios  $T_{on}/(T_{on} + T_{off})$ , the machining over-cut and surface roughness can be reduced during gravity-feed drilling [71,136]. The drawback is the increased machining time for a given microhole depth. An example is shown in Fig. 7.10. A tungsten carbide flat sidewall (200  $\mu\text{m}$  diameter and 100  $\mu\text{m}$  thickness) rotated tool-electrode (at 500 rpm) in 5 M KOH solution at 40 V was used and the drilling depth was 450  $\mu\text{m}$  [136]. The pulse-on time was selected to be slightly higher than the mean gas film formation time, which was measured to be about 1.5 ms for the electrode-electrolyte combination used.

The entrance diameter decreases with  $T_{off}$  due to the reduced mean heat power supplied to the workpiece. Another reason for this behaviour is the periodic destruction of the gas film. This allows the electrolyte to flow inside the microhole and therefore results in a more homogenous chemical etching of the hole compared with DC voltage machining where the spark activity progressively moves to the top of the tool-electrode as the drilling goes deeper.

The drilling time increases with  $T_{off}$  as less heat power is available for machining. Optimal parameters can be identified for which the drilling time shows almost no increase whereas at the same time the entrance diameter is significantly reduced. The result of the microhole drilling with an optimized set of parameters is shown in Fig. 7.11. Note how the microhole is almost cylindrical although the drilling depth is high and passes through the hydrodynamic regime.



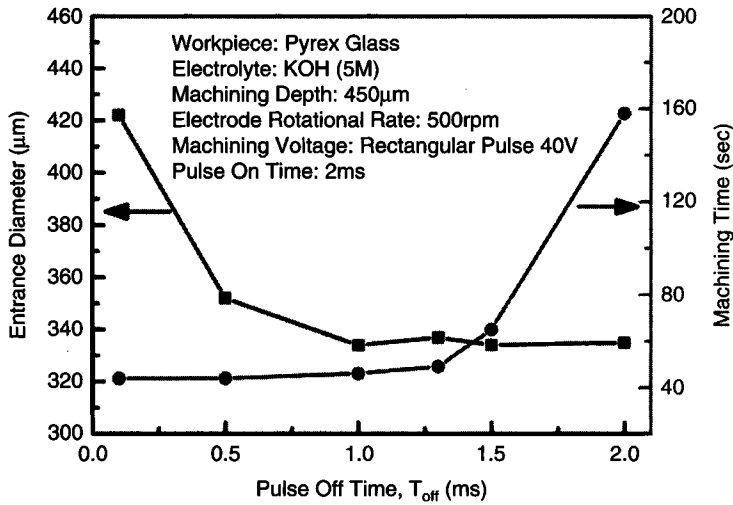


**Figure 7.10** Glass gravity-feed drilling using a pulsed voltage supply: the entrance diameter decreases with increasing  $T_{off}$  whereas the drilling time increases. Reprinted from [136] with the permission of the *Journal of Micromechanics and Microengineering*.

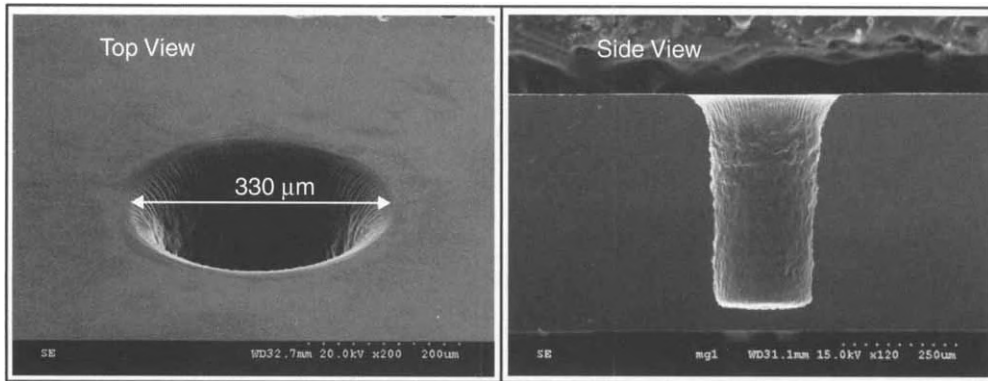


**Figure 7.11** Microholes in glass drilled by gravity-feed using a pulsed voltage supply. The main machining parameters are:  $T_{on}:T_{off} = 2:1$  and tool-electrode rotation of 500 rpm at 40 V. Reprinted from [136] with the permission of the *Journal of Micromechanics and Microengineering*.

The combination of tool-electrode rotation, tool shape, and optimal pulse duty ratio results in this excellent result.

### 7.3.3.2 2D and 3D Machining

As for the case of microhole drilling, Zheng et al. [137] showed that a well chosen set of parameters  $T_{on}$  and  $T_{off}$  for a given machining voltage  $U$  gives several improvements compared with DC voltage machining (Fig. 7.12). In particular, reduced machining over-cut and sharper sidewalls are obtained.

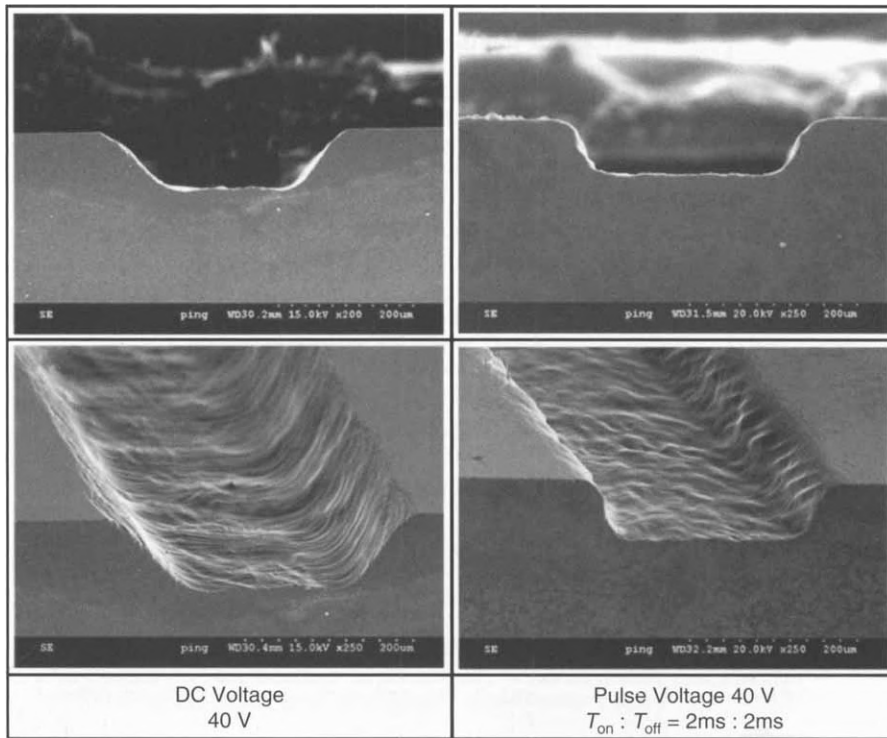


**Figure 7.12** Microchannels in glass machined with a pulsed voltage supply. The main machining parameters are:  $T_{on}:T_{off} = 2:2$  and tool-electrode rotation of 500 rpm at 40 V. Reprinted from [137] with the permission of the *Journal of Micromechanics and Microengineering*.

For a machining voltage of 40 V, the authors selected  $T_{on} = 2$  ms (slightly above the gas film formation time that was determined to be about 1.5 ms for the electrode-electrolyte configuration used at 40 V) and studied the effect of  $T_{off}$  between 0.5 and 8 ms. The tool-electrode was a 0.2 mm diameter cylindrical tungsten carbide rod and a 5 M KOH solution was used as the electrolyte. With increasing  $T_{off}$ , the machining over-cut is reduced (Fig. 7.13) and the sidewall taper angle of the microchannel profile is decreased from  $45^\circ$  to  $24^\circ$ . As for microhole drilling, this effect is due to the combined action of the reduced heat power and the periodic destruction-reconstruction of the gas film. The latter promotes chemical etching due to increased electrolyte flow, resulting in sharper sidewalls (compare with Fig. 7.12). This is a similar effect to that obtained by adding tool-electrode rotation.

A further increase in the tool-electrode rotation improves the channel quality (Fig. 7.14). The sidewall taper angle of the microchannel profile decreases to almost  $0^\circ$  and the machining over-cut is also reduced. This effect is due to the improved electrolyte flow, promoting chemical etching of the glass.

Similar to DC voltage machining, the travel speed of the tool-electrode has to be selected in the appropriate range in order to obtain optimal surface

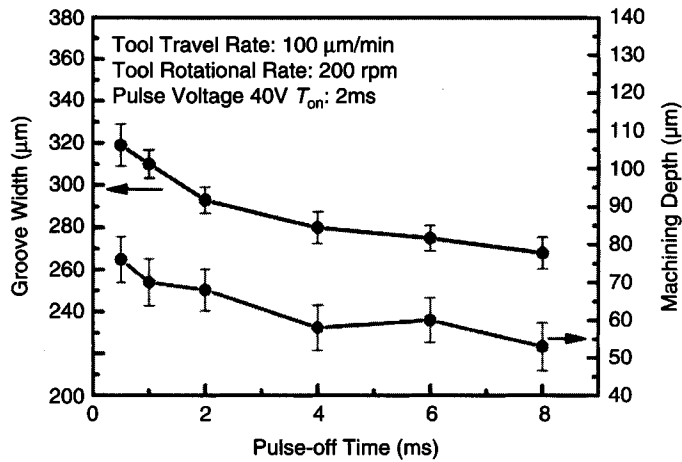


**Figure 7.13** Effect of pulse-off time in 2D glass micromachining by SACE. The depth and width of the microchannel are reduced with increasing pulse-off time. Reprinted from [137] with the permission of the *Journal of Micromechanics and Microengineering*.

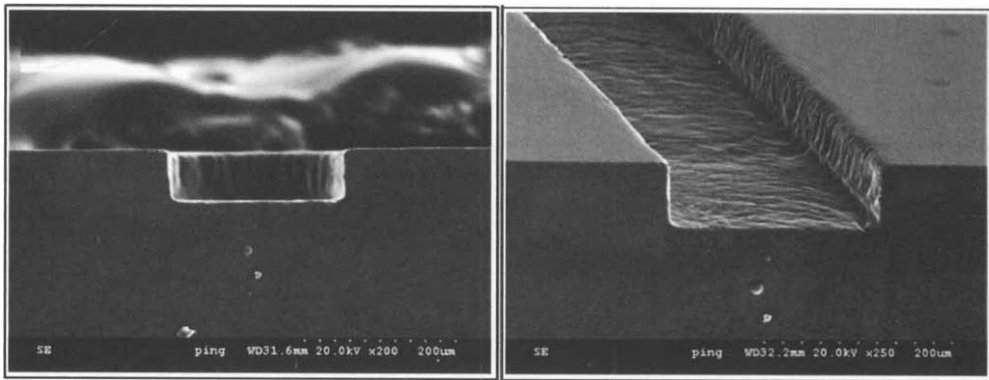


**Figure 7.14** Microchannels in glass machined using a pulsed voltage supply. The main machining parameters are:  $T_{on}:T_{off} = 2:2$  and tool-electrode rotation of 1500 rpm at 40 V. Reprinted from [137] with the permission of the *Journal of Micromechanics and Microengineering*.

qualities. Zheng et al. [137] also showed that by using optimal selected parameters ( $T_{on}:T_{off} = 2:2$ , tool-electrode rotation of 1500 rpm, and tool travel speed of 1 mm/min), the process becomes reproducible enough to obtain controlled depths of microstructures by carrying out successive layer by layer machining (Fig. 7.15). These results clearly demonstrate the potential of SACE micromachining and the direction to follow for future improvements. The key lies in controlling the heat power released by the electrochemical discharges (to avoid heat affected zones), overcoming the instability of the gas film, and promoting electrolyte flow to enhance chemical etching, which is the main effect responsible for excellent surface qualities.

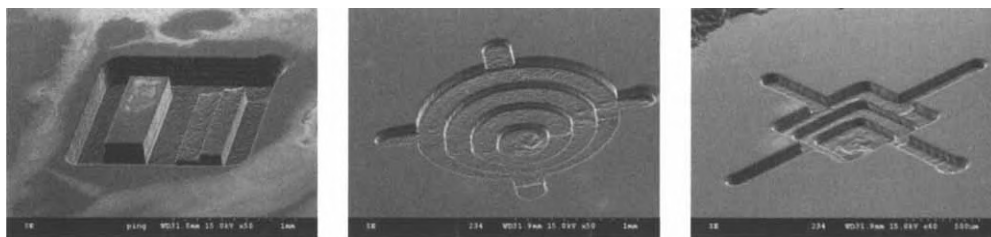


**Figure 7.15** Examples of 3D microstructures in Pyrex glass. Reprinted from [137] with the permission of the *Journal of Micromechanics and Microengineering*.

### 7.3.3.3 Travelling Wire Electrochemical Discharge Machining

Using a pulsed voltage supply in travelling wire electrochemical discharge machining (TW-ECDM) gives interesting results similar to drilling and 2D machining. Not only can the machined surface be improved but the risk of the wire breaking can also be reduced by choosing appropriate pulse-off times [133]. Another effect is the reduction of the over-cut.

## 7.4 Controlling the Tool–Workpiece Gap

Controlling the gap between the tool-electrode and the workpiece (termed *machining gap* in the following) can provide several benefits to the machining process, such as

- optimising the development of the gas film between the workpiece and the tool-electrode;
- optimising the discharge activity at the tip of the tool-electrode tip;
- promoting chemical etching by increased electrolyte flow below the tool-electrode.

In 2D machining the machining gap can be controlled, whereas this is not an easy task in drilling. To date there is no known method to measure the machining gap during drilling. A partial control of the machining gap has been achieved in gravity-feed drilling (here the gap is controlled to be zero) and in constant feed drilling (here the gap is of the same order of magnitude as the mean machining depth).

One way to overcome this difficulty was proposed by Jain et al. [62]. They used abrasive cutting tools. The feed of the tool-electrode was chosen in such a manner so as to always keep contact between the tool and the workpiece. Thus, the machining gap is of the same order of magnitude as the size of the abrasive particles on the tool-electrode (a few micrometres). The researchers showed that the material removal rate achieved with the abrasive tools is higher than that obtained with the conventional tools. This effect may be attributed to the increased gap, but, at the same time, as tool rotation (20 rpm)

was used, the increase in material removal rate is also certainly due to the effect of abrasive cutting. This is also confirmed by micrographs of the drilled holes showing grinding marks.

## 7.5 Searching for Process Control Signals

Before developing any control strategy, one should ask what exactly should be controlled. Ideally, the quality of machining (e.g., the geometrical tolerance of the microholes drilled) should be maintained in a given range. However, the quality of machining cannot be monitored directly online (unless some vision system is used). Two different strategies may be applied to overcome this problem.

The first strategy would be to try to control the evolution of the tool-electrode according a specified path and to try to keep all the other parameters as constant as possible. The path has to be then chosen such that the quality of machining is acceptable. However, this is not an active control strategy for the quality.

A better strategy would be to monitor indicators of quality loss, such as the local temperature in the machining zone, and then to react accordingly. For drilling, an indicator of the quality of a drilled hole of a given depth could be the time needed to drill it. A very high local temperature may result in a very fast drilling, which will result in heat affected zones. A very long drilling time could be an indicator of a leak of the electrolyte, which will result in reduced surface quality as chemical etching will not be optimal. As expected, once a very slow, or very fast, drilling is observed, it may already be too late, as the microhole with poor quality is already drilled. Statistical quality control could be a solution to this problem. By monitoring a run chart of the drilling time a process whose status is out of control can be detected before the quality actually becomes unacceptable.

At present, controlling the machining process in SACE is one of the greatest challenges and to date no active control has been achieved. In the ideal case, the local temperature, electrolyte composition, concentration, and the tool-electrode motion have to be both observable and controllable. The direct measurement of the local parameters is a very challenging task. However, the local parameters may be observed indirectly by easily accessible signals.

Not every signal is useful in controlling SACE. First, the information content of a signal necessary for observation or control of a system should be defined. As the machining and system state cannot be clearly defined at this moment, controllability and observability remain open questions. However, the signals that are available can be evaluated based on their information content. Therefore, only some qualitative considerations will be made. It has to be highlighted that even if a signal for control of SACE is available, the problem is far from being solved. Such a signal would give information on the machining status but the question "What has to be done to influence this status?" would remain open. Despite these difficulties, several strategies to take partial control of the process have been proposed and investigated to date, as was discussed in this chapter.

A non-exhaustive list of the potential control signals is given below, with the aim of stimulating new research in this domain.

1. *Tool-electrode displacement in gravity-feed drilling:* In gravity-feed drilling the progress of the tool-electrode  $z(t)$  provides direct information about the machining status. Some high-level control strategies can be developed based on this signal. For example, major problems such as the lack of electrolyte in the machining zone can be detected [130]. To date, this signal has never been used to develop any control strategy. Possible attempts could be to adjust the following parameters as function of  $z(t)$ :
  - the force acting on the tool-electrode;
  - the on and off time of the machining voltage;
  - the frequency of vibrations of the tool-electrode.
 A possible target would be to reduce the hydrodynamic regime in favour of the discharge regime. Some promising results were recently published by Morrison et al. [140]. The authors showed that the variance of gravity-feed drilling can be drastically reduced by some very simple control algorithms acting on the machining voltage.
2. *Tool-workpiece gap:* As shown by Peng and Liao [92], in TW-ECDM the gap between the tool and the workpiece can be observed using optical sensors and it is useful in improving the machining performance. It is obvious that the observation of this parameter in the case of drilling would also be very useful, in particular to avoid the problems linked to the hydrodynamic regime. Electrolyte flow and chemical etching could be optimised. However, to date there is no known method to measure the tool-workpiece gap during drilling.
3. *Force acting on the tool-electrode during drilling:* The force acting on the tool-electrode if it is moved inside the workpiece can be measured [122]. Using a very simple drilling algorithm, which consists of moving the tool-electrode down as long as the force measured is lower than a well-chosen threshold, it was shown that appearance of microcracks in glass could be largely avoided [122]. The use of a force-feedback control for SACE seems to be an interesting possibility.
4. *Local temperature:* Kulkarni et al. [74] demonstrated that it is possible to measure the local temperature using a pyrometer and that the local temperature is directly correlated with the current pulses observed during the electrical discharges. Furthermore, it is possible to obtain an indication of the local temperature by monitoring the gas film formation time [130].
5. *Current signal:* The current contains at least two important details. It is correlated with the local temperature of the workpiece [74]

and it can be used to monitor the status of the gas film [130]. Besides this, it contains information about the discharge activity and allows the qualitative estimation of the mean local temperature [130]. Another advantage of this signal is its easy access.

## 7.6 Summary

The following methods can be used to improve the machining quality (surface roughness, reduction of the heat affected zone) and the material removal rate in SACE:

- appropriate tool-electrode motion (rotation, vibration);
- using a pulsed voltage supply;
- adding abrasives to the electrolyte;
- appropriate tool-electrode material;
- appropriate tool-electrode shape (promoting flow of the electrolyte).

## 8 Designing a SACE Micromachining Set-up

---

The aim of this chapter is to provide some guidelines and design rules for the construction of a micromachining facility based on electrochemical discharges. The focus will be mainly on the specific characteristics of the SACE process, but some general practical aspects are also discussed.

A SACE micromachining facility is composed of following main elements:

- Electrodes
- Processing cell
- Power supply
- Positioning system

Depending on the application more components can be added, such as various sensors (e.g., current sensor, tool displacement sensor in gravity-feed drilling) or electrolyte supply systems.

Some general design aspects are discussed in Section 8.1. Section 8.2 is dedicated to drilling set-ups whereas Section 8.3 will discuss 2D micromachining set-ups.

### 8.1 General Design Rules

In this section, we discuss some general guidelines for the design of the various components of a micromachining facility using electrochemical discharges.

#### 8.1.1 Electrodes

Two electrodes are needed: one is the tool-electrode and the other is the counter-electrode. For both electrodes, appropriate materials should be selected.

The counter-electrode chosen should be as large as possible and made up of a material that is resistant to the electrolyte used. For sodium hydroxide, a good choice is stainless steel or nickel. As the counter-electrode is generally used with anodic polarisation, one should be aware that some electrochemical dissolution will take place. If the electrode surface is very large, current densities will remain small and therefore limit anodic dissolution of the electrode material. The geometry of the counter-electrode should be such that the inter-electrode resistance will remain constant during machining. This resistance should also



be minimised in order to reduce the gas film formation time as much as possible. A simple solution is to choose a large cylindrical ring surrounding the machining zone.

For the tool-electrode, the material should be chosen keeping in mind the following aspects. The tool-electrode should be as stiff as possible in order to avoid bending in drilling operations. The material has to be resistant to the electrolyte used. The thermal properties of the material influence the quantity of heat removed from the machining zone and the discharge activity as discussed in Section 7.3.1. The shape of the electrode also has a significant effect on the machining. Needle shaped tools are interesting geometries as they concentrate the discharge activity at the tool tip (Fig. 8.1). They generally result in better machining performances, especially from the point of view of the surface quality of the machined work sample. Commercially available needles are a cheap and excellent solution for laboratory set-ups. In general, stainless steel is a good material for the tool-electrode.

To date very little is known about tool wear. The two major causes of tool wear are chemical etching and anodic dissolution. The discharge activity at the tool-electrode may also cause some tool wear, but to date this has never been quantified. Based on the author's personal experience, tool wear is not a serious problem, and even after machining with the same tool-electrode (stainless steel) for several hours, no significant tool-wear could be measured.

Tool-electrodes can be fabricated in several ways. An excellent and flexible solution is wire electrical discharge grinding (WEDG), which is well suited for microfabrications [85]. An alternative way is to use anodic etching of tungsten. As shown by Lim et al. [82] very thin cylindrical electrodes (down to 50  $\mu\text{m}$ ) with controlled diameters can be fabricated. The important point is to use a high concentration of the electrolyte (typically 5 M KOH) and relatively high current densities around 10  $\text{mA}/\text{mm}^2$ . Thus, the diffusion layer around the electrode can be controlled in order to achieve various tool shapes by anodic

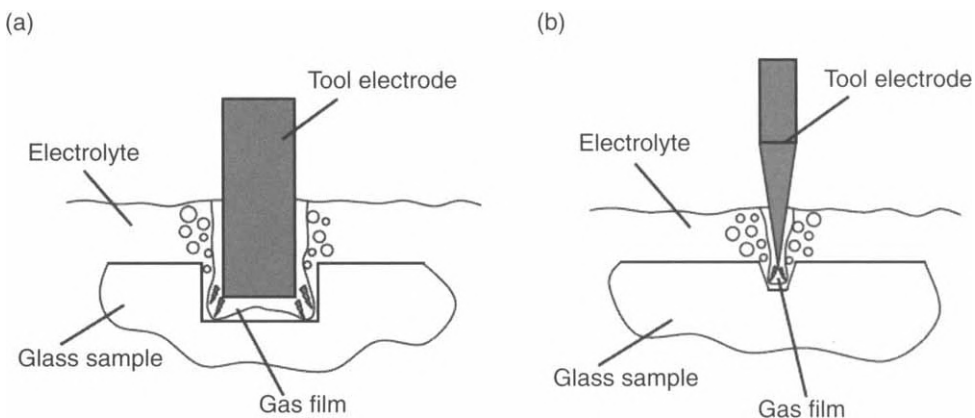


**Figure 8.1** Discharge activity around (a) a cylindrical and (b) a needle shaped tool-electrode [55].

dissolution. Note that from a practical point of view this method is very interesting, as it does not require any other equipment than that already used for the SACE facility.

### 8.1.2 Processing Cell

The machining takes place in the processing cell. Its main function is to hold the workpiece and the electrolyte. Care should be taken in order to use a geometry in which the electrolyte level can be controlled by some means. The electrolyte level is indeed an important parameter that affects the machining process. A variable electrolyte level results, in particular, in a variable inter-electrode resistance, variable discharge activity, and also affects the chemical etching of the SACE process. One has to be aware that during machining the electrolyte will evaporate and therefore fresh electrolyte has to be provided. An ideal solution is to have a processing cell that provides a continuous supply of the electrolyte [80]. Thus, the properties of the electrolyte are maintained relatively constant (concentration, temperature, and the level above the workpiece).

The processing cell should be made of a chemically inert material. Plexiglas is a good choice as it is transparent, which facilitates the observation of the machining process. The cell should be designed to minimise projection of the electrolyte on the other parts of the set-up.

### 8.1.3 Electrolyte

The electrolyte has two functions. First, it provides the electrical conductivity required to allow the formation of the gas film around the tool-electrode. Second, it etches the workpiece during machining. As a consequence, an appropriate electrolyte should be chosen for each material to be machined. Until now, systematic investigations on the optimal electrolyte composition were done only for glass micromachining. As discussed in previous chapters, alkaline electrolytes, in particular NaOH or KOH, are a good choice. The concentration can be chosen as a function of the desired machining performances. A concentration of about 30% by weight is a good choice and is commonly used for glass micromachining. If very thin substrates have to be machined, the concentration should be reduced [120]. Adding abrasive particles, such as SiC, to the electrolyte can also significantly improve the machining performances.

The mean temperature of the electrolyte affects the material removal rate. The utilisation of a preheated electrolyte at about 60–80°C is recommended.

### 8.1.4 Power Supply

For the simplest machining strategies a DC power supply is enough. However, the supply should be able to provide voltages and currents that are high

enough to build a gas film. Recall that the current density needed to build a gas film on the tool-electrode has a magnitude of about  $1 \text{ A/mm}^2$ . For a tool-electrode of a few square millimetres, this results in a power supply that can provide a current of a few amperes. The power supply should also be stable enough during the machining process. Commercially laboratory supplies are generally well suited.

For more advanced machining strategies the power supply should be able to operate in pulse mode. A cheap way to obtain this supply is to use a circuit similar to the Wehnelt current interrupter (Section 2.2). The utilisation of high-power pulse generators offers more flexibility. Typical values required for the pulse duration are in the millisecond range.

## 8.2 Drilling Set-ups

Three different types of drilling set-ups are described. The first set-up is a very simple one that can be made directly from the standard components available in a laboratory or machine workshop. The other two set-ups are more advanced ones that need more investment but allow more precise drilling.

One should be aware that during drilling some vapours are formed for all configurations and therefore the machining head should be protected against these corrosive vapours.

### 8.2.1 Manual Drilling

In this simplest configuration the operator pushes down the tool-electrode manually. By adding a mechanical stopper, the drilling depth may be controlled up to a certain extent.

### 8.2.2 Constant Feed Drilling

By mounting the tool-electrode holder on a motor-controlled stage, drilling can be done at a constant speed. Depending on the motor controller used, more or less complex velocity profiles can be used. By synchronising the vertical motion with tool rotation, it is possible to drill threads in glass as shown by Lee et al. [79].

It should be possible to control speeds in the range of a few micrometres per second (depending on the material to be machined) during the translation stage. For control of the depth, one should be able to measure the position of the workpiece. This may be done visually by touching the workpiece surface or by incorporating a profilometer into the set-up.

### 8.2.3 Gravity-Feed Drilling

This set-up is very flexible and offers several ways to control drilling accurately. It is also, to date, the most popular configuration for microdrilling using electrochemical discharges. In the design of the set-up, care should be taken to avoid friction in the guiding mechanism, as this would induce stick-slip motions that will reduce the precision for the control of the drilling depth. A possible solution is shown in Fig. 8.2.

The tool-electrode is mounted on a flexible structure that controls the vertical guidance of the tool. An optical sensor measures the tool displacement. An optional voice-coil motor can be added in order to control the force at which gravity-feed drilling is done. This motor can also be used to add vertical vibrations to the tool to promote the flow of the electrolyte inside the microhole. Rotation can also be included.

The flexible structure can be used to machine metals by electrical discharge machining or polymers by conventional machining. The stiffness of the structure is controlled by the geometry of the four hinges. In the case of circular hinges the overall stiffness  $K$  is given by:

$$K = \frac{8Ebe^{2.5}}{9\pi a^2\sqrt{r}}, \quad (8.1)$$

where  $E$  is the elastic modulus of the material used for the flexible structure. The geometric parameters are defined in Fig. 8.3. Note that the thickness  $e$  of the hinge is one of the most dominant factors. When using wire electrical discharge machining, it is possible to reduce  $e$  down to typically 100  $\mu\text{m}$ .

The configuration shown in Fig. 8.2 can also be used as a profilometer to detect the workpiece surface. By adding a controller, it is possible to keep the distance between the tool-electrode and the optical sensor constant. In this mode, the structure can be used as a force sensor (zero-displacement force

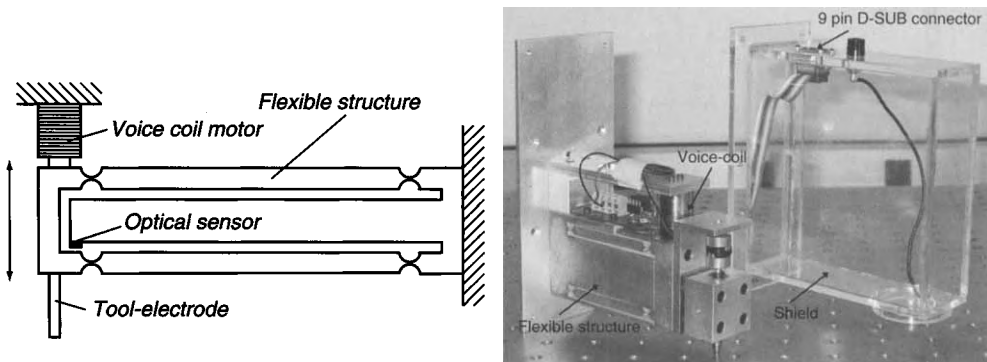


**Figure 8.2** Configuration of a gravity-feed drilling machining head.

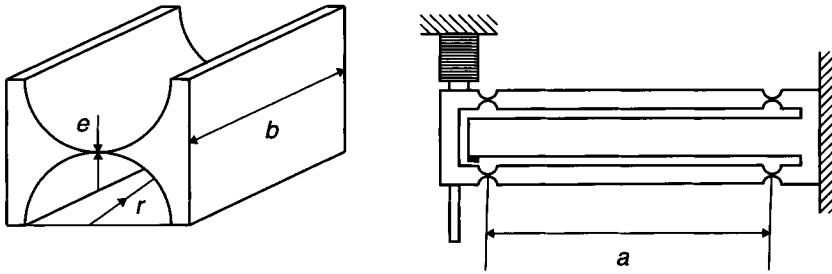


**Figure 8.3** Geometric parameters of a gravity-feed drilling machining head. Left: Detail of the geometry of the hinges used to build the flexible structure on the right.

measurement principle). This mode may be useful in constant feed drilling as it can provide a protection mechanism against too high feeding speeds [122].

### 8.3 2D Machining Set-ups

By using a manipulator with three degrees of freedom, 2D-SACE machining can be achieved. One may mount either the machining head or the processing

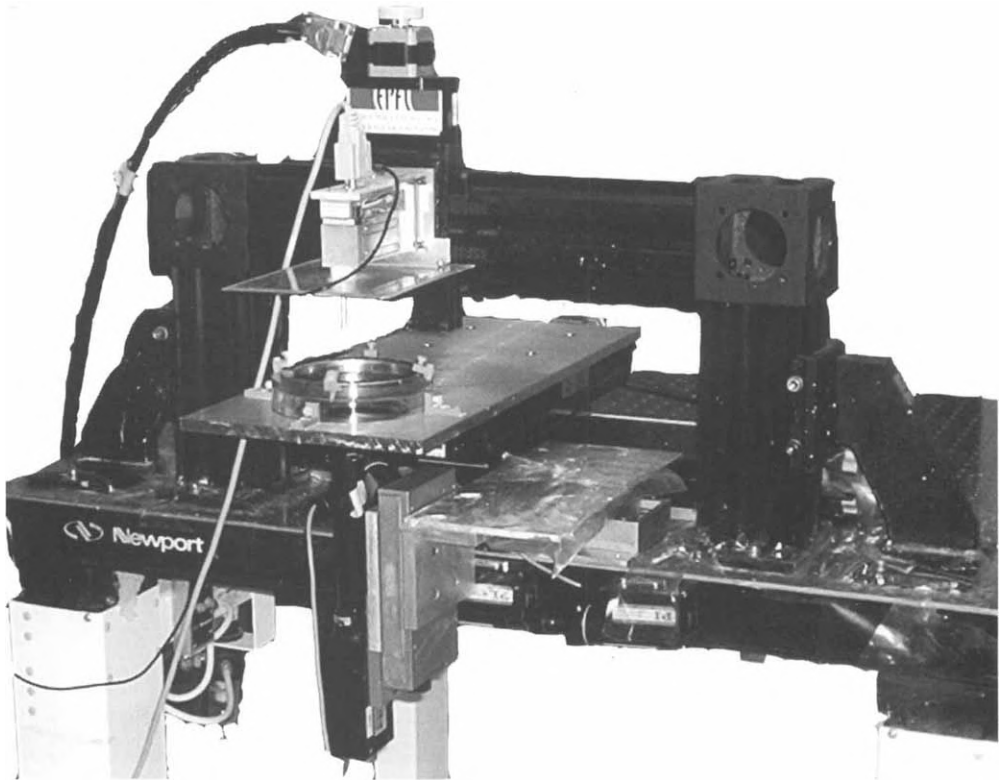


**Figure 8.4** A typical example of a SACE machining set-up realised with commercially available translation stages. Reprinted from [128] with permission from Elsevier.

cell on the XY stage. All the axes should be able to provide constant speeds of a few micrometres to a few hundred micrometres per second (the typical range of speeds used in 2D machining, as discussed in Section 6.3).

Commercially available translation stages are well suited for this purpose. Care should be taken when selecting the controller of the manipulator. Because SACE is still an unconventional micromachining technology, a controller that is as flexible as possible should be selected. Thus, different improvements can be made to the process.

In general, the possibility of detecting the workpiece surface should be added in order to be able to correct misalignment between the workpiece and the tool-electrode motion. A profilometer incorporated into the machining head, as presented in Fig. 8.2, is a good solution [127].

The example shown in Fig. 8.4 incorporates an additional vision system from below, which is helpful for alignment purposes. With the aid of this type of configuration, SACE machining can be used to modify glass substrates machined by other technologies such as wet etching [22].

Until now, micromachining with electrochemical discharges has proven to be an interesting technology for various hard to machine materials. In particular for glass micromachining, the degree of knowledge available has reached a level high enough to allow interesting applications. It is only recently that some potential control strategies for the process have begun to be investigated. A lot of work remains to be done in the field.

Just as further work on the process control is needed, there is also much to investigate on taking advantage of the properties of electrochemical discharges. Until now, only the heat produced by electrochemical discharges has been used. But more applications are possible: electrochemical discharges carry electrons and therefore localised electrochemical reactions can be carried out. The work done so far on contact glow discharge electrolysis shows the great potential that can be tapped by taking advantage of these reactions. Potential applications could be localised surface modifications of the machined substrate.

Another very interesting application was presented recently by the author. Electrochemical discharges can be used for the synthesis of metallic nanoparticles [78,141]. The principle is very simple. A metallic salt, such as copper sulphate, is added in low concentration to a supporting electrolyte. Electrochemical discharges are applied for a few hours. When the solution is dried (in order to remove the supporting electrolyte) metallic nanoparticles are obtained. The electrochemical discharges locally reduce the metal salt.

The mechanism of growth of the particles has not been clearly understood so far. However, it is believed that the particles are formed at the gas film–electrolyte interface. One possibility is that the size is determined by the amount of charge carried by each discharge and the concentration of the metal ions near the gas film. A typical discharge lasts for a few microseconds and carries a current of about 1 A. If we consider metal ions  $M^+$  with a concentration of a few millimolars and assume that the discharge electron reduces either an  $M^+$  ion or a  $H^+$  ion from water in the ratio of their concentrations, one discharge would give a metal particle of about 300 nm diameter. However, the formation of such a large particle in a single step is quite unlikely. A more probable growth mechanism is progressive nucleation discharges that reduce metal ions some of which form stable nuclei that in turn grow by adding atoms during successive discharges. Another mechanism that may contribute is the reduction of the metal ions by the hydrogen atmosphere of the gas film.

Figure 9.1 shows an example of nanoparticles formed from  $H_2PtCl_6$  and  $NaAuCl_4$  (below 10 mM). The supporting electrolyte was  $HClO_4$  (1 M). Energy dispersive X-ray (EDX) analysis revealed that the particles formed are an alloy

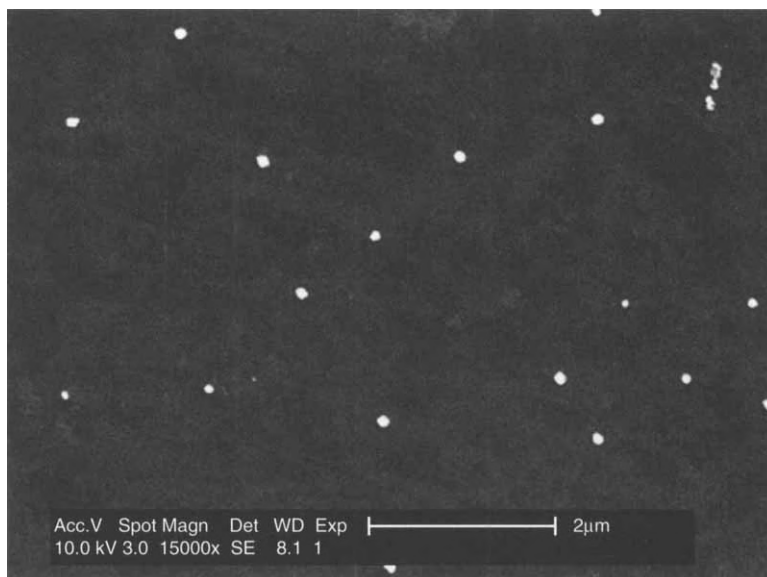


**Figure 9.1** Micrograph of nanoparticles formed by electrochemical discharges from  $\text{H}_2\text{PtCl}_6$  and  $\text{NaAuCl}_4$  in  $\text{HClO}_4$ . The active cathode was rotated at 2000 rpm. Reprinted from [78] with permission from Elsevier.

of platinum and gold. The exact physical structure is not yet clear and still has to be investigated. In this experiment the active cathode is rotated in order to control the size of the particles.

The rotating electrode causes the solution near it to rotate too, which in turn provides a centrifugal force to the particles to move away from the electrode. The basic idea is that once the nanoparticles reach a given mass, they will leave the reaction zone and stop growing.

The author is convinced that the potential of electrochemical discharges in micromachining and nanoscience is enormous and that we are only at the initial stages of making use of this tremendous potential. Electrochemical discharges provide heat and electrons at high energy localised in space and time. The combination of these two effects and its wise utilisation may certainly open up new and exciting applications and research. The author hopes that the present book will contribute in this direction and also stimulate new ideas.



# References

1. K. Allesu: *Electrochemical Discharge Phenomenon in Manufacturing Processes*, PhD Thesis, Indian Institute of Technology, Kanpur (1988).
2. K. Allesu, A. Ghosh, M.K. Muju: "Preliminary qualitative approach of a proposed mechanism of material removal in electrical machining of glass." *European Journal Mech. Eng.* **36** (1992), p. 202.
3. H. Ammagnat: "Contribution à l'étude de l'interrupteur Wehnelt." *Comptes rendus hebdomadaires des séances de l'Académie des Sciences* **CXXVIII** (1899), p. 988.
4. H. Angerstein-Kozłowska, B.E. Conway, B.A. Sharp: "The real conditions of electrochemically oxidized platinum surfaces. Part I. Resolution of component process." *Electroanalytical Chemistry and Interfacial Electrochemistry* **43** (1973), p. 9.
5. K. Azumi, T. Mizuno, T. Akimoto, T. Ohmori: "Light emission from Pt during high-voltage cathodic polarisation." *Journal of the Electrochemical Society* **146** (1999), pp. 3374–3377.
6. I. Basak: *Electrochemical Discharge Machining Mechanism and a Scheme for Enhancing Material Removal Capacity*, PhD Thesis, Indian Institute of Technology, Kanpur (1991).
7. I. Basak, A. Ghosh: "Mechanism of spark generation during electrochemical discharge machining: a theoretical model and experimental verification." *Journal of Materials Processing Technology* **62** (1996), pp. 46–53.
8. I. Basak, A. Ghosh: "Mechanism of material removal in electrochemical discharge machining: a theoretical model and experimental verification." *Journal of Materials Processing Technology* **71** (1997), p. 350.
9. E. Becquerel: "Note sur le passage des courants électriques au travers des gaz incandescents." *Comptes rendus hebdomadaires des séances de l'Académie des Sciences* **LXV** (1867), pp. 1097–1099.
10. J. Bergonié: "Les rayons X et leurs applications médicales." *Revue philomatique de Bordeaux et du Sud-Ouest* (1900), pp. 49–68.
11. B. Bhattacharyya, B.N. Doloi, S.K. Sorkhel: "Experimental investigations into electrochemical discharge machining (ECDM) of non-conductive ceramic materials." *Journal of Materials Processing Technology* **95** (1999), p. 145.
12. P. Boissonneau, P. Byrne: *Journal of Applied Electrochemistry* **30** (2000), pp. 767–775.
13. E. Bouchotte: "Dialyse des courants d'induction." *Comptes rendus hebdomadaires des séances de l'Académie des Sciences* **LXV** (1867), pp. 759–760 and 995–998.
14. N.St.J. Braithwaite: *Plasma Sources Sci. Technol.* **9** (2000), pp. 517–527.
15. S.R. Broadbent, J.M. Hammersley: *Proceedings of the Cambridge Philosophical Society* **53** (1957), pp. 629–641, MR **19**:989e.
16. D.A.G. Bruggeman: *Annalen der Physik* **24** (1935), pp. 636–664.
17. E.W. Calwell: "A new liquid interrupter." *Electr. Rev. (N.Y.)* **34** (1899), p. 277.
18. J.M. Chin Kwie Joe, L.J.J. Janssen, S.J.D. van Strelen, J.H.G. Verbunt, W.M. Sluyter: *Electrochimica Acta* **33** (1988), pp. 769–779.
19. S.K. Chark, P.V. Rao: "Trepanning of Al<sub>2</sub>O<sub>3</sub> by electro-chemical discharge machining (ECDM) process using abrasive electrode with pulsed DC supply." *International Journal of Machine Tools & Manufacture* **47** (2007), pp. 2061–2070.
20. F. Collins: *The Radio Amateur's Hand Book*, Thomas Y. Corwell Co., New York (1922).
21. N.H. Cook, G.B. Foote, P. Jordan, B.N. Kalyani: "Experimental studies in electro-machining." *Trans. ASME, Journal of Engineering for Industry* (1973), pp. 945–950.
22. A. Daridon, V. Fascio, J. Lichtenberg, R. Wüthrich, H. Langen, E. Verpoorte, N.F. De Rooij: *Fresenius J. Anal. Chem.* **371** (2001), pp. 261–269.

23. T.F. Didar, A. Dolatabadi, R. Wüthrich: "Characterization and modeling of 2D-glass micro-machining by spark-assisted chemical engraving (SACE) with constant velocity." *Journal of Micromechanics and Microengineering* **18** (2008).
24. T.F. Didar, A. Dolatabadi, R. Wüthrich: "Local hardness and density variation in glass substrates machined with Spark Assisted Chemical Engraving (SACE)." *Materials Letters* **63** (2009), pp. 51–53.
25. P.P. Ewald (editor): *Fifty Years of X-Ray Diffraction*, International Union of Crystallography (1962).
26. K.T. Compton: "A study of the Wehnelt electrolytic interrupter." *Physical Review* **30** (1910), p. 161.
27. J.A. D'Arsonval: "Interrupteur électrolytique." *Comptes rendus hebdomadaires des séances de l'Académie des Sciences CXXVIII* (1899), p. 529.
28. R. Wüthrich, B. Despont, P. Maillard, H. Bleuler: "Improving drilling speed in Spark Assisted Chemical Engraving (SACE) by tool vibration." *Journal of Micromechanics and Microengineering* **16** (2006), pp. N28–N31.
29. J. Eigeldinger, H. Vogt: *Electrochimica Acta* **45** (2000), pp. 4449–4456.
30. M. Esashi, Y. Matsumoto, S. Shoji: "Absolute pressure sensors by air-tight electrical feedthrough structure." *Sensors and Actuators A21–A23* (1990), pp. 1048–1052.
31. V. Fascio, R. Wüthrich, D. Viquerat, H. Langen: *International Symposium on Micromechanics and Human Science (MHS'99)* (1999), pp. 179–183.
32. V. Fascio: *Etude de la microstructuration du verre par tincelage assist par attaque chimique: une approche électrochimique*, PhD Dissertation Thesis 2691, Swiss Federal Institute of Technology (EPFL), Lausanne (2002).
33. V. Fascio, H.H. Langen, H. Bleuler, Ch. Comninellis: "Investigation of the spark assisted chemical engraving." *Electrochemistry Communications* **5** (2003), pp. 203–207.
34. V. Fascio, R. Wüthrich, H. Bleuler: "Spark assisted chemical engraving in the light of electrochemistry." *Electrochimica Acta* **49** (2004), p. 3997.
35. H. Fizeau, L. Foucault: "Recherches sur l'intensité de la lumière émise par le charbon dans l'expérience de Davy." *Annales de Chimie et de Physique XI*, 3ème série (1844), p. 370.
36. R.A. Fressenden: "Receiver for electromagnetic waves." US Patent No. 727,331 (1903).
37. R. Fox: "The John Scott Medal." *Proceedings, American Philosophical Society* **112** (1968), p. 416.
38. C. Gabrielli, F. Huet, M. Keddam, A. Sahar: *Journal of Applied Electrochemistry* **19** (1989), pp. 683–696.
39. A.M. Gadalla, B. Bozkurt, N.M. Faulk: "Modeling of thermal spalling during electrical discharge machining of titanium diboride." *Journal of the American Society* **74** (1991), pp. 801–806.
40. N. Gautam, V.K. Jain: "Experimental investigations into ECSD process using various tool kinematics." *International Journal of Machine Tools and Manufacture* **38** (1998), p. 15.
41. A. Ghosh: "Electrochemical discharge machining: principle and possibilities." *Sādhana* **22** (1997), pp. 435–447.
42. J.P. Glas, J.W. Westwater: *International Journal of Heat and Mass Transfer* **7** (1964), pp. 1427–1443.
43. W.R. Grove: "On the electro-chemical polarity of gases." *Philosophical Transactions of the Royal Society of London* **142** (1852), p. 87.
44. J. Gubkin: *Annalen der Physik* **32** (1887), p. 114.
45. Ch. Guilpin: Dissertation Thesis, Université Paris VI (1975).
46. Ch. Guilpin, J. Garbaz-Olivier: "Analyse de la lumière émise aux électrodes pendant les effets d'électrodes, dans des solutions aqueuses d'électrolyte." *Spectrochimica Acta* **32B** (1977), p. 155.
47. Ch. Guilpin, J. Garbaz-Olivier: *Spectrochimica Acta* **32B** (1977), pp. 155–164.
48. E.A. Guggenheim: "The conceptions of electrical potential differences between two phases and individual activities of ions." *Journal of Physical Chemistry* **33** (1929), p. 842.

49. J.M. Hammersley: *Ann. Math. Statist* **28** (1957), pp. 790–795.
50. M.-S. Han, B.-K. Min, S.J. Lee: “Improvement of surface integrity of electro-chemical discharge machining process using power-mixed electrolyte.” *Journal of Materials Processing Technology* **191** (2007), p. 224.
51. M.-S. Han, B.-K. Min, S.J. Lee: “Modeling gas film formation in electrochemical discharge machining process using a side-insulated electrode.” *Journal of Micromechanics and Microengineering* **18** (2008), 045019.
52. A. Hessenbruch: “Rutherford’s 1901 experiment on radiation energy and his creation of a stable detector.” *Archive for History of Exact Sciences* **54** (2000), p. 403.
53. A. Hickling, M.D. Ingram: “Contact glow discharge electrolysis.” *Transaction of the Faraday Society* **60** (1964), p. 783.
54. A. Hickling, M.D. Ingram: “Glow discharge electrolysis.” *Journal of Electroanalytical Chemistry* **8** (1964), p. 65.
55. L. Hof: “3D-microstructuring of glass.” Master’s Thesis, TU Delft, Netherlands (2003).
56. P. Hoho: “Phénomène calorifique produit par le courant électrique au contact d’un solide et un liquide.” *La lumière électrique* **52** (1894), p. 165.
57. W.J. Humphrey: “The Wehnelt electrolytic break.” *Physical Review* **9** (1899), p. 30.
58. V.K. Jain, P.S. Rao, S.K. Choudhury, K.P. Rajurkar: “Experimental investigations into travelling wire electrochemical spark machining (TW-ECSM) of composites.” *Trans. ASME, Journal of Engineering for Industry* **113** (1991), p. 75.
59. V.K. Jain: “ECSM—a new way to machine polymer composites.” *Proc. INCARF-93 Conf.*, IIT, Delhi (December 1993).
60. V.K. Jain, P.M. Dixit, P.M. Pandey: “On the analysis of the electrochemical spark machining process.” *International Journal of Machine Tools and Manufacture* **39** (1999), p. 165.
61. V.K. Jain, S.K. Chak: “Electrochemical spark trepanning of alumina and quartz.” *Machining Science and Technology* **4** (2000), pp. 277–290.
62. V.K. Jain, S.K. Choudhury, K.M. Ramesh: “On the machining of alumina and glass.” *International Journal of Machine Tools and Manufacture* **42** (2002), pp. 1269–1276.
63. V.K. Jain, S. Adhikary: “On the mechanism of material removal in electrochemical spark machining of quartz under different polarity conditions.” *Journal of Materials Processing Technology* **200** (2008), pp. 460–470.
64. H.M. Jaeger, S.R. Nagel: *Science* **255** (1992), p. 1524.
65. M. Jalali, P. Maillard, R. Wüthrich: “Towards a better understanding of glass gravity-feed micro-hole drilling with electrochemical discharges.” *Journal of Micromechanics and Microengineering*, accepted.
66. L.J.J. Janssen, S.J.D. van Stralen: *Electrochimica Acta* **26** (1981), pp. 1011–1022.
67. L.J.J. Janssen: *Electrochimica Acta* **34** (1989), pp. 161–169.
68. S.F. Jones, G.M. Evans, K.P. Glavin: “Bubble nucleation from gas cavities—a review.” *Advances in Colloid and Interface Science* **80** (1999), pp. 27–50.
69. P. Kasteleyn, C. Fortuin: *Journal of the Physical Society of Japan* **26**(Suppl.) (1969), pp. 11–14.
70. H.H. Kellogg: “Anode effect in aqueous electrolysis.” *Journal of the Electrochemical Society* **97** (1950), p. 133.
71. D.-J. Kim, Y. Ahn, S.-H. Lee, Y.-K. Kim: “Voltage pulse frequency and duty ratio effects in a electrochemical discharge microdrilling process of Pyrex glass.” *International Journal of Machine Tools and Manufacturing* **46** (2006), p. 1064.
72. E. Klupathy: “Zur Theorie des Wehneltunterbrechers.” *Annalen der Physik* **9** (1902), p. 147.
73. H. de B. Knight: *The Arc Discharge: Its Application to Power Control*, Chapman & Hall Ltd, London (1960).
74. A. Kulkarni, R. Sharan, G.K. Lal: “An experimental study of discharge mechanism in electrochemical discharge machining.” *International Journal of Machine Tools and Manufacturing* **42** (2002), pp. 1121–1127.

75. A. Kulkarni, R. Sharan, G.K. Lal: "Measurement of temperature transients in the electrochemical discharge machining process." *Temperature: Its measurement and Control in Science and Industry* **7** (2003), p. 1069.
76. H. Kurafuji, K. Suda: "Electrical discharge drilling of glass." *Annals of the CIRP* **16** (1968), p. 415.
77. D. Kondepudi, I. Prigogine: *Modern Thermodynamics—From Heat Engines to Dissipative Structures*, John Wiley & Sons (1999).
78. A. Lal, H. Bleuler, R. Wüthrich: "Fabrication of metallic nanoparticles by electrochemical discharges." *Electrochemistry Communications* **10** (2008), pp. 488–491.
79. E.S. Lee, D. Howard, E. Liang, S.D. Collins, R.L. Smith: "Removable tubing interconnects for glass-based micro-fluidic systems made using ECDM." *Journal of Micromechanics and Microengineering* **14** (2004), pp. 535–541.
80. Y.-S. Liao, W.-Y. Peng: "Study of hole-machining on Pyrex wafer by electrochemical discharge machining (ECDM)." *Materials Science Forum* **505–507** (2006), p. 1207.
81. G. Liger-Belair, M. Vignes-Adler, C. Voisin, B. Robillard, Ph. Jeandet: "Kinetics of gas discharging in a glass of champagne: the role of nucleation sites." *Langmuir* **18** (2002), pp. 1294–1301.
82. H.-J. Lim, Y.-M. Lim, S.H. Kim, Y.K. Kwak: "Self-aligned micro tool and electrochemical discharge machining (ECDM) for ceramic materials." *Proceedings of SPIE* **4416** (2001), pp. 348–353.
83. P. Ludewig: "Zur Theorie des Wehneltunterbrechers." *Annalen der Physik* **29** (1909), p. 175.
84. P. Maillard, B. Despont, H. Bleuler, R. Wüthrich: "Geometrical characterization of micro-holes drilled in glass by gravity-feed with spark assisted chemical engraving (SACE)." *Journal of Micromechanics and Microengineering* **17** (2007), pp. 1343–1349.
85. T. Masuzawa, M. Fujino, K. Kobayashi, T. Suzuki: *Annals of the CIRP* **34** (1985), p. 431.
86. M. Mousa, A. Allagui, H.D. Ng, R. Wüthrich: "The effect of thermal conductivity of the tool electrode in spark assisted chemical engraving gravity-feed micro-drilling." *Journal of Micromechanics and Microengineering* **19** (2009), accepted (November 2008).
87. J.C. Maxwell: *A Treatise on Electricity and Magnetism*, 3rd edn, Vol. 1, Clarendon Press, Oxford (1892), p. 440.
88. M. Jalali, P. Maillard, S.P. Mishra, L. Kadem, R. Wüthrich: "Modeling gravity feed micro hole drilling by electrochemical discharge." *2nd International Conference on Micro-Manufacturing*, September 10–13, 2007, Greenville, South Carolina, USA.
89. H.W. Morse: "Spectra from the Wehnelt interrupter. I." *Astrophysical Journal* **19** (1904), p. 162.
90. H.W. Morse: "Spectra from the Wehnelt interrupter. II." *Astrophysical Journal* **21** (1905), p. 223.
91. V.V. Nesarikar, V.K. Jain, S.K. Choudhury: "Travelling wire electrochemical spark machining of thick sheets of Kevlar-epoxy composites." *Proceedings of the Sixteenth AIMTDR Conference* (1994), pp. 672–677.
92. W.Y. Peng, Y.S. Liao: "Study of electrochemical discharge machining technology for slicing non-conductive brittle materials." *Journal of Materials Processing Technology* **149** (2004), pp. 363–369.
93. R. Poplar: *Phénomènes électriques dans les gaz*, Monographies Dunod 41, Paris (1963).
94. Quet: "Sur divers phénomènes électriques." *Comptes rendus hebdomadaires des séances de l'Académie des Sciences* **XXXVI** (1853), p. 1012.
95. Y.P. Raizer: *Gas Discharge Physics*, Springer Verlag, Berlin (1991).
96. M.E. Rose, S.S. Korff: *Phys. Rev.* **59** (1941), p. 850.
97. B.R. Sarkar, B. Doloi, B. Bhattacharyya: "Parametric analysis on electrochemical discharge machining of silicon nitride ceramics." *International Journal of Advanced Manufacturing Technology* **28** (2006), pp. 873–881.
98. S.K. Sengupta, R. Singh, A.K. Srivastava: *Journal of the Electrochemical Society* **145** (1998), pp. 2209–2213.

99. H. Th. Simon: "Das Wirkungsgesetz des Wehnelt-Unterbrechers." *Wiedemann's Ann. (Annalen der Physik)* **68** (1899), p. 273.
100. Y.P. Singh, V.K. Jain, P. Kumar, D.C. Agrawal: "Machining piezoelectric (PZT) ceramics using electrochemical spark machining (ECSM) process." *Journal of Materials Processing Technology* **58** (1996), pp. 24–31.
101. D. Stauffer, A. Aharony: *Introduction to Percolation Theory*, Taylor & Francis, London (1998).
102. S. Tandon: *Machining of Composites—A New Approach*, M.Tech. Thesis, IIT Kanpur, India (July 1987).
103. S. Tandon, V.K. Jain, P. Kumar, K.P. Rajurkar: "Investigations into machining of composites." *Precision Engineering* **12** (1990), pp. 227–238.
104. H. Tokura, I. Kondoh, M. Yoshikawa: "Ceramic material processing by electrical discharge in electrolyte." *Journal of Materials Science* **24** (1989), p. 991.
105. H. Tsuchiya, T. Inoue, M. Miyazaki: "Wire electro-chemical discharge machining of glasses and ceramics." *Bull. Japan Soc. of Prec. Engg.* **19** (1985), p. 73.
106. C. Tsutsumi, K. Okano, T. Suto: "High quality machining of ceramics." *Journal of Materials Processing Technology* **37** (1993), p. 639.
107. J.C. Valognes, J.P. Bardet, P. Mergault: *Spectrochimica Acta* **43B** (1988), pp. 799–809.
108. V.S.M. van der Willigen: "Ueber Licht und Wärme-Erscheinungen bei kräftigen galvanischen Batterie; Bildung des Lichtbogens zwischen Metall und Flüssigkeit, und Auftreten von Licht an einer der in die Flüssigkeit getauchten Elektroden." *Annalen der Physik* **169** (1854), p. 285.
109. J. Venczel: *Electrochimica Acta* **15** (1970), pp. 1909–1920.
110. J. Violle, M. Chassagny: "Revue des travaux récents en électricité: Sur l'électrolyse." *Comptes rendus hebdomadaires des séances de l'Académie des Sciences* **CVIII** (1889), p. 284.
111. H. Vogt: *Comprehensive Treatise of Electrochemistry* **6** (1983), p. 445.
112. H. Vogt: *Journal of Applied Electrochemistry* **13** (1983), pp. 87–88.
113. H. Vogt: *Electrochimica Acta* **29** (1984), pp. 167–173.
114. H. Vogt: *Electrochimica Acta* **29** (1984), pp. 175–180.
115. H. Vogt: *Electrochimica Acta* **34** (1989), pp. 1429–1432.
116. H. Vogt: *Journal of Applied Electrochemistry* **29** (1999), pp. 137–145.
117. H. Vogt, J. Thonstad: "Review of the causes of anode effects in aluminium electrolysis." *Aluminium* **79** (2003), pp. 98–102.
118. A. Voller, B. Walter: "Ueber die Vorgänge im Wehnelt'schen elektrolytischen Unterbrecher." *Wiedemann's Ann. (Annalen der Physik)* **68** (1899), p. 526.
119. A. Wehnelt: "Ein elektrolytischer Stromunterbrecher." *Wiedemann's Ann. (Annalen der Physik)* **68** (1899), p. 233. The article was originally published in *Elektrotechnische Zeitschrift* **4** (1899), p. 76.
120. J. West, A. Jadhav: "ECDM methods for fluidic interfacing through thin glass substrates and the formation of spherical microcavities." *Journal of Micromechanics and Microengineering* **17** (2007), pp. 403–409.
121. R.F. Wolfenbittel: *Silicon Sensors and Circuits: On-Chip Compatibility*, Sensor Physics and Technology Series, Chapman & Hall, London (1995).
122. R. Wüthrich, V. Fascio, D. Viquerat, H. Langen: "In situ measurement and micro-machining of glass." *International Symposium on Micromechatronics and Human Science (MHS'99)*, Nagoya (1999) p. 185.
123. R. Wüthrich: "Spark assisted chemical engraving—a stochastic modelling approach." Dissertation Thesis 2776, Swiss Federal Institute of Technology, EPF Lausanne (2003).
124. R. Wüthrich, E.A. Baranova, H. Bleuler, Ch. Comninellis: "A phenomenological model for macroscopic deactivation of surface processes." *Electrochemistry Communications* **6** (2004), pp. 1199–1205.

125. R. Wüthrich, Ch. Comninellis, H. Bleuler: "Bubble evolution on vertical electrodes under extreme current densities." *Electrochimica Acta* **50** (2005), p. 5242.
126. R. Wüthrich, L.A. Hof, A. Lal, K. Fujisaki, H. Bleuler, Ph. Mandin, G. Picard: "Physical principles and miniaturization of Spark Assisted Chemical Engraving (SACE)." *Journal of Micromechanics and Microengineering* **15** (2005), pp. 268–275.
127. R. Wüthrich, K. Fujisaki, Ph. Couthy, L.A. Hof, H. Bleuler: "Spark assisted chemical engraving (SACE) in microfactory." *Journal of Micromechanics and Microengineering* **15** (2005), pp. 276–280.
128. R. Wüthrich, V. Fascio: "Machining of non-conductive materials using electrochemical discharge phenomenon—an overview." *International Journal of Machine Tools and Manufacture* **45** (2005), pp. 1095–1108.
129. R. Wüthrich, L. Hof: "The gas film in spark assisted chemical engraving (SACE)—a key element for micro-machining applications." *International Journal of Machine Tools and Manufacture* **46** (2006), p. 828.
130. R. Wüthrich, U. Spaelter, H. Bleuler: "The current signal in Spark Assisted Chemical Engraving (SACE), what does it tell us?" *Journal of Micromechanics and Microengineering* **16** (2006), p. 779.
131. R. Wüthrich, U. Spaelter, Y. Wu, H. Bleuler: "A systematic characterisation method for gravity feed micro-hole drilling in glass with Spark Assisted Chemical Engraving (SACE)." *Journal of Micromechanics and Microengineering* **16** (2006), p. 1891.
132. C.T. Yang, S.S. Ho, B.H. Yan: "Micro hole machining of borosilicate glass through electrochemical discharge machining (ECDM)." *Key Engineering Materials* **196** (2001), pp. 149–166.
133. C.T. Yang, S.L. Song, B.H. Yan, F.Y. Huang: "Improving machining performance of wire electrochemical discharge machining by adding SiC abrasive to electrolyte." *International Journal of Machine Tools and Manufacture* **46** (2006), pp. 2044–2050.
134. A. Zastawny: *Nucl. Instr. and Meth. in Phys. Res.* **A385** (1997), p. 239.
135. I. Zaytsev, G. Aseyev: *Properties of Aqueous Solution of Electrolytes*, CRC Press, Boca Raton, (1992).
136. Z.-P. Zheng, H.-C. Su, F.-Y. Huang, B.-H. Yan: "The tool geometrical shape and pulse-off time of pulse voltage effects in a Pyrex glass electrochemical discharge microdrilling process." *Journal of Micromechanics and Microengineering* **17** (2007), p. 265.
137. Z.-P. Zheng, W.-H. Cheng, F.-Y. Huang, B.-H. Yan: "3D microstructuring of Pyrex glass using the electrochemical discharge machining process." *Journal of Micromechanics and Microengineering* **17** (2007), p. 960.
138. J. Macintyre: "Wehnelt's new interrupter: improvement in X-ray apparatus." *Journal of Laryngology, Rhinology, and Otology* **XIV** (1899), pp. 169–170.
139. R. Zallen: *The Physics of Amorphous Solids*, Wiley-VCH (1998).
140. A. Morrison, L. Rodrigues, R. Wüthrich: "Reducing variability in spark assisted chemical engraving gravity feed drilling of glass." *1st Microsystems and Nanoelectronics Research Conference* (MNRC 2008), October 15, 2008, Ottawa, Canada (available on IEEE Explorer).
141. R. Wüthrich, A. Lal, H. Bleuler: "A table-top set-up for nano-particles production with electrochemical discharges." *5th International Workshop on Microfactories*, October 25–27, Besençon, France.

# Index

- Abrasive jet machining, 7
- Activation, 31
- Active anode, 83, 97, 106, 111
- Active cathode, 70, 74, 82–83, 87–88, 97, 111
- Active electrode, 14, 73, 75–76, 80–83, 85, 87–88, 91, 93–94
  - temperature of, 80
- Adherence region, bubble.
  - See* Bubble adherence region
- Adhesion force. *See* Force, adhesion
- Anode, 39
  - active, 21–22, 33
  - effect, 30
- Anodic bonding, 1
- Anodic dissolution, 138
- Anodic etching, 158
- Anodic reaction, 41
- Arc discharge.
  - See also* Discharge, arc
  - region, 89, 127
- Avalanche, 24, 27
  
- Bending of the tool-electrode, 124–125, 127
- Bethe lattice. *See* Lattice
- Bistability, 61
- Breakdown voltage. *See* Voltage, breakdown
- Bruggeman equation, 48–50
- Bubble adherence region, 51–58
  - bubbles, 52
  - cluster, 52
  - infinite cluster, 55–57
  - model of, 57–58
  - percolation theory, 52–55
  - percolation threshold, 55–57
- Bubble bulk region, 50
  - resistances of, 50
- Bubble coalescence, 3, 47, 52, 79–80, 92
- Bubble coverage fraction, 29, 35, 48, 51, 59–60, 63–65, 74, 78–79
- Bubble departure radius, 46
- Bubble detachment frequency, 59, 75
- Bubble detachment time.
  - See* Bubble detachment frequency
- Bubble diffusion region, 49–51
  - resistance of, 50–51
- Bubble distribution, 52
- Bubble evolution
  - equation, normalised, 78
  - on gas evolving electrode, 59–61
- Bubble formation
  - during electrolysis, 44–47
- Bubble growth, 45, 75, 80
- Bubble height, 60, 77
- Bubble layer, 3, 47–49
- Bubble nucleation, 58
- Bubble shape, 74
- Bubble size, 51, 55, 58–59
- Bubble, gas(s), 19, 21, 35, 44–45, 59–60
- Bubble, probability of growth, 52
- Bulk region. *See* Bubble, bulk region
- Bulter-Volmer equation, 40–41
- Buoyancy force. *See* Force, Buoyancy
  
- Caldwell-Simon current
  - interrupter, 70
- Caley tree. *See* Lattice
- Capillary force. *See* Force, capillary
- Cathode, 39
- Cathode spot, 27
- Cathode, active, 22, 33
- Cathodic reaction, 41

- Cell
  - electrochemical. *See also* Electrochemical cell
  - galvanic. *See also* Galvanic cell
  - voltage. *See also* Terminal voltage
- Ceramic, 97, 99, 102, 109–110
  - drilling, 118
  - micromachining
    - application to, 107
- CGDE. *See* Contact glow discharge electrolysis
- Characteristics, current-voltage.
  - See* Current-voltage characteristics
- Charge transfer resistance, 37
- Chemical etching, 7, 97–101, 107, 109–112, 119, 127, 132–134, 137
  - promoting chemical etching, 138–144
    - adding abrasive to electrolyte, 144
  - tool-electrode rotation, 143–144
  - tool-electrode shape effect, 139–140
  - tool-electrode vibration effect, 140–142
- Chemical machining, ECDM, 7
- Chemical potential, 35
- Cluster, 52. *See also* Infinite cluster; Normalized cluster number
  - size, 55, 58
- Coefficient of faradic gas
  - generation, 59
- Conductivity, molar ionic. *See* Molar ionic conductivity
- Constant feed drilling, 160
- Constant velocity feed, 115
  - drilling, 127–128
- Contact angle, 45–46, 92
- Contact glow discharge electrolysis (CGDE), 29–33, 165
  - anodic CGDE, 32–33
  - cathodic CGDE, 33
  - glow discharge electrolysis, 30–32
- Corrosion, 42
- Counter-electrode, 2, 157
- Coverage fraction, bubble.
  - See* Bubble coverage fraction
- Coverage fraction, gas film.
  - See* Gas film coverage fraction
- Cracks, thermal.
  - See* Thermal cracks
- Critical current, 74, 76–77.
  - See also* Current, critical
- Critical voltage, 2, 75–77, 88–89, 127, 145. *See also* Voltage, critical
  - mean, 75
  - reducing the, 92–93, 147–148
- Current, critical, 63–65
- Current density. *See also* Exchange current density; Local current density, Nominal current density
  - local, 75, 80
  - nominal, 71, 75
    - increase in, 74
- Current fluctuations, 89, 91
- Current interrupter.
  - See* Electrolytic interrupter
- Current, normalised, 65
- Current-voltage characteristics, 61–67
  - electrochemical discharge region, 63
  - instability region, 63
  - limiting current region, 63
  - normalised voltage, 65
  - ohmic region, 62–63
  - over potential region, 62
  - thermodynamic, 62
- Depth increase rate, 134–135
- Depth, drilling. *See* Drilling depth
- Depth, microchannel.
  - See* Microchannel depth
- Detachment frequency. *See* Bubble, detachment frequency
- Diameter, of microhole, 122–123
- Diffusion region. *See* Bubble, diffusion region



- Direct polarity machining, 97
- Discharge activity, 115–116,  
118–119, 121, 124, 127–128,  
136, 140, 144, 146–147,  
152, 155  
inside the gas films, 83–92  
    current evolution equations,  
        89–90  
    electrochemical discharges  
        probability distribution,  
            84–86  
    fluctuations in current, 90–92  
    mean current, 90–92  
    terminal voltage, function of,  
        86–89
- Discharge, electrochemical  
    arc, 27–29  
    glow, 29–33. *See also* Contact  
        glow discharge electrolysis  
    self-sustained, 25–27  
    townsend, 23–27
- Discharge regime, 118, 139–141,  
147, 154
- Drag coefficient, 119
- Drag force, 119
- Drift velocity, 43–44
- Drilling depth, 118, 120–126, 128  
    limiting, 118  
    time, 120–121
- Drilling set-up, 160–162  
    constant feed drilling, 160  
    gravity feed drilling, 161–162  
    manual drilling, 160
- Drilling speed, 139–140, 142, 147  
    limiting, 118
- Drilling time, 140–141, 143,  
148–149, 153
- Drilling, ceramic, 118
- Drilling, constant feed.  
    *See* Constant feed drilling
- Drilling, glass. *See* Glass drilling
- Drilling, gravity-feed.  
    *See* Gravity-feed drilling
- Drilling, manual. *See* Manual  
drilling
- ECM. *See* Electrochemical  
machining
- EDM. *See* Electrical discharge  
machining
- Electrical arcs, 13, 17
- Electrical conductivity  
    in electrolytes, 43–44
- Electrical discharges, 13–14, 21, 23,  
29–30
- Electrical discharge machining  
(EDM), 1, 97–98, 100, 110, 138
- Electrical field, 24, 26–28, 31, 36, 43,  
83, 88, 91  
    reduced, 24
- Electrochemical cell  
    out of thermodynamic  
        equilibrium, 37–40
- Electrochemical discharge, 29,  
115–116, 119, 134–135  
    contact glow discharge  
        electrolysis, 29–33. *See also*  
            *individual entry*  
    early application, discovery, 13–15  
    heat power of, 98, 109  
    historical view, 13–34  
    nature of, 22–29  
        arc discharge, 27–29  
        townsend discharge, 23–27  
    plasma electrolysis, 13  
    probability distribution of, 84–86  
    spectrum of, 21–22  
    Wehnelt interrupter, 15–21
- Electrochemical discharge machining  
(ECDM). *See* Spark-assisted  
chemical engraving
- Electrochemical discharge region, 63
- Electrochemical double layer, 36
- Electrochemical machining (ECM),  
1, 138
- Electrochemical potential, 36
- Electrochemical spark machining.  
    *See* Spark-assisted chemical  
        engraving
- Electrode, 157  
    active. *See* Active electrode

- counter-electrode, 157
- surface roughness, 46
- wettability, 46, 60, 63
- wetting of the, 74–75
- Electrode effects.
  - See* Electrochemical discharge
- Electrodes, gas evolving, 35–67
  - bubble adherence region, 51–58.
    - See also individual entry*
  - bubble diffusion region, 49–51
  - bubble evolution, gas evolving electrode, 59–61
  - bubble formation during electrolysis, 44–47
  - bubble layer, 47–49
  - electrochemistry, 35–44
    - charge transfer current characteristics, 40–41
    - electrical conductivity, electrolytes, 43–44
  - electrochemical cell,
    - thermodynamic equilibrium, 37–40
  - hydrogen evolution, 41–42
  - Nernst equation, 35–37
  - oxygen evolution, 41–42
  - mean stationary current–voltage characteristics, 61–67.
    - See also individual entry*
- Electrolysis, 38
- Electrolyte concentration, 43, 110, 112–113
- Electrolyte conductivity, 37
- Electrolyte level, 159
- Electrolyte temperature, 110, 113
- Electrolyte, local flow, 138
- Electrolyte, strong, 44
- Electrolyte, weak, 44
- Electrolytic interrupter, 15–18, 81–82
- Electromotive force, 38
- Electron emission, 27–28
- Electron transfer, 37
- Electron yield. *See* Probability of discharge
- Electrostatic bonding, 1
- Emission
  - field, 28–29
  - thermal-assisted field, 29
  - thermionic, 28, 33
- Energy dispersive X ray spectroscopy, 110, 165
- Entrance diameter, 122–123
- Entropy, 38–39, 42
- Equations. *See* Bruggeman equation; Bubble evolution; Butler-Volmer equation; Maxwell equation; Nernst equation
- Etching, 97–101, 107, 109–112, 119, 127–128, 132–134 anodic.
  - See also* Anodic etching
- Exchange current density, 40
- Excitation energy, 22
- Excitation potential. *See* Potential, excitation
- Faraday's constant, 59
- Faraday's law, 35, 59
- Field emission, 83, 87–89.
  - See also* Emission, field
- Field-assisted thermal bonding, 1
- First Townsend coefficient.
  - See* Townsend coefficient
- Fluctuations, current.
  - See* Current fluctuations
- Force
  - adhesion, 58
  - buoyancy, 45–47, 58
  - capillary, 45–47
- Formation time, of the gas film, 121
- Galvanic cell, 38
- Gas bubbles. *See* Bubbles, gas
- Gas constant. *See* Universal gas constant
- Gas evolution, 73
  - electrochemical gas film formation by, 74–75
- Gas evolving electrodes.
  - See* Electrode, gas evolving

- Gas film, 3, 14, 18–19, 21, 26–27, 29, 32–33  
controlling the gas film, 92–94  
    gas film controlling stability, 93–94  
    gas film shape controlling, 94  
    reducing the critical voltage, 92–93  
coverage fraction, 88  
discharge activity, 83–92.  
    *See also individual entry*  
formation of, 69–81  
    electrochemical gas evolution, 74–75  
    electrode geometry, influence of, 75–76  
    electrolyte concentration, influence of, 76–77  
    hybrid mechanisms, 80–81  
    by local electrolyte evaporation, 70–73  
    random variable, critical voltage, 75  
formation time, 21, 77–79  
instability, 148  
key elements, 69–94  
lifetime, 61  
shape of the, 81–83  
stability, 69, 92–94  
thickness, 26–27, 69, 82  
Gas ionisation, 23  
Gas void fraction, 48–49  
GDE. *See* Glow discharge electrolysis  
Glass drilling, 117–118, 122  
Glass micromachining, 97  
    application to, 105–107  
Glass transition temperature, 119  
Glass viscosity, 119  
Glow discharge. *See* Contact glow discharge electrolysis  
Glow discharge electrolyses (GDE), 30–32  
Gravity-feed drilling, 116–127, 139–140, 142–143, 146–149, 154, 161–162  
discharge regime, 118–119  
drilling repeatability, 120  
drilling time, 120–121  
hydrodynamic regime, 119–120  
inter-electrode resistance  
    influence, 121–122  
machining quality, 125–127  
microhole dimensions, 122–125  
Half reaction, 37  
Heat affected zone, 3, 126  
Heyrovsky reaction, 42  
Hole diameter, 122–124, 127–128  
Hydrodynamic regime, 119–120, 139–141, 146–148, 154  
Hydrogen evolution, 74  
    reaction, 37, 41–42  
Hydrogen peroxide, 30–32, 42  
Indium-tin-oxide, 110  
Infinite cluster, 58  
Instability region, 15, 61, 63, 88, 127  
Inter-electrode resistance, 37, 74, 77, 81, 93, 121–122, 157, 159  
Ion mobility, 43  
Ionisation, 23–24, 31  
    potential. *See also* Potential, ionisation  
Joule heating, 29, 69–71, 73, 75, 80, 82, 88, 92  
Laser machining, 8  
Lattice  
    bethe, 55–57  
    square, 54  
Leaching, 110  
Lifetime, gas film.  
    *See* Gas film, lifetime  
Limiting current region, 63  
Limiting drilling depth, 118  
Limiting drilling speed, 118  
Local current density, 48, 61, 63  
Local heat generation, 138

- 2D and 3D Machining, 128–135
  - machined microchannels depth, 133–134
  - machined microchannels quality, 129–132
  - tool distance workpiece, influence of, 134–135
  - tool travel speed, 132–133
- Machining depth, 100, 113
- Machining gap, 138
- Machining over-cut, 119, 136, 148–150
- Machining process, controlling, 137–155
  - heat generated, controlling, 144–152
  - heat transfer influencing
    - through electrolyte, 145
    - through tool-electrode, 146–147
  - critical voltage, reducing, 147–148
  - pulsed voltage machining, 148–152. *See also* Pulsed voltage machining
  - process analysis, 137–138
  - process control signals
    - searching for, 153–155
  - promoting chemical etching, 138–144. *See also* Chemical etching
  - tool-workpiece gap, controlling, 152–153
- Machining quality, 125–127
- 2D Machining set-up, 162–163
- Machining strategies, 115–136
  - constant velocity feed drilling, 127–128
  - gravity-feed drilling, 116–127. *See also individual entry*
  - 2D and 3D machining, 128–135. *See also individual entry*
  - TW-ECDM, 135–136
- Machining temperature, 101, 118
- Machining time, 141–143, 148–149
- Machining tool. *See* Tool-electrode
- Machining voltage, 97–99, 102, 105–106, 108, 110, 113
- Machining zone, 98–100, 107–109
  - viscosity. *See under* Viscosity of the machining zone
- Machining, tapping mode. *See* Tapping mode machining
- Manual drilling, 160
- Material removal mechanism, 97–113
  - chemical contributions, 110–112
  - considerations, 97–100
  - high depths machining, 107–109
  - low depths machining, 100–107
    - ceramic micromachining applications, 107
    - glass micromachining applications, 105–107
  - material removal rate, 103–105
  - thermal model, 100–102
- Material removal rate, 69, 97–98, 100, 103–105, 115–120, 122–123, 127, 129, 136
- Maxwell equation, 48–49
- Mean critical voltage, 75
- Mechanical drilling, 7
- Mechanical machining, ECDM, 7
- MEMS. *See* Microelectromechanical systems
- Microchannel, 129–132
  - depth, 132, 134–135
  - increase rate, 135
- Microdrilling, 115
- Microelectromechanical systems (MEMS), 1
- Microhole, 122–125
  - diameter, 109, 123
- Micromachining, 1, 4
  - technology, 6–8
- Molar ionic conductivity, 43–44
- Monte-Carlo simulation, 54
- Nanoindentation, 111
- Nanoparticle, 165
  - micrograph of, 166
- Nanotechnology, 5, 6

- Nernst equation, 35–37
- Nominal current density, 61.  
*See also* Current density, nominal
- Normalised bubble evolution equation. *See* Bubble evolution equation, normalised
- Normalised current. *See* Current, normalised
- Normalised current-voltage characteristics.  
*See* Current-voltage characteristics
- Normalised heat power, 104–106
- Normalised voltage, 78–79.  
*See also* Voltage, normalised
- Normalized cluster number, 54
- Nucleation probability, 55, 58
- Nucleation site, 46  
activation, 46, 58
- Ohmic drop, 39, 83
- Ohmic region, 62–63
- Order parameter, 57
- Over Potential region, 62
- Over-cut, 119, 123, 132, 136, 144, 148–150, 152
- Oxidation reaction, 37
- Oxido-reduction reaction, 40
- Oxygen evolution reaction, 42
- Passivation, 42
- Percolation  
phase transition, 53, 57  
theory, 52–55  
threshold, 53, 55–57
- Photofabrication, 7
- Plasma electrolysis.  
*See* Electrochemical discharge
- Poisson distribution, 85–87, 90
- Poisson process, 84–86
- Positioning system, 157
- Potential drop, 39, 50–51, 83
- Potential region, over. *See* Over potential region
- Potential, chemical. *See* Chemical potential
- Potential, electrochemical.  
*See* Electrochemical potential
- Potential, excitation, 24
- Potential, ionisation, 23–24, 27
- Potential, water decomposition.  
*See* Water decomposition potential
- Powder blasting, 7
- Power supply, 159–160
- Probability of discharge, 85
- Probability, nucleation.  
*See* Nucleation probability
- Processing cell, 159
- Pulsed voltage, 93
- Pulsed voltage machining, 148–152  
2D and 3D machining, 149–152  
microhole drilling, 148–149  
TW-ECDM, 152
- Quality, machining. *See* Machining quality
- Quality, statistical quality control.  
*See* Statistical quality control
- Quality, surface. *See* Surface quality
- Quartz machining, 106, 110
- Reaction(s). *See* Anodic reaction; Cathodic reaction; Half reaction; Heyrovsky reaction; Hydrogen evolution reaction; Oxidation reaction; Oxido-reduction reaction; Oxygen evolution reaction; Redox reaction; Reduction reaction; Tafel reaction; Volmer reaction
- Redox reaction, 36
- Reduced electrical field.  
*See* Electrical field
- Reduction reaction, 37
- Resistance(s). *See* Bubble bulk region, resistance; Bubble diffusion region, resistance; Charge transfer resistance; Inter-electrode resistance

Reverse polarity machining, 97  
Rotation, tool-electrode.

*See* Tool-electrode rotation

Roughness, surface. *See* Surface roughness

Roundness error, 124

Ruhmkorff coil, 16

SACE. *See* Spark-assisted chemical engraving

s-cluster, 52–54, 57–58

Second Townsend coefficient.

*See* Townsend coefficient

Secondary electron, 25, 28

Softening Littleton point, 119

Spark. *See also* Discharge, electrochemical distance, 29

Spark-Assisted Chemical Engraving (SACE), 2–9, 69

2D machining set-up, 162–163

definition of, 2–3

design rules, 157–160

electrodes, 157–159

electrolytes, 159

power supply, 159–160

processing cell, 159

designing, micromatching set-up, 157–163

drilling set-up, 160–162.

*See also individual entry*

historical view, 5–6

machining examples, 3–5

micromachining technology, 6–8

chemical machining, 7

mechanical machining, 7

thermal machining, 8

Square lattice. *See* Lattice

Stability of the gas film, 116

Stationary current-voltage characteristics, 61–67

Statistical quality control, 153

Stick-slip, 161

Stoichiometric number, 59

Strong electrolyte. *See* Electrolyte, strong

Surface quality, 97, 110, 115, 132

Surface roughness, 127–128, 136, 144–145, 148, 155

Surface tension, 45–46

Surfactant, 92

Tafel reaction, 42

Tapping mode machining, 140

Temperature of the active electrode.

*See* Active electrode

Temperature, glass transition.

*See* Glass transition temperature

Temperature, machining.

*See* Machining temperature

Terminal voltage, 38

Thermal assisted field emission, 83, 146

Thermal conductivity of the tool-electrode, 146

Thermal cracks, 144

Thermal diffusivity, 101

Thermal machining, ECDM, 8

Thermal-assisted field emission. *See* Emission

Thermionic emission.

*See* Emission

Thermodynamic region, 62

Tool feeding mechanism, 115

Tool-electrode, 2, 157–161, 163

Tool-electrode bending. *See* Bending of the tool-electrode

Tool-electrode material, 120

Tool-electrode rotation, effect of, 143–44

Tool-electrode shape, 120

Tool-electrode temperature, 147

Tool-electrode, thermal conductivity. *See* Thermal conductivity of the tool-electrode

Tool-electrode vibration, effect of, 140–142

Tool-electrode wear, 117

Tool-travel speed, 129

- Townsend coefficient  
  first, 25  
  second, 25
- Townsend discharge, 23–27
- Transition voltage, 89, 127
- Travelling wire electrochemical discharge machining (TW-ECDM), 135, 145, 152
- TW-ECDM. *See* Travelling wire electrochemical discharge machining
- Ultrasonic machining, 7
- Universal gas constant, 35, 59
- Velocity, drift. *See* Drift velocity
- Vibration, tool-electrode.  
  *See* Tool-electrode vibration
- Viscosity, 119  
  of the machining zone, 119
- Volmer reaction, 41
- Voltage scan rate, 75
- Voltage, breakdown, 25, 27–29
- Voltage, cell. *See also* Terminal voltage  
  critical, 63, 65, 67  
  normalised, 65
- Voltage, critical, 14–15, 20.  
  *See also* Critical voltage
- Voltage, machining. *See* Machining voltage
- Voltage, normalised, 20.  
  *See also* Normalised voltage
- Voltage, pulsed. *See* Pulsed voltage
- Voltage, transition. *See* Transition voltage
- Water decomposition potential, 41, 62, 64
- Water jet machining, 7
- Weak electrolyte.  
  *See* Electrolyte, weak
- Wear, tool-electrode.  
  *See* Tool-electrode wear
- WEDG. *See* Wire electrical discharge grinding
- WEDM. *See* Wire electrical discharge machining
- Wetting, 74–75, 81
- Wire electrical discharge grinding (WEDG), 4, 158
- Wire electrical discharge machining (WEDM), 136
- Wire electrochemical discharge machining, 6
- Work function, 28
- Working point, 119